



TEZ ŞABLONU ONAY FORMU
THESIS TEMPLATE CONFIRMATION FORM

1. Şablonda verilen yerleşim ve boşluklar değiştirilmemelidir.
2. **Jüri tarihi** Başlık Sayfası, İmza Sayfası, Abstract ve Öz'de ilgili yerlere yazılmalıdır.
3. İmza sayfasında jüri üyelerinin unvanları doğru olarak yazılmalıdır. Tüm imzalar **mavi pilot kalemle** atılmalıdır.
4. **Disiplinlerarası** programlarda görevlendirilen öğretim üyeleri için jüri üyeleri kısmında tam zamanlı olarak çalıştıkları anabilim dalı başkanlığının ismi yazılmalıdır. Örneğin: bir öğretim üyesi Biyoteknoloji programında görev yapıyor ve biyoloji bölümünde tam zamanlı çalışıyorsa, İmza sayfasına biyoloji bölümü yazılmalıdır. İstisnai olarak, disiplinler arası program başkanı ve tez danışmanı için disiplinlerarası program adı yazılmalıdır.
5. Tezin **son sayfasının sayfa** numarası Abstract ve Öz'de ilgili yerlere yazılmalıdır.
6. Bütün chapterlar, referanslar, ekler ve CV sağ sayfada başlamalıdır. Bunun için **kesmeler** kullanılmıştır. **Kesmelerin kayması** fazladan boş sayfaların oluşmasına sebep olabilir. Bu gibi durumlarda paragraf (¶) işaretine tıklayarak kesmeleri görünür hale getirin ve yerlerini **kontrol edin**.
7. Figürler ve tablolar kenar boşluklarına taşmamalıdır.
8. Şablonda yorum olarak eklenen uyarılar dikkatle okunmalı ve uygulanmalıdır.
9. Tez yazdırılmadan önce PDF olarak kaydedilmelidir. Şablonda yorum olarak eklenen uyarılar PDF dokümanında yer almamalıdır.
10. Tez taslaklarının kontrol işlemleri tamamlandığında, bu durum öğrencilere METU uzantılı öğrenci e-posta adresleri aracılığıyla duyurulacaktır.
11. Tez yazım süreci ile ilgili herhangi bir sıkıntı yaşarsanız, [Sıkça Sorulan Sorular \(SSS\)](#) sayfamızı ziyaret ederek yaşadığınız sıkıntıyla ilgili bir çözüm bulabilirsiniz.

1. Do not change the spacing and placement in the template.
2. Write **defense date** to the related places given on Title page, Approval page, Abstract and Öz.
3. Write the titles of the examining committee members correctly on Approval Page. **Blue ink** must be used for all signatures.
4. For faculty members working in **interdisciplinary programs**, the name of the department that they work full-time should be written on the Approval page. For example, if a faculty member staffs in the biotechnology program and works full-time in the biology department, the department of biology should be written on the approval page. Exceptionally, for the interdisciplinary program chair and your thesis supervisor, the interdisciplinary program name should be written.
5. Write **the page number of the last page** in the related places given on Abstract and Öz pages.
6. All chapters, references, appendices and CV must be started on the right page. **Section Breaks** were used for this. **Change in the placement** of section breaks can result in extra blank pages. In such cases, make the section breaks visible by clicking paragraph (¶) mark and **check their position**.
7. All figures and tables must be given inside the page. Nothing must appear in the margins.
8. All the warnings given on the comments section through the thesis template must be read and applied.
9. Save your thesis as pdf and Disable all the comments before taking the printout.
10. This will be announced to the students via their METU students e-mail addresses when the control of the thesis drafts has been completed.
11. If you have any problems with the thesis writing process, you may visit our [Frequently Asked Questions \(FAQ\)](#) page and find a solution to your problem.

Yukarıda bulunan tüm maddeleri okudum, anladım ve kabul ediyorum. / I have read, understand and accept all of the items above.

Name : Hossein
Surname : Jodati
E-Mail : hossein.jodati@metu.edu.tr
Date :
Signature : _____

3-DIMENSIONAL BORON-DOPED HYDROXYAPATITE/BAGHDADITE
POROUS SCAFFOLDS FOR BONE TISSUE ENGINEERING

A THESIS SUBMITTED TO
THE GRADUATE SCHOOL OF NATURAL AND APPLIED SCIENCES
OF
MIDDLE EAST TECHNICAL UNIVERSITY

BY

HOSSEIN JODATI

IN PARTIAL FULFILLMENT OF THE REQUIREMENTS
FOR
THE DEGREE OF DOCTOR OF PHILOSOPHY
IN
BIOMEDICAL ENGINEERING

JANUARY 2023

Approval of the thesis:

**3-DIMENSIONAL BORON-DOPED HYDROXYAPATITE/BAGHDADITE
POROUS SCAFFOLDS FOR BONE TISSUE ENGINEERING**

submitted by **Hossein Jodati** in partial fulfillment of the requirements for the degree of **Doctor of Philosophy in Biomedical Engineering, Middle East Technical University** by,

Prof. Dr. Halil Kalıpcılar
Dean, Graduate School of **Natural and Applied Sciences**

Prof. Dr. Vilda Purutcuoğlu
Head of the Department, **Biomedical Engineering**

Prof. Dr. Zafer Evis
Supervisor, **Engineering Sciences, METU**

Prof. Dr. Volkan Şahin
Co-Supervisor, **Prosthodontics, Kırıkkale University**

Examining Committee Members:

Prof. Dr. Ayşen Tezcaner
Engineering Sciences, METU

Prof. Dr. Zafer Evis
Engineering Sciences, METU

Prof. Dr. Fatih Akkurt
Chemical Engineering, Gazi University

Prof. Dr. Dilek Keskin
Engineering Sciences, METU

Assist. Prof. Dr. Ammar Z. G. Alshemary
Biomedical Engineering, Karabük University

Date: 16.01.2023

I hereby declare that all information in this document has been obtained and presented in accordance with academic rules and ethical conduct. I also declare that, as required by these rules and conduct, I have fully cited and referenced all material and results that are not original to this work.

Name Last name : Hossein Jodati

Signature :

ABSTRACT

3-DIMENSIONAL BORON-DOPED HYDROXYAPATITE/BAGHDADITE POROUS SCAFFOLDS FOR BONE TISSUE ENGINEERING

Jodati, Hossein
Doctor of Philosophy, Biomedical Engineering
Supervisor: Prof. Dr. Zafer Evis
Co-Supervisor: Prof. Dr. Volkan Şahin

January 2023, 184 pages

A wide range of biomaterials is used to fabricate scaffolds for hard tissue engineering. However, perfect scaffolds with the required characteristics to answer all clinical needs have not been produced yet. In this thesis, a novel ceramic-based chemical combination of boron-doped hydroxyapatite (BHA) and baghdadite (BAG) was employed to fabricate composite 3-dimensional (3D) porous scaffolds to promote scaffolds' properties. The ultimate goal was achieved through the following steps: 1) BHA powders with different molar ratios of boron dopant were synthesized, their physicochemical, mechanical, as well as *in vitro* biological characteristics were evaluated, and the optimum group was selected. 2) Through the modified sol-gel technique, which was proposed and optimized for the first time, synthesis and characterization of BAG nanoparticles were accomplished by overcoming the premature gelation problem. 3) The novel ceramic-based 3D porous composite scaffolds were successfully prepared using BHA and BAG as the primary and secondary components. The incorporation of BAG contributed to making more porous scaffolds (over 40 %) with larger surface area and micropore volumes. The

composite scaffolds almost solved the low degradation problem of BHA, where their higher degradations matched the degradation rate appropriate for the gradual transfer of loads from implants to newly formed bone. Besides higher bioactivity, enhanced cell proliferation, and higher osteogenic differentiation were observed in composite scaffolds. Eventually, BHA-BAG composite scaffolds converged the advantages of both components to satisfy the various requirements needed for bone tissue engineering applications and took us one step forward on the road to producing an ideal scaffold.

Keywords: Boron-doped hydroxyapatite, Baghdadite, Composite, Scaffold

ÖZ

KEMİK DOKU MÜHENDİSLİĞİ İÇİN 3-BOYUTLU BORON KATKILI HİDROKSİAPATİT/BAĞDADİT GÖZENEKLİ İSKELELER

Jodati, Hossein
Doktora, Biyomedikal Mühendisliği
Tez Yöneticisi: Prof. Dr. Zafer Evis
Ortak Tez Yöneticisi: Prof. Dr. Volkan Şahin

Ocak 2023, 184 sayfa

Kemik doku mühendisliğinde kullanılmak üzere bir çok farklı biyomalzemeden doku iskeleleri üretilmektedir. Ancak, gerekli özelliklere sahip ve tüm klinik ihtiyaçlara cevap veren mükemmel iskeleler henüz üretilmemiştir. Bu tezde, iskelelerin özelliklerini geliştirmek amacıyla, bor katkılı hidroksiapatit (BHA) ve bağdadit (BAG)'ın seramik bazlı yeni bir kimyasal kombinasyonu 3-boyutlu (3B) kompozit iskelelerin üretiminde kullanılmıştır. Nihai hedefe aşağıdaki adımlarla ulaşılmıştır: 1) Farklı molar oranda bor içeren BHA tozları sentezlenmiştir, sentezlenen malzemelerin fizyokimyasal, mekanik ve ayrıca in vitro biyolojik özellikleri değerlendirilmiştir, ve birbirleriyle karşılaştırılarak optimum grup seçilmiştir. 2) İlk kez önerilen ve optimize edilen modifiye sol-jel yöntemiyle, erken jelleşme probleminin üstesinden gelinerek, BAG sentezi ve karakterizasyonu gerçekleştirilmiştir. 3) Birincil ve ikincil bileşenler olarak, BHA ve BAG tozları kullanılarak, seramik tabanlı 3B gözenekli kompozit iskeleler başarılı bir şekilde hazırlanmıştır. Bağdaditin dahil edilmesi, daha geniş yüzey alanına ve mikrogözenek hacmine sahip olan ve daha gözenekli iskelelerinin (%40'ın üzerinde) yapılmasına katkıda bulunmuştur. Kompozit iskelelerin yüksek bozunma oranları, implanttan

yeni oluřan kemięe kademeli yk aktarımının saęlanması iin gerekli bozunma oranı ile rtřerek, BHA'nın dřk bozunma oranı problemini byk lde zmřtr. Kompozit iskelelerde, daha yksek biyoaktivitenin yanısıra, geliřmiř hcre ęalması ve daha yksek osteojenik farklılařma gzlemlenmiřtir. Sonu olarak, BHA-BAG kompozit iskeleler, her iki bileřenin avantajlarını bir araya getirerek, kemik doku mhendislięi uygulamaları iin ihtiya duyulan eřitli gereksinimleri karřılamıř ve ideal iskele retiminde bizi bir adım ileriye gtrmřtr.

Anahtar Kelimeler: Bor katkılı hidroksiapatit, Baędadit, Kompozit, Iskele

To my parents and my wife

ACKNOWLEDGMENTS

I would like to express my gratitude to my dear advisor, Prof. Dr. Zafer Evis. It was not possible to accomplish my Ph.D. program and this thesis without his guidance, support, and advice.

I would also express my appreciation to my co-advisor Prof. Dr. Volkan Şahin, as well as Prof. Dr. Ayşen Tezcaner, Assist. Prof. Dr. Ammar Alshemary, and Prof. Dr. Erdal Çelik for their contributions.

I want to thank my friends, Dr. Ali Motameni, Dr. Engin Pazarçeviren, Milad Fathi, and Sema Akbaba for their help and valuable friendship.

Finally, I would like to express my special thanks to my precious father and mother for their kindness and endless support, and to my beautiful wife, Samira, for her unconditional love and her patience.

TABLE OF CONTENTS

ABSTRACT.....	v
ÖZ.....	vii
ACKNOWLEDGMENTS.....	x
TABLE OF CONTENTS.....	xi
LIST OF TABLES.....	xiv
LIST OF FIGURES.....	xv
LIST OF ABBREVIATIONS.....	xix
CHAPTERS	
1 INTRODUCTION.....	1
1.1 Bone tissue and bone defect treatment.....	2
1.2 Ideal scaffold for BTE.....	6
1.2.1 Structural features.....	7
1.2.2 Biological and mechanical requirements.....	8
1.2.3 Composition.....	10
1.3 Boron-doped hydroxyapatite (BHA).....	13
1.4 Baghdadite (BAG).....	16
1.5 Composite scaffolds.....	18
1.5.1 Fabrication of composite scaffolds.....	19
1.5.2 BAG incorporated scaffolds.....	22
1.6 Aim of the thesis.....	27
2 MATERIALS AND METHODS.....	31
2.1 Materials.....	31

2.2	Methods	32
2.2.1	Synthesis and characterization of BHAs	32
2.2.2	Synthesis and characterization of BAG	40
2.2.3	Preparation and characterization of BHA-BAG composite scaffolds	48
2.2.4	Statistical analyses	55
3	RESULTS AND DISCUSSION.....	57
3.1	Characterization of BHAs	57
3.1.1	Density and mechanical properties of HA and BHAs	64
3.1.2	Biological characterization of HA and BHAs	68
3.1.3	<i>In vitro</i> cell culture studies.....	74
3.2	Characterization of BAG	82
3.2.1	Solution (sol) characterization and optimization	82
3.2.2	Thermal behavior of BAG	84
3.2.3	FTIR analysis of BAG	85
3.2.4	Phase analysis and microstructure of BAG	87
3.2.5	Mechanical properties of BAG.....	93
3.2.6	Biological properties of BAG	96
3.3	Characterization of 3D porous BHA-BAG composite scaffolds	108
3.3.1	Microstructural and physicochemical properties of scaffolds	109
3.3.2	Mechanical properties of scaffolds	116
3.3.3	<i>In vitro</i> bioactivity and biodegradability of scaffolds.....	118
3.3.4	Cell culture studies of scaffolds.....	124
4	CONCLUSION	131
	REFERENCES	133

APPENDICES

A. Calibration Curve used to calculate ALP Activity.....179

B. Calibration Curve Used to Calculate Intracellular Calcium180

C. Calibration Curve Used in BCA assay.....181

D. Calibration Curve Used to Calculate DNA Using Pricogreen Dye182

CURRICULUM VITAE183

LIST OF TABLES

TABLES

Table 1.1 Various scaffold fabrication techniques and their advantages and disadvantages	20
Table 1.2 BAG incorporated scaffolds for BTE in the literature	25
Table 2.1 The nominal composition of HA and BHA powders	33
Table 2.2 Reagents and their amounts to prepare 1 liter SBF solution	37
Table 2.3 The nominal composition of scaffolds based on wt.% of components ..	48
Table 3.1 Lattice parameters and crystallinity degree of HA and BHA powder samples (n=3)	59
Table 3.2 Theoretical and experimental elemental composition of HA and BHA samples in terms of molar ratio (n=3)	60
Table 3.3 Elemental analysis of BAG nanoparticles (n=3).....	92
Table 3.4 Density, porosity, microhardness, and diametral strength of BAG	96
Table 3.5 Chemical composition of prepared scaffolds according to wt.% of constitutional elements (n=3)	110
Table 3.6 Crystallinity degree (CD) of scaffolds, as well as unit cell parameters and Phase percentage of scaffolds' constituent materials	113
Table 3.7 Porosity (n=3), specific surface area (SSA), micropore volume, and micropore sizes of scaffolds	116

LIST OF FIGURES

FIGURES

Figure 1.1. Basics of bone tissue engineering.....	5
Figure 1.2 An ideal scaffold's requirements for BTE.....	6
Figure 1.3. Crystal structure of BAG along a-axis	17
Figure 3.1. XRD patterns of HA and BHA powders sintered at 900 °C for 2 h	58
Figure 3.2. SEM images of HA and BHA powders sintered at 900 °C for 2 h. (a) HA; (b) 0.05BHA; (c) 0.1BHA; (d) 0.25BHA; (e) 0.5BHA. Scale bar length is 2 µm.....	61
Figure 3.3. FTIR spectra of HA and BHA powders sintered at 900 °C for 2 h	62
Figure 3.4. Relative density (n=3) of HA and BHA samples. Significant differences ($p \leq 0.05$) between groups were shown by the asterisk (*)	65
Figure 3.5. The microhardness values of HA and BHAs, where (*) represents the significant difference ($p \leq 0.05$) between the mean values of groups	66
Figure 3.6. Diametral tensile strength of HA and BHAs	67
Figure 3.7. SEM images of the surface of HA and BHA samples after 1 and 14 days of incubation in SBF, and EDX results of the newly formed apatite particles. Scale bar length is 5 µm in zoomed images (left column) and 20 µm in other images.	69
Figure 3.8. Ion release profiles of Ca, P, B, and pH changes of SBF filtrate during 14 days of incubation (n=3) in the water bath at 37 °C	71
Figure 3.9. <i>In vitro</i> biodegradability of HA and BHAs during 28 days incubation in acidic buffer at 37 °C (n=3). There was no significant difference between the groups at each specific time point. However, the degradation rate increased with time. Asterisk (*) sign indicates statistically significant differences between groups.....	72
Figure 3.10. Relative cell viability on HA and BHA samples during 7 days of culturing (n=4). Cell viability of HA after 1 day was considered 100%. Asterisk (*) indicates a significant difference ($p \leq 0.05$) between the mean values of groups	74
Figure 3.11. SEM micrographs (scale bar = 20 µm) of Saos-2 cells on the disks after 1 and 7 days of incubation: (a) HA-day1, (b) HA-day 7, (c) 0.05BHA-day1, (d)	

0.05BHA-day 7, (e) 0.1BHA-day1, (f) 0.1BHA-day 7, (g) 0.25BHA-day1, (h) 0.25BHA-day 7, (i) 0.5BHA-day1, (j) 0.5BHA-day 7. Scale bar length is 20 μm .	
Figure 3.12. ALP activity (upper) and intracellular Ca^{2+} contents of Saos-2 cells seeded on HA and BHAs disks after 7 and 14 days incubation in osteogenic differentiation medium at 37 $^{\circ}\text{C}$ (n=5). Asterisk (*) indicated statistically significant differences between the mean values of groups	78
Figure 3.13. Optical microscopy images of Alizarin Red S (ARS) of Saos-2 cells for calcium deposition, 7 and 14 days after incubation. Scale bar length is 100 μm ...	81
Figure 3.14. The solutions (sol) after dissolving Ca, Zr, and Si precursors for 5 h on the stirrer. (a) TEOS:ethanol: HNO_3 =1:21:1, (b) TEOS:ethanol: HNO_3 equal to 1:30:1, and (c) TEOS:ethanol: HNO_3 =1:42:1	83
Figure 3.15. TGA and DTA curves of BAG gel dried at 100 $^{\circ}\text{C}$ for 24 h	85
Figure 3.16. FTIR spectra of BAG powders heat-treated at 50 $^{\circ}\text{C}$, 200 $^{\circ}\text{C}$, 300 $^{\circ}\text{C}$, 400 $^{\circ}\text{C}$, and 600 $^{\circ}\text{C}$ for 30 min, as well as sintered at 1150 $^{\circ}\text{C}$ for 3 h in the air ...	87
Figure 3.17. XRD patterns of prepared BAG with different TEOS:ethanol: HNO_3 ratios. Note that B stands for baghdadite and L stands for larnite (PDF No. 33-0302) with the formula Ca_2SiO_4	88
Figure 3.18. SEM micrograph, and particle size distribution of BAG powder sintered at 1150 $^{\circ}\text{C}$ for 3 h in the air	91
Figure 3.19. Force-displacement curves of BAG during diametral tensile strength test	93
Figure 3.20. SEM micrographs of BAG disk sample sintered at 1150 $^{\circ}\text{C}$ for 3 h in the air used in mechanical tests	95
Figure 3.21. SEM micrographs and EDX of BAG disk's surface after immersion in SBF for different time periods	98
Figure 3.22. Element concentration profiles of a) Ca, b) Si, c) P, and d) pH changes of SBF filtrate during 14 days of incubation (n=3) in the water bath at 37 $^{\circ}\text{C}$	99
Figure 3.23. Weight loss percentage of BAG samples (n=3) that incubated in acetic acid and sodium acetate buffer for 28 days at 37 $^{\circ}\text{C}$	100

Figure 3.24. Upper: MTT assay results of Saos-2 cells after direct contact with various concentrations of BAG powder ($\mu\text{g/ml}$) for 24 and 48 h of incubation (n=3). Lower: relative cell viability of Saos-2 cells after direct contact with various concentrations of BAG powder ($\mu\text{g/ml}$) with respect to the control group without any BAG particles after 24 and 48 h of incubation (n=3). Note that Asterisk (*) indicates significant differences between the groups ($p<0.05$)..... 103

Figure 3.25. Optical microscope images of Saos-2 cells in direct contact with different concentrations of the BAG particles throughout 48 h of incubation time at 37 °C. Scale bar length is 100 μm 104

Figure 3.26. Upper: ALP activity (n=3), Lower: intracellular calcium ion deposition of cells incubated in osteogenic medium containing different concentrations of BAG particles (n=3). there is no significant difference ($p<0.05$) between groups at both 7 and 14 days for ALP and intracellular calcium deposition of cells in the osteogenic medium with the ascorbic acid and β -glycerophosphate 106

Figure 3.27. ALP activity of Saos-2 during 14 days of incubation in the medium (without ascorbic acid and β -glycerophosphate) containing BAG particles (12 $\mu\text{g/ml}$) (n=5). Note that the Asterisk (*) indicates significant differences between the groups ($p<0.05$)..... 107

Figure 3.28. The general appearance of the scaffold and SEM image of pores on the scaffold after the removal of polymeric porogen agents 108

Figure 3.29. TGA-DSC graphs of scaffolds that were performed between 25 °C to 1200 °C 109

Figure 3.30. XRD pattern of BHA and composite BHA-BAG scaffolds after removing polymeric porogen agents. and The (*) indicates the presence of BAG phases in the XRD of samples 112

Figure 3.31. FTIR spectra of BHA and composite BHA-BAG scaffolds after removing polymeric porogen agents 114

Figure 3.32. The Mean and standard deviation values of compressive strength (n=5), diametral tensile strength (n=5), and microhardness (n=30) of scaffolds. (*) indicates a significant difference between that groups ($p< 0.05$)..... 118

Figure 3.33. Apatite formation on scaffolds after specified immersion time inside SBF, as well as SEM micrographs of scaffolds' surface before immersion (Day 0). The scale bar of magnified images in red windows is 5 μm , while the scale bar on main images is 200 μm 120

Figure 3.34. Ion release profiles of Ca, Si, and B; pH of SBF filtrate during bioactivity test 122

Figure 3.35. Biodegradation rate (n=3) of scaffolds throughout 4 weeks of incubation. The asterisk mark indicates a significant difference between groups 123

Figure 3.36. Relative cell viability histogram of composite BHA-BAG scaffolds with respect to BHA (100%) at each time point of incubation (n=4), and laser scanning confocal microscopy analysis of hFOB cells on scaffolds after 7 days of incubation. The (*), (#), (\$), (α), and (β) marks on bar histograms indicate significant differences ($p \leq 0.05$) between groups. The groups with the same marks are not different statistically. Green and red colors on the confocal images are representing F-actin filaments and nuclei of cells, respectively; and the scale bars are 400 μm 125

Figure 3.37. SEM images of the morphology of hFOB cells on scaffolds after 1 and 7 days of incubation at 37 $^{\circ}\text{C}$. The scale bar is 20 μm length 128

Figure 3.38. ALP activity and intracellular Ca^{2+} deposition of hFOB cells seeded on scaffolds after 7 and 14 days of incubation at 37 $^{\circ}\text{C}$. The Asterisk mark indicates significant differences between groups 130

LIST OF ABBREVIATIONS

ABBREVIATIONS

3D:	3 dimensional
ALP:	Alkaline phosphatase
AM:	Additive manufacturing
ARS:	Alizarin Red Stain
B:	Boron
BAG:	Baghdadite
BCA:	Bincinchoninic acid assay
BET:	Brunauer-Emmett-Teller analysis
BG:	Bioactive glass
BHA:	Boron-doped hydroxyapatite
BMSC	Bone marrow mesenchymal stem cell
BSA:	Bovine serum albumin
BTE:	Bone tissue engineering
C:	Compressive strength
Ca:	Calcium
CaO:	Calcium oxide
CaP:	Calcium phosphate
CaSi:	Calcium silicate
CD:	Crystallinity degree
CO ₂ :	Carbone dioxide
COL I:	Collagen type 1
CSLM:	Confocal laser scanning microscopy
D:	Diameter
DEX:	Dexamethasone

dH ₂ O:	Distilled water
DMEM:	Dulbecco's modified eagles medium
DSC:	Differential scanning calorimetry
ECM:	Extracellular matrix
EDX:	Energy-dispersive X-ray analysis
FBS:	Fetal bovine serum
FESEM:	Field emission scanning electron microscopy
FTIR:	Fourier-transform infrared spectroscopy
FWHM:	Full width at half maximum
GM:	Growth medium
GPa:	Giga Pascal
h:	Hours
HA:	Hydroxyapatite
HV:	Vicker's microhardness
ICP-MS:	Inductively coupled plasma mass spectrometry
ICP-OES	Inductively coupled plasma-optic emission spectrometry
Mg:	Magnesium
min:	Minutes
ml:	Milliliter
mm:	Millimeter
MPa:	Mega Pascal
N:	Newton
NSF:	National Science Foundation
OCN:	Osteocalcin
OD:	Optical density
OM	Osteogenic medium
P:	Phosphorous
PBS:	Phosphate-buffered saline
PCL:	Polycaprolactone

PEEK:	Polyether ether ketone
PEG:	Polyethylene glycol
PLA:	Polylactic acid
PLGA:	Poly lactic-co-glycolic acid
PNPP	Para-nitrophenyl phosphate
PPF:	Polypropylene fumarate
PVA:	Polyvinyl alcohol
RT:	Room temperature
S:	Diametral tensile strength
SSA:	Specific surface area
SBF:	Simulated body fluid
SEM:	Scanning electron microscopy
TCP:	Tricalcium phosphate
TE:	Tissue engineering
TGA:	Thermogravimetric analysis
UV:	Ultraviolet
Wt.%	Weight percentage
X _c :	Degree of crystallinity
XRD	X-ray diffraction
Zn:	Zinc
Zr:	Zirconium

CHAPTER 1

INTRODUCTION

This Ph.D. thesis focuses on the fabrication of 3-dimensional (3D) porous bioceramic-based composite scaffolds that contribute to improving the performance of scaffolds in bone tissue engineering (BTE) applications. The composite scaffolds were made of two different bioceramics including boron-doped hydroxyapatite (BHA), as the main component, and baghdadite (BAG), as the second component in various weight ratios after evaluation of BHA with different boron dosages and synthesis of BAG through my proposed novel modified sol-gel method. Boron doping concentration in the structure of hydroxyapatite (HA) and the BAG amount in the composite's structure was designed to benefit its presence in terms of structural features, bioactivity, biodegradability, and effect of bioceramic-based scaffolds on cell behaviors. The following research and review articles were published in international-refereed SCI journals by the author and permitted to be included in the thesis and dissertation in full or in part.

1. Materials from: Hossein Jodati et al., Effects of the doping concentration of boron on physicochemical, mechanical, and biological properties of hydroxyapatite, *Ceramics International*, Published in 2022, Elsevier (Jodati et al., 2022a).
2. Materials from: Hossein Jodati et al., A review of bioceramic porous scaffolds for hard tissue applications: Effects of structural features, *Ceramics International*, Published in 2020, Elsevier (Jodati et al., 2020c).
3. Materials from: Hossein Jodati et al., Calcium zirconium silicate (baghdadite) as a biomaterial, *Ceramics International*, Published in 2020, Elsevier (Jodati et al., 2020b).

4. Materials from: Hossein Jodati et al., Synthesis of baghdadite using modified sol-gel route and investigation of its properties for bone treatment applications, Journal of the Korean Ceramic Society, Published in 2022, Springer (Jodati et al., 2022b).

1.1 Bone tissue and bone defect treatment

Bone tissue consists of extracellular matrix (ECM), water, and different bone cells (Marks and Odgren, 2002). Its ECM is mainly made up of plate-like nano-crystalline HA inorganic minerals with a thickness of 1.5–4 nm as well as lengths of 50 nm × 25 nm by 60-65% of the weight, and organic components, such as triple helix collagen type I with ~1.5 nm diameter and ~300 nm length by ~95% (Feng, 2009; Xiaojian Wang et al., 2016; Zhou and Lee, 2011). The inorganic components of bone ECM give rise to its strength. However, bone's flexible properties originate from the organic part of ECM. Besides composition, the structure of the bone also plays an important role in determining its characteristic properties. Nanostructured ECM of bone affects the adhesion, proliferation, and differentiation of several bone cell types including osteoblasts, osteoclasts, osteocytes, and bone lining cells. In fact, both constituents and the way these components have been structured and arranged must be addressed as the determining factors of the properties of bone (Blair et al., 2007; Kobayashi et al., 2016; Zhang et al., 2016).

Mineralized biological tissues, such as bones, evolved to execute increased and optimized mechanical strength. Organized porous features of inorganic/organic structures of bone are at the center of this enhancement (Chen et al., 2008). Bone tissue is a nanocomposite with a highly organized hierarchical structure. Each structural level mirrors the material and mechanical properties of its constituents, where those features give the bone high strength and toughness but a low modulus of elasticity (Ginebra et al., 2018; Rho et al., 1998). Bone tissue is morphologically divided into an inner loosely arranged grid of trabecular (or spongy) bone and the compact structure of outer cortical bones. Spongy bone with 50-90% porosity and a

pore size of about 1mm in diameter (Keaveny et al., 2001) is surrounded by an exterior layer of densely packed cortical (or compact) bone with 3-12% porosity (Cooper et al., 2016, 2004). While a highly porous mesh of trabeculae makes the structure of spongy bone, osteons (10-500 nm) with a series of voids (e.g. Haversian canals) are the building blocks of cortical bones. The structure, degree of mineralization, and mechanical properties of bone vary according to bone type, location, and function (Florencio-Silva et al., 2015; Follet et al., 2004).

Dynamic nature of bone tissue allows for preserving its healthy condition, adapting the architecture of the bone when mechanical loads change, and restoring damaged parts of itself through the non-stop process of *remodeling* throughout life (Kohli et al., 2018). Bone remodeling is a key process for bone repair and it depends on a dynamic equilibrium between bone resorption of osteoclasts and bone formation of osteoblast cells in response to biomechanical stimuli (Florencio-Silva et al., 2015; Seeman, 2009). Bone has small cracks in cross-sections, typically about 100 µm in length and slightly longer in the longitudinal direction (Taylor and Lee, 2003). Bone tissue has a self-healing capacity and its potential is enough to repair such small bone damages.

Bone's self-regenerative mechanism cannot answer the need to repair larger critical-sized bone defects caused by trauma, resection of bone due to infection or tumors, pseudarthrosis, inherent genetic disorders, or aging (Crouzier et al., 2011; Turnbull et al., 2018). A large number of patients throughout the world are suffering from damaged or diseased bone tissue problems and are in urgent need of bone substitutes or regeneration (Faour et al., 2011). Interestingly, bone is the second most transplanted tissue after blood with nearly 4 million operations using different bone treatment alternatives annually (Turnbull et al., 2018). The gold standard to treat bone defects is using autograft (bone tissue from patients themselves) due to its natural osteoconductive, osteogenic, and osteoinductive properties (Blokhuis, 2013; Wang and Yeung, 2017). Allografts, which are harvested from an individual other than the patient, offered an alternative to eliminate the disadvantages of autografts,

such as donor site morbidity and short supply (Baumhauer et al., 2014; J. Zhang et al., 2014). However, the allograft technique suffers from impaired strength of grafted bone, the risk of pathogen transfer and infection, as well as immunological rejection and poor healing because of the difference in the bone quality of donor and recipient (Delloye et al., 2007; Moore et al., 2001). Synthetic bone grafts are among many alternatives that have been developed to address limitations related to autografts and allografts. During the last decades, the market of bone substitutes has placed among top-ranked products in the orthopedic industry with approximately 2 billion dollars gross in 2013 (“MediPoint: Bone Grafts and Substitutes - Global Analysis and Market Fore...,” n.d.) with a trend to prefer synthetic products over natural ones (Wang and Yeung, 2017). Different bone substitute biomaterials, as well as their pros and cons, were investigated in many studies (Campana et al., 2014; Fernandez de Grado et al., 2018; García-Gareta et al., 2015).

Tissue engineering (TE) and regenerative medicine, are interdisciplinary fields that emerged during the past few decades to create biological replacements that can mimic tissues for disease diagnosis or modeling and replace/regenerate unfunctional or injured tissues (Berthiaume et al., 2011). The term 'tissue engineering' emerged at a National Science Foundation (NSF) workshop in Granlibakken, California, and was later published in 1988. The definition was reconsidered by Vacanti and Langer (Vacanti and Langer, 1999) and the process was divided into three groups: (1) cells, which can be tissue-specific, stem cells, or embryonic stem cells (autologous or allogenic), (2) the matrix (natural or synthetic), which may be in different forms, such as fibrous, a foam, or a hydrogel, (3) *in vitro* culture systems which can be in static, stirred, or dynamic flow conditions. They also added that TE products could have the benefit of controlled drug delivery methods for the release of growth factors that may enhance angiogenesis or help in new tissue formation.

TE shows signs of success to overcome complications and disadvantages associated with traditional methods such as autografts, allografts, and bone substitute biomaterials (Bouet et al., 2015; Henkel et al., 2013; Howard et al., 2008; O’Keefe

and Mao, 2011). In BTE through the combination of life sciences and engineering principles, a substrate (scaffold) is serving as structural guidance, and anchorage site for cells, to develop engineered structures by a combination of scaffolds and living cells to restore, maintain or improve bone tissue function (Figure 1.1.). The scaffold is also contributing to the remodeling of ECM to ensure the integration with surrounding host tissues, and at the same time, is establishing an interface to respond to biological and physiological changes *in vivo* (Alvarez-Urena et al., 2017).

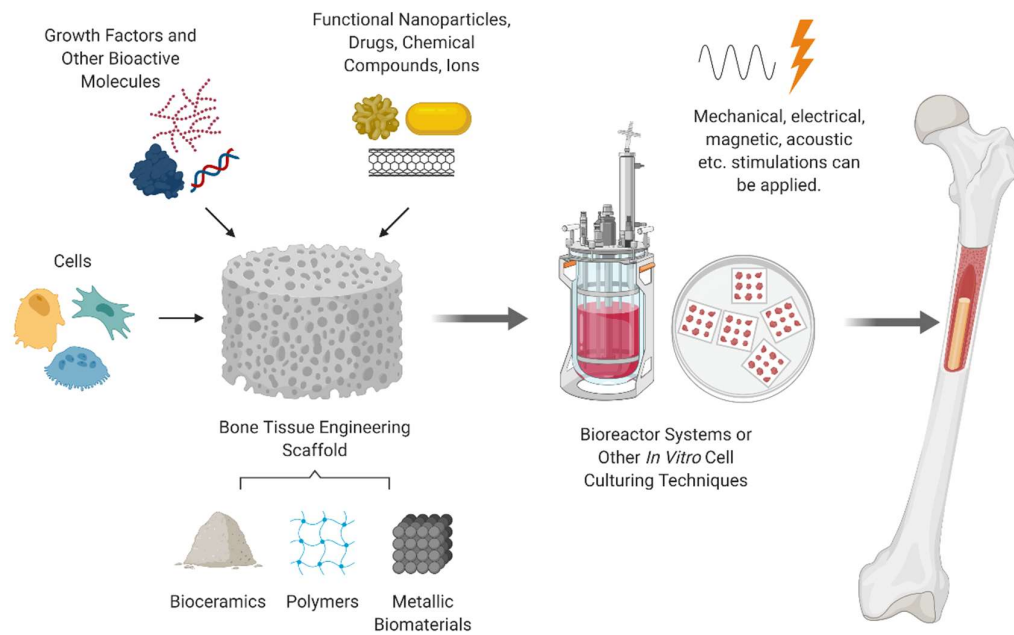


Figure 1.1. Basics of bone tissue engineering

1.2 Ideal scaffold for BTE

The ideal bone scaffold should resemble the natural bone tissue in each and every way as a general rule. The scaffold is a transient implant that must create an appropriate environment for cells to stay viable, attach, proliferate, differentiate and deposit ECM to replace it. Scaffolds should allow vasculature formation for better integration with host tissues, and withstand loads anywhere that are required (Amini et al., 2012). Production of an ideal scaffold, which can satisfy all requirements, is a great challenge for researchers up to the present time (Webber et al., 2015). Scaffold requires specific biological, structural, and mechanical properties in BTE applications, where modifying and developing novel material compositions as well as manufacturing processes offer the opportunity to promote these properties and produce scaffolds with superior properties (Figure 1.2).

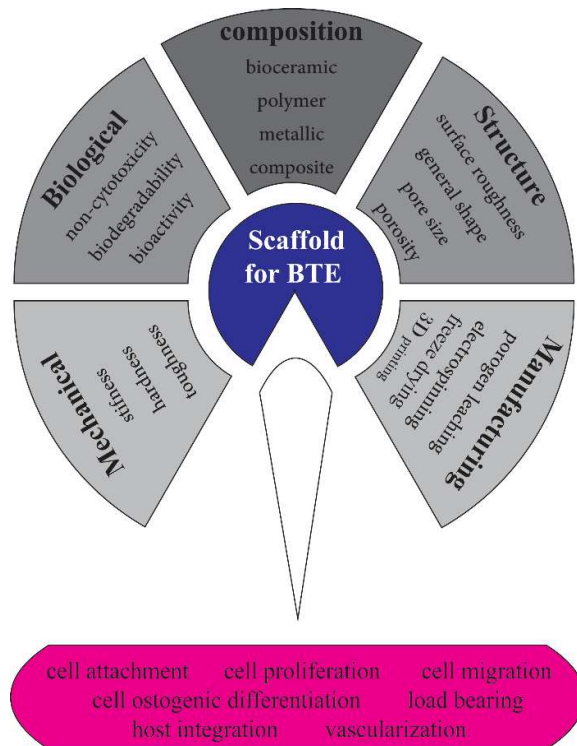


Figure 1.2. An ideal scaffold's requirements for BTE applications.

1.2.1 Structural features

3D architecture of scaffolds is a crucial design parameter to achieve excellent performance in bone regeneration (Loh and Choong, 2013; Melchels et al., 2010). Original structure of natural bone is porous which has voids referred to as *pores*. Porosity of scaffolds is defined as the volume of void space within its structure; whereas, interconnectivity referred to pore volume that could be accessed from the outside of the scaffold through the pore network (Perez and Mestres, 2016). The highly porous architecture of scaffolds with interconnected pores allows cells to penetrate and migrate into the structure (Bonfield, 2006). It provides sufficient surface area for interactions of scaffold and cells, as well as surrounding host tissues (Hing et al., 2004). A proper design also allows nutrient and oxygen diffusion, the expulsion of waste products, and even enhanced vascular ingrowth possibility for *in vivo* angiogenesis (Karageorgiou and Kaplan, 2005). While the minimum acceptable pore size of 100 μm is essential for angiogenesis, pore sizes of 300 μm and larger are recommended to allow vascularization and new bone formation during *in vivo* and clinical applications (Haugen et al., 2019). Increase in porosity causes to have high permeability and degradation of scaffolds (Pérez et al., 2013). However, the negative effect of porosity on the mechanical properties of scaffolds should not be neglected (Hollister et al., 2002). Adequate porosity, which contributes to cell accommodation and ingrowth, without compromising the mechanical strength of scaffolds is a challenging issue for research.

Pore size is another feature that plays an important role in the success of scaffolds as well as porosity (Lee et al., 2010; Murphy et al., 2010). According to IUPAC, the porosity of dense materials is classified into three main categories concerning diameter: micropores ($d < 2 \text{ nm}$), mesopores ($2 < d < 50 \text{ nm}$), and macropores ($d > 50 \text{ nm}$) (Ali et al., 2017). However, pore size is frequently classified into two classes in TE: macropores ($d > 50 \mu\text{m}$) and micropores ($d < 50 \mu\text{m}$) (Perez and Mestres, 2016). The decrease in pore size would lead to an increase in surface area and consequent promotion of cell-scaffold interaction by increasing the availability of scaffolds

ligands for cells to bind (cell colonization) (Rouahi et al., 2006). Micropores have a role in adsorbing proteins on the surface of biomaterials and determining stem cells' fate through cell-protein interaction (Woo et al., 2003). However, the mesopores and micropores might halt cell migration into scaffolds. On the other hand, macropores provide a more appropriate structure for cells to penetrate and migrate, which results in better integration with host tissues and a higher potential for later *in vivo* vascularization (Walthers et al., 2014). The overall porosity of a scaffold, as well as pore size, pore interconnectivity, and even pore shape (Gariboldi and Best, 2015; Gauvin et al., 2012), are significant structural features that should be engineered, optimized, and balanced in order to direct an ideal scaffold with desired biological and mechanical properties for bone tissue regeneration.

1.2.2 Biological and mechanical requirements

Materials used in scaffold production and their degradation products should be biocompatible. Being non-cytotoxic and allowing cells to attach, proliferate, and differentiate as planned, is an inevitable characteristic of all scaffolds' materials. In addition, they must possess non-inflammatory properties and evoke minimal immune responses (Bouet et al., 2015). Another crucial aspect that ideal scaffolds should have is biodegradability or bio-resorbability to allow full regeneration as the material degrades in the physiological environment and the degradation products are fully eliminated (Liu et al., 2017). It is also important, especially for BTE where the tissue experiences load-bearing conditions. On one hand, at a quick degradation rate, mechanical failure could happen if the load was transferred to newly formed tissue before it gained adequate strength. The decrease in mechanical strength of the degrading scaffold should be compensated by the increase in the strength of regenerating bone tissue (O'Brien, 2011). On the other hand, the slow rate might cause an inflammatory response, and impair of newly regenerated tissue (Mountziaris and Mikos, 2008). In fact, an optimum degradation rate is required to make a balance between the rate of scaffold degradation and new bone tissue growth

in order to conserve the mechanical strength of the construct at the required value, prevent stress shielding, and avoid the removal operation of implanted scaffolds (Alvarez-Urena et al., 2017).

Bioactivity is another significant characteristic of scaffolds that makes them able to evoke a biological response and interact with surrounding host tissues. Unlike bio-inert materials (e.g. alumina or zirconia) that are encapsulated by fibrous tissue when implanted, bioactive scaffolds integrate with surrounding living tissues. Bioactivity covers two biological processes: osteoconductivity and osteoinductivity. Osteoconductive scaffolds act as a substrate that triggers bone deposition on the surface of the material in non-osseous sites, while osteoinductivity means the capability of scaffolds to employ immature stem cells and direct their differentiation toward bone cells, such as preosteoblasts (Albrektsson and Johansson, 2001). Although the formation of the HA layer, similar to apatite layer of bone, has been accepted as the main mechanism of bonding between bioactive material and surrounding bone tissue, a mechanism that explains the osteoinductive property of bioactive scaffolds has not been understood exactly (Syed-Picard et al., 2013). However, the release of calcium and phosphate ions from the calcium phosphate (CaP) material's surface and the absorption of osteoinductive agents by bioactive materials are two proposed hypotheses (Barradas et al., 2011; Motamedian et al., 2015).

On one hand, scaffolds should have sufficient strength to support themselves and act as a template for cell adherence, proliferation, and differentiation; on the other hand, they must tolerate loads that might be imposed from the environment, especially in load-bearing situations. From the mechanical point of view, it is preferred to have scaffolds, whose elastic modulus, compressive, and fatigue strengths match the host bone tissue to preserve structural integrity and permit cell mechano-regulation to function properly *in vivo* (Ma et al., 2019; Zhang et al., 2018). Stress shielding phenomenon and resultant bone resorption have been reported for the materials which were much stiffer than host surrounding tissues (Kitamura et al., 2004).

Whereas, the ability of the substrate to be in compliance with host tissue stiffness influences cell attachment and migration (Brown et al., 2005). Besides the crucial role of scaffold architecture, the intrinsic properties of the materials constitute the other significant aspect that determines the mechanical characteristic of scaffolds. Mechanical properties of a material, such as stiffness, and its ability to be shaped in the desired architecture should be considered in BTE scaffold design.

1.2.3 Composition

A wide range of biomaterials is used to produce scaffolds for BTE (Ren et al., 2022). Bioceramics, polymers, and composite scaffolds (Corcione et al., 2017; Eliaz and Metoki, 2017; Inzana et al., 2014) can find more applications than conventional non-degradable metallic biomaterials (Roseti et al., 2017). However, metallic scaffolds, such as Ti and its alloys, which are generally utilized in load-bearing applications to provide mechanical and structural support for example in joint arthroplasties and long bone and vertebral fractures, are also investigated in BTE (Chen et al., 2017; Wang et al., 2019).

Polymers can be classified into two categories: natural and synthetic. Polycaprolactone (PCL), polylactic acid (PLA), polypropylene fumarate (PPF), poly-lactic-co-glycolic acid (PLGA), and polyether ether ketone (PEEK) are just a few examples of synthetic polymers while, collagen, hyaluronic acid, silk, and chitosan are considered as well-known natural polymers (Bhattacharjee et al., 2017; J. Wang et al., 2016). Main disadvantage of polymers is their poor mechanical properties that restrict their applications in load-bearing tissues like bone (Stratton et al., 2016). Natural polymers consisting of proteins (e.g. collagen, gelatin, and fibrinogen), polysaccharides (e.g. glycosaminoglycans), and polynucleotides (e.g. DNA and RNA) exhibit better osteoinductivity over synthetics due to the resemblance to native ECM, however, their mechanical properties are not good enough and biodegradability is less controllable (Haugen et al., 2019). In addition, polymeric carriers can be used, for example, for the effective delivery of a drug,

metabolic supplement, or a growth factor to the body. Natural polymers have an opposite charge compared to bioactive molecules, which lead to ionic interactions between them. This creates a strong relationship that can protect the molecules in their stable form and may adversely affect the release process. A combination of a natural and synthetic polymer may be preferred to regulate the sustained release of the molecule from the composite (Rao et al., 2018).

Ceramics, with either natural or synthetic origin, are promising biomaterials that are used frequently in BTE applications (Gao et al., 2014). The span of bioceramics has been extended from amorphous bioactive glasses (BGs) to crystalline ceramics such as HA, tricalcium phosphate (TCP), or calcium silicate (CaSi). Their advantages can be listed as similar chemical composition to the inorganic portion of the bone tissue and consequent biocompatibility, high compressive strength, bioactivity, osteoconductivity, as well as possible osteoinductivity (Barradas et al., 2011; C. Zhao et al., 2022). However, being brittle due to primary covalent and ionic bonds, and low ductility are major drawbacks of bioceramics that partially limit their applications to non-load bearing and filling of bone defects, as well as metallic implant coatings (Ma et al., 2018).

Calcium phosphates (CaP) might be one of the most widely studied and used bioceramics in bone tissue regeneration (Dorozhkin, 2018; Eliaz and Metoki, 2017). Among all CaPs, HA has the closest chemical composition to the inorganic part of the natural bone and has profoundly been investigated (Du et al., 2021). HA can form a strong bond with surrounding host tissues and promote alkaline phosphatases (ALP) activity, a natural enzyme secreted by cells through osteogenesis, and consequent differentiation of stem cells by way of encouraging of BMPs expression as osteogenic growth factors or releasing of ions (Hendi, 2017). Despite its advantages, HA suffers from a slow degradation rate and poor mechanical properties, like high brittleness and low fracture toughness (Bohner et al., 2012; Lu et al., 2002). TCP is another popular member of the CaP family that has been applied in many BTE studies (Kucko et al., 2018). TCP has four known polymorphs: α , β , γ , and

super- α . The latter two phases are only observed at high temperatures and pressures. β -TCP is the most frequently used one and has a faster degradation rate in the body than some other CaPs such as HA (Bohner et al., 2020). Although TCP shows higher fracture toughness than HA (Wu et al., 2011; Zhang et al., 2017), it is not a good candidate for load-bearing applications. This is because of having lower mechanical strength than cortical bone and the rate mismatch between β -TCP degradation and new bone formation (Hench, 2015). The other calcium orthophosphate phases, α -TCP cannot take part in many applications in BTE due to very fast resorption rates (Habraken et al., 2016).

Bioactive glasses (BGs) are amorphous members of the bioceramics family that have been used in orthopedic clinical applications after the first introduction in the late 1960s by Hench (Hench et al., 1971). They were recognized as biocompatible and non-cytotoxic materials. One of the attractive aspects of BGs is the ease of control over the chemical composition, which lets to regulate their degradation rate (Fu, 2019). Besides being osteoconductive and integrating through bonds with surrounding host bone tissues, they possess osteoinductive properties (Jones, 2015). However, being highly soluble, and having poor mechanical characteristics, similar to many bioceramics, could be cited as BGs disadvantages (Hench, 2015; Yazdanpanah et al., 2012). To date, rapid development in BGs application could be traced, specifically as composite biomaterials fabricated for bone defect repair (Guo et al., 2019; Soni et al., 2019). Calcium silicates (CaSi) are biocompatible materials that have been considered an interesting alternative for bone substitute and TE applications owing to their good bioactivity and biodegradability (Feng et al., 2014). An osteoconductive aspect of calcium silicates was reported in many studies and they also could contribute to the formation of new bone tissues through a gradual release of Si and Ca ions (Ding et al., 2009). Calcium silicates promote the proliferation and differentiation of bone marrow mesenchymal stem cells (BMSCs) or osteoblast cells (Ni et al., 2007). However, like many other bioceramics, the brittle nature and low toughness of calcium silicates are the main obstacles that hinder their development in load-bearing applications.

1.3 Boron-doped hydroxyapatite (BHA)

HA is a member of CaPs, which is widely used in the restoration and regeneration of bone defects (Habracken et al., 2016). HA resembles the inorganic constituent of bones or teeth, and its biocompatible feature allows it to act as a bioactive material, which could form chemical bonds with surrounding host tissues. Its applications as a potent bioceramic, cover a wide range from bone grafts, orthopedic/dental implant coating, scaffolds for BTE, and bone fillers to drug delivery systems (Dewi and Ana, 2018; Lin et al., 2013). Chemically, the composition of natural HA that forms the mineral part of human bone differs from stoichiometric one, due to the substitution of Ca^{2+} , and PO_4^{3-} or OH^- of the crystal lattice with some necessary ions such as Mg^{2+} , Na^+ , Sr^{2+} , Zn^{2+} , F^- , Cl^- , and CO_3^{2-} (Gaffney-Stomberg, 2019). Deprivation of those ions in the structure of synthetic HA leads to poor performance in living systems, compared to biological ones. Therefore, ion substitution or element doping was introduced to HA structures to resemble biological apatites more realistically and overcome the low mechanical strength, poor biodegradation rate, and even improve bioactivity and osteoinduction properties of synthetic HA (Chen et al., 2018; Evis and Webster, 2013; Yilmaz et al., 2019).

HA's chemical structure is suitable to be a host for both cations (substituted with Ca^{2+}) and anions (substituted with PO_4^{3-} and/or OH^-) to modify its characteristics for various biomedical applications. The number and variety of studies that used cations are greater than those that used anions. The larger surface area of doped HA with cations like Cu^{2+} , Ni^{2+} , and Co^{2+} was reported in the literature (Sadetskaya et al., 2021), which could facilitate cell attachment and proliferation. Doping of cations, such as Zn^{2+} , Sr^{2+} , and Co^{2+} caused osteogenesis effects (Kahaie Khosrowshahi et al., 2021; Maleki-Ghaleh et al., 2021), and doping of anions, such as SiO_4^{4-} increased bioactivity and mechanical strength (Thian et al., 2006; Wang et al., 2021). Furthermore, antibacterial features were observed in doped HA samples doped with Li^+ , Ag^+ , F^- , etc (Alhilou et al., 2016; Keikhosravani et al., 2021; Sri Devi and Vijayalakshmi, 2020; C. Zhao et al., 2022). Doping techniques depend on the HA

synthesis method, which includes several approaches. However, chemical precipitation methods are more popular and frequently used. The comprehensive comparison of methods and effects of different ions is beyond the scope of this research study, but reviews, like the one conducted by Panda et al. (Panda et al., 2021), offer valuable information.

Boron (B) is a non-metal trace element that influences many biological processes, as well as bone health, growth, and maintenance (Rondanelli et al., 2020). B accumulation is remarkably more significant in bone than in soft tissues or blood, where in-take amounts determine its concentration (Yilmaz and Evis, 2016). The beneficial functions of dietary B have been reported in normal bone formation, function, and development (Hunt, 2012). B together with calcium, magnesium, and vitamin D plays a role in the mineralization and metabolism of bone, generally through participation in hydroxylation reactions (Devirian and Volpe, 2003; Gaffney-Stomberg, 2019). Dietary B's impact on the stimulation of osteogenesis was also observed in post-menopausal women through increasing steroid hormone concentrations (Meacham et al., 2010). In another study, Uysal et al. (Uysal et al., 2009) observed increased bone formation, mineralized bone area, and osteoblast numbers in rabbit groups with 10 and 20 days of B in-take dietary, compared to groups without B.

B is usually found as borates in nature rather than as a pure element (Yilmaz and Evis, 2016). *In vitro* studies exhibited an enhanced significant effect of B on the proliferation and differentiation of osteoblast-like cells. For example, a study by Hakki et al. (Hakki et al., 2010) demonstrated enhanced expression of bone formation markers, such as collagen type I (COL I), osteocalcin (OCN), and RunX2 in pre-osteoblastic cells. More recently, Capati et al. (Capati et al., 2016) investigated the mechanism by which B affects osteoblastic cells' behavior *in vitro*. Moreover, a decrease in bone strength and a change in its mineral composition were reported in B-deficient cases (Ghanizadeh et al., 2014). Some believe that B shows its effect through indirect mechanisms such as regulating hormone levels, and the absorption

of macro minerals, such as calcium, magnesium, or vitamin D (Abdelnour et al., 2018; Gaffney-Stomberg, 2019).

B was first introduced into the structure of HA by Ternane et al. (Ternane et al., 2002), using the solid-state reaction method. That study was limited to structural features and no biological properties were examined. Barheine et al. (Barheine et al., 2011) studied B-doped HA using the same synthesis method, except for boron oxide as a B precursor instead of boric acid. Their study was also restricted to structural aspects and biodegradability merely. After the findings of Hakki et al. (Hakki et al., 2010) and Ying et al. (Ying et al., 2011), who demonstrated a positive osteogenic effect of purely boric acid on cells, Gümüşderelioğlu et al. (Gümüşderelioğlu et al., 2015) studied chitosan polymeric scaffolds decorated with encapsulated boric acids for bone tissue applications.

According to the literature, Kolmas et al. (Kolmas et al., 2017) used both conventional wet precipitation and dry methods for the synthesis of boron-doped HA (BHA), where the single-dose BHA samples (no data of B release amount) were studied based on structural features, biocompatibility, and synthesis method. In the same year, Tunçay et al. (Tunçay et al., 2017) used microwaved assisted wet precipitation technique in simulated body fluid (SBF) to prepare BHA, and further, only 2 weight percentage (wt.%) of BHA was used to coat polymeric scaffolds, which excluded *in vitro* biodegradation, bioactivity, and mechanical tests. The BHA was synthesized by applying the sol-gel method and using boron alkoxide in the study by Atila et al. (Atila et al., 2019). Similar to Tunçay's study, no dose-dependency was evaluated. In the investigation of BHA nanoparticles by Gizer et al. (Gizer et al., 2020), results were restricted to cell viability and osteogenic activity without any further information about synthesis methods, B source, or other physicochemical and mechanical properties. Concerning the study by Pazarçeviren et al. (Pazarçeviren et al., 2021), the biphasic BHA/ β TCP was examined, in which the presence of β TCP phase might interfere with the inspection of B effect on characteristics of HA.

1.4 Baghdadite (BAG)

BAG with the chemical formula of $\text{Ca}_3\text{ZrSi}_2\text{O}_9$ or $\text{Ca}_3\text{Zr}(\text{Si}_2\text{O}_7)\text{O}_2$ is a calcium zirconium silicate mineral, which was first discovered in Qala-Dizeh, North East of Iraq, from melilite skarns and reported in 1986 (Al-Hermezi et al., 1986). Afterward, it was also found in melilite skarns of Flekkeren, Oslo Rift, Norway, Akaggane mine, Iwate prefecture, Japan, spurrite-rich skarns of Fuka, Okayama prefecture, Japan, and skarned carbonate xenoliths in the Yoko-Dovyren massif, Russia (Biagioni et al., 2010; Shiraga et al., 2001). Moreover, existence of a solid solution between BAG, cuspidine, and niocalite was reported in the Canary Islands (Casillas et al., 2008).

In the last two decades, calcium-silicate (CaSi) based ceramics have drawn huge attention as potential biomaterials for bone and skeletal tissue regeneration applications (Singh et al., 2022; Wu and Chang, 2013). The high bioactivity and biodegradability of these ceramics are their major beneficial characteristics in the biomedical field (De Aza et al., 2004; Xue et al., 2005). However, besides their brittle nature and poor strength, the high dissolution rate is a major disadvantage of Ca-Si ceramics that influences cell growth (due to high pH values) and subsequent osseointegration as well as the long-term stability of those materials (Mohammadi et al., 2014; Sadeghzade et al., 2016). Incorporating the third component into the structure of the CaSi ceramics is considered one of the well-known techniques to overcome the disadvantages of those materials (Wu et al., 2008b). Zinc (Zn) (Wu et al., 2008a), Magnesium (Mg) (Luo et al., 2012), and zirconium (Zr) (Guerreiro-Tanomaru et al., 2014) are some of those elements which were added to CaSi ceramics to improve or control their chemical stability, bioactivity, and mechanical properties. Zr has been extensively used as a biomaterial in making implants and prosthetic devices because of its biocompatible nature and appropriate mechanical strength, especially in bone and dental applications (Kosmač and Kocjan, 2012; Piconi and Maccauro, 1999). Similar to Ti and Si (Chen et al., 1999), Zr is a quadrivalent ion and has the potential to build a network that ionically binds Ca ions,

and therefore enhances the stability of CaSi based ceramics and enables the formation of BAG.

Natural BAG is a fairly rare mineral, which is a member of cuspidine, silicates series with a general formula of $M_4(Si_2O_7)X_2$, where M is assigned to cations with various charges. Unit cell parameters of natural BAG are $a=10.432\text{\AA}$, $b=10.163\text{\AA}$, $c=7.356\text{\AA}$, $\beta=90.96^\circ$, and the symmetry of the crystal is described by the space group $P2_1/a$. Lattice parameters of these natural BAG crystals complied with the crystal structure of synthetic BAG (Figure 1.3.), which was determined for the first time by Plaisier et al. from the neutron powder diffraction data (Plaister et al., 1995). The structure of $Ca_3HfSi_2O_9$, which was determined from X-ray powder diffraction data, was used as the trial model. Preference for $P2_1/a$ space group in natural BAG, over $P2_1/c$ of synthetic, was the only difference between crystal structures, and that was just because of having the same orientation with other cuspidine group members. The crystal structure of BAG is composed of 4-columns-wide polyhedral walls. Unit cell includes four independent cation polyhedra, where three of them are Ca-centered and the other is Zr-centered. Each disilicate group $(Si_2O_7)^{6-}$ connects three walls, and each wall is linked to six disilicate groups and four other walls (Biagioni et al., 2010).

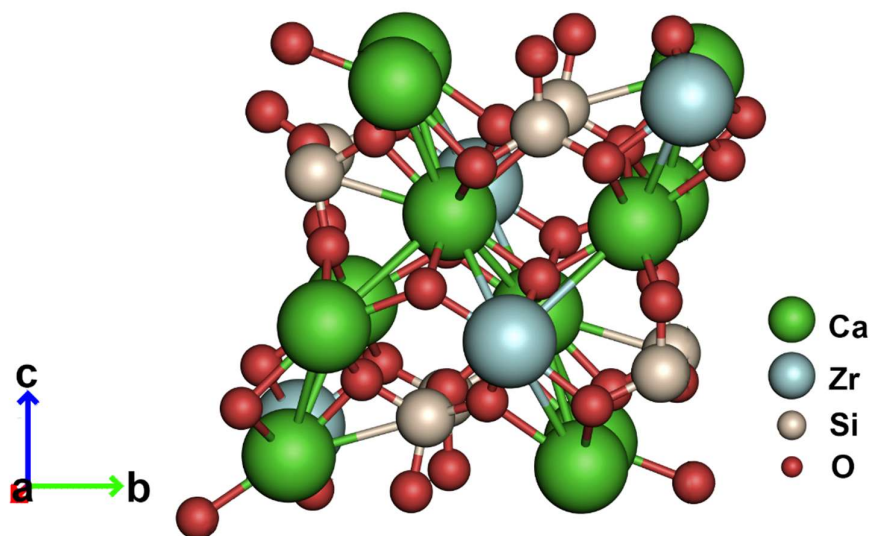


Figure 1.3. Crystal structure of BAG along the a-axis

1.5 Composite scaffolds

From the material perspective, each type of solid biomaterials, including ceramics, polymers, and metals possesses its specific advantages and disadvantages, which couldn't satisfy all requirements needed for bone defect treatment and scaffolds used in BTE applications when they were employed alone. Thus, blending two or more different materials and making composite scaffolds was introduced as an effective approach to overcome the disadvantages of each component and/or improve the various properties of scaffolds (Deb et al., 2018). HA has been extensively applied to fabricate composite scaffolds in recent years. Using polymers along with metals or ceramics as components of composite scaffolds has been explored in a large number of studies throughout the decades (Gritsch et al., 2021; Shuai et al., 2020). Concerning HA, also many studies investigated the properties of scaffolds composed of HA and biopolymer, either natural or synthetic origin (Farokhi et al., 2018; Sathiyavimal et al., 2020), which are out of the scope of this thesis.

Using two bioceramics is another alternative combination to produce composite scaffolds and benefit from the advantages of two components. HA/TCP composite scaffolds are the most known and studied ones that compensate for the inappropriate degradation rate and mechanical strength of monophasic scaffolds made from HA or TCP merely (Mohammadi Zerankeshi et al., 2022). Combinations of HA with other ceramics, such as graphene, were also investigated in the literature (M. Li et al., 2018). Producing composite scaffolds using CaSi materials due to their high degradation and bioactivity is an interesting combination for researchers. Reinforcement of CaSi incorporated scaffolds should be considered as the major function of another component of the composite scaffold. This goal could be achieved by using bioceramic materials like Zr (He et al., 2022) and HA (Feng et al., 2014). Therefore, the fabrication of HA-based composite scaffolds along with Zr-containing ceramic appeared as an interesting combination for BTE, which requires further investigations.

1.5.1 Fabrication of composite scaffolds

Architecture of composite bioceramic scaffolds could be influenced by the scaffold's preparation technique. Each method generates a distinct range of porosity, pore distribution, pore shape, pore size, and pore interconnectivity. As explained before, structural features play a principal role in the interaction between cells and scaffolds and the performance of scaffolds during *in vitro*, *in vivo*, and clinical trials. Scaffold fabrication methods can be roughly divided into two groups: conventional and additive manufacturing (AM) techniques. Table 1.1 summarizes the pros and cons of various scaffold fabrication methods. AM is referred to any method by which the scaffold is produced layer by layer through the computer-aided design (CAD) file. The material, which is used to make scaffolds dictates the AM method that can be applied. Selective laser sintering (SLS), fused deposition modeling (FDM), stereolithography (SLA), and inkjet 3D printing are among the most used AM techniques. Being able to create complicated morphologies and maximal control over structural features and geometrical details is the main advantage of AM methods. However, conventional methods are still being used widely due to practical procedures, easy manipulation, low cost, and other advantages listed in Table 1.1.

It is worth explaining the conventional space holder method because this one will be used in this thesis to produce composite scaffolds in the following chapters. This technique is appropriate for producing a wide range of porosity with tunable homogenous pore size and shape (Wu et al., 2009). The technique is very similar to the solvent casting/particle leaching method with nearly the same drawbacks, such as low interconnectivity of pores and being restricted to simple shapes (Baino et al., 2015). Burning out of polymeric porogen agents (space holders) and resultant burning gas might cause crack formation inside the scaffold's structure (Bretcanu et al., 2014). This technique generally involves 3 steps; obtaining a homogenous mixture of ceramic components and space-holding (porogen) powders, compressing the mixture in the desired shape, and heat treatment of the compact to omit the

porogen agents, and consolidation of the green scaffold through sintering (Mawuntu and Yusuf, 2019; Mohammadi Zerankeshi et al., 2022).

Table 1.1 Various scaffold fabrication techniques and their advantages and disadvantages (Bose et al., 2018; Darus et al., 2018; Turnbull et al., 2018; Xiaohong Wang et al., 2016).

Manufacturing technique		Advantages	Disadvantages
Conventional methods	Gas foaming	<ul style="list-style-type: none"> - No chemical solvent - Low cost 	<ul style="list-style-type: none"> - Difficult to control pore size and shape - Difficult to the inclusion of cells and bioactive molecules to scaffold due to high pressure - No pore orientation
	Foam replication	<ul style="list-style-type: none"> - Large scaled pores - Interconnected pores - More complex shapes 	<ul style="list-style-type: none"> - Inconsistent thermal expansion coefficient - crack formation
	Solvent casting/particle leaching	<ul style="list-style-type: none"> - High regular porosity - Controllable pore size 	<ul style="list-style-type: none"> - Poor mechanical properties - Low interconnectivity - Limited to simple shapes
	Space holder	<ul style="list-style-type: none"> - Pore size homogeneity 	<ul style="list-style-type: none"> - Post sintering - Low mechanical strength due to crack formation

Table 1.1 (continued)

Manufacturing technique		Advantages	Disadvantages
Conventional methods	Freeze-drying	<ul style="list-style-type: none"> - No need for solid porogen - Improved mechanical properties - Interconnected pores - No harm to the environment 	<ul style="list-style-type: none"> - Long processing time - Irregular porosity - High energy consumption - Cytotoxic solvents
	Electrospinning	<ul style="list-style-type: none"> - Scaffold with a large surface area - Low cost and simple to use 	<ul style="list-style-type: none"> - Scaffold with irregular and non-homogenous pores distribution - Limited mechanical properties
AM	Direct inject 3D printing	<ul style="list-style-type: none"> - Mild condition of the process lets living cells and biomolecules plotting - Both ceramics and polymers - Well defined geometry 	<ul style="list-style-type: none"> - Post-processing is needed for some materials Optimization - Cytotoxic binders - High-cost instrumentation
	SLS	<ul style="list-style-type: none"> - No support is needed 	<ul style="list-style-type: none"> - Resolution limitation because of laser width

Table 1.1 (continued)

Manufacturing technique		Advantages	Disadvantages
AM	SLA	<ul style="list-style-type: none"> - Complex internal architecture can be produced - High resolution 	<ul style="list-style-type: none"> - Only photopolymers can be used - Finding biodegradable photopolymers
	FDM	<ul style="list-style-type: none"> - No need for a platform or support - Multiple nozzles for several materials 	<ul style="list-style-type: none"> - Resolution limitation because of the nozzle tip - Limited materials because of the need for melted phase

1.5.2 BAG incorporated scaffolds

Table 1.2 represents the summary of studies in which BAG was used to fabricate scaffolds for BTE. Following the study by Ramaswamy et al. (Ramaswamy et al., 2008), where they evaluated the biological properties of BAG nanoparticles and exhibited its possible applications in bone tissue regeneration, Roohani et al. (Roohani-Esfahani et al., 2012) were the first researchers, who developed BAG-based porous scaffolds for the treatment of critical size bone defects in 2012. Radiographical images of rabbit radial bone defects in their study depicted that there were better bone ingrowth and complete bridging in those defects with press-fit implanted BAG scaffolds after 12 weeks, compared to TCP/HA scaffolds. In addition to the higher new bone volume of BAG implanted scaffolds, the histological analyses demonstrated that the bone grew within the pores of these ceramic scaffolds in contrast to TCP/HA, where the bone tended to grow between the bone and

scaffold. The interaction of human osteoblasts and human adipose-derived mesenchymal stem cells with BAG was investigated by Lu et al. (Lu et al., 2014) to determine the influence of BAG on osteogenic gene expression of these cells and their cross-talk in co-culture. The results indicated that the attachment and spreading of cells on BAG and TCP/HA scaffolds were similar after 24 h of seeding. On the other hand, the expression of osteopontin, osteocalcin, bone sialoprotein, and RUNX2 genes of osteoblast cells was measured higher when they were cultured on BAG, compared to TCP/HA scaffolds. The analysis of indirect co-culture systems of cells on BAG and TCP/HA scaffolds showed that BAG scaffold modifies the interaction between HOBs and ASCs and led to the promotion of osteogenic differentiation of both cultured cells through raising the level of bone morphogenetic protein-2 (BMP2) expression.

In vitro cell viability results of MTT assay with human bone osteosarcoma cells (Saos-2) confirmed that BAG-based scaffolds have no cytotoxicity with respect to the control group cultured on tissue culture plastic (Arefpour et al., 2019b). Based on SEM images, good cell attachment and growth on the surface of scaffolds were reported. These findings imply that the chemical composition of $\text{Ca}_3\text{ZrSi}_2\text{O}_9$ scaffolds influences the viability, attachment, and proliferation of cells. A good cell attachment and spread were reported in another study in which the extract of BAG scaffolds had no cytotoxic effect on MG63 osteoblast cells (Bakhsheshi-Rad et al., 2017). In addition to enhanced cell viability and proliferation, addition of BAG to PCL/graphene-based electrospun nanocomposite scaffolds promoted the adhesion of P19 embryonal carcinoma cells on scaffolds (Samani et al., 2019). The cytocompatibility of BAG was confirmed and the improved viability and proliferation of MG63 and bone marrow stem cells cultured on different composites of BAG were reported in the most recent studies through *in vitro* tests (Abbasian et al., 2020; Sadeghzade et al., 2020).

Li et al. (J. J. Li et al., 2016) treated large bone defects in sheep tibia by using BAG scaffolds with and without PCL/bioactive glass coating. The implanted scaffolds could tolerate physiological loads and the results of *in vivo* tests demonstrated

remarkable bridging and induced new bone formation around the defect site. During one of the rare researches that concerned *in vivo* interaction between the material and host tissue to investigate the long-term potency and reliability of bone implants (J. J. Li et al., 2018), no unfavorable chronic inflammation or formation of a fibrous capsule around the implant was observed 26 weeks after the implantation of BAG scaffolds in sheep tibia to treat critical size bone defects. Meanwhile, a considerable new bone tissue formation around the scaffold, as well as the incorporation of a part of the implant and newly formed bone tissue were observed due to the appropriate degradation rate of the implanted scaffold.

The high apatite formation and bioactivity were reported on HA scaffolds containing BAG (Karamian et al., 2017). The porous BAG scaffolds were fabricated through a sponge template method and were used by Sehgal et al. (Sehgal et al., 2017) to develop a bioactive scaffold with the ability to sustain the delivery of an osteoinductive drug (dexamethasone disodium phosphate). The controlled release of osteogenic cues was confirmed through an *in vitro* release kinetics study in which the drug-loaded samples were dialyzed against phosphate-buffered saline (PBS) solution at 37°C up to 126 h. The effect of controlled delivery of drug from the scaffolds on MG63 cells was evaluated and the results demonstrated a significant increase in osteogenic differentiation of MG63 cells on BAG scaffolds, which were coated with drug-encapsulated chitosan nanoparticles compared to the uncoated BAG scaffolds. Additionally, the antibacterial activity of 1, 3, and 5 wt. % vancomycin-loaded BAG scaffolds were documented by Bakhsheshi-Rad et al. (Bakhsheshi-Rad et al., 2017) against *Staphylococcus aureus*. The bactericidal property of drug-loaded BAG scaffolds could reduce post-surgery infection risk which is an important failure factor in the treatment of bone defects.

Table 1.2 BAG incorporated scaffolds for BTE in the literature.

Composition	Scaffold Production Method	BAG Synthesis Method	Ref.
BAG (85 wt.%) + Diopside	Space holder	Sol-gel	(Sadeghzade et al., 2020)
BAG(3-10 wt.%) + Biomimetic nylon N6	Template sacrificial	Sol-gel	(Abbasian et al., 2020)
BAG (75-95 wt.%) + Diopside	Space holder	Sol-gel	(Sadeghzade et al., 2019)
PCL + Graphene + BAG	Electrospinning	Commercial	(Samani et al., 2019)
BAG + PCL as dip coating	Sponge replica	Sol-gel	(Arefpour et al., 2019b)
BAG		Sol-gel	(J. J. Li et al., 2018)
BAG (95-99 wt.%) + vancomycin	Salt leaching	Sol-gel	(Bakhsheshi-Rad et al., 2017)
BAG + XP-CN-GX hydrogel-coated	Sponge replica	Sol-gel	(Sehgal et al., 2017)
BAG (10-30 wt.%) + HA	Sponge replica	Sol-gel	(Karamian et al., 2017)
BAG	Space holder	Sol-gel	(Sadeghzade et al., 2017)
BAG	Sponge replica	Sol-gel	(J. J. Li et al., 2016)
BAG	Sponge replica	Sol-gel	(Kariem et al., 2015)
BAG	Freeze casting	Solid state	(Sadeghpour et al., 2014)
BAG	Sacrificial template	Sol-gel	(Lu et al., 2014)
BAG	Sacrificial template	Sol-gel	(Roohani-Esfahani et al., 2012)

Sadeghpour et al. (Sadeghpour et al., 2014) focused on the mechanical properties of BAG-based scaffolds, which were produced through the freeze casting method, and investigated the scaffolds with various porosities and mechanical strengths and their relationship with the cooling rate or solid loading. The expected inverse relationship between mechanical strength and porosity was noticed for BAG scaffolds; while higher cooling rates enhanced the mechanical properties of fabricated scaffolds. Since the porosity-stiffness (or microstructure-elasticity) relation plays a major role in the design of scaffolds for BTE, Kariem et al. (Kariem et al., 2015) conducted a comprehensive study to determine the relationship between porosity and stiffness of BAG scaffolds fabricated by using polymer sponge replica method, and to estimate mechanical properties of dense BAG as a potential biomaterial. Their findings confirmed the classical general inverse relationship between porosity and stiffness of polycrystal ceramics.

Porous BAG scaffolds with interconnected pores were fabricated by applying the space holder technique in which NaCl salt was used as the spacer to be removed by heat treatment (Sadeghzade et al., 2017). The results were compared with the mechanical properties of human compact and trabecular bones. It was concluded that BAG scaffolds with a porosity of ~75 % and pore size of 200-500 μm possessed appropriate compressive strength to serve as a candidate for spongy bone tissue regeneration. Most recently, the mechanical behavior of BAG and BAG/diopside composite scaffolds, sintered at different temperatures was evaluated (Sadeghzade et al., 2019). As the sintering temperature raised from 1300°C to 1400°C, compressive strength and elastic modulus of the scaffolds increased as expected. The maximum compressive strength (1.33 MPa) and elastic modulus (155 MPa) was obtained in scaffolds with BAG/diopside ratio of 80/20 wt.% which were sintered at 1400°C.

1.6 Aim of the thesis

TE is considered a possible solution to overcome problems of traditional bone defect treatments by a combination of scaffolds and living cells. A scaffold plays the leading role and serves as a transient structural template for cells to attach, interact, proliferate, differentiate, and secrete ECM in order to form new bone tissue. Composition and structural features of scaffolds should be designed and optimized to have scaffolds with appropriate physical features, mechanical strengths, and biological properties, such as biocompatibility, bioactivity, biodegradability, osteoconductivity, and osteoinductivity to achieve the ultimate goal of further *in vivo* and clinical bone formation and vascularization.

In this thesis, I aimed to propose a novel chemical composition, which contributes to modifying and improving the properties of scaffolds intended to be used in BTE applications through the steps below:

1. Using ion-doped HA and investigating the efficiency of this approach, which gained more popularity in recent years (Uskoković, 2020) through synthesizing BHA bioceramic powder with different molar ratios of dopant B and examining the influence of B doping dosage on various physicochemical, mechanical, and biological properties of HA nanoparticles. I hope this part of the thesis contributes to determining the appropriate B doping amount to boost HA properties for bone restoration or regeneration applications. I also think that my findings would help to clear up some debates about the effects of B on toxicity, cell growth, and osteogenic differentiation of stem cells that have been reported in the literature.

2. There are two approaches to produce BAG powder synthetically: sol-gel method and the direct solid-state reaction. However, sol-gel is the most common technique that has been used in many studies (Jodati et al., 2020b). Being time-consuming, requiring higher sintering temperatures (Schumacher et al., 2015), having chemical inhomogeneity, and appearing impurities during ball milling, and coarser particle sizes (Fu et al., 2004) are drawbacks that limit solid-state reaction applications. Concerning the sol-gel technique, the complete dissolution of Si, Ca, and Zr precursors inside a solvent and obtaining a clear solution (sol) is necessary before the gelation of the mixture. However, upon my pre-study efforts to reproduce the BAG by following the proposed sol-gel procedure in the literature (Table 1.1), I faced premature gel formation before the complete dissolving of Zr- precursor, and the larnite was the primary phase after the sintering process. Therefore, in this thesis, the BAG powder is going to be synthesized through the modified sol-gel method, where all precursors are dissolved completely to have a clear solution (sol). Later, synthesized powders are characterized to determine their physicochemical, mechanical, and biological properties for making further composite scaffolds.

3. Making composite scaffolds is one of the well-known methods to improve the properties of scaffolds used in BTE. In this thesis, novel bioceramic-based 3D porous composite scaffolds will be prepared using BHA with the optimum dosage of B, as the primary component, and BAG, as the secondary component. Later, the effects of making composites on the properties of BHA scaffolds will be investigated in terms of physicochemical, mechanical, and biological characteristics. I hope both the methods that will be applied to produce scaffolds and the incorporation of BAG contributes to make porous scaffolds with sufficient porosity, larger surface area, and even micropore presence. I hypothesize that composite scaffolds will be able to solve the low degradation problem of BHA through the exhibition of higher biodegradation

rates, as well as higher bioactivity, enhanced cell proliferation, and osteogenic differentiation due to both physical and chemical modifications in composite scaffolds. Eventually, I hope these novel composite scaffolds converge the advantages of both CaP and CaSi components to satisfy the various requirements needed for BTE applications and move one step forward on the road to fabricate an ideal scaffold.

CHAPTER 2

MATERIALS AND METHODS

2.1 Materials

Calcium nitrate tetrahydrate ($\text{Ca}[\text{NO}_3]_2 \cdot 4\text{H}_2\text{O}$, Merck, Germany), di-ammonium hydrogen phosphate ($[\text{NH}_4]_2\text{HPO}_4$, Merck, Germany), and boric acid (H_3BO_3 , Merck, Germany), ammonia solution (NH_3OH , Emsure[®] 25%, Merck, Germany), acetic acid (CH_3COOH , Sigma-Aldrich, Germany), sodium acetate (CH_3COONa , Sigma-Aldrich, Germany), sodium chloride (NaCl , Merck, Germany), sodium bicarbonate (NaHCO_3 , Merck, Germany), potassium chloride (KCl , Merck, Germany), dipotassium hydrogen phosphate trihydrate ($\text{K}_2\text{HPO}_4 \cdot 3\text{H}_2\text{O}$, Merck, Germany), magnesium chloride hexahydrate ($\text{MgCl}_2 \cdot 6\text{H}_2\text{O}$, Merck, Germany), hydrochloric acid (HCl , 1.0 M, Merck, Germany), calcium chloride (CaCl_2 , Merck, Germany), sodium sulfate (Na_2SO_4 , Merck, Germany), Tris ($\text{C}_4\text{H}_{11}\text{NO}_3$, Merck, Germany), Dulbecco's modified eagle's medium (DMEM, BI), Trypsin EDTA (BI), L-Glutamine Solution (BI), penicillin-streptomycin solution (Pen-Step, BI), foetal bovine serum (FBS, BI), 5-diphenyltetrazolium bromide (MTT), para-nitrophenyl phosphate (PNPP, Thermo Scientific, USA), alamarBlue cell viability reagent (Invitrogen), L-ascorbic acid ($\text{C}_6\text{H}_8\text{O}_6$, Alrich, Germany), β -glycerophosphate (β -GP), dexamethasone (DEX), ethanol (EMSURE, Merck, Germany), sodium azide (NaN_3 , Fluka), dimethyl sulfoxide ($\text{C}_2\text{H}_6\text{OS}$, SERVA), ethanolamine, 8-hydroxyquinoline (ACS reagent, ARCOS), o-cresolphthalein complexone (Sigma-Aldrich, Germany), sodium carbonate (Na_2CO_3 , Sigma-Aldrich, Germany), Sodium bicarbonate (NaHCO_3 , Sigma-Aldrich, Germany), triton X 100, PicoGreen[™], Zirconium [IV] oxynitrate hydrate ($\text{ZrO}[\text{NO}_3]_2 \cdot x\text{H}_2\text{O}$, Aldrich, USA), tetraethyl orthosilicate (TEOS, $\text{Si}[\text{C}_2\text{H}_5\text{O}]_4$, Merck, Germany), Alizarin Red S (ARS),

bicinchoninic acid solution (Sigma, Germany), sulfate pentahydrate ($\text{CuSO}_4 \cdot 5\text{H}_2\text{O}$, Sigma, Germany). All chemicals were reagent grade.

2.2 Methods

2.2.1 Synthesis and characterization of BHAs

2.2.1.1 Synthesis of BHA nanoparticles

The microwave-assisted wet chemical precipitation reflux method was utilized to synthesize nanocrystalline HA and BHA powders (Sadat-Shojai et al., 2013). Analytical grade calcium nitrate tetrahydrate ($\text{Ca}[\text{NO}_3]_2 \cdot 4\text{H}_2\text{O}$, Merck, Germany), di-ammonium hydrogen phosphate ($[\text{NH}_4]_2\text{HPO}_4$, Merck, Germany), and boric acid (H_3BO_3 , Merck, Germany) were used as calcium (Ca), phosphate (P) and boron (B) sources, respectively. To synthesize HA, 47.23 g of calcium nitrate tetrahydrate and 15.85 g of di-ammonium hydrogen phosphate were dissolved in 200 ml distilled water (dH_2O), separately. Then, a clear aqueous solution of di-ammonium hydrogen phosphate was poured dropwise into the calcium solution, which was stirring in a beaker. The pH of the suspension was maintained above 10 by adding an ammonia solution (NH_3OH , Emsure[®] 25%, Merck, Germany). After stirring for another 30 minutes (min), the suspension was irradiated for 15 min in an 800W microwave (SAMSUNG, MS23F301EAW, South Korea) during which it was refluxed. The produced precipitate was filtered, washed with dH_2O until pH dropped to ~ 7 , dried in an oven at 90 °C overnight, and heated at 200 °C for 2 h. The product was ground into a fine powder using a mortar and pestle and later sintered in a muffle furnace at 900 °C for 2 h. To synthesize BHA groups with different molar amounts of B in a way that the $\text{Ca}/(\text{P}+\text{B})$ molar ratio was equal to 1.67 (Table 2.1), a corresponding amount of boric acid was dissolved in di-ammonium hydrogen phosphate solution before adding into calcium solution.

Table 2.1 The nominal compositions of HA and BHA powders.

Sample	Reactants molar ratios		
	Ca	P	B
HA	10	6	0
0.05BHA	10	5.95	0.05
0.1BHA	10	5.9	0.1
0.25BHA	10	5.75	0.25
0.5BHA	10	5.5	0.5

2.2.1.2 XRD analysis of BHAs

The phase purity of HA and BHA powders was determined using an X-ray diffractometer (Rigaku Ultima IV) operated at 40 kV and 30 mA utilizing $\text{CuK}\alpha$ radiation, at a step size of 0.02° and a step time of 1 second. All diffractograms were obtained in the range of $20\text{--}60^\circ$ of 2θ angles. The degree of crystallinity (X_C) was calculated ($n=3$) according to the fraction of the crystalline phase available in the analyzed volume from X-ray diffraction data using Equation (1):

$$X_C = [1 - (V_{112/300} / I_{300})] \cdot 100 \quad (1)$$

where I_{300} is the intensity of (3 0 0) reflection, and $V_{112/300}$ is the intensity of the hollow between (1 1 2) and (3 0 0) reflection (Alshemary et al., 2015). The crystallite size of materials (D) was calculated ($n=3$) by applying Equation (2):

$$D = k\lambda / \beta \cos\theta \quad (2)$$

Where k is a constant that depends on crystallite morphology and its value is ~ 0.9 for spherical shapes; λ is the wavelength of X-ray (1.5405 \AA); β is the value of full

width at half-maximum (FWHM) of the peak of the (002), (210), (211), (112), (300), (202), (310), and (222) planes; and θ is the diffraction angle. Moreover, lattice parameters (a , c , and unit cell volume V) were calculated by Rietveld refinement using UNIT CELL software.

2.2.1.3 Elemental composition of BHAs

Elemental analysis and chemical composition of synthesized powders were determined ($n=3$) by inductively coupled plasma mass spectrometry (ICP-MS, Perkin Elmer DRC II model). Samples were prepared by the open digestion method. Approximately 100 mg of the sample was weighed. Then, 2 ml nitric acid (HNO_3) was added and the sample/blank was diluted to the final volume of 50 ml with deionized water before injecting inside analyzing chamber of ICP-MS. The ICP-MS provides the weight of elements that exist in the samples. By using the molar mass of elements we converted these values to molar values and calculated measured molar ratios of Ca/P, Ca/(P+B), and B/P.

2.2.1.4 FTIR and morphology of BHAs

FTIR spectra were recorded within the frequency range of $4000\text{-}400\text{ cm}^{-1}$, using a Fourier transform infrared spectrophotometer (Bruker IFS66/S) to study the presence of the functional groups. The microstructure and morphology of HA and BHA powders were examined by scanning electron microscopy (QUANTA 400F Field Emission SEM, U.S.). The intercept method was applied to calculate the average particle size (grain size) from SEM images by using ImageJ software.

2.2.1.5 Density of BHAs

To measure the density and mechanical properties of HA and BHAs, material powders (before sintering) were passed through a sieve with $212\text{ }\mu\text{m}$ orifices. They

were pressed in the shape of disks (~12 mm diameter and ~3 mm thickness) via an automatic hydraulic cold press device (Carver, USA) under the imposed force of ~22.24 kN for 3 minutes before analysis. Disks were sintered at 900 °C for 2 h and their bulk densities were calculated by dividing the measured dry weight by volume (n=3). The relative density of samples was calculated by dividing the measured density by the theoretical density. Equation (3) was applied to calculate the theoretical density of samples, where Z is the number of molecules per unit cell, M is the molecular weight of the material, V is the unit cell volume derived from XRD results, and N is Avogadro number (Kaya et al., 2021):

$$\rho_t = \frac{ZM}{VN} \quad (3)$$

2.2.1.6 Mechanical properties of BHAs

The Vicker's microhardness (HV) of samples was measured using a microhardness test device (HMV-2, Shimadzu, Japan). Three disks were used and 7 measurements were performed on each disk to have a total of 21 measurements for each group. During the test, a diamond tip applied a force of 2.942 N for 15 seconds and the indent diameter was measured by an optic microscope. Equation (4) was used to calculate HV (GPa), where P is the applied load (N), and d is the length of indent (mm):

$$HV = 0.0018544P/d^2 \quad (4)$$

To measure diametral tensile strength, disks (n=4) were subjected to compression force by a universal testing system (Instron 5944, USA). In the course of compression, the maximum tensile force is created across the surface diameters of disks perpendicular to the compressive load direction. Equation (5) was employed to calculate the tensile strength of the samples, where S is tensile strength (MPa), F is failure force (N), t is disk thickness (mm), and D is the sample's diameter (mm):

$$S = \frac{2F}{\pi Dt} \quad (5)$$

2.2.1.7 Biodegradability and bioactivity of BHAs

In vitro biodegradability of HA and BHA samples was investigated through the measurement of weight loss (n=3) in acetic acid and sodium acetate buffer solution (AcOH-AcONa, pH=5.5), which simulates osteoclastic resorption of HAs (Ito et al., 2006). After measurement of the dry weight of disk samples (w_{bi}), they have immersed into the buffer solution inside paraffin-sealed polystyrene bottles and incubated at 37 °C for 1, 7, 14, 21, and 28 days. At each incubation time, the samples were taken out, gently rinsed twice with dH₂O to remove residual salts, and air-dried inside a fume hood for 48 h. Dry weight of disks was measured again (w_{ai}) and weight losses were calculated using Equation (6):

$$\text{weight loss \%} = \frac{w_{bi} - w_{ai}}{w_{bi}} \times 100 \quad (6)$$

In vitro bioactivity was investigated according to the procedure reported by Kokubo and Takadama (Kokubo and Takadama, 2008). The disk-form samples (n=3) were immersed in simulated body fluid (SBF) with a pH of 7.4 (Table 2.2) and incubated at 37 °C for 1, 4, 7, and 14 days. At the end of each incubation period, the samples were taken out, rinsed with dH₂O gently, and air-dried inside a fume hood for 48 h. SEM/EDX (QUANTA 400F Field Emission SEM, U.S.) was used to observe the morphology of apatite depositions on the surface of HA and BHA samples; Ca/P ratios of the depositions were also measured using energy dispersive X-ray analysis (EDX). Moreover, after measuring the pH of the filtrates (pH meter, Thermo Orion 3 star), the variation of Ca²⁺, PO₄³⁻, and BO₃³⁻ ions in SBF filtrate was determined using ICP-MS.

Table 2.2 Reagents and their amounts to prepare 1 liter SBF solution.

Order	Reagent	Amount
1	Sodium chloride	8.035 g
2	Sodium bicarbonate	0.355 g
3	Potassium chloride	0.225 g
4	Dipotassium hydrogen phosphate trihydrate	0.231 g
5	Magnesium chloride hexahydrate	0.311 g
6	Hydrochloric acid (1M)	39 ml
7	Calcium chloride	0.292 g
8	Sodium sulfate	0.072 g
9	Tris	6.118 g

2.2.1.8 *In vitro* cell studies of BHAs

In vitro cell studies were conducted with human bone osteosarcoma cells (Saos-2). The cells were cultured in a growth medium consisting of Dulbecco's Modified Eagle's medium (DMEM) supplemented, with 10% fetal bovine serum (FBS) and 100 U penicillin/streptomycin at 37 °C in a humidified atmosphere of 95% air and 5% CO₂ (5215 Shel Lab., Cornelius, OR, USA). After reaching 80% confluency, cells were subcultured using 0.1% of the trypsin/EDTA solution.

2.2.1.8.1 Cell proliferation of BHAs

Cell proliferation on disks was evaluated by the alamarBlue™ viability assay using the supplier's protocol. Disks were sterilized by heating at 200 °C for 2 h and exposing them to UV for 1 h. Later, they were placed into wells of 24-well plates, seeded with Saos-2 cells at an initial seeding density of 10×10^3 cells/disk, and were incubated at 37 °C under a 5% CO₂ atmosphere. At different incubation periods, disks (n=4) were rinsed twice with sterile phosphate-buffered saline (PBS) then alamarBlue solution (1/9 [v/v] ratio of reagent to growth medium) was added to the wells and well plates were kept inside a 5% CO₂ incubator. After 4 h, aliquots were collected and their absorbance was recorded at 570 nm as primary and 600 nm as reference wavelengths using Microplate Reader (μQuant™, BioTek, Winooski, VT, USA). Cell culture growth medium was added to the wells with disks for continuing the cultivation of the cells on the disks. Cell viability on HA disks was taken as 100% and used as a control to study the effect of B dopant of different amounts on the biological properties of HA, while cell-free disks served as a negative control.

Field emission scanning electron microscopy (FESEM, QUANTA 400F) was used to examine the morphology of cells seeded on disks after 1 and 7 days of incubations. The samples were washed 3 times with PBS gently, and cells were fixed with 4% paraformaldehyde solution for 15 minutes. Then, they were dehydrated with graded ethanol-water solution series (30%, 50%, 70%, 80%, 90%, and 100%), and hexamethyldisilazane. Finally, the samples were vacuum-dried, and gold sputter coated.

2.2.1.8.2 ALP activity and intracellular calcium deposition of BHAs

Alkaline phosphatase (ALP) activity, as an early osteogenic marker (Yang et al., 2018), and intracellular calcium quantification assays were used to evaluate the influence of synthesized materials on the osteogenic activity of Saos-2 cells (n=5). The density of seeded cells (passage 8) was 70×10^3 cells/disk. The cells on the disks were incubated in an osteogenic medium (growth medium plus 50 $\mu\text{g/ml}$ ascorbic acid, 10 mM β -glycerophosphate, and 10^{-8} M dexamethasone) for 7 and 14 days. The osteogenic medium was changed every two days. At the end of each incubation period, the medium was removed from the wells, and disks were washed with PBS. Afterward, wells were filled with 600 μl fresh cell lysis buffer (1:9 v/v Triton X100-1% and carbonate buffer) and the cells on the disks were burst by the two cycles of the freeze-thaw process. To measure ALP activity, 50 μl of the cell lysates was incubated in 100 μl para-nitrophenyl phosphate (PNPP) working solution at 37 °C for 60 minutes, and absorbance of the solution was measured at 405 nm by the microplate reader (Alshemary et al., 2018). DNA content of the cell lysates was determined by PicoGreen™ and later used to normalize ALP activity (Pazarçeviren et al., 2021). To measure DNA within the cell lysates, PicoGreen™ was diluted 100 times in TE buffer (10 mM Trishydroxyamino methane + 1mM EDTA), cell lysate was added to the prepared dye (1:1 v/v), and the solution was shaken at 120 rpm for 10 minutes. After reading fluorescence at 485 nm excitation and 538 nm emission, DNA amount was quantified using a calibration curve constructed with different concentrations of DNA (0-250 ng/ml).

Intracellular calcium content of the cell lysates was measured through o-cresolphthalein dye assay (Pazarçeviren et al., 2019). Briefly, the lysates in 100 μl aliquots were mixed with 100 μl Ca^{2+} indicator dye (o-cresolphthalein complexone, 8-hydroxyquinoline, hydrochloride acid, and ethanolamine) by shaking on an orbital shaker for 5 minutes, and the intensity of color was measured by reading absorbance at 570 nm using the microplate reader. The calcium amounts were calculated by using the calibration curve constructed with different concentrations of calcium

chloride (Merck, Germany) in dH₂O. To normalize intracellular calcium amounts, protein amounts of the cell lysates were determined using Bicinchoninic Acid assay (BCA) (Pazarçeviren et al., 2018). The cell lysate and BCA stain (1:7 v/v) were incubated at 37 °C for 1 h and absorbance was measured at 562 nm with the microplate reader. A calibration curve constructed with different concentrations of bovine serum albumin was used to quantitate the total protein amount in the lysates.

2.2.1.8.3 Matrix mineralization of BHAs

The matrix mineralization on the cells was examined using Alizarin Red S (ARS) after incubation of cells in the osteogenic medium for 7 and 14 days. At each time point, the seeded cells were washed with PBS, stained with 2% ARS solution (pH=4.1) for 30 min at room temperature (RT), and rinsed 3 times with dH₂O gently to wash out the excess dye. The images were taken after 30 minutes of drying of samples in the air using light microscopy (Nikon, Japan).

2.2.2 Synthesis and characterization of BAG

2.2.2.1 Synthesis of BAG nanoparticles

The modified sol-gel route was employed for the synthesis of BAG powder, in which two different features were changed compared to conventional sol-gel methods: (a) dissolving Zr precursor separately in ethanol, and (b) using different TEOS:ethanol: HNO₃ molar ratio. Zirconium [IV] oxynitrate hydrate (ZrO(NO₃)₂.xH₂O, Aldrich, USA), tetraethyl orthosilicate (TEOS, Si(C₂H₅O)₄, Merck, Germany), and calcium nitrate tetrahydrate (Ca(NO₃)₂.4H₂O, Merck, Germany) were used as Zr, Si, and Ca precursors, respectively. Amount of each precursor was calculated according to 1:2:3 molar ratios of Zr:Si:Ca in the BAG chemical formula. Briefly, 2.335 g of zirconium [IV] oxynitrate hydrate was dissolved in 50 ml pure ethanol (EMSURE[®], Merck, Germany) using the stirrer.

Meanwhile, 1 ml nitric acid (HNO_3 , 2M, Isolab, Turkey), as a chelating agent, was added into the 50 ml ethanol (EMSURE[®], Merck, Germany) that had 4.45 ml TEOS, and obtained mixture of TEOS:ethanol: HNO_3 with molar ratios of 1:42:1 mixed in a separate beaker on the stirrer for hydrolysis. Nitric acid, in addition to the modification of the molecular structure of sol, acts as a chelating agent and stabilizes the sol by reducing the alkoxide reactivity (Ahmad and Rusop, 2009). After the complete dissolving of Zr precursor in ethanol, this solution and 7.084 g of calcium nitrate tetrahydrate were added into the mixture of TEOS:ethanol: HNO_3 , and a clear solution (sol) was obtained after 5 h of stirring before gelation. The prepared sol was heated at 60 °C for 24 h and at 100 °C for another 24 h inside the oven to have dried gel as a powder. Finally, the dried powder was heat treated and sintered at 1150 °C for 3 h in the air. Moreover, different ratios of TEOS:ethanol: HNO_3 (1:8:0.16, 1:21:1, 1:30:1, and 1:42:1) were examined to figure out the optimum value for the TEOS:ethanol: HNO_3 mixture. The clarity of the sol (ethanol after dissolving all precursors), and the phase structure of the powder after heat treatment and sintering at 1150 °C for 3 h were two criteria that were used to control the quality of the final product. After the naked eye visual inspection of the solution's turbidity, the pH values were measured by a standard pH meter.

2.2.2.2 Heat treatment and thermal analysis of BAG

Heat treatment gives the opportunity to manipulate the properties of the materials by controlling the rate of diffusion and the cooling rate within the microstructure. To synthesize BAG powder, first gel powder was dried at 60 °C for 24 h in the air and subsequently dried at 100 °C for 24 h in the air again on the hot plate. Then the obtained samples were placed in the furnace for drying at 300 °C for 30 minutes with a heating rate of 5 °C/min, oxidizing at 600 °C for 30 minutes, and sintering at 1150 °C for 3 h in the air. After the sintering process, the sample was left to cool in the furnace. Thermal properties of dried gel were analyzed with thermogravimetry

analysis-differential thermal analysis (TGA-DTA, Setaram Labsys), to determine reaction types of powders at a scan rate of 5°/min from 25 to 1200 °C.

2.2.2.3 XRD and FTIR analyses of BAG

X-ray diffraction (XRD, Rigaku Ultima IV) was used to determine the BAG phase purity, lattice parameters, and cell unit volume of the material. The XRD test was operated at 40 kV and 30 mA utilizing CuK_α radiation on a step size of 0.1° and a step time of 1 second, and a diffractogram was obtained in the range of 10–70 ° of 2θ angles. Using XRD data, the modified Scherrer Equation (7) was applied to estimate the size of crystallite of BAG (Monshi et al., 2012), where D is the size of crystallite, k is constant that depends on crystallite morphology and its value is ~0.9; λ is the wavelength of X-ray (1.5405 Å); β is the value of full width at half-maximum (FWHM) of the peaks of the (202), (113), (0 2 3), (0 3 2), (2 1 3), (2 4 2) planes; and θ is the diffraction angle corresponding to peaks in radian.

$$\ln\beta = \ln(1/\cos \theta) + \ln(k\lambda/D) \quad (7)$$

Lattice parameters and cell volume unit of material were derived by refinement of XRD data using Cell software of Holland and Redfern (Kaya et al., 2021). Moreover, the crystallinity percentage of BAG was calculated using XRD data by a ratio of the area of crystalline peaks to the total area of all amorphous and crystalline peaks together using OriginLab software. Fourier Transform Infrared Spectroscopy (FTIR, Bruker IFS66/S) was used to identify functional groups in the synthesized BAG. FTIR spectrum was recorded within the frequency range of 4000-400 cm⁻¹.

2.2.2.4 Physicochemical properties of BAG

Inductively coupled plasma mass spectrometry (ICP-MS, Perkin Elmer DRC II model) was used to analyze the elemental and chemical composition of synthesized BAG powder. Moreover, the microstructure and morphology of the powder were examined by scanning electron microscopy (QUANTA 400F Field Emission SEM, U.S.). The gold (Au) sputtering was applied to coat the surface of the sample before taking SEM images. The particle size distribution of BAG was measured by a laser diffraction particle size analyzer (Mastersizer 2000, Malvern, UK). The particles were passed through the sieve with an orifice size of 212 μm before measuring their size with the laser diffraction particle size analyzer.

2.2.2.5 Density and mechanical properties of BAG

For measuring the density, BAG was sieved through a sieve with an orifice of 212 μm , the powder was pressed in the shape of a disk (~13 mm diameter), using an automatic hydraulic cold press device (Carver, USA). The pressing force of ~22.24 kN was imposed for 3 minutes, and the disks were sintered at 1150 $^{\circ}\text{C}$ for 3 h before measurement. The density (ρ) and porosity of samples were measured by applying Archimedes principles and Equations (8) and (9) (Evis et al., 2013; Moonesi Rad et al., 2019), where $wt_{.air}$ is the weight of dry disk in the air, $wt_{.wet}$ is the weight of water-saturated wet disk in the air, and $wt_{.sub}$ is the weight of submerged disk in the water. The measured density was divided by the theoretical density of BAG ($\rho_{th}= 3.84 \text{ g/cm}^3$) (Kariem et al., 2015) to calculate the relative density of samples.

$$\rho = \frac{wt_{.dry}}{wt_{.dry} - wt_{.sub}} \times \rho_{water} \quad (8)$$

$$\text{porosity (\%)} = \frac{wt_{.wet} - wt_{.dry}}{wt_{.wet} - wt_{.sub}} \times 100 \quad (9)$$

Diametral tensile strength of BAG samples (n=6) was measured by subjecting disks to compression load using the universal testing system (Instron 5944, USA). Note that in the course of compression, the surface diameters of the disk that were perpendicular to the compressive force direction are where the maximum tensile force would be created across. The samples were prepared and tested according to ASTM Standard D3967-08, and Equation (5) was used to calculate the tensile strength (Method, 2008), where S and F are tensile strength (MPa) and failure force (N), respectively, while D is the sample's diameter (mm), and t was disk thickness (mm).

The microhardness test device (HMV-2, Shimadzu, Japan) was employed to measure the Vicker's hardness (HV) of samples. Three samples were prepared and 10 measurements were performed on each disk to have a total number of 30 measurements. The diamond tip applied a force of 490.3 mN for 15 seconds and the optical microscope measured the indent diameter. The hardness value HV (GPa) was calculated by using Equation (4), in which P was applied load (N), and d was the length of indent (mm) (ASTM International, 2017).

2.2.2.6 Biological analyses of BAG

2.2.2.6.1 *In vitro* biodegradability and bioactivity of BAG

Weight loss of samples in acetic acid and sodium acetate buffer solution (0.1 M, pH=5.5) was measured to examine *in vitro* biodegradability of BAG. Briefly, the dry BAG disks (n=3) were weighed (w_{bi}), then, submerged in the prepared buffer solution inside polystyrene falcon tubes, and incubated at 37 °C shaking water bath for 28 days. The buffer solutions were changed each day to minimize the pH change in solutions. At each time point of 1, 7, 14, 21, and 28 days, after removing the buffer solution, the samples were rinsed 3 times with dH₂O, and their weights were

measured after air-drying disks (w_{ad}). Equation (6) was used to calculate weight losses.

Kokubo and Takadama's protocol (Kokubo and Takadama, 2008) was applied to study *in vitro* bioactivity of BAG. The disk samples (n=3) were kept in SBF with a pH of 7.4 for specified incubation periods at 37 °C. The volume of used SBF was ~ 31 ml, which was 1/10 of the surface area of the specimen (~310 mm²). To evaluate bioactivity, the samples were gently rinsed with dH₂O and air-dried using the fume hood at the end of each incubation period (1, 4, 7, and 14 days). The formation, morphology, and Ca/P ratios of apatite deposition on the surface of BAG disks were examined by Scanning Electron Microscopy and Energy Dispersive X-ray analysis (SEM/EDX, QUANTA 400F Field Emission SEM, U.S.). Furthermore, changes in the concentration of Ca, P, and Si of the filtrate were determined using ICP-MS (Perkin Elmer DRC II model), and the pH of the filtrate was measured using a pH-meter (Thermo Orion 3 star).

2.2.2.6.2 *In vitro* cell culture studies of BAG

The Saos-2 was used throughout *in vitro* cell culture studies. Saos-2 is a human osteosarcoma cell line that exhibits several characteristics of osteoblastic cells, like having high alkaline phosphatase activity and producing a mineralized matrix, which makes them an attractive source of bone-related molecules for research (Murray et al., 1987). Cells were cultured in a growth medium (GM) consisting of Dulbecco's Modified Eagle's medium (DMEM), 10% fetal bovine serum (FBS), and 100 U penicillin/streptomycin and maintained in a humidified atmosphere of 95% air and 5% CO₂ (5215 Shel Lab., Cornelius, OR, USA) at 37 °C. Saos-2 cells reached almost 80 % confluency before subculturing them with 0.1% of the trypsin/EDTA solution to evaluate the cytotoxicity of BAG powders. BAG particles were sterilized at 200 °C for 2 h before adding to the cell growth medium. Cells were seeded at the initial density of 1.0×10^4 cells per well in 96-well plates. After 24 h, they were exposed to the cell growth medium containing different concentrations of BAG particles (25,

12.5, 6.25, and 3.125 $\mu\text{g/ml}$) and incubated for 24 and 48 h. Cell viability was measured using MTT assay at each time point (Pazarçeviren et al., 2021). Briefly, the growth media were discarded, wells were rinsed with phosphate-buffered saline (PBS, 0.1 M, pH=7.4), and 200 μl MTT solution (0.5 mg/ml in DMEM without phenol red) was added to each well. Then, the plate was maintained in the incubator at 37 °C for 4 h. Afterward, MTT solutions were vacated and 200 μl dimethyl sulfoxide (DMSO) was added to each well for dissolving precipitated formazan crystals formed inside the cells. Finally, the optical density (OD) of the solutions in wells was read at 570 nm (n=3) using Microplate Reader ($\mu\text{Quant}^{\text{TM}}$, BioTek, Winooski, VT, USA). Cells were also cultured in the plastic base of the plate (TCPS) and exposed to a growth medium without the BAG particles and served as the positive control group. Cell viability (%) was calculated using Equation (10), where the viability of the positive control was taken as 100% (Hu et al., 2017):

$$\text{Cell viability (\%)} = \left(\frac{[(\text{OD})_{\text{sample}} - (\text{OD})_{\text{blank}}]}{[(\text{OD})_{\text{Control}} - (\text{OD})_{\text{Blank}}]} \right) \times 100\% \quad (10)$$

The ALP activity and intracellular calcium quantification assays were used to examine the influence of BAG on the osteogenic activity of Saos-2 cells. The initial density of seeded cells (passage 22) was 3×10^4 cells/well in 24 well-plate (n=3). After 24 h, the GM in the wells was replaced with an osteogenic medium (OM) that included BAG particles with different concentrations of 50, 25, 12.5, 6.25, and 3.125 $\mu\text{g/ml}$. Plates were incubated for 7 and 14 days in a humidified atmosphere of 95% air and 5% CO_2 (5215 Shel Lab., Cornelius, OR, USA) at 37 °C. The OM consisted of GM, BAG particles with mentioned concentrations, 50 $\mu\text{g/ml}$ ascorbic acid, 10 mM β -glycerophosphate, and 10^{-8} M dexamethasone (DEX), which was changed every two days. At the end of each incubation period, the medium (OM+BAG) was removed from the wells, and cells were washed with PBS. Afterward, wells were filled with 600 μl fresh cell lysis buffer (Triton X100-1%,

carbonate buffer, 1:9 v/v) and the cells were burst by the two cycles of the freeze-thaw process. To measure ALP activity, 50 μ l of the cell lysate was incubated in a 100 μ l para-nitrophenyl phosphate (PNPP) working solution at 37 °C for 60 minutes, and absorbance of the solution was measured at 405 nm by the microplate reader (Alshemary et al., 2018).

Intracellular calcium content of the cell lysates was measured through o-cresolphthalein dye assay (Pazarçeviren et al., 2019). Briefly, the lysates in 100 μ l aliquots were mixed with 100 μ l Ca^{2+} indicator dye (o-cresolphthalein complexone, 8-hydroxyquinoline, hydrochloride acid, and ethanolamine) using shaking on an orbital shaker for 5 minutes, and the intensity of color was measured by reading absorbance at 570 nm using the microplate reader. Calcium amounts were calculated by using the calibration curve constructed with different concentrations of calcium chloride (Merck, Germany) in distilled water. To normalize ALP activity and intracellular calcium, protein amounts of the cell lysates were determined using a Bicinchoninic Acid assay (BCA) (Pazarçeviren et al., 2018). The cell lysate was mixed with BCA stain (1:7 v/v) and incubated at 37 °C for 1 h. The absorbance was then measured at 562 nm with the microplate reader. A calibration curve constructed with different concentrations of bovine serum albumin was used to quantitate the total protein amount in the lysates. Moreover, ALP activity of cells cultured in the absence of an osteogenic medium (OM), where GM merely contained 10^{-8} M DEX and 12 μ g/ml BAG, was measured by following the same steps as mentioned above (n=5).

2.2.3 Preparation and characterization of BHA-BAG composite scaffolds

2.2.3.1 Fabrication of 3D porous BHA-BAG composite scaffolds

To prepare composite scaffolds, first, the homogenous mixture of BHA and BAG was obtained by stirring two powders in ethanol for 3 h, based on weight percentages (wt.%) represented in Table 2.3. The ethanol was later evaporated at 40 °C overnight. Second, BHA-BAG powders were added to the PVA solution (10 w/v %, P-1763, SIGMA, USA), mixed for 2 h, and dried overnight at RT. Mortar and pestle were used to grind the dried mixture to small particles (size $\leq 212 \mu\text{m}$). Third, 10 wt.% of the polymeric porogen agents (polyethylene glycol, PEG 6000, Merck, Germany) with particle sizes between 212-425 μm were homogeneously dispersed in 90 wt.% of the powder mixture. Forth, cylindrical green scaffolds were created by applying 3000 lbs of uniaxial compression force for 3 min on the powder-porogen mixture using cold press apparatus (Carver, USA). Eventually, the porous composite scaffolds were obtained through the removal of polymeric binding and porogen agents (PVA and PEG) from the green scaffolds by heating them at 900 °C for 2 h in the muffle furnace.

Table 2.3 The nominal composition of scaffolds, based on wt.% of components.

Sample	BHA wt.%	BAG wt.%
BHA	100	0
BHA-BAG-5	95	5
BHA-BAG-10	90	10
BHA-BAG-15	85	15
BHA-BAG-20	80	20

2.2.3.2 Microstructure and physicochemical characterization of scaffolds

Field Emission Scanning Electron Microscopy (FESEM, QUANTA 400F, US) was used to monitor the morphology and microstructure of scaffolds. The surface of the scaffolds was coated with gold (Au) sputtering prior to imaging. Elemental analysis of all scaffolds was conducted using Inductively Coupled Plasma Mass Spectrometry (ICP-MS, Peka Elmer DRC II model). The Differential Scanning Calorimeter-Thermogravimetric analysis (TA Instruments SDT 650 Simultane DSC-TGA) was applied from 25 °C to 1200 °C at the scan rate of 10°/minute for the evaluation of the thermal properties of scaffolds, especially the removal of polymeric agents.

Presence of phases was determined by an X-ray diffractometer (Rigaku Ultima IV), which was operated at 40 kV and 30 mA. Diffractograms were obtained in the range of 10° to 90° of 2 θ angular degrees, utilizing CuK α radiation with a size step of 0.02° at the scan speed of 1 second per step. Rietveld refinement was employed, using Highscore Plus v.3 software, to calculate the percentage of two phases in composite scaffolds, as well as the unit cell parameters of each phase. The crystallinity degree (CD) of scaffolds was calculated based on the ratio of crystalline area to crystalline plus amorphous area (whole XRD pattern).

The functional groups of elemental constituents were identified by Fourier Transform Infrared Spectroscopy (FTIR, Bruker IFS66/S, Germany). All spectra were recorded between 4000 cm⁻¹ and 400 cm⁻¹ wavenumber frequency. The specific surface area (SSA), micropore size, and pore volume of scaffolds were measured using multipoint Brunauer-Emmett-Teller analysis (BET, Quantachrome Corporation – Autosorb 6, USA). Equation (9) was used to calculate the porosity of scaffolds based on Archimedes's principle (Jodati et al., 2020a), where w_{air} is the weight of a dry scaffold in the air, while w_{sub} and w_{wet} are weights of the submerged scaffold in the water and the water-saturated wet one in the air respectively.

2.2.3.3 Mechanical characterization of scaffolds

Right cylindrical scaffolds were subjected to compressive load (Instron 5944, USA), and the compressive strength (C) of each test specimen in MPa ($n=5$) was calculated using Equation (11), where P is the total load on the specimen at failure (N), and A is the calculated area of the bearing surface of the specimen (mm^2):

$$C=P/A \quad (11)$$

ASTM standard (D3967-08) was used to measure the diametral tensile strength (S) of scaffolds in MPa ($n=5$), based on Equation (5). In the course of the test, although the test specimens were subjected to compressive load, the maximum tensile force would be developed across perpendicular surface diameters to the force's direction. Note that in Equation (5), F is failure load (N), while D (mm), and t (mm) are the diameter and thickness of the cylindrical scaffold, respectively.

Vicker's microhardness (HV) of scaffolds was measured using the microhardness test device (HMV-2, Shimadzu, Japan). 3 scaffolds were tested and 10 measurements were executed on each scaffold to have a total number of 30 measurements. A force of 0.4903 N was applied by the diamond indenter for 15 seconds and the indent diameter was measured by the optical microscope. The hardness value HV (GPa) was calculated by substituting applied load P (N), and length of indent d (mm) values in Equation (4) (Kaya et al., 2021).

2.2.3.4 *In vitro* biological characterizations of scaffolds

In vitro biodegradation rate of scaffolds was measured through a weight loss inside buffer solution (n=3). After weighing, specimens were immersed in the 0.1M acetic acid and sodium acetate buffer solution with a pH of 5.5, which simulates the pH of the defective area in the bone tissue, and incubated inside the water bath at 37 °C for specific periods. At specific time points (1, 4, 7, 14, 21, and 28 days) the scaffolds were taken out, rinsed with dH₂O three times, and air-dried to remove the liquid buffer completely. Equation (6) was used to calculate the degradation percentage of scaffolds after measuring their dried weight, where w_{bi} and w_{ad} are the dry weight of scaffold specimens before and after immersion, respectively. Note that the buffer solution was changed every day to keep the pH about 5.5 throughout immersion.

In vitro bioactivity of scaffolds was conducted following Kokubo and Takadama's protocol (Kokubo and Takadama, 2008). The specimens (n=3) were immersed in simulated body fluid (SBF, pH=7.4) and incubated for specified periods at 37 °C. The volume of SBF solution (20 ml) was adjusted to 1/10 of the surface area of the specimen (~200 mm²) based on protocol. At the end of each incubation period (1, 4, 7, and 14 days), after measuring the pH of the solution with a pH meter (Thermo Orion 3 star), scaffolds were taken out, gently rinsed with dH₂O, and then air-dried inside the fume hood. The bioactivity was evaluated by detecting the formation of apatites on the surface of scaffolds using Field Emission Scanning Electron Microscopy and Energy Dispersive X-ray analysis (FESEM/EDX, QUANTA 400F, U.S.).

In vitro ion release test was conducted in dH₂O with 0.2% sodium azide (Sigma, USA). Scaffolds were immersed in that solution with a concentration of 0.2 mg/ml and incubated at 37 °C for different time intervals (1, 4, 7, and 14 days). At each time point, the samples in falcon tubes were centrifuged at 8000 rpm for 5 min and the filtrate was then collected. The release profiles of Ca, B, and Si ions were measured using Inductively Coupled Plasma Optic Emission Spectrometry ICP-OES(Perkin Elmer Optima 4300DV).

2.2.3.5 *In vitro* cell culture studies of scaffolds

Human fetal osteoblast cells (hFOB, ATCC 1.19 CRL-11372, passage 10) were used to conduct *in vitro* cell culture studies. Cells were cultured in a growth medium (GM), composed of 89% (v/v) Dulbecco's Modified Eagle's medium (DMEM/F12), 10% (v/v) fetal bovine serum (FBS), and 1% (v/v) antibiotic cocktail (penicillin-streptomycin, 100U), and incubated inside an incubator (5215 Shel Lab., Cornelius, OR, USA) with the humidified atmosphere of 5% CO₂ and 95% air at 37 °C to reach 80% confluency before seeding on scaffolds. Prior to cell seeding, scaffolds were sterilized by heating at 200 °C for 2 h, following UV radiation for 1 h, and later incubated inside GM at 37 °C for 24 h.

2.2.3.5.1 Cell proliferation of scaffolds

For cell proliferation, cells were seeded on scaffolds (n=4) at an initial density of 2×10^4 cells/scaffold. The GM was added to cell-cultured specimens placed in 24-well plates and were incubated for specific time points (1, 4, and 7 days). At each time point, after discarding media, the scaffolds were rinsed with sterile phosphate-buffered saline (PBS, 0.1M, pH=7.4) two times, and cell proliferation was evaluated using the alamarBlue™ viability assay. For this purpose, the alamarBlue reagent was mixed with DMEM/F12 without phenol red (1:9 v/v), and the solution was added to wells that contained scaffolds. After 4 h in the 5% CO₂ incubator at 37 °C, the wells were taken out, aliquots were transferred to a new plate, and the absorbance was recorded at 570 nm and 600 nm wavelengths by Micro-plate Reader (μQuant™, BioTek, Winooski, VT, USA). After discarding the alamarBlue solution and washing specimens with PBS, new GM was added to the wells with scaffolds for continuing the cultivation of the cells on the scaffolds. while cell-free scaffolds served as a blank control, cell viability on the BHA scaffold was assumed 100%, as a control group, to evaluate cell the composite scaffolds' effect on cell proliferation.

2.2.3.5.2 Imaging of cells on scaffolds

The morphology of hFOB cells on scaffolds was explored by FESEM after 1 and 7 days of incubation. To obtain SEM micrographs, after transferring scaffolds to the new well plate and 3 times washing them with sterile PBS, cells were fixed on scaffolds with 4% paraformaldehyde for 20 min. Then, the scaffolds were dehydrated by keeping them in an increasing series of ethanol-water solutions from 30% to 100%. The process was accomplished by immersion of them in hexamethyldisilazane for 10 min, and later air-drying for 24 h.

Confocal laser scanning microscopy (CSLM Leica DM2500, Germany) was also used for further analysis of cells on scaffolds after 1 week of incubation. Similar to specimens preparation for SEM imaging, cells were fixed on scaffolds, but after fixation cells were washed with PBS and later permeabilized by keeping them in 1% (v/v) Triton X-100 (in PBS) for 5 minutes. Next, 1% (w/v) Bovine Serum Albumin (BSA) in PBS solution was added, and cells were incubated for half an hour at 37 °C. To stain the cytoskeleton of cells, Alexa Fluor 488 phalloidin solution (FITC, 1% in 0.1% BSA solution) was used, and cells were incubated in it at 37 °C for 1 h. In the next step, incubating cells at 37 °C in the DRAQ5 solution (1 µg/ml in BSA-PBS) for 10 min was applied for staining cells' nuclei. Eventually, after the removal of excess dyes from wells and washing of cells with sterile PBS, the specimens were stored at 4 °C for CLSM analysis. The fluorescence excitation of FITC (green) and DRAQ5 (red) was recorded at 488 nm and 650 nm, respectively.

2.2.3.5.3 Osteogenic differentiation of cells on scaffolds

For osteogenic differentiation evaluation, scaffolds (n=3) were treated before cell seeding (similar to the cell viability test), and the hFOB cells were seeded on them at the density of 5×10^4 cells/scaffold. After 24 h incubation in GM, the media was changed with osteogenic medium (OM) and samples were incubated in the incubator with a humidified atmosphere of 5% CO₂ and 95% air for specific periods (7 and 14 days) at 37 °C. Meanwhile, the OM that consisted of GM, 10 mM β -glycerophosphate 50 μ g/ml ascorbic acid, plus 10^{-8} M dexamethasone was changed every 2 days. At each time point, the OM media were discarded and after washing specimens two times with PBS, the 0.5 ml lysis buffer (1 % Triton X-100 in carbonate buffer, 1:9 v/v) was added to each well. Eventually, cells on scaffolds were lysed using the freeze-thaw process repeated for 3 times. After centrifuging the lysate-scaffold particles mixture at 8000 rpm for 3 min to avoid any particles, the lysates were collected and aliquoted to measure Alkaline Phosphatase activity (ALP), intracellular Ca²⁺ deposition, and protein concentrations individually.

To measure ALP activity, a 100 μ l of working solution of para-nitrophenyl phosphate (PNPP) was added to 50 μ l of the cell lysate and incubated at 37 °C for 1 h. Later, the absorbance of the solution was recorded at 405 nm by the microplate reader. The ALP activity of each scaffold was determined as the rate of PNPP conversion normalized against total protein concentration. Note that the amount of converted 4-nitrophenol was calculated through the calibration curve, which was obtained beforehand by specified concentrations (0-300 μ M) of 4-nitrophenol (Sigma Aldrich, USA). Bicinchoninic Acid assay (BCA) was applied to measure protein amounts of the cell lysates (Pazarçeviren et al., 2018). For this purpose, the mixture of BCA stain and cell lysate (7:1 v/v) was incubated at 37 °C and after 1 h the absorbance was read at 562 nm using the microplate reader. The total protein amount in the lysates was quantitated using a calibration curve, which was constructed with different concentrations of BSA beforehand.

To measure intracellular calcium based on previously reported o-cresolphthalein assay (Jodati et al., 2022a), 100 μl of Ca^{2+} indicator dye (8-hydroxyquinoline, o-cresolphthalein complexone, hydrochloride acid, and ethanolamine) was added to 100 μl aliquot of cell lysate, and after 5 min of shaking on the orbital shaker, the absorbance was measured by the microplate at 570 nm. Calcium amount was calculated through the calibration curve constructed beforehand, using known various concentrations of calcium chloride (Merck, Germany) in dH_2O . The results were again normalized due to total protein concentration.

2.2.4 Statistical analyses

One-way analysis of variance (ANOVA) was employed for the statistical analysis of data. SPSS software (version: 21, IBM, USA) was used to determine the differences between the mean values of groups, and a p-value ≤ 0.05 was considered significant.

CHAPTER 3

RESULTS AND DISCUSSION

3.1 Characterization of BHAs

XRD patterns of synthesized HA and BHAs sintered at 900 °C are depicted in Figure 3.1. Patterns complied with the diffraction pattern of the standard hexagonal HA crystal with JCDPS # 09-0432. The absence of peaks related to other additional phases, such as previously reported calcium oxide (CaO) (Alshemary et al., 2018), calcium borate (JCDPS # 26-0347), β -TCP (Khoshsima et al., 2018), or α TCP (JCPDS # 09-0348) (Nakamura et al., 2012), verifies the purity of synthesized materials. XRD peaks have slightly been shifted upward to higher 2θ values in B incorporated samples, compared to HA.

Substitution of ions with smaller ionic radii leads to the shifting of XRD peaks to higher 2θ values (Alshemary et al., 2019b). Thus, the slight shift upward to the higher 2θ values in XRD patterns of BHAs could be assigned to the substitution of smaller borate ions (BO_3^{3-}) with the larger phosphate (PO_4^{3-}) inside the HA crystal. For instance, in the 0.5BHA XRD pattern, it was observed that main peaks (2 1 1), (1 1 2), and (3 0 0) have shifted to the right by 0.013, 0.30, and 0.014 values of 2θ , respectively. Broadening of peaks and reduction in their intensities were also observed in doped groups. Less intense peaks and/or wider peaks were addressed as the results of the incorporation of doping elements into the structure of HA as also reported in other studies (Alshemary et al., 2018; Safarzadeh et al., 2019).

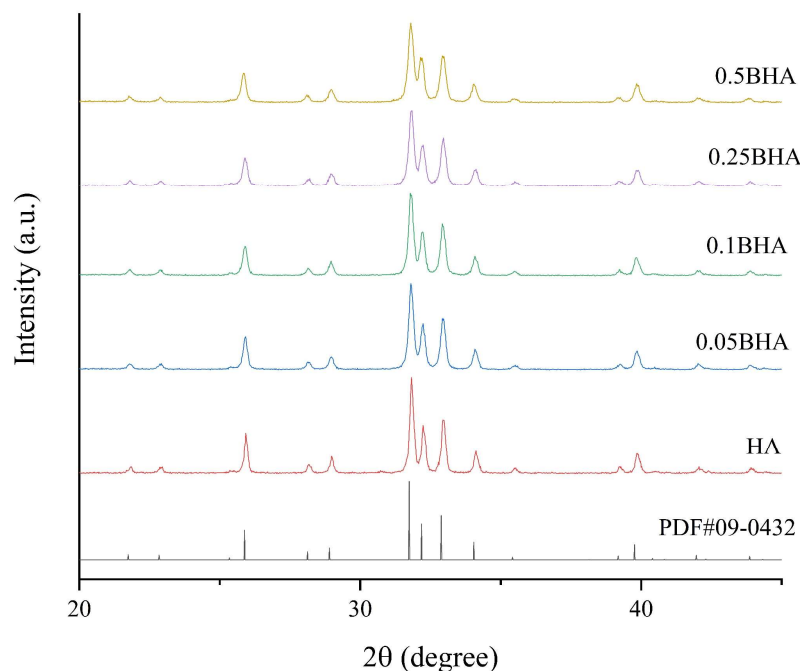


Figure 3.1. XRD patterns of HA and BHA powders sintered at 900 °C for 2 h.

Decreased unit volume and lattice parameters were noticed in my BHA samples, represented in Table 3.1. Similar to other studies, this change happens when dopant ions with smaller ionic radii are substituted with larger ions of the HA lattice (Basar et al., 2010; Lou et al., 2015). The radius difference between the dopant and the replaced element led to a smaller unit cell volume in B-doped groups (Table 3.1). These results are in agreement with studies conducted by Barheine et al. (Barheine et al., 2011). Although the small variations in lattice parameters could be assigned to the dehydroxylation of the hydroxyl group (Rajesh et al., 2012), or the formation of oxyapatite at higher sintering temperatures (Tampieri et al., 2012), which is not the case in this study, due to lower sintering temperature compared to those studies. Furthermore, reduced intensities of the XRD peaks, which indicate lesser crystalline samples, could be assigned to successful doping of B into the structure of HA, whilst

the increase in broadening of the peaks demonstrated that samples with higher B had smaller grain or crystallite sizes (Table 3.1).

Table 3.1 Lattice parameters and crystallinity degree of HA and BHA powder samples (n=3).

Name	Lattice Parameters			Crystallite Size (nm)	Crystallinity degree (%)	Particle size measured using SEM (nm)
	<i>a</i> (Å)	<i>c</i> (Å)	<i>V</i> (Å ³)			
HA	9.422±0.003 [#]	6.881±0.004	529.06±0.52 [#]	57.25±1.53 ^{\$}	95.19±0.61 [*]	106±11 ^{**}
0.05BHA	9.417±0.006	6.877±0.006	528.77±0.18	52.68±3.21	93.77±0.74	89±9
0.1BHA	9.419±0.003	6.878±0.001	528.22±0.13	51.49±0.79	93.35±0.31	86±9
0.25BHA	9.417±0.003	6.877±0.002	528.26±0.52	50.02±1.46	92.16±0.36	81±5
0.5BHA	9.415±0.003	6.885±0.004	528.56±0.10	42.28±1.77	89.90±0.45	85±10

Unit cell parameters ([#]), crystallite size (^{\$}), particle size (^{**}), and crystallinity degree (^{*}) of pure HA were significantly higher compared to B-doped samples.

Presence of B in the chemical composition of synthesized BHA samples was also confirmed by ICP-MS analysis (Table 3.2). Results showed that there was a decently slight deviation from the theoretical values of B/P molar ratio in the microwave-assisted wet precipitated powders. Generally, various impurities such as carbonates or acidic phosphates located in the crystal core cause to produce HA with a slightly lower molar ratio (calcium deficient) compared to stoichiometric one (Li et al., 2012), especially in wet methods, such as microwave-assisted route (Demirtaş et al.,

2015). Results of ICP-MS also demonstrated Ca/(B+P) ratio changed in a range of 1.59 ± 0.24 for the material containing a 0.05 mol amount of B to 1.50 ± 0.24 for the material containing 0.5 mol B ions. Biological HAs are generally calcium deficient and carbonated ones and about 4-8 wt.% carbonate exists in bone minerals HA (Von Euw et al., 2019). In fact, my synthesized Ca-deficient samples could resemble bones' chemical composition, which naturally includes calcium-deficient HA.

Table 3.2 Theoretical and experimental elemental composition of HA and BHA samples in terms of molar ratio (n=3).

Sample	Theoretical Molar Ratio			Measured Molar Ratio by ICP-MS		
	Ca/P	Ca/(P+B)	B/P	Ca/P	Ca/(P+B)	B/P
HA	1.67	1.67	0	1.61 ± 0.25	1.61 ± 0.25	0
0.05BHA	1.68	1.67	0.008	1.60 ± 0.24	1.59 ± 0.24	0.008 ± 0.001
0.1BHA	1.69	1.67	0.017	1.62 ± 0.27	1.60 ± 0.26	0.015 ± 0.001
0.25BHA	1.74	1.67	0.043	1.62 ± 0.26	1.56 ± 0.25	0.036 ± 0.002
0.5BHA	1.82	1.67	0.091	1.60 ± 0.25	1.50 ± 0.24	0.071 ± 0.003

Morphologies of HA and BHAs powders are depicted in Figure 3.2. The irregular spherical-shaped nanoparticles were observed in all samples, which agglomerated to some extent. Agglomerated BHA spherical particles with smaller dimensions (30 nm, compared to 50 nm of HA), were reported in other studies (Tunçay et al., 2017). However, Albayrak reported that B incorporation into HA structure did not affect the size of needle-like particles even when B content was increased to 2 wt.% (Albayrak, 2016). In this study, no significant difference was observed in the

calculated average grain size of BHA samples. However, HA's grain size (106.3 ± 11 nm) was statistically larger than all BHA samples with a mean size of 85 nm (Table 3.1). The dopant ion effect on crystal growth through modification of surface charge could be addressed as a reason for the size change of particles in B-doped samples (Xiang et al., 2015).

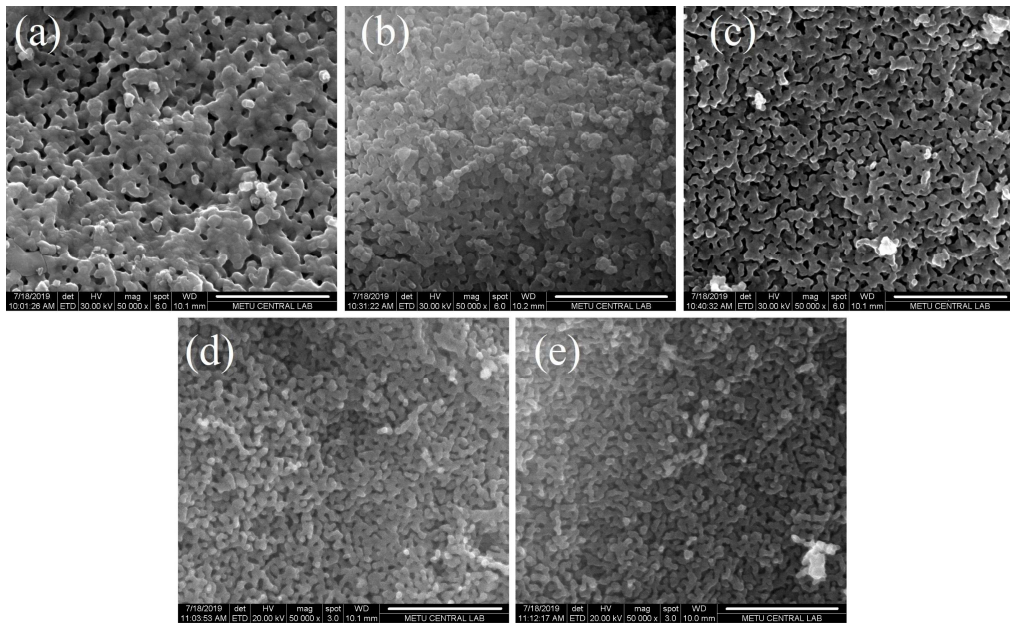


Figure 3.2. SEM images of HA and BHA powders sintered at 900 °C for 2 h. (a) HA; (b) 0.05BHA; (c) 0.1BHA; (d) 0.25BHA; (e) 0.5BHA. Scale bar length is 2 μm.

The FTIR spectra of HA and BHA powders included all characteristic functional groups of the apatite structure (Figure 3.3). The dominant bands at 1087 cm^{-1} and 1023 cm^{-1} belong to antisymmetric stretching (ν_3), while the vibrational bands at 562-564 cm^{-1} and 598-600 cm^{-1} are antisymmetric bending (ν_4) of PO_4^{3-} . Bands located at 473 cm^{-1} could be assigned to symmetric bending (ν_2) of the phosphate group (P-O), and the presence of vibrational bands at 962 cm^{-1} wavenumbers indicates symmetric stretching (ν_1) dedicated to PO_4^{3-} (Table 3.3) (Uysal et al., 2020; Ye et al., 2009). The absence of a band at 867 cm^{-1} indicates that samples, with or without B, were free of HPO_4^{2-} (Alshemary et al., 2013). The small, narrow band at approximately 3573 cm^{-1} and the band at 628–630 cm^{-1} were assigned to stretching ν_s and libration ν_L bands of the hydroxyl groups, respectively (Kolmas et al., 2017; Mondal et al., 2019; Ye et al., 2009).

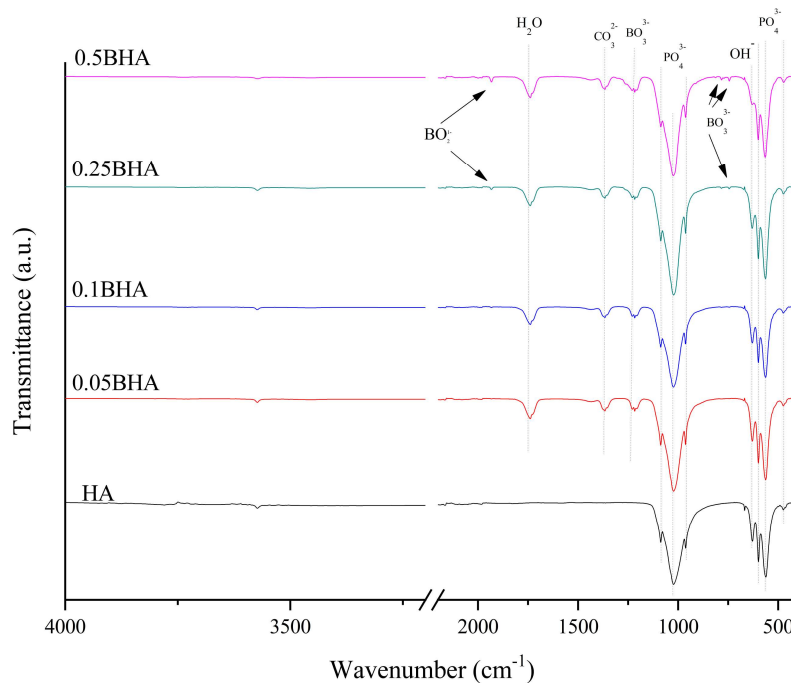


Figure 3.3. FTIR spectra of HA and BHA powders sintered at 900 °C for 2 h.

Appearance of a band at 1740 cm^{-1} was related to the H_2O (Hu et al., 2011) in B-doped materials. The intensity of the OH^- band at 3573 cm^{-1} , and especially the one at approximately $628\text{--}630\text{ cm}^{-1}$, decreased when B was added to HA. A similar decrease was also reported in HA doped with other ions (Padmanabhan et al., 2014). It means that OH^- group has been substituted with phosphate groups in doped materials. Incorporation of B into the structure of HA had a noticeable influence on the FTIR spectra of the materials. Presence of vibrational bands at 1365 cm^{-1} was attributed to the formation of CO_3^{2-} in these groups (Bonfield and Gibson, 2002; Demirtaş et al., 2015). By detection of carbonate, it could be stated that a part of OH^- groups were substituted by carbonate, which led to the reduction of OH^- band at $628\text{--}630\text{ cm}^{-1}$.

In the structure of HA, the carbonate ions could substitute with either OH^- (type A) or PO_4^{3-} ions (type B) in the structure of HA (Lafon et al., 2008). B-type carbonate substitution could decrease the crystallinity, or conversely, increase solubility and even the mechanical strength of HA (Murugan and Ramakrishna, 2006). A-type carbonated HA is recognized by CO_3^{2-} bands at $1455\text{--}1545\text{ cm}^{-1}$ and the signature band at 1546 cm^{-1} , and B-type is generally observed at $1410\text{--}1455\text{ cm}^{-1}$ with a signature band at 1464 cm^{-1} (Ren and Leng, 2012). In my samples, FTIR bands corresponding to CO_3^{2-} are B-type that have been shifted slightly compared to the other studies. However, similar to a study by Tuncay et al. (Tunçay et al., 2017), the carbonate ion presence was higher in BHA samples.

The bands originating from borate (BO_3^{3-}) and metaborate ions (BO_2^-) vibrations were observed in samples enriched with B. Bands at $1228\text{--}1217\text{ cm}^{-1}$ and $783\text{--}744\text{ cm}^{-1}$ are attributed to the antisymmetric stretching ν_3 and symmetric bending ν_2 modes of BO_3^{3-} groups, respectively (Güler et al., 2011; Uysal et al., 2020). Weak peaks at 2000 cm^{-1} and 1932 cm^{-1} are ascribed to the $^{10}\text{B}\text{--O}$ and $^{11}\text{B}\text{--O}$ antisymmetric stretching ν_3 mode of the linear BO_2^- groups, respectively (Albayrak, 2016). Note that in 0.25BHA and 0.5BHA, both bands of BO_3^{3-} and BO_2^- were observed, while the samples with 0.1 or fewer B moles only had BO_3^{3-} ions bands. The sintering stage

is required to initiate the chemical reaction between HA and boric acid, and the presence of the bands related to the BO_3^{3-} and/or BO_2^- groups in the FTIR spectra of the sintered samples could serve as further proof of the B doping into the HA structure, by substitution of phosphate and/or hydroxyl groups' respectively (Barheine et al., 2009; Hayakawa et al., 2008).

3.1.1 Density and mechanical properties of HA and BHAs

Relative densities, microhardness, and diametral strength values of HA and BHA samples are depicted in Figures 3.4, 3.5, and 3.6, respectively. There was no significant difference between the relative densities of 0.05BHA, 0.1BHA, and 0.25BHA groups. However, the relative density of HA was higher than all BHA groups, while 0.5BHA's relative density was lower than all the other groups (Figure 3.4). In this study, B doping reduced the densification of HA materials, which was in agreement with some other studies that reported reduced density due to the incorporation of B into the structure of HA (Albayrak, 2016; Yedekçi et al., 2021).

Appearance of a liquid phase during the sintering leads to enhance densification, and doping of compounds or elements with lower melting points (e.g. sodium phosphates) improves the sintering ability of HA (Suchanek et al., 1997). Thus, it seems B-doping has moderately inhibited the formation of the liquid phase during the sintering process, due to its higher melting point (Okamoto, 2008), and resulted in lower densities. Some researchers believe that materials' density is controlled by atomic weight (element densities) and bond lengths (Aldaadaa et al., 2018). So, the lighter atomic weight of substituted B (10.811) than P (30.974), and the smaller atomic radius of borate might lie beyond less dense BHAs, compared to HA. Furthermore, it was noticed that reduced densities were attributed to an inhomogeneous distribution of the doping additives in some studies (Khoshshima et al., 2018). However, this is not the case here because they fabricated composites rather than doped HA.

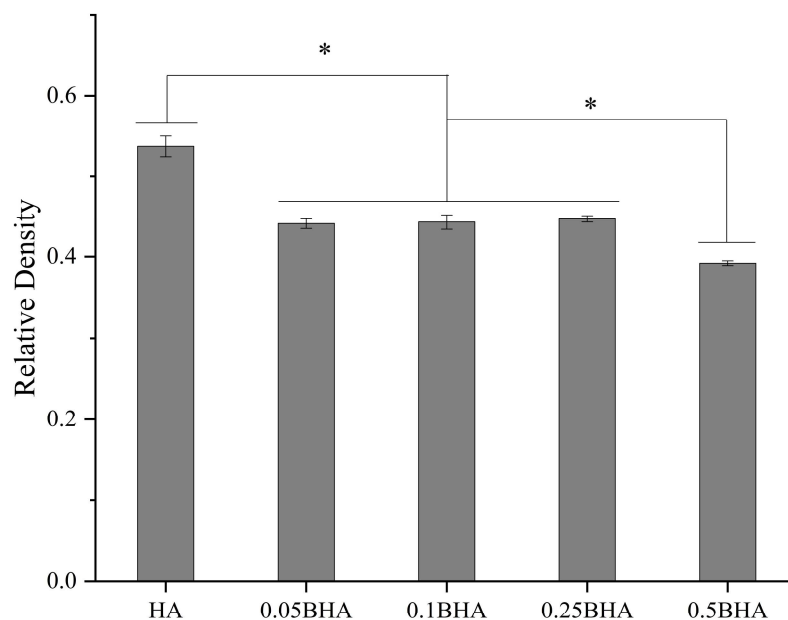


Figure 3.4. Relative density (n=3) of HA and BHA samples. Significant differences ($p \leq 0.05$) between groups were shown by the asterisk (*).

The same pattern as relative density was observed in the microhardness values of HA and BHA groups. No significant difference was detected between 0.05BHA, 0.1BHA, and 0.25BHA. However, HA had a higher hardness value than the doped groups, and 0.5BHA samples possessed the lowest values of hardness values (Figure 3.5). In the literature, density (Jodati et al., 2020c), and crystallinity degree (Basu and Banerjee, 1994) were addressed as primary and secondary reasons, which affect the strength of materials. Thus, lower densities (higher porous structure) and lower crystallinity degree (Table 3.1) could be presented as the reasons for the lower hardness of BHA samples. A similar correlation between microhardness and density was also reported in the study conducted by Albayrak (Albayrak, 2016), where the increase of B content resulted in the reduction of hardness. Concerning crystallinity,

lower values mean a more amorphous phase that reduced the sinterability of samples with B content and resulted in lower hardness values.

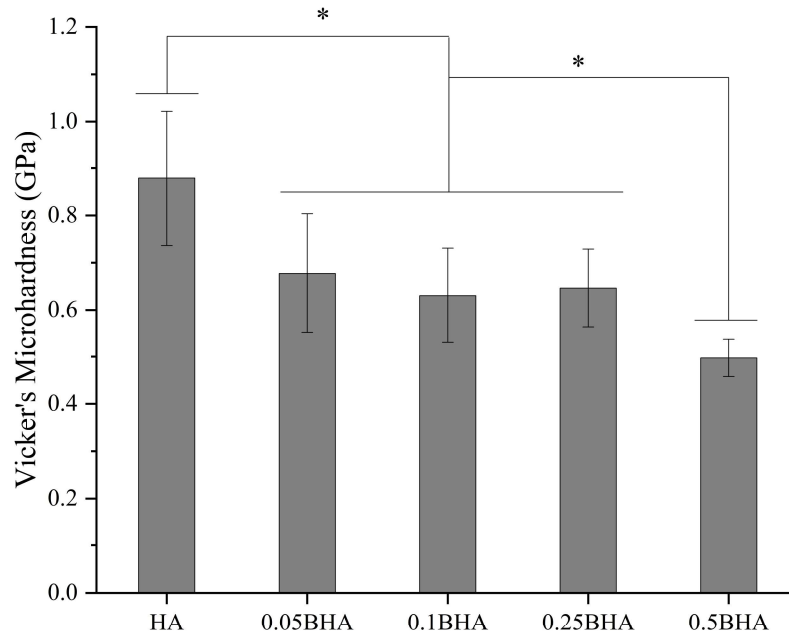


Figure 3.5. The microhardness values of HA and BHAs, where (*) represents the significant difference ($p \leq 0.05$) between the mean values of groups.

Diametral tensile strength of HA and BHAs (Figure 3.6) was changed from 3.22 MPa to 2.51 MPa. Although 0.5BHA appeared weaker than the other groups, there was no significant difference between BHA groups and HA. Similar to microhardness, it was expected that samples with the highest density (the lowest porosity) and higher crystallinity degree would show the highest strength in the diametral test (Seyed Shirazi et al., 2015). However, I believe that the presence of carbonate in BHA (Murugan and Ramakrishna, 2006), and more importantly, finer

powder sizes (more grain boundaries) (Aguirre et al., 2019; Obada et al., 2020), which prevent the progression of microcracks (Jodati et al., 2020a) are the reasons that explain the supreme mechanical properties of BHA. These reasons also contributed to the enhanced mechanical properties of B-incorporated composite materials (Aguirre et al., 2019; Tozar and Karahan, 2018). Absence of the second phase also contributed to preserve the mechanical strength of BHA (Tahmasebifar and Evis, 2013). Mechanical properties play an influential role in the performance and even final clinical success of biomaterials (Wang et al., 2020). In this study, the mechanical properties of BHA samples (strength~3MPa and hardness ~0.6GPa) matched with the properties of the natural bone, especially cancellous bone (strength ~2-45 MPa and hardness ~0.76 GPa) (Hannink and Arts, 2011; Zysset et al., 1999). Therefore, it reduces failure, especially because of the stress-shielding phenomenon.

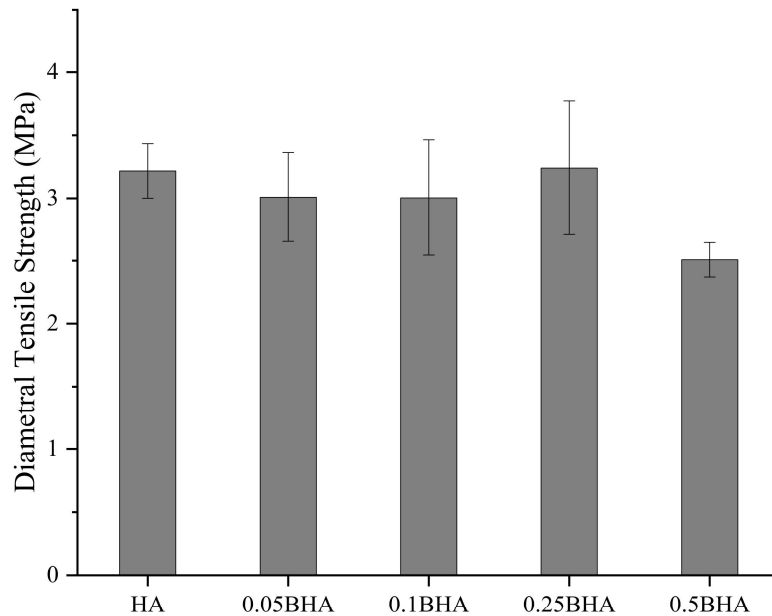


Figure 3.6. Diametral tensile strength of HA and BHAs.

3.1.2 Biological characterization of HA and BHAs

The bonding of materials to the surrounding host tissue through the formation of CaP apatites on the surface is defined as the bioactivity of materials. The surface ability to form apatite in SBF can be interpreted as the bioactivity of the materials. *In vitro* bioactivity of my materials was examined by submerging disks in SBF solution at 37°C for 14 days. As depicted in SEM images (Figure 3.7), newly-formed apatite was observed on the surface of all samples after 14 days of incubation. Higher apatite deposition on the surface of samples with a higher B concentration showed that B ion doping increased the bioactivity of HA samples. Different morphology of aggregated apatites observed on BHA surfaces, compared to flake-like crystals of HA, is associated to the differences in the chemical composition of newly formed apatite depositions. Apatites are primarily made of Ca, P, O, and C elements, verifying their CaP nature. In this study, EDX results (Figure 3.7) determined that the Ca/P ratio of newly-formed apatites on BHA was in the range of 1.71 to 1.78. In contrast, apatites on HA disks had Ca/P of 1.88 and were accompanied by a lower oxygen amount, which led to their different morphology.

Changes in the concentrations of Ca, P, and B elements in SBF, and the pH of SBF filtrates were measured throughout the bioactivity test (Figure 3.8). Since the SBF is a metastable supersaturated CaP solution, which tends to become stable by forming apatite crystals (Yilmaz et al., 2020), as soon as disks were immersed in it, the negatively charged surface of synthetic HA and BHA samples attracted positively charged Ca^{2+} ions from SBF, and Ca^{2+} accumulated on the surface of disks reacted with PO_4^{3-} negative ions immediately to form amorphous CaPs during the first day of soaking. These changes were confirmed by the demonstration of decreasing calcium and phosphate concentrations in SBF during the first day (Figure 3.8). Meanwhile, B began to diffuse from submerged disks to SBF solution, which is similar to a low release rate of B in a short time after immersion inside SBF reported in other studies (Balasubramanian et al., 2016).

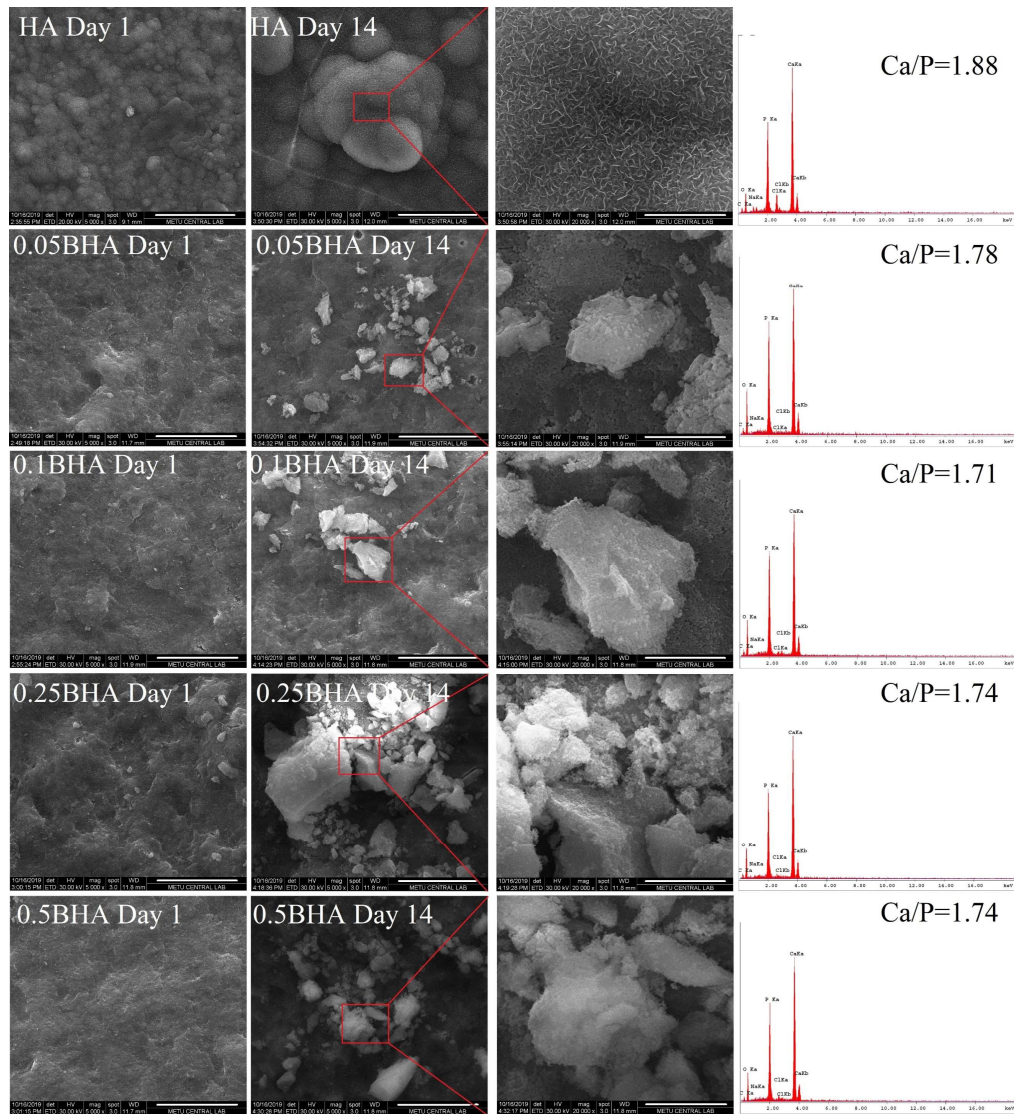


Figure 3.7. SEM images of the surface of HA and BHA samples after 1 and 14 days of incubation in SBF, and EDX results of the newly formed apatite particles. Scale bar length is 5 μm in zoomed images (left column) and 20 μm in other images.

From day 1 to day 4, the accumulation of negatively charged phosphate and borate ions on the surface continued, and therefore, calcium-poor amorphous apatite became negatively charged again and started interacting with Ca^{2+} . This cycle continued until day 14, where amorphous apatites eventually were converted to more stable crystalline apatites and the balance between precipitated and diffused ions among the surface of disks and SBF solution was sustained (Figure 3.8). The instant decrease of Ca^{2+} and PO_4^{3-} ions in SBF indicates that apatite deposition on the disks' surface started from the first day of immersion, which is beneficial for the rapid growth of the new apatite layer. However, after the initial deposition of these ions, it seems Ca^{2+} ion release from BHAs, especially 0.5BHA increased in SBF during the next 3 days of incubation. This behavior could be due to the lesser crystalline structure of those samples (Alshemary et al., 2016). Herein, the rapid reduction of phosphate concentration over 14 days might be because of its continuous consumption during the apatite formation process throughout the incubation period (Alshemary et al., 2018). A faster consumption rate of phosphate (and even calcium ions after 4 days) in BHA groups, compared to HA, could be due to greater apatite formation and/or smaller Ca/P ratio of newly formed apatites, which was previously mentioned in EDX results (Figure 3.7). The ability of B-doped materials to establish more apatite formation has also been documented in other studies (Uysal et al., 2020).

Furthermore, some researchers claimed that the binding of a fraction of borate to apatite is weak (Sasaki et al., 2018) and the immobilization of B happens in the absence of phosphate in the environment (Uysal et al., 2020). Therefore, the existence of phosphate in SBF could be addressed as a reason for the second increase of B content in SBF (day 7), after its primary deposition through weak bonds during the first 4 days of incubation (Figure 3.8). The pH changes of samples as a function of incubation time (Figure 3.8), indicate an increase in value after 1 day, where the initial pH of SBF (7.4) raised to 7.55. The ionic exchange between H^+ ions of SBF and Ca^{2+} ions from the sample surface lies beneath this event. However, after one

day and the disappearance of an initial alkaline effect of dissolved HA, the pH of the filtrate solution stabilized at a range of 7.4-7.5 values.

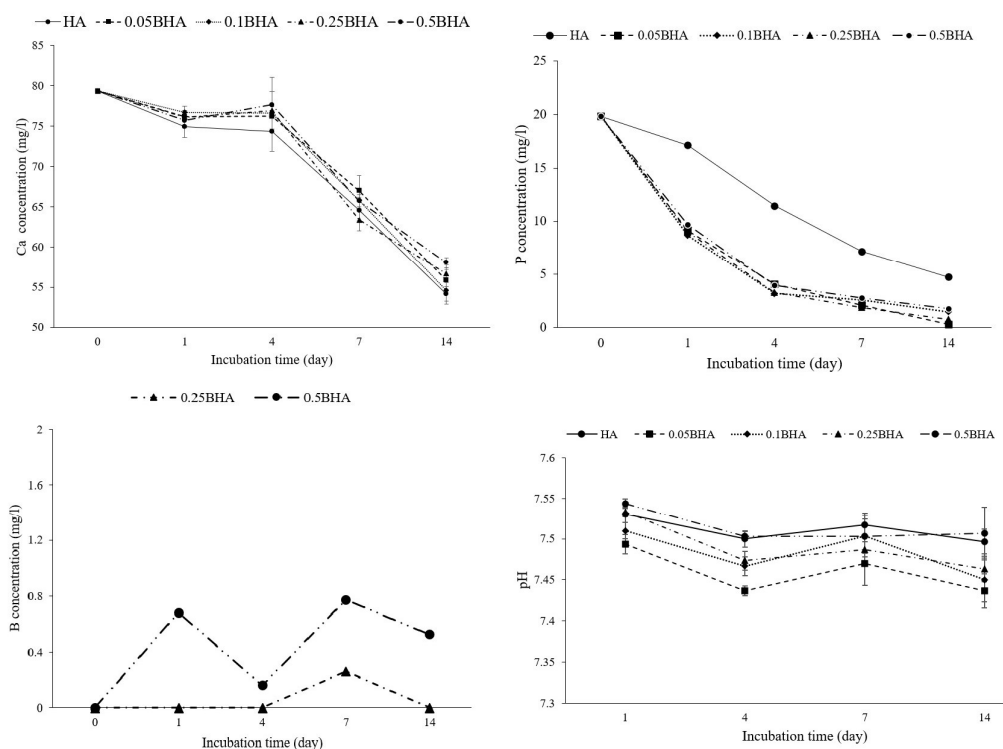


Figure 3.8. Ion release profiles of Ca, P, B, and pH changes of SBF filtrate during 14 days of incubation (n=3) in the water bath at 37 °C.

The mass loss percentage of HA and BHA samples in acetic acid and sodium acetate (AcOH-AcONa) buffer throughout 28 days of incubation at 37 °C is given in Figure 3.9. Measurement of weight loss (as a function of time) under acidic conditions (buffer solution with pH=5.5), which simulates osteoclastic resorption (Hayakawa et al., 2013), was introduced as a better tool to demonstrate biodegradability. Although the weight loss of all samples significantly increased with time from less than 1 % at day 1 to even more than 4 % at end of 28 days, there was no significant

difference (<0.05) in the degradation rate between BHA groups and also with HA at each time point.

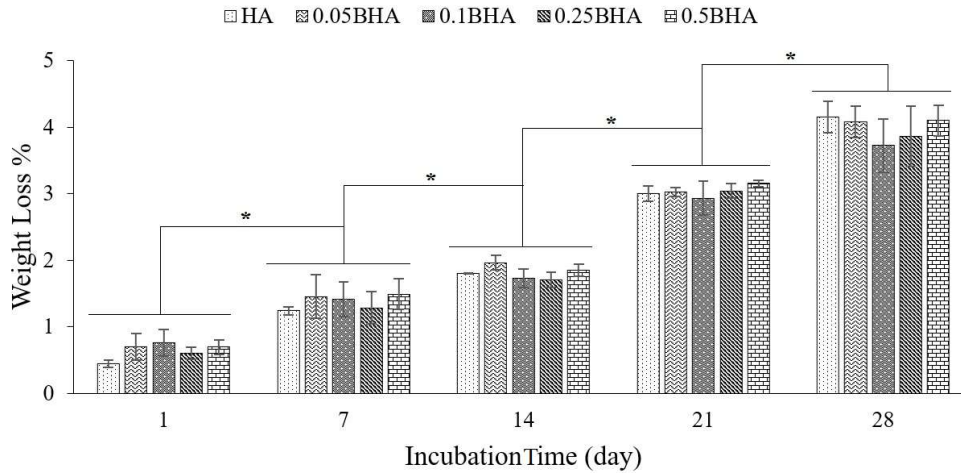


Figure 3.9. *In vitro* biodegradability of HA and BHAs during 28 days incubation in acidic buffer at 37 °C (n=3). There was no significant difference between the groups at each specific time point. However, the degradation rate increased with time. Asterisk (*) sign indicates statistically significant differences between groups.

In orthopedic or dental applications, the biodegradability of bone substitutes is an important requirement that improves the daily life quality of patients. Stoichiometric HA has the minimum dissolution rate and despite its sufficient osteoconductivity, it suffers from not being biodegradable (Hayakawa, 2015). Except for β TCP and HA, other CaP ceramics generally are not appropriate to be used as bone substitutes alone, especially in load-bearing applications, due to their faster degradation rate than tissue regeneration rate (Hayakawa, 2015). Concerning HA, making biphasic calcium phosphates by mixing HA with more soluble TCP is an alternative way to increase

its degradation rate (Kim et al., 2014). Some studies indicated the rate of dissolution increased when ions such as orthosilicate (Aminian et al., 2011) and carbonate (Takemoto et al., 2004) were incorporated into the structure of HA. Ion doping was introduced as another technique to enhance and control the degradation rate of bioceramics to produce desirable resorbable biomaterials for tissue engineering and regenerative medicine (Hayakawa et al., 2013).

In literature, the substitution of BO_3^{3-} and BO_2^- with constituent phosphate (PO_4^{3-}) or hydroxyl group (OH^-) increased the solubility and the biodegradation rate of HA (Barheine et al., 2011, 2009; Hayakawa et al., 2008). Destabilized apatite lattice as a result of different negative charges of doped ions was addressed as a reason for more solubility. However, Atila et al. (Atila et al., 2019) reported that composite scaffolds, which were reinforced by BHA, underwent lower weight loss (5.91%) than those reinforced by HA (8.90%) and B doping decreased the degradation.

In this thesis, the highly crystalline structure (over 89%), and a small content of carbonate in the samples' structure were reasons for almost the same biodegradability rate of BHAs, compared to pure HA. Furthermore, pH is another feature that plays a role in the degradation of HA. Hanh et al. (Hanh et al., 2021) reported higher biodegradation at a pH of about 9 or 10 rather than a pH of 7.5 for HA. Thus, in this study, non-remarkable pH change (Figure 3.8) could be listed among the reasons for the bio-stability of BHA materials. Note that a faster degradation rate of biomaterials, which is not synchronized with the rate of regenerating tissue replacement, might cause problems in de novo deposition and maturation of the extracellular matrix (ECM), and even failure of implants (Wang et al., 2020). Therefore, increased bioactivity besides no change in the degradability rate of BHA materials could contribute to having both advantages of B-doping and preserving mechanical integrity simultaneously.

3.1.3 *In vitro* cell culture studies

Cytocompatibility of the materials was investigated in terms of the mitochondrial respiratory activity of Saos-2. The observed increase in the cell viability of cultured cells, as a function of time, indicated that synthesized HA and BHA materials were non-cytotoxic (Figure 3.10). The results demonstrated a significant increase in cell viability on B-doped samples, compared to HA. Meanwhile, cell proliferation was higher in samples with a higher content of B. However, there was no significant difference between 0.05BHA and 0.1BHA groups at both incubation time points, and 0.25BHA and 0.5BHA samples did not exhibit statistical differences on the 7th incubation day.

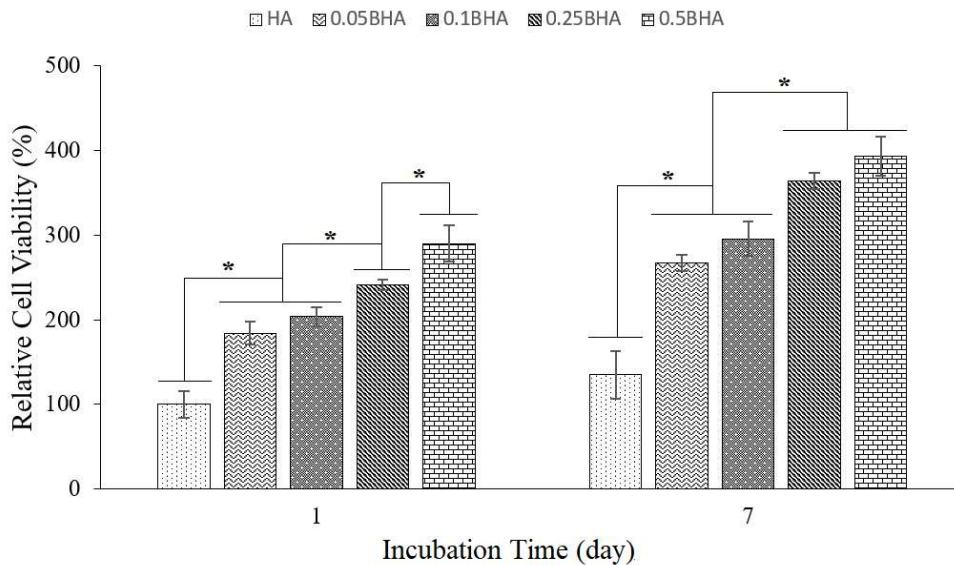


Figure 3.10. Relative cell viability on HA and BHA samples during 7 days of culturing (n=4). Cell viability of HA after 1 day was considered 100%. Asterisk (*) indicates a significant difference ($p \leq 0.05$) between the mean values of groups.

SEM examination was used to evaluate the morphology of cells seeded on HA and BHA samples after 1 and 7 days of incubation (Figure 3.11). On day 1, the cells had a round shape in the HA group, whilst, cells had partially spread shapes on B-doped disks, especially with higher B content, such as 0.25BHA and 0.5BHA samples. SEM monitoring of cells on day 7 confirmed the cell viability test results and higher cell proliferation was observed on B-doped samples, compared to HA. After 7 days of incubation, although both round and spread cells were seen on the HA sample (Figure 3.11, b), the cells adhered more to surfaces of BHA diss. The cells attached to BHA samples had even characteristic filopodia-like processes (Figure 3.11, d, f, h, and j).

The beneficial influence of borate release on cell attachment and resultant proliferation was previously reported on bioglass materials (H. Fu et al., 2009; Moonesi Rad et al., 2019), or calcium silicates (Lu et al., 2016). Concerning HA, better cell attachment, enhanced cell proliferation, and higher ECM deposition by the cells were reported by Tuncay et al. (Tunçay et al., 2017) in B-containing HA scaffolds, compared to HA. Enhanced cell activity due to the presence of B is attributed to the stimulatory action of B in cell migration through the association with phosphorylation of focal adhesion kinase together with p38 closely linked to migratory signaling cascades (Haro Durand et al., 2014; Lu et al., 2016). Atila et al. (Atila et al., 2019) exhibited that composite scaffolds with 2% (w/w) of B in HA's structure showed higher cell viability than HA. Acceleration of Ca^{2+} flux by adding B was introduced by Capati et al. (Capati et al., 2016) as one of the possible reasons for promoted *in vitro* proliferation and differentiation of osteoblastic cells. Moreover, the smaller grain size of B-containing samples (Table 3.1) has a stimulatory effect on cells in terms of cell proliferation. For instance, Veljovic et al. (Veljović et al., 2012) observed higher osteoblastic cell proliferation in HA samples with smaller grain sizes than the samples with larger grains.

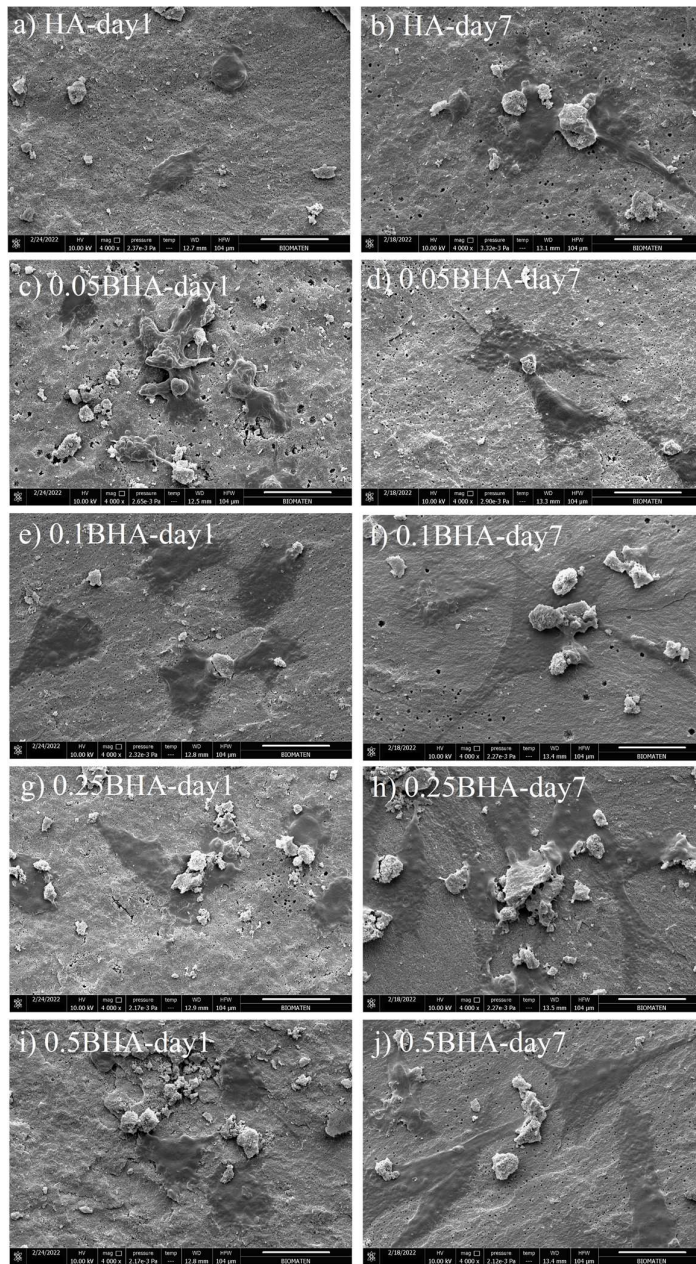


Figure 3.11. SEM micrographs (scale bar = 20 μm) of Saos-2 cells on the disks after 1 and 7 days of incubation: (a) HA-day1, (b) HA-day 7, (c) 0.05BHA-day1, (d) 0.05BHA-day 7, (e) 0.1BHA-day1, (f) 0.1BHA-day 7, (g) 0.25BHA-day1, (h) 0.25BHA-day 7, (i) 0.5BHA-day1, (j) 0.5BHA-day 7. Scale bar length is 20 μm .

However, there are some controversies on the negative cytotoxic effect of B incorporation on cells, and some studies claimed that the presence of borate ions above a specific threshold value (e.g. 5 mM) could inhibit cell proliferation (Balasubramanian et al., 2018, 2016) through activation MAPK (the mitogen-activated protein kinase) signaling pathway (Gümüřdereliođlu et al., 2015; Park et al., 2004). Herein, it could be stated that B release of 260 $\mu\text{g/l}$ observed in 0.25BHA or even 770 $\mu\text{g/l}$ of 0.5BHA groups (Figure 3.8) had no cytotoxic effect and supported cell proliferation, similar to another study, where B-loading on HA composite had a positive effect on cell proliferation of Saos-2 cells (Gizer et al., 2020). Moreover, Kolmas et al. (Kolmas et al., 2017) demonstrated that HA with even higher B doping than my study (2 times) was still biocompatible. However, B release was not investigated in their study.

ALP activity and intracellular calcium value of cells on disks, which were exposed to an osteogenic medium for 7 and 14 days, were employed to evaluate the effect of B doping on the osteogenic activity of cells. After 7 days of incubation, ALP activity of HA, 0.05 BHA, and 0.1 BHA was higher than the other two groups that had a higher content of B. Concerning intracellular calcium, all BHAs had the same amount of calcium, while the calcium level of cells on HA disks was slightly higher than the values of doped groups. Among all groups, the highest two ALP activities belonged to HA and 0.05BHA samples at end of day 14 (Figure 3.12). Similarly, intracellular Ca^{2+} content was higher in these groups than 0.25BHA and 0.5BHA as depicted in Figure 3.12.

Although the positive influence of B release on ALP activity or Ca^{2+} deposition of doped HA has been reported before (Arslan et al., 2018; Atila et al., 2019), it is more likely that the effect of B on the osteogenic activity of cells is a dosage and time-dependent event (Hakki et al., 2010). On one hand, Kolmas et al. (Kolmas et al., 2017) claimed that the incorporation of B into HA did not affect the osteogenic differentiation of stem cells. Li et al. (X. Li et al., 2016) also stated that 1-25 mg/l of B adding did not cause any change in ALP activity. On the other hand, Gümüřdereliođlu et al. (Gümüřdereliođlu et al., 2015) demonstrated that cells on

chitosan scaffolds had a higher ALP activity, when a B release value was 26.13 ± 1.13 μg , compared to the scaffolds with greater B release value (~ 110 μg) or without B after 14 days of incubation. Collagen type I (COL I), as a major organic component of mineralized ECM and primary function of osteogenic differentiation, had a similar pattern in that study, and scaffolds with the greater B release possessed a smaller amount of COL I than the scaffolds without B on 14th day.

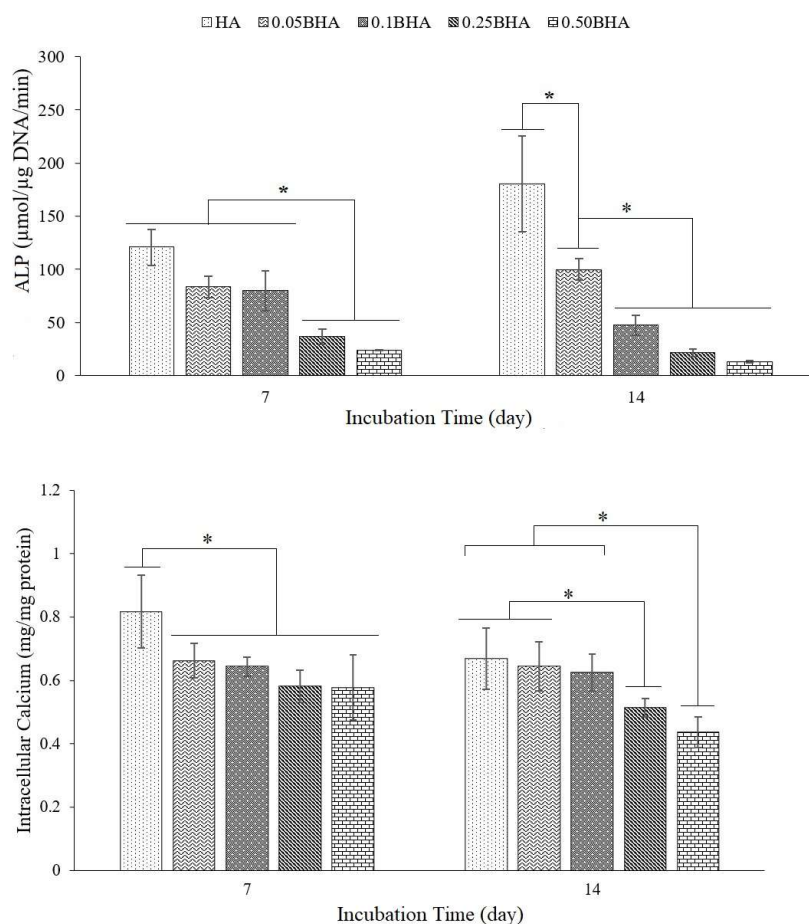


Figure 3.12. ALP activity (upper) and intracellular Ca^{2+} contents of Saos-2 cells seeded on HA and BHAs disks after 7 and 14 days incubation in osteogenic differentiation medium at 37°C ($n=5$). Asterisk (*) indicated statistically significant differences between the mean values of groups.

Based on ALP results, Gizer et al. (Gizer et al., 2020) reported that scaffolds with B release of 6 $\mu\text{g/l}$ had the best osteogenic effect on human bone mesenchymal stem cells (hBMSCs) on day 7. While the higher concentrations of B in scaffolds reduced the osteogenic differentiation in a dose-dependent way until day 21. Similar to Gizer, Najafabadi and Abnosi also reported boosted ALP activity in groups with 6 $\mu\text{g/l}$ release of boric acid on days 5, 10, and 15 of incubation and enhanced intracellular Ca^{2+} accumulation after 5 and 10 days (Movahedi Najafabadi and Abnosi, 2016). Note that Ying et al. (Ying et al., 2011) exhibited higher levels of B (10-100 $\mu\text{g/l}$) had a positive effect on the ALP activity of BMSCs. Dose-dependent manner of B incorporation in the osteogenic activity of cells was also demonstrated in the study by Pazarçeviren et al. (Pazarçeviren et al., 2021), where ALP activity of dental pulp stem cells on biphasic HA/ β -TCP samples with 105 $\mu\text{g/l}$ B release was higher than samples with 185 $\mu\text{g/l}$ B release. In this study, it seems that ALP activity and Ca^{2+} accumulation, two markers of osteogenic activity, had dose-dependent behaviors. The higher B release from 0.25BHA (260 $\mu\text{g/l}$) and 0.5BHA (770 $\mu\text{g/l}$) samples decreased the osteogenic activity of the cells compared to HA. Compared to lower values in other mentioned studies in the literature, the remarkably higher B-release concentration could be the reason for this reduction. However, the osteogenic activity of cells in HA groups with lower B doping, especially 0.05BHA group, was not affected by doping and it is possible that even lower amounts of B-doping would increase ALP activity of cells.

The ARS staining (Figure 3.13) revealed the calcium deposition by cultured cells with matrix mineralization, which is in agreement with ALP data. Although calcium deposition was not evident after 7 days of incubation, A remarkable increase in calcium deposition was observed as an osteogenic activity marker after 14 days. Similar to ALP results, the highest calcium deposition was observed in the HA and 0.05 BHA groups, while the mineralized matrix decreased in the other doped groups with higher amounts of B and the lowest calcium deposition was detected in the 0.5BHA samples. The ALP activity is evidence of initial stages of osteogenic activity, the observation of ARS nodules after 14 days indicates later osteogenic

activity and mineralization (Q. Fu et al., 2009), which is higher in lower B-containing groups again in a dosage-dependent manner. ARS data confirmed that higher dosages of doping, which resulted in the release of B >260 µg/l influenced the osteogenic activity of cells adversely.

In this part of the thesis, B was successfully doped into the structure of HA in different molar concentrations (0.05, 0.1, 0.25, and 0.5 molar ratios), and subsequent changes in microstructure, physicochemical, mechanical, as well as biological properties of HA, as one of the most used biomaterials in bone defect treatment, were evaluated. Results indicated the successful B incorporation led to the synthesis of HA with less crystalline microstructure, smaller crystallite size, and finer grain boundaries. These changes were greater in doped groups with a higher amount of B dopant. The morphology of HA nanoparticles did not change due to B doping. A more porous microstructure of BHAs contributed to enhanced cell proliferation on them, whilst no change was measured in the diametral compression strength of HA due to B doping. However, smaller relative densities of BHAs and their lower crystallinity could be addressed as the reason for reduced microhardness values in doped groups.

The B dosage in this study seems enough to escalate the bioactivity of doped HA. The samples with higher doped B exhibited greater bioactivity. However, B doping did not change the microstructure to the extent that causes an increase in the biodegradation of HA. Concerning *in vitro* cell studies, there are two points to consider: first, the amount of B release is a more important factor than the doped amount; second, the cell viability and osteogenic activity exhibited a dose-dependent manner. Herein, B release resulted in promoted cell proliferation of Saos-2 cells. Even samples with 0.25 and 0.5 B molar ratios had no cytotoxic effect. However, these higher B releases did not positively influence the osteogenic activity of cells. Thus, lower doping dosages than 0.25 mol of B, especially 0.05, could be more appropriate values due to enhanced bioactivity, higher cell proliferation, and no negative effect on mechanical properties and osteogenic activities of HA; and I continued my thesis study by selecting 0.05BHA group as optimum BHA sample.

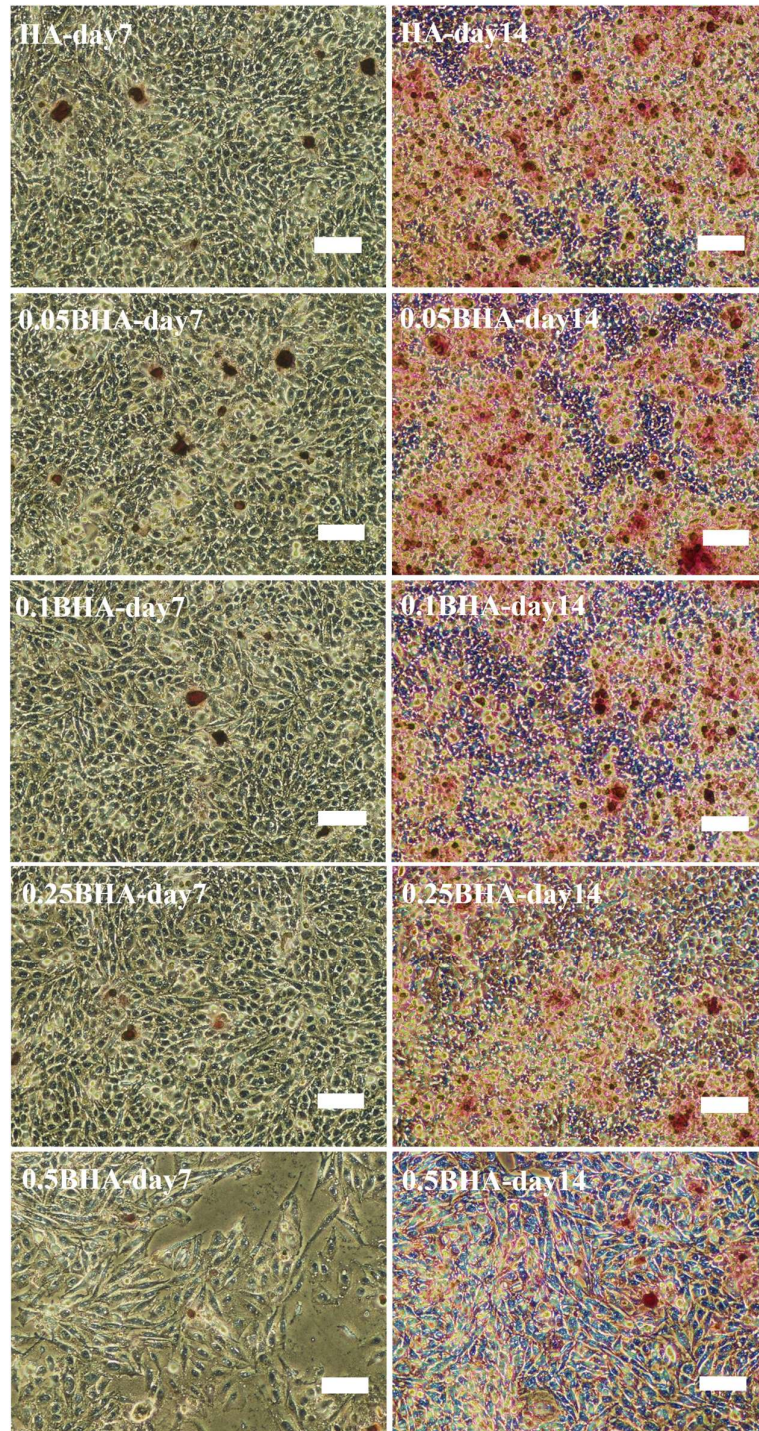


Figure 3.13. Optical microscopy images of Alizarin Red S (ARS) of Saos-2 cells for calcium deposition, 7 and 14 days after incubation. Scale bar length is 100 μm .

3.2 Characterization of BAG

3.2.1 Solution (sol) characterization and optimization

Once BAG was synthesized by following the proposed sol-gel procedure in the literature (Abbasian et al., 2020; Arefpour et al., 2019a; Doostmohammadi et al., 2019) with TEOS:ethanol: HNO₃ at a molar ratio of 1:8:0.16, the sol started gelling before the complete dissolution of Zr precursor, and a transparent solution (sol) could not be obtained. Thus, to solve these problems I (1) increased the amount of ethanol, as the solvent, used more (2) nitric acid (HNO₃, 2M), as the chelating agent, (3) and dissolved zirconium [IV] oxynitrate hydrate in ethanol separately. Different ratios of TEOS:ethanol: HNO₃ were tried during optimization to obtain crystalline BAG powder. No premature gelation or insoluble zirconium [IV] oxynitrate hydrate powder was observed in samples that had a higher amount of ethanol than conventional sol (TEOS:ethanol: HNO₃=1:8:0.16). However, as pictured in Figure 3.14, after dissolving Ca, Si, and Zr precursors, the clarity of the solution (sol) became clearer (lower turbidity) as the amount of ethanol increased. The lowest turbidity was observed in the sol of the sample with TEOS:ethanol: HNO₃ at a molar ratio of 1:42:1. It was a quality that we are desiring during sol-gel methods and it means higher dissolution of salts like calcium nitrate tetrahydrate and zirconium [IV] oxynitrate hydrate.

Generally speaking, the key factor for achieving a good transparent solution is the solubility of powder-based precursors. The clarity indicates that the precursors are completely dissolved in the solvent, which is reducing the possibility of possible different structures in the synthesis of the full stoichiometric BAG structure as Ca₃ZrSi₂O₉ or Ca₃Zr(Si₂O₇)O₂. Bear in mind that if the turbidity was high, it would indicate undissolved powder precursors in solution, therefore the fully stoichiometric BAG structure would not be produced.

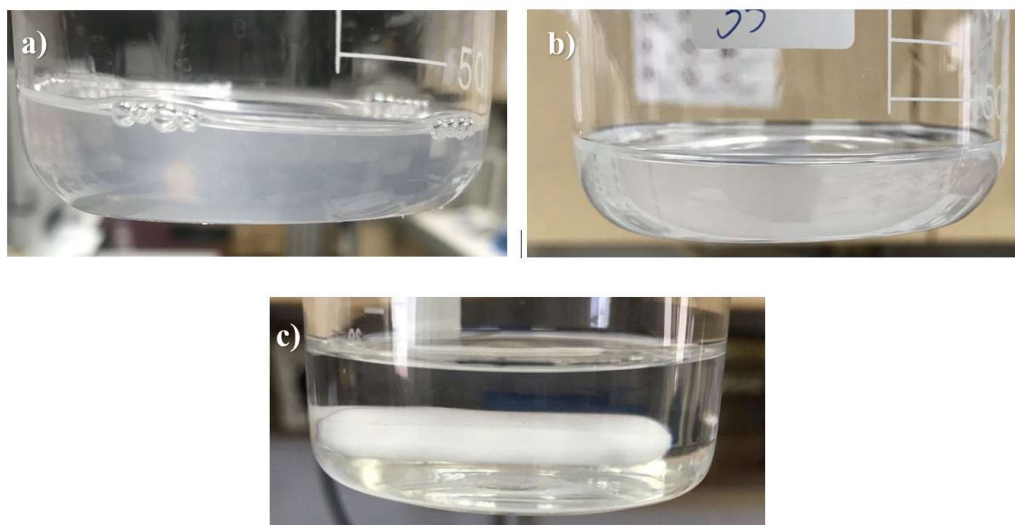


Figure 3.14. The solutions (sol) after dissolving Ca, Zr, and Si precursors for 5 h on the stirrer. (a) TEOS:ethanol: HNO_3 =1:21:1, (b) TEOS:ethanol: HNO_3 equal to 1:30:1, and (c) TEOS:ethanol: HNO_3 =1:42:1.

The pH value of the solution in which the precursors were dissolved was measured to be approximately 2 on account of the NO_3^- and $\text{C}_2\text{H}_5\text{O}^-$ anions coming from Zr-, Ca-, and Si-based precursors in the solution. In addition to NO_3^- and $\text{C}_2\text{H}_5\text{O}^-$ anions, ethanol, and HNO_3 added to the solution are other factors affecting the pH value. These results emphasize the importance of the choice of processing procedures. Typically, the gel structure, which depends on the pH of the solution, regulates further tailorable characteristics, such as phase structure, microstructure, mechanical, and biological properties. This facilitates the formation of pure phases in further processes.

3.2.2 Thermal behavior of BAG

Thermal behavior of BAG dried gel was evaluated using TGA-DTA, which is depicted in Figure 3.15. The first endothermic peak occurred at around 60 °C, which is related to the removal of ethanol (Quiroga et al., 2017), whilst the second one, which was observed around 100 °C, is assigned to water evaporation (Lawson-wood and Robertson, 2016). The nitrate removal from zirconium nitrate happens at about 500 °C (Alzahrani et al., 2022), and the removal of nitrate from the calcium nitrate occurs between 550 °C and 600 °C (A. Zhao et al., 2022). Nitrate removal from my sample is observed at 560 °C as seen in Figure 3.15. The exothermic peak at 950 °C corresponds to the formation of baghdadite. However, the exothermic peak at 875 °C is due to the crystallization of calcium silicate (Ca_2SiO_4) (Coldrey and Purton, 2007), or wollastonite (CaSiO_3) phases (Lakshmi et al., 2013). Unlike the study that reported a lower sintering temperature (800 °C) for the synthesis of crystalline BAG nanoparticles using P123 surfactant (Mehrafzoon et al., 2018), crystalline BAG particles were observed without using any surfactant at ≥ 900 °C, compared to conventional sol-gel (>1100 °C) (Sadeghzade et al., 2017), or solid-state (~ 1350 °C) (Schumacher et al., 2014) techniques.

These results contributed to determining suitable drying, oxidation/annealing, and sintering temperatures/regimes. Depending on thermal analyses, it was found appropriate to apply the heating process at 60 °C for 24 h as well as an extra 24 h at 100 °C for drying, 30 minutes at 300 °C for heat treatment, 30 minutes at 600 °C for annealing, and ultimately at 1150 °C for 3 h under the air in the furnace. Heating the gel to higher temperatures is necessary to obtain more stable phases. Gels in their first form, before heat treatment, do not have the chemical composition that a technical ceramic should have. With the heat treatment, the matter composing the solid network undertakes a crystallographic reorganization, and the pore texture changes. This deformation cannot be the most stable thermodynamic phase, therefore metastable structures emerge. The temperature range approximately between 100 °C and 1000 °C is called the intermediate temperature range and mostly

produces a crystalline transition phase. These metastable phases eventually transform into a stable thermodynamic phase like $\text{Ca}_3\text{ZrSi}_2\text{O}_9$ or $\text{Ca}_3\text{Zr}(\text{Si}_2\text{O}_7)\text{O}_2$ at high temperatures (1150 °C).

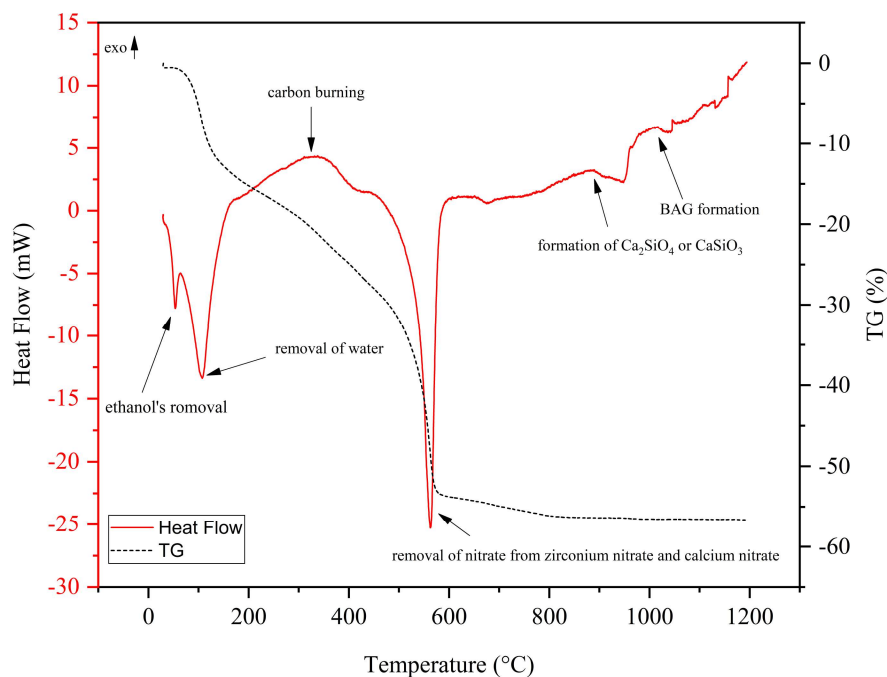


Figure 3.15. TGA and DTA curves of BAG gel dried at 100 °C for 24 h.

3.2.3 FTIR analysis of BAG

In conjunction with the TGA-DTA analysis, the FTIR results clearly showed the effect of all reactions on the performance of the final material production, starting at room temperature with gel structure, and continuing to oxide formation and perovskite formation temperatures until the desired phase is obtained. This influence can be seen in FTIR spectra of BAG samples as represented in Figure 3.16, which were heat-treated at 50 °C, 200 °C, 400 °C, 600 °C for 30 min, and 1150 °C for 3 h

in the air. The result was obtained in the range of wavenumbers of 4000-400 cm^{-1} . FTIR spectrum reveals that there are functional groups related to BAG. In Figure 3.16 those curves that represent the FTIR spectra of the gel, which was heat-treated at 50 °C, 200 °C, and 400 °C, contain strong symmetric and antisymmetric stretching in-plane bending of NO_3^- at approximately 840-880 cm^{-1} (Yurddaskal and Celik, 2018). Whilst those bands disappeared when the dried gel was heat-treated at 600 °C and above, which is in agreement with TGA-DTA results. In the same curves, the bands at 1360-1480 cm^{-1} represent the vibration mode of the carboxylic group (COO), and $=\text{CH}_2$ structure (Chen et al., 2009).

In addition, there is a peak around 1626 cm^{-1} which belongs to the hydroxyl (OH^-) group (Yurddaskal and Celik, 2018). Symmetrical and asymmetrical expansions, namely OH expansions, are ascribed by the peaks in the range of 2800-3800 cm^{-1} (Spahiu, 2015). It is highly expected that these bonds are being seen as a result of FTIR analysis in the structure of gel and dried/heat-treated samples that have not yet been annealed, and phases have not formed until 500 °C. In the FTIR spectrum (top curve) of BAG samples sintered at 1150 °C for 3 h in the air, it is seen that the functional groups containing C, H, and N were removed from the dried gel owing to the high temperature.

In fact, after the burning of organic structures, NO group was decomposed, and oxide structures were formed. For instance, the analysis results displayed that bands in the frequency range of 800 cm^{-1} to 950 cm^{-1} are assigned to isolated SiO_4 (Bakhsheshi-Rad et al., 2017; Najafinezhad et al., 2017). The absorbance bands in the range of 450 cm^{-1} and 600 cm^{-1} wavenumbers correspond to Ca-O (F. Pahlevanzadeh et al., 2018), while the absorbance band at $\sim 1009 \text{ cm}^{-1}$ is associated with Si-O-Zr, and those in the range of 600 cm^{-1} and 750 cm^{-1} belong to Si-O-Si vibration (Fu et al., 2014; Pickup et al., 1999).

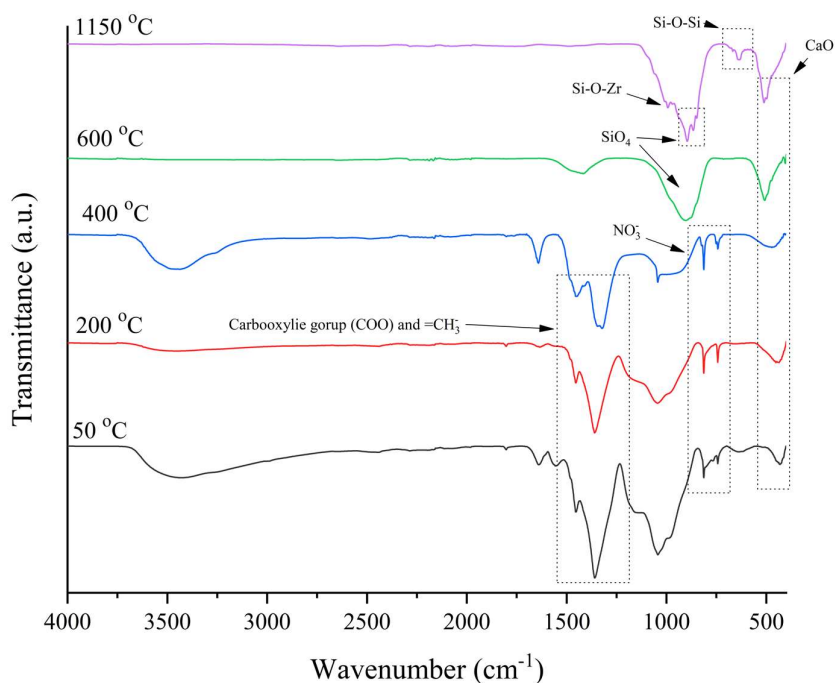


Figure 3.16. FTIR spectra of BAG powders heat-treated at 50 °C, 200 °C, 300 °C, 400 °C, and 600 °C for 30 min, as well as sintered at 1150 °C for 3 h in the air.

3.2.4 Phase analysis and microstructure of BAG

As far as the crystal structures and phase of the BAG powders are concerned, XRD was thoroughly studied for the powder samples sintered at 1150 °C for 3 h in the air (Figure 3.17). It is obvious that despite the presence of the BAG phase, the major phase was larnite with PDF # of 33-0302 in samples with TEOS:ethanol:HNO₃ equal to 1:8:0.16 and 1:21:1. In the sample with 1:30:1 ratio of TEOS:ethanol:HNO₃, the intensity of BAG peaks increased but the crystal plane with the greatest intensity belonged to larnite. However, in my proposed ratio (TEOS:ethanol:HNO₃=1:42:1) the BAG was a major phase with high purity and consistency with the standard in terms of atomic planes in the crystal lattice. Nevertheless, the CaZrO₃ phase existed

in all samples but with a lower amount in my material. **Therefore, I continued characterization tests with the purest synthesized powder, which has optimum TEOS:ethanol: HNO₃ ratio equal to 1:42:1.**

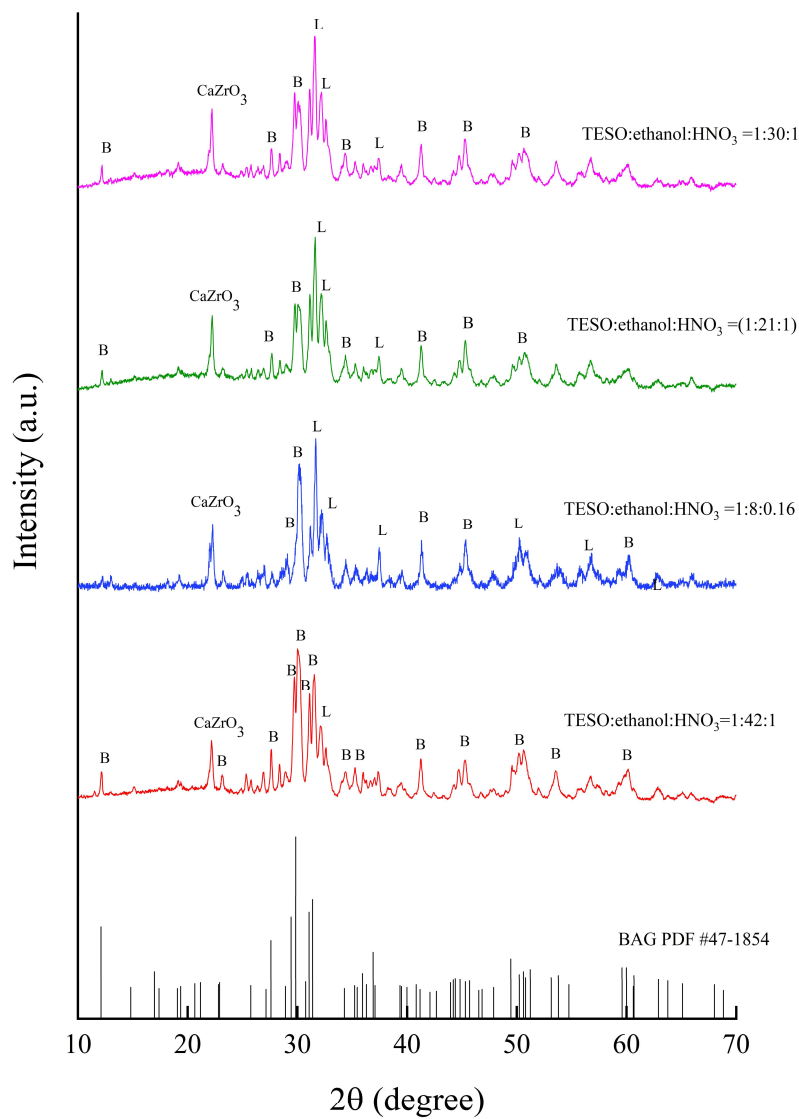


Figure 3.17. XRD patterns of prepared BAG with different TEOS:ethanol: HNO₃ ratios. Note that B stands for baghdadite and L stands for larnite (PDF No. 33-0302) with the formula Ca₂SiO₄.

The main reason for the presence of a larnite phase in samples with TEOS:ethanol: HNO₃ rather than 1:42:1 ratio could lie beneath TEOS hydrolysis and the fact that the Zr precursor didn't dissolve completely in ethanol because the amount of solvent (ethanol) and HNO₃ were not sufficient in the synthesis conditions other than the optimum proposed value of 1:42:1 for TEOS:ethanol: HNO₃. Then, the gelation happened when the composition of the sol was not equal to 1:2:3 in terms of the molar ratio of Zr:Si:Ca, which led to the presence of another Ca-Si phase like larnite. Using a higher volume of ethanol and nitric acid lets for sufficient amounts of solvent and chelating agent, which are needed to complete the hydrolysis of TEOS (Sadeghzade et al., 2017).

Moreover, Zr-source (zirconium [IV] oxynitrate hydrate) was dissolved in ethanol separately and later added with Ca-source to TEOS solution before forming a polymeric network of huge silica molecules and condensation. In this way, we succeeded in obtaining a clear solution (sol) with completely dissolved zirconium [IV] oxynitrate hydrate and calcium nitrate tetrahydrate and, before gelation as the next step toward the formation of BAG.

As just mentioned, Figure 3.17 also represents the detailed XRD pattern of optimum BAG after sintering at 1150 °C for 3 h. Herein, the logic of sintering BAG at 1150 °C was based on the fact that we wanted to restrict variable features to the modified procedure of synthesis merely. Then, in terms of sintering temperature, we kept consistency with other literature studies that used the sol-gel route. The observed peaks of the powder complied with the peaks of the standard synthetic baghdadite with JCPDS No.47-1854, which has unit cell parameters of $a = 10.45 \text{ \AA}$, $b = 10.18 \text{ \AA}$, $c = 7.36 \text{ \AA}$, $\beta = 90.87^\circ$, $\text{volume} = 782.8 \text{ \AA}^3$ with space group $P2_1/c$ that describes the symmetry of the crystal. The crystallinity degree of my synthesized BAG was ~87%, Its crystallite size was 16 nm based on the modified Scherrer equation, in which error sources have been minimized using the least-squares technique. The size of the crystallite (grain) was smaller than previously reported crystallite sizes (38-52 nm) (Sadeghzade et al., 2017), which were prepared using the conventional sol-gel method. Moreover, its monoclinic crystal possessed unit cell parameters of $a = 10.44$

\AA , $b = 10.19 \text{ \AA}$, $c = 7.34 \text{ \AA}$, $\beta = 90.87^\circ$, with volume $= 780.7 \text{ \AA}^3$. The sintered samples were not 100 % pure and there were a small fraction of other phases, like calcium zirconium oxide (JCPDS No. 35-0790), calcium silicate called larnite (JCPDS No. 33-0302), and wollastonite (JCPDS No. 27-0088). The minor phases, such as $\text{CaZrSi}_2\text{O}_7$, have also been observed in other studies (Khandan et al., 2015; Sadeghzade et al., 2017). The presence of these impurities might be due to using hydrated Zr and Ca precursors in the synthesis of BAG as reported by Lee (Lee et al., 2017).

It is worth pointing out that the surface morphology of sol-gel-derived BAG powders essentially depends on solution properties, sol-gel parameters, and heating regimes (Arya et al., 2021). The surface morphology and particle size of these sol-gel-derived BAG powders sintered at $1150 \text{ }^\circ\text{C}$ for 3 h in the air are depicted in Figure 3.18. The semi-spherical crystallites of BAG powder agglomerated after sintering at $1150 \text{ }^\circ\text{C}$. Each agglomerate included many crystals that formed an irregular shape, which was also reported in other studies (Abbasian et al., 2020; Sadeghpour et al., 2014; Sadeghzade et al., 2020). However, Mehrafzoon et al. (Mehrafzoon et al., 2018) observed needle-like particles when surfactant was added during the sol-gel synthesis process.

The particle size of sintered samples changed between 1 and $100 \text{ }\mu\text{m}$ as depicted in Figure 3.18. Approximately 61 % of particles had a size between $10\text{-}50 \text{ }\mu\text{m}$, while 24% of them were $\leq 10 \text{ }\mu\text{m}$, and only about 15% of particles were larger than $50 \text{ }\mu\text{m}$. Knowing the particle size distribution of synthesized BAG could help researchers promote the quality of their products. In a study by Zadorozhnaya et al. (Zadorozhnaya et al., 2019), different wear resistance as a function of particle size distributions was reported in Zr-containing materials. Recently, Averardi et al. (Averardi et al., 2020) demonstrated the importance of particle size distribution on the strength and quality of products fabricated using additive manufacturing, as one of the advanced developments in bone treatment applications.

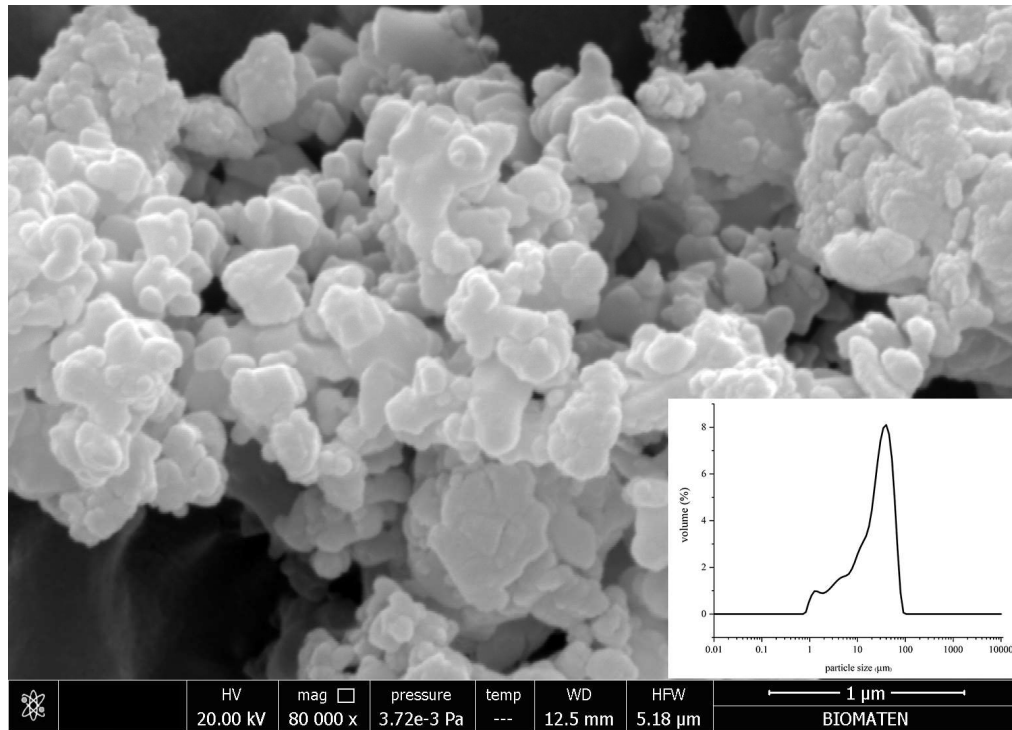


Figure 3.18. SEM micrograph, and particle size distribution of BAG powder sintered at 1150 °C for 3 h in the air.

Elemental analysis of BAG powder confirmed the presence of Ca, Zr, and Si in the samples sintered at 1150 °C. Table 3.3 represents the theoretical and measured molar ratios of elements in BAG. Regarding to the chemical composition of BAG ($\text{Ca}_3\text{ZrSi}_2\text{O}_9$), theoretical molar ratios of Ca:Zr:Si are equal to 3:1:2. The ICP-MS results indicated that the Ca value matches the theoretical molar ratio, whilst measured Zr and Si values are slightly smaller than the theoretical ones. However, Zr/Si ratio (0.47) is almost the same as the theoretical value (0.5) in the synthetic sample. Furthermore, the Zr/Si ratio (~ 0.5) seems to be an influential element in particle size distribution. Now that my results comply with a study, conducted by Fu et al. (Fu et al., 2014), where they reported similar particle distribution with the same Zr/Si ratio.

Existence of other CaSi phases, like larnite, as a minor phase, demonstrates that part of the Si source reacts quickly with the Ca source, which is highly soluble even before mixing with the Zr source and forming other calcium silicate phases. In the presence of zirconia, the calcium oxide can form CaZrO_3 (Evis, 2007), and therefore a tiny quantity of Zr ion failed to be located in the BAG lattice and reacted with Ca to form a small fraction of CaZrO_3 phase. Other studies brought the presence of likewise minor phases as a reason behind lower molar ratios in the experiment, especially when the Ca/Si ratio of the theoretical stoichiometric formula is higher than one (Martín-Garrido et al., 2020). As mentioned previously, hydrating nature of precursors of Zr and Ca facilitates the formation of these impurities and leads to the measurement of lower experimental Ca:Zr:Si ratios in BAG powders.

Table 3.3 Elemental analysis of BAG nanoparticles (n=3).

Molar ratio	Elements		
	Ca	Zr	Si
Theoretical	3	1	2
Measured	3 ± 0.07	0.71 ± 0.01	1.52 ± 0.03

3.2.5 Mechanical properties of BAG

Mechanical properties are the key factors for the clinical application of BAG in the human body (Wagoner Johnson and Herschler, 2011). Using the universal testing machine, the diametral tensile strength of BAG samples (n=6) was measured by subjecting disks to compression load. A diametral compression test involves applying a stress load or force to the point where a material object is split in half. This test indirectly measures the tensile property of the BAG sample, as the particles of the material are pushed apart in opposite directions, similar to what happens to particles in a direct tensile strength test (Ranjakesh et al., 2016). In this case (Figure 3.19), the average strength was measured 3.86 ± 0.19 MPa, which is higher than other Ca-Si, such as wollastonite (Kunjalukkal Padmanabhan et al., 2013), and even compressive strength of BAG (0.28 ± 0.02 MPa or 1.6 MPa, respectively) available in the literature (Khandan et al., 2015; Sadeghzade et al., 2019).

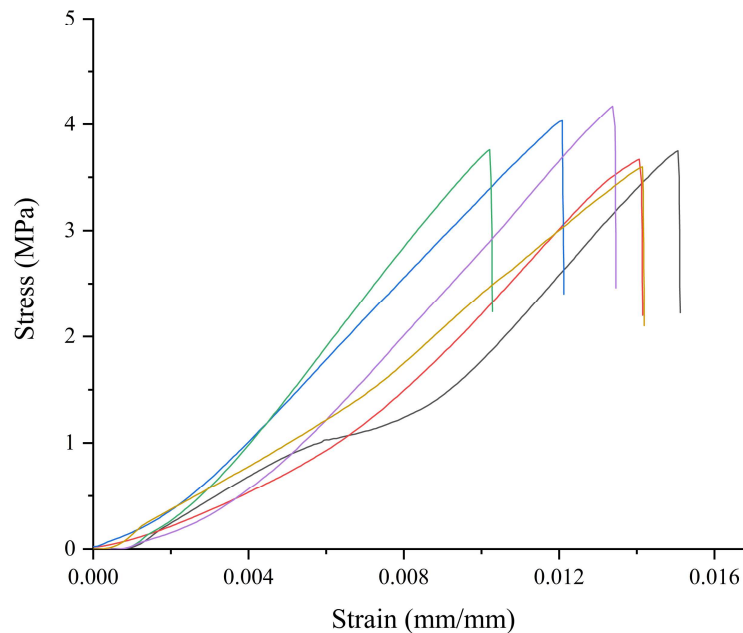


Figure 3.19. Force-displacement curves of BAG during diametral tensile strength test.

Mechanical properties of BAG were studied by Schumacher et al. (Schumacher et al., 2014) for the first time, where they measured the bending strength and hardness of the samples. Later, Najafinezhad et al. (Najafinezhad et al., 2017) demonstrated that the compressive strength of BAG was higher than diopside and akermanite, two other members of Ca-Si materials. BAG coating exhibited superior microhardness and modulus than even HA due to a study by Pham et al. (Pham et al., 2019). BAG also enhanced the compressive strength of samples when it is used as a secondary component (No et al., 2019; Samani et al., 2019).

BAG samples had an average microhardness value of 0.47 ± 0.05 GPa. In other studies, the microhardness value was reported among 6-8 GPa (Pham et al., 2019; Schumacher et al., 2015, 2014). In fact, porosity (density) has been addressed as the main factor that affects the strength of materials (Kariem et al., 2015; Punj et al., 2021), while crystallinity, grain size, and morphology are other factors that play minor roles (Basu and Banerjee, 1994; Knudsen, 1959; Zhao et al., 2013). The relation between densification and mechanical properties could be explained more by changes that occur in the structure of silicates by adding elements.

It seems that the incorporation of some elements, like Mg, inhibits the movement of calcium atoms in the structure and makes it more stabilized (Najafinezhad et al., 2017). Considering that the BAG ceramic is sorosilicate with two silicate tetrahedrons linked by one oxygen ion (Tsui et al., 1998), it is hypothesized that the ZrO_6 octahedral and Si_2O_7 group can form a more stable network that ionically binds the Ca ions (Liang et al., 2010). This may improve the chemical stability of calcium silicate-based ceramics. Therefore, the different porosity (density) can be addressed as the main reason for observing the difference between my results and other studies. To illustrate this, the less porous samples (15%) (Schumacher et al., 2014) had higher hardness values than this thesis results, where the porosity of samples was about 34 % (Table 3.4). Similarly, the samples with higher porosity (78%) (Sadeghzade et al., 2019) had lower compressive strength than my samples. Furthermore, the smaller grain size of my sample might be a minor reason for its enhanced mechanical strength (Naghizadeh and Mirzadeh, 2019).

The microstructure of the disk samples that have been sintered at 1150 °C for 3h is represented in Figure 3.20. Generally, the particles are composed of several grains of varying smaller sizes. Grain size, derived from SEM images, sometimes matches the crystallite size, which is figured out from XRD data, but grains are often constructed due to the combination of several crystallites and are larger than them.

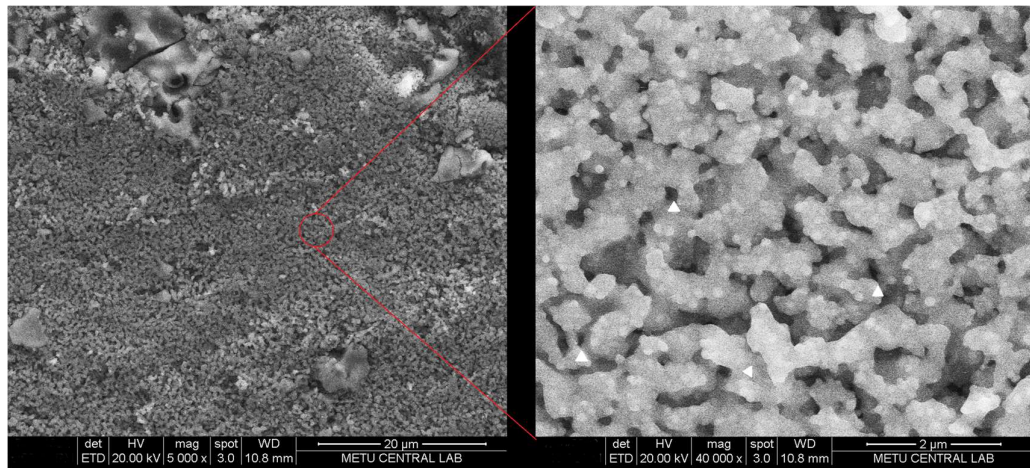


Figure 3.20. SEM micrographs of BAG disk sample sintered at 1150 °C for 3 h in the air used in mechanical tests.

Figure 3.20 shows that my BAG disk samples have been made of 1 µm-sized particles that are packed together almost evenly with small holes (white triangular marks) in between. Like the microstructure of the powder (Figure 3.18), those particles are made up of many smaller grains (hundreds in nm), which in turn are made of 16 nm-long crystalline material. As mentioned above smaller grain sizes resulted in more grain boundaries that prevent the development of defects and led to enhanced mechanical strength in my samples. The ultimate strength and microhardness of human cancellous bone have been reported in the range of 1.5-9.3 MPa (Keller and Liebschner, 2000) and 0.46-0.49 GPa (Boivin et al., 2008). It implies that BAG (Table 3.4) could withstand loads imposed on them in bone treatments like bone grafts or BTE.

Table 3.4 Density, porosity, microhardness, and diametral strength of BAG.

Archimedes Density (g/cm ³)	Relative Density (g/cm ³)	Porosity (%)	Vicker's Microhardness (GPa)	Diametral tensile strength (MPa)
2.75±0.04	0.72±0.01	33.82±0.41	0.47±0.05	3.86±0.19

3.2.6 Biological properties of BAG

3.2.6.1 *In vitro* bioactivity and biodegradability

In vitro bioactivity is referred to the formation of apatite on the surface of materials, which are submerged in a medium. In fact, *in vitro* bioactivity test serves as a tool to predict the bonding of materials to the surrounding host tissue through CaP apatite formation during *in vivo* and clinical tests (Kokubo and Takadama, 2006). Different media types, sample geometry, and immersion conditions are factors that affect *in vitro* testing (Punj et al., 2021). Herein, we used SBF with ionic concentration similar to the inorganic part of human blood plasma, proposed by Kokubo, as a well-known protocol used in many studies (Yilmaz et al., 2020).

Figure 3.21 demonstrates the BAG sample before soaking in SBF and after soaking. There is no apatite-like material on the sample before soaking, which was confirmed by EDX where no P element was detected in the chemical composition of the sample. However, apatite formation was observed on the surface of the BAG sample after 24 h of soaking. Tiny spherical agglomerated apatite particles started to cover the surface of the BAG sample after 1 day of soaking in SBF.

The chemical composition of these particles contains CaP, which is the main component of apatites. The texture of the formed apatite layer, which included loosely packed agglomerated particles on the first day, started to change after soaking in SBF for a longer time. On day 7 apatite ball-like particles were more like flake crystals than smooth particles. After two weeks of soaking in SBF, flake-like apatites covered the surface of the BAG sample extensively. The change in morphology is assigned to the crystallinity degree of formed apatites (Siriphannon et al., 2002). The amorphous apatites converted to more crystalline particles during immersion time that gave rise to those shapes.

Changes in the concentrations of Ca, P, and Si elements in SBF, and pH of SBF filtrates were measured throughout the bioactivity test (Figure 3.22). As soon as the BAG was immersed, the Ca and Si concentrations in the SBF solution raised sharply due to the hydrolyzation of BAG in the medium (Fig 3.22, a and b). The rate of calcium ion diffusion was higher than Si ions in SBF. Immediately positively charged Ca^{2+} ions reacted with PO_4^{3-} negative ions (available in SBF), which were attached to the sample's surface, and formed amorphous calcium phosphates during the first day of soaking, which could be detected through a steep reduction of P concentration from SBF (Liu et al., 2002) (Figure 3.22, c).

These calcium phosphates are more like carbonated HA, rather than stoichiometric ones (Lepry et al., 2017). Later, Si ions, released from BAG, made silanol groups on the surface of the sample that changed the surface's charge to negative and caused further deposition of Ca ions on the surface (Sadeghzade et al., 2017).

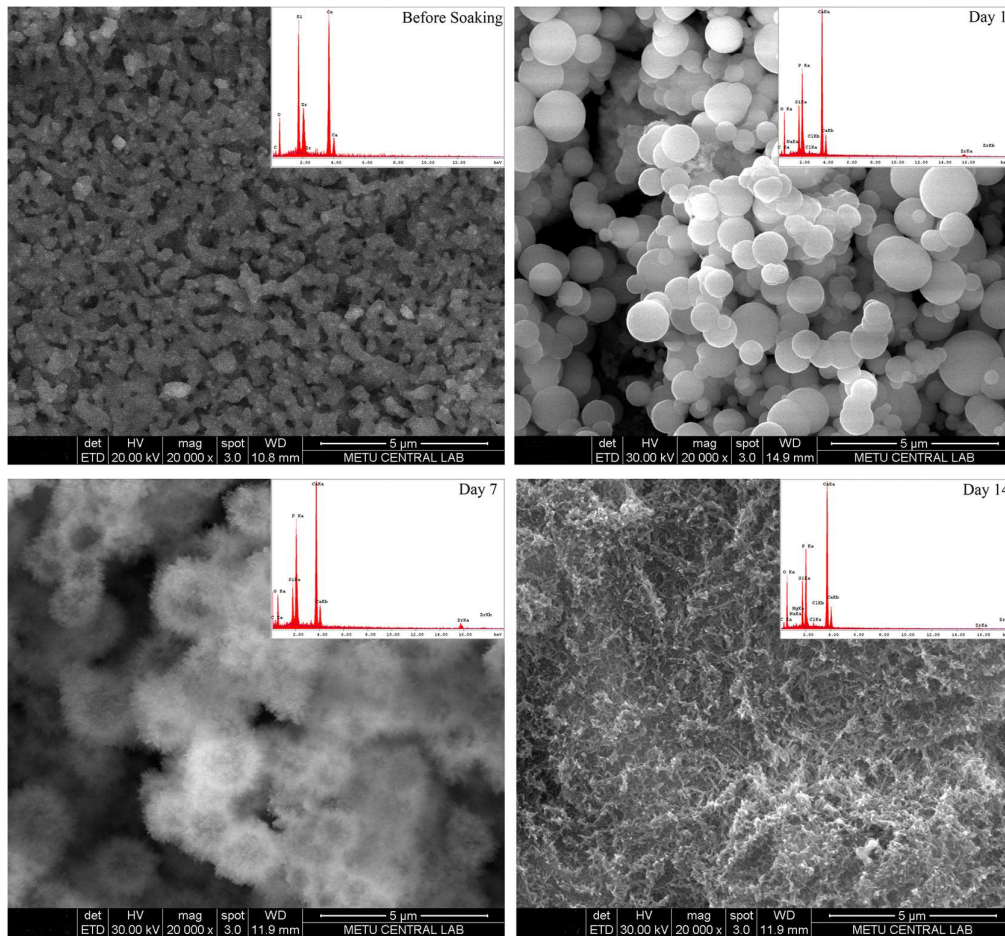


Figure 3.21. SEM micrographs and EDX of BAG disk's surface after immersion in SBF for different time periods.

The concentration of the Zr was less than 0.02 mg/l in SBF. However, the presence of Zr element in the EDX (Figure 3.21) confirms that Zr-OH groups participated in apatite formation similar to Si-OH groups (Najafinezhad et al., 2017). The EDX also indicated Si-rich apatites on disks. This cycle continued until day 14, where amorphous apatites eventually were converted to more stable crystalline apatites and the balance between precipitated and diffused ions among the disk's surface and SBF solution was sustained. The pH changes of SBF filtrate as a function of incubation time (Figure 3.22, d) indicated a steep increase in value during the first 4 days, where the pH of SBF increased from 7.4 to 8.6. The ionic exchange between H^+ ions of

SBF and Ca^{2+} and Zr^{4+} ions from the disk surface lies beneath this event. However, this parameter tended to stabilize after 14 days because the precipitate reduces ion exchange between SBF and sample (Sadeghpour et al., 2014). Eventually, the apatite formation mechanism on the surface of BAG follows the nucleation and growth mechanism of an apatite-like layer on ceramic materials (Liu and Ding, 2002).

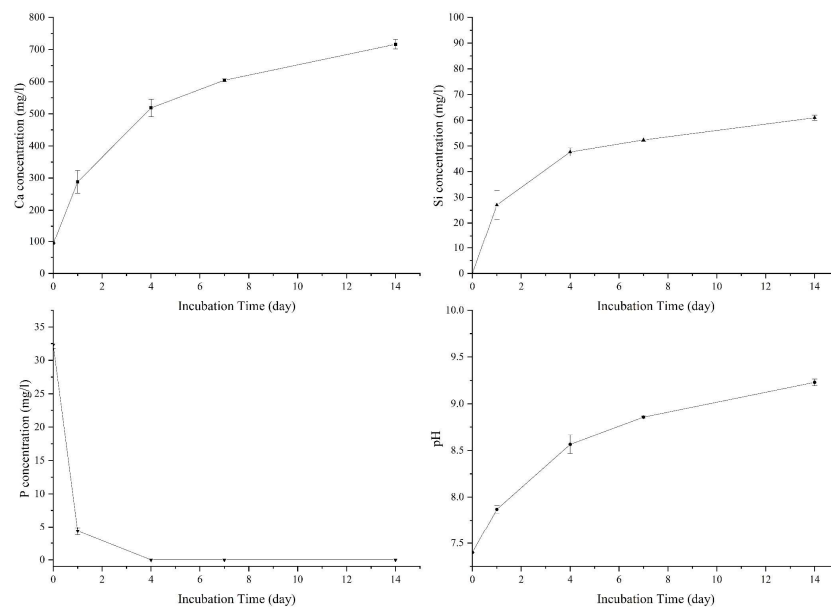


Figure 3.22. Element concentration profiles of a) Ca, b) Si, c) P, and d) pH changes of SBF filtrate during 14 days of incubation (n=3) in the water bath at 37 °C.

In vitro biodegradability of the BAG was investigated by measuring weight loss (n=3) in acetic acid and sodium acetate buffer solution (AcOH-AcONa, pH=5.5), which simulates osteoclastic resorption of bone (Ito et al., 2006). The degradation rate of samples increased from almost 1% at 1 day to a maximum value of 21% after about 1 month of soaking in the buffer at 37 °C (Figure 3.23). The slower degradation rate of samples during the initial days (< 2 % after 7 days) was followed by the faster rate throughout the 2nd, 3rd, and 4th weeks of immersion. A quadratic equation (Figure 3.23) could predict the degradation rate with an admissible accuracy.

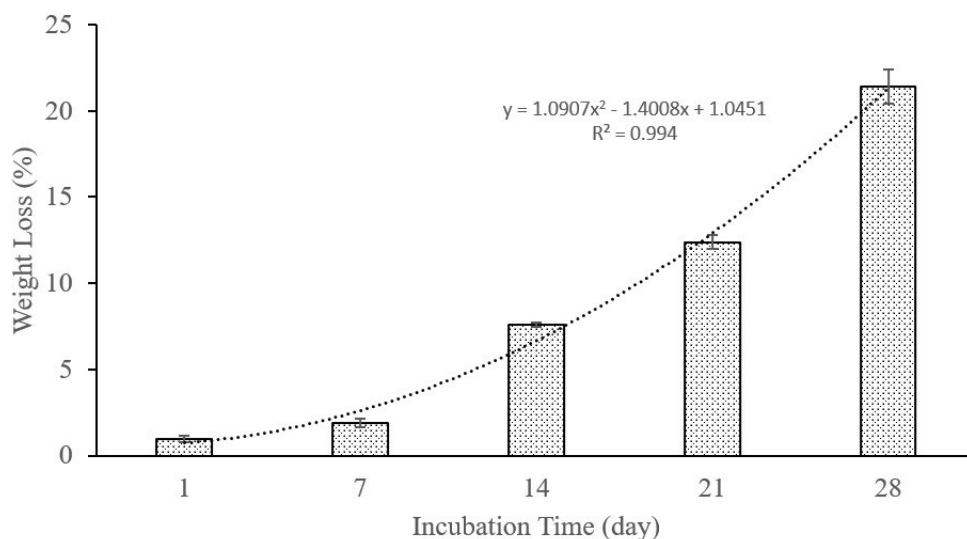


Figure 3.23. Weight loss percentage of BAG samples (n=3) that incubated in acetic acid and sodium acetate buffer for 28 days at 37 °C.

Degradability, also referred to as dissolution rate, plays a major role in the further success of biomaterials during *in vivo* and clinical applications. Initially, an appropriate dissolution rate contributes to having adequate ions like Ca and Si, which leads to higher bioactivity of materials and enhanced cellular proliferation or differentiation (Punj et al., 2021). Herein, the initial dissolution rate of my prepared BAG seems enough to trigger apatite formation on the surface of samples (Figure 3.21).

More importantly, maintaining the balance between the degradation rate of implanted samples and the healing process of bone is necessary to support the gradual transfer of loads from the implant to the newly formed bone and avoid any implant failure. Slower degradation of BAG samples in the initial days coincides with the primary stage of implantation, which is accompanied by an inflammation phenomenon in the patient's body and the beginning of bone formation.

Therefore, a synthetic implant tolerates loads and prevents excessive force on newly formed bone. Later, by the higher degradation rate of samples during the 3rd and 4th weeks, a fraction of loads transfer on newly formed bone and that is essential for the natural growth of bone. Degradation of BAG samples (~20 wt%) after 28 days was less than those analyzed by Sadeghzadeh et al. (Sadeghzade et al., 2019) with degradation of 51 wt% and was greater than samples of Roohani et al. (Roohani-Esfahani et al., 2012) (~10 wt%) at the end of 28 days. Impressively, my results showed excellent compatibility with the appropriate strengthening of newly formed bone tissue and degradation percentages of implants in terms of time (Chandra and Pandey, 2020).

3.2.6.2 Cell viability and osteogenic activity of BAG

Figure 3.24 represents the results of the MTT assay that was performed with the direct contact of various concentrations of material with Saos-2 cells to evaluate the cytocompatibility of BAG. Figure 3.24 (upper one) demonstrates that there is a significant time-dependent increase in absorbance for both the positive control group (P.C.) and BAG samples, which indicates that cells proliferated (Figure 3.24). Additionally, relative cell viabilities were calculated for BAG-containing groups, where the viability of cells in the control group was taken 100%. All BAG-containing groups exhibited relative cell viability greater than 80 % with respect to the positive control group (TCPS without any BAG particles) after 24 and 48 h, depicted in lower part of Figure 3.24.

Although there was no significant difference when the relative viability of samples was compared between 24 h and 48 h, the confluency over 80% could be the reason for the slight decrease of cell viability in two groups with higher BAG particle concentrations (12 and 25 $\mu\text{g/ml}$) after 48 h incubation at 37 °C, compared to 24 h (Figure 3.25). The results confirmed that BAG particles had no cytotoxic effect on *in vitro* cultured Saos-2 cells. Ca, Si, and Zr ions, released from BAG, did play significant roles in cell spreading and proliferation (Marie, 2010; Ramaswamy et al., 2008; Sun et al., 2007).

For example, silica provides negatively charged silanol groups that could interact with functional groups to facilitate cell spreading and growth (Diba et al., 2012). Similar results were reported in recent studies, where non-cytotoxic effect and improved cell attachment and viability have been observed in Saos-2 osteosarcoma cells (Arefpour et al., 2019b), and MG6 osteoblast cells (Abbasian et al., 2020; Bakhsheshi-Rad et al., 2017)

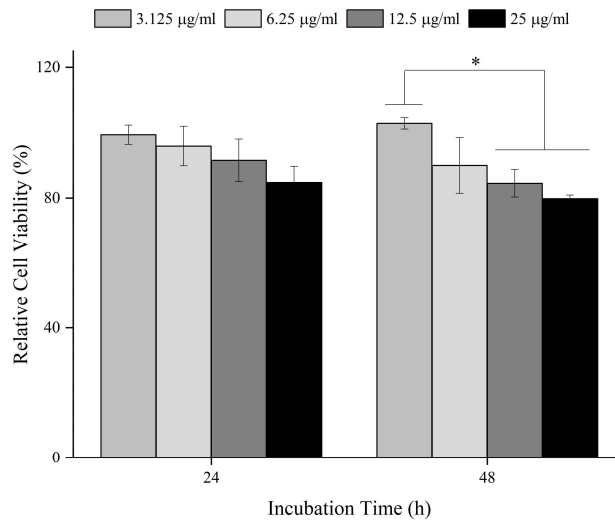
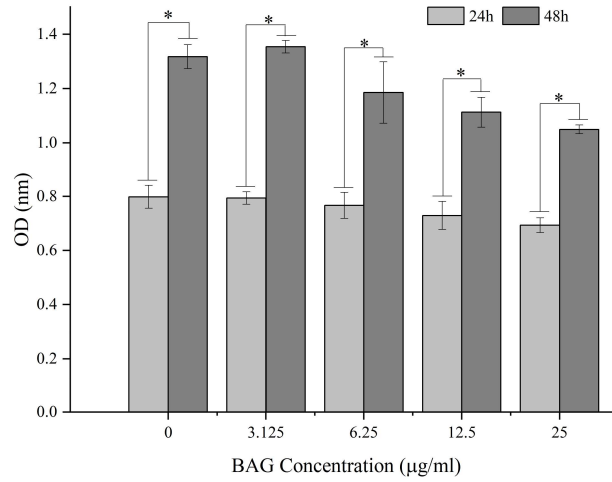


Figure 3.24. Upper: MTT assay results of Saos-2 cells after direct contact with various concentrations of BAG powder ($\mu\text{g/ml}$) for 24 and 48 h of incubation ($n=3$). Lower: relative cell viability of Saos-2 cells after direct contact with various concentrations of BAG powder ($\mu\text{g/ml}$) with respect to the control group without any BAG particles after 24 and 48 h of incubation ($n=3$). Note that the Asterisk (*) indicates significant differences between the groups ($p<0.05$).

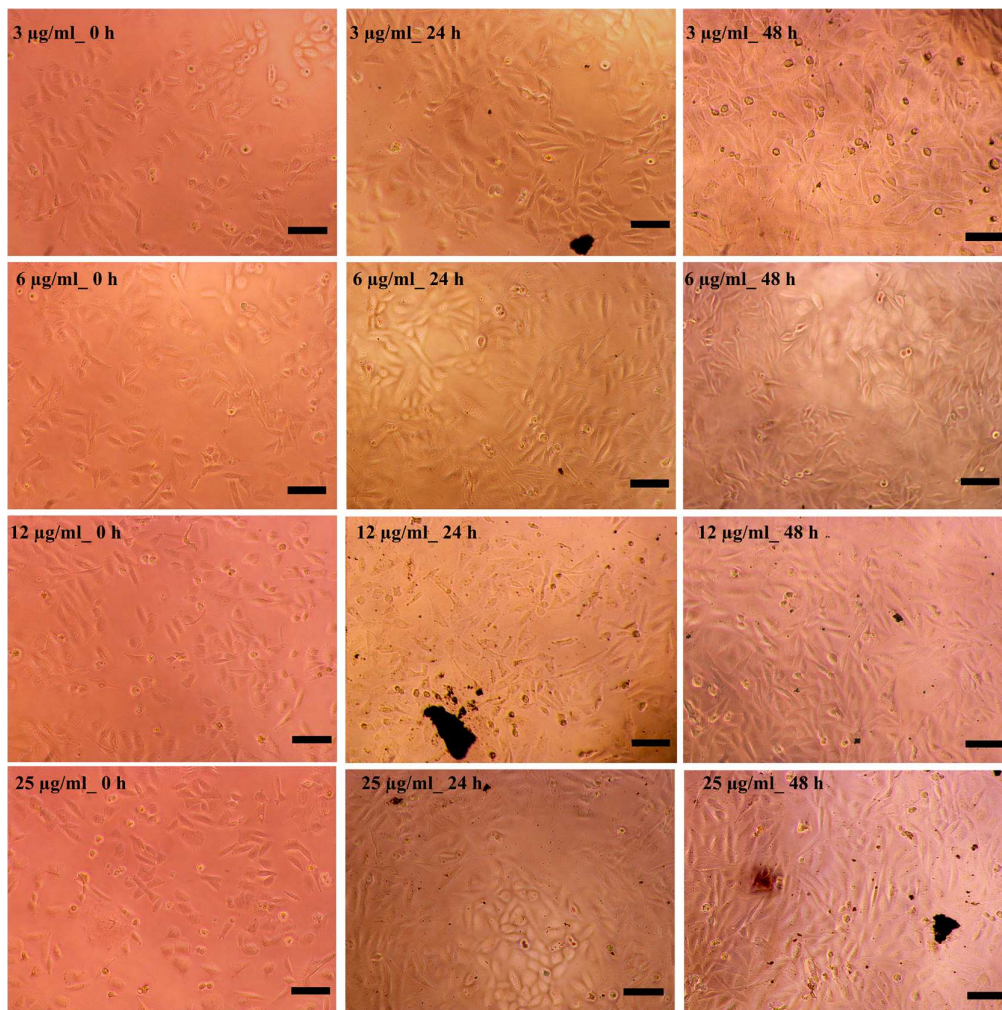


Figure 3.25. Optical microscope images of Saos-2 cells in direct contact with different concentrations of BAG particles throughout 48 h of incubation at 37 °C. Scale bar length is 100 µm.

The alkaline phosphatase activity of Saos-2 cells in direct contact with different concentrations of BAG particles is depicted in Figure 3.26. Statistically, there was no difference ($p < 0.05$) among groups at both 7 and 14 days. The same pattern was observed for intracellular Ca ion deposition after 7 and 14 days (Figure 3.26). It seems that the presence of ascorbic acid and β -glycerophosphate in the osteogenic medium (OM) triggered osteogenic activity and mineralization of Saos-2 cells cultured in TCPS as a blank group (Langencach and Handschel, 2013). A similar result was reported by Tsigkou et al. (Tsigkou et al., 2009) when they tested the ALP activity of 45S5 Bioglass® (with the linear formula of $\text{CaO} : \text{SiO}_2 : \text{P}_2\text{O}_5$) in the presence of OM. I believe that the presence of ascorbic acid and β -glycerophosphate masks or affects the influence of BAG dissolution products. Furthermore, Zhang et al. (X. Zhang et al., 2014) observed no difference in ALP activity between BAG and blank groups when the concentration was $\leq 6 \mu\text{g/ml}$.

Nevertheless, my result of ALP activity in the absence of ascorbic acid and β -glycerophosphate revealed that cells in wells with $12 \mu\text{g/ml}$ of BAG particles had higher osteogenic activity (ALP) than cells without any BAG material in their medium (Figure 3.27). Ionic products of BAG (Ca, Si, and Zr ions) and their influences on the activation of osteogenic-related gene expression have been reported to promote osteogenic activity in cells (Lu et al., 2014; X. Zhang et al., 2014). This finding indicated that the osteogenic feature of BAG could contribute to its performance as a promising candidate for bone defect treatments.

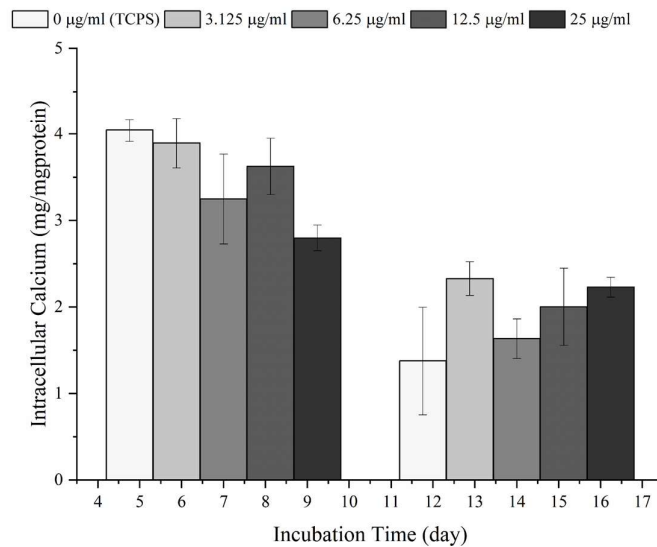
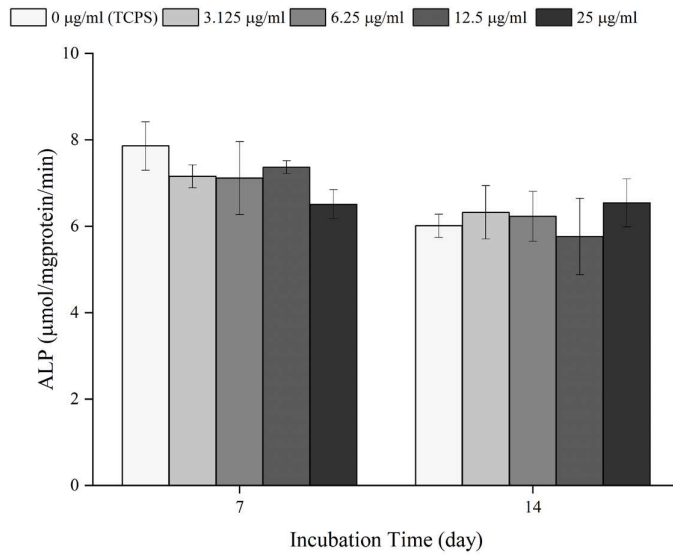


Figure 3.26. ALP activity (n=3), and intracellular calcium ion deposition of cells incubated in osteogenic medium containing different concentrations of BAG particles (n=3). there is no significant difference ($p < 0.05$) between groups at both 7 and 14 days for ALP and intracellular calcium deposition of cells in the osteogenic medium with the ascorbic acid and β -glycerophosphate.

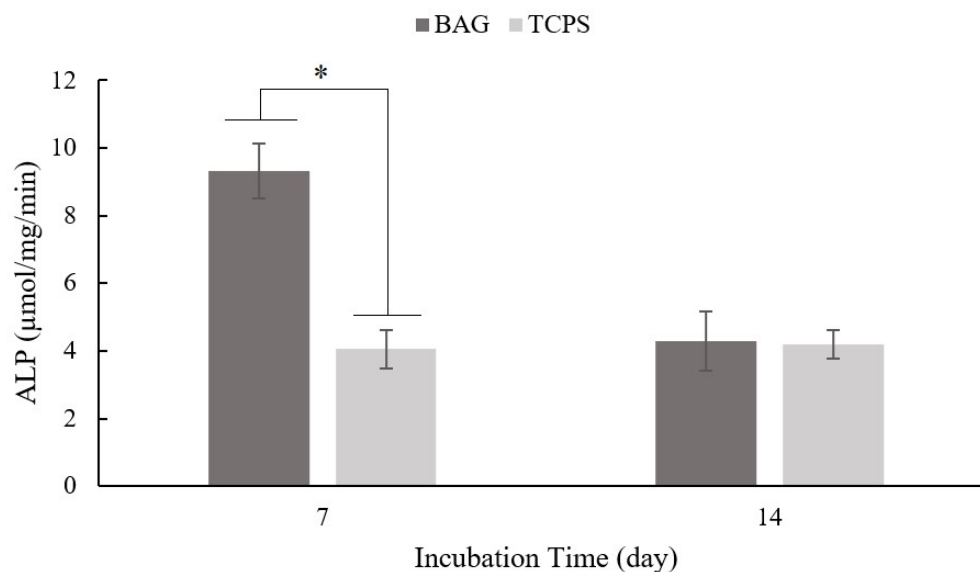


Figure 3.27. ALP activity of Saos-2 during 14 days of incubation in the medium (without ascorbic acid and β -glycerophosphate) containing BAG particles (12 $\mu\text{g}/\text{ml}$) ($n=5$). Note that the Asterisk (*) indicates significant differences between the groups ($p<0.05$).

In this part of the thesis, a modified sol-gel route was proposed to synthesize BAG bioceramic, and various properties of produced BAG were comprehensively characterized to examine its suitability for bone defect treatments. My proposed sol-gel approach led to the preparation of a transparent solution (sol), which indicates the complete dissolution of precursors and is essential for the quality of the final product, by using optimum amounts of solvent (ethanol) and chelating agent (nitric acid), as well as dissolving Zr-source (zirconium [IV] oxynitrate hydrate) separately. Physicochemical characterization results demonstrated that prepared BAG had a highly crystalline structure and acceptable purity with minor impurities. The enhanced mechanical strength ($\sim 4\text{MPa}$), the biodegradation rate of $\sim 20\%$ after a month, as well as promoted bioactivity and osteoconductivity, due to the extensive formation of apatite on samples in SBF, were observed. Furthermore, *in vitro* cell-

culture tests revealed the non-cytotoxic feature and the promoted osteoinductive effect of my material in the absence of an osteogenic medium. Thus, synthesized BAG satisfies the essential requirements, such as bioactivity, biodegradation rate, mechanical strength, biocompatibility, and having osteogenic effect to serve as a promising candidate for making final composite scaffolds.

3.3 Characterization of 3D porous BHA-BAG composite scaffolds

Following the synthesis of BHA powders, and selecting the 0.05BHA samples as the optimum group in terms of B doping dosage, as well as the successful production of BAG powder through modified sol-gel techniques, proposed for the first time in this thesis, these powders were applied to prepare composite scaffolds in order to benefit advantages of both ingredients. Figure 3.28 demonstrates that 3D porous scaffolds were successfully fabricated after the removal of polymeric agents from green scaffolds. The different sizes of pores, which were dispersed non-homogeneously, correspond to the sizes of porogen particles that changed from 212 μm to 425 μm .

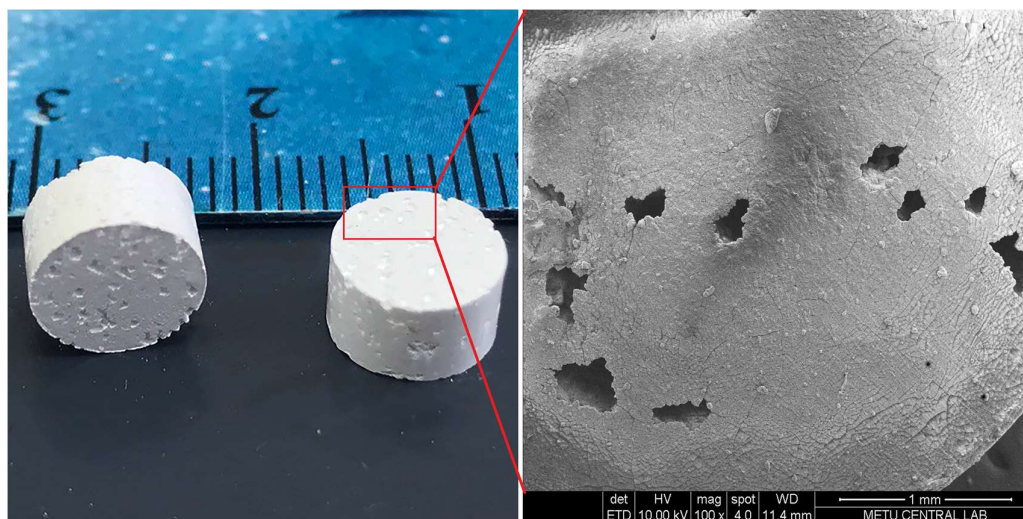


Figure 3.28. The general appearance of the scaffold and SEM image of pores on the scaffold after the removal of polymeric porogen agent

3.3.1 Microstructural and physicochemical properties of scaffolds

Elimination of porogen agents and the thermal stability of scaffolds were inspected by TGA-DSC analysis (Figure 3.29). The minor weight losses (1.06%-1.50%) happened below 180 °C due to the removal of residual water molecules (Hu et al., 2015). However, the major weight losses (21%-31%) occurred between 180 °C and almost 480 °C in scaffolds. The first endothermic peak observed in the DSC graphs in the range of 180-250 °C could be assigned to the loss of CO₂ and CO components; meanwhile, the larger endothermic peaks between 250 °C and 480 °C belong to the elimination of PVA/PEG agents (Alshemary et al., 2019a; Thangavel et al., 2016). The TGA graph becomes stable after 480 °C and the negligible mass loss after that temperature could be due to the complete removal of polymeric agents.

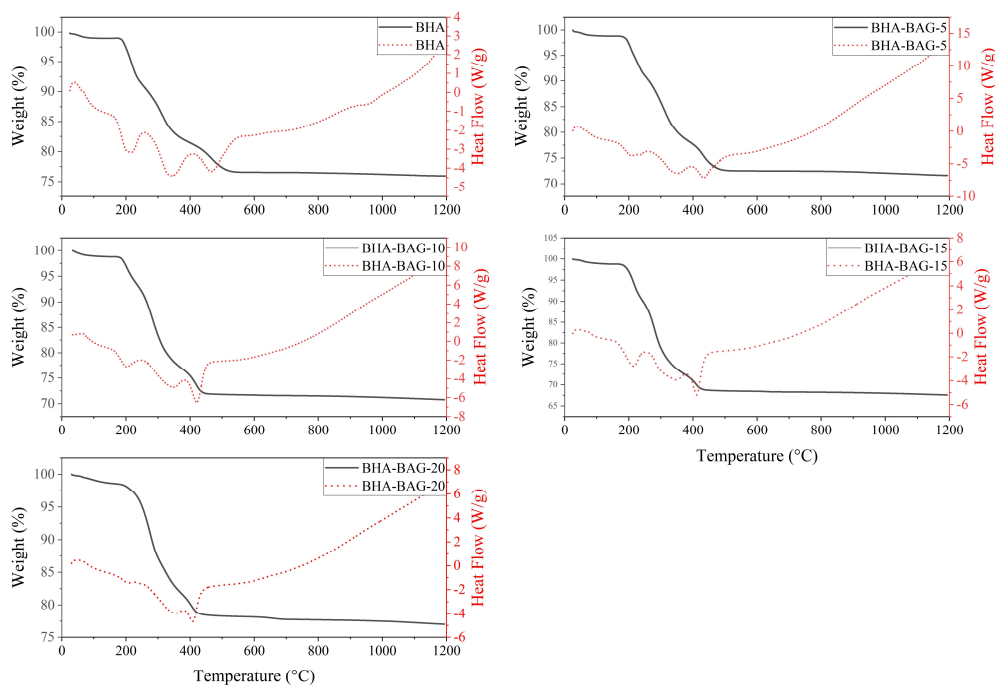


Figure 3.29. TGA-DSC of scaffolds that were performed between 25 °C to 1200 °C.

Results of the ICP-MS analysis confirmed the presence of predominant Ca and P elements as well as minor B in the elemental composition of the BHA and composite scaffolds. Si and Zr elements appeared only in the chemical composition of composite BHA-BAG scaffolds (Table 3.5). As we expected, the amount of Si and Zr elements increased in scaffolds that had greater percentages of BAG material in their composition. On the other hand, the reduction of P and B amounts of composite samples represents the lower percentage of BHA used in the making of those scaffolds; the more the BAG percentage the lesser amount of BHA and therefore P and B elements.

Table 3.5 Chemical composition of prepared scaffolds according to wt.% of constitutional elements (n=3).

Sample	Ca	P	B	Si	Zr
BHA	41±1	19.5±0.1	0.046±0.001	0	0
BHA-BAG-5	40±1	18.8±0.4	0.042±0.001	0.71±0.03	0.81±0.01
BHA-BAG-10	40±1	17.5±0.5	0.042±0.001	1.40±0.03	1.69±0.002
BHA-BAG-15	39±1	16.7±0.2	0.038±0.001	2.2±0.1	2.60±0.1
BHA-BAG-20	36±1	14.6±0.2	0.036±0.002	2.9±0.1	3.30±0.1

XRD patterns of BHA and 4 different groups of composite BHA-BAG scaffolds, based on wt.% (5, 10, 15, 20) of the BAG component, are depicted in Figure 3.30. The results demonstrated that major peaks complied with the diffraction pattern of the BHA crystal, which is the primary component of my samples. The comparative XRD patterns of scaffolds revealed that the presence of BAG gave rise to additional peaks, remarked by (*), compared to the BHA's pattern.

These peaks correspond to major (2 0 -2) and (1 1 3) planes of BAG (PDF# 47-1854) that appeared in the composite scaffolds, and their intensity increased gradually with increasing amounts of BAG in samples. Even more peaks of the BAG phase related to planes (0 2 3) at 31.12°, (0 3 1) at 27.72°, and (1 0 0) at 12.22° were detected in scaffolds with greater BAG percentages (15 and 20 wt.%). Moreover, a very tiny (0.1 wt.%) additional crystalline phase of β TCP (PDF# 09-0169), which corresponds to the (0 2 10) diffraction plane at 30.917° (Khoshsima et al., 2018), disappeared in the composite samples XRD patterns.

Due to Rietveld refinement results (Table 3.6), the unit cell parameters of both BHA and BAG materials in composite scaffolds were held in accordance with standard PDF cards. However, the unit cell parameter *a* and unit cell volume (*v*) of the BHA phase were slightly smaller in composite scaffolds, compared to the BHA group. This change might have happened due to the substitution of some phosphate ions or borate ions in BHA with available ions of silicate in the composite scaffolds. A similar reduction of unit cell volume or other lattice parameters was previously reported when the replacement of ionic entities with each other had happened (Alshemary et al., 2019a; Rajesh et al., 2012).

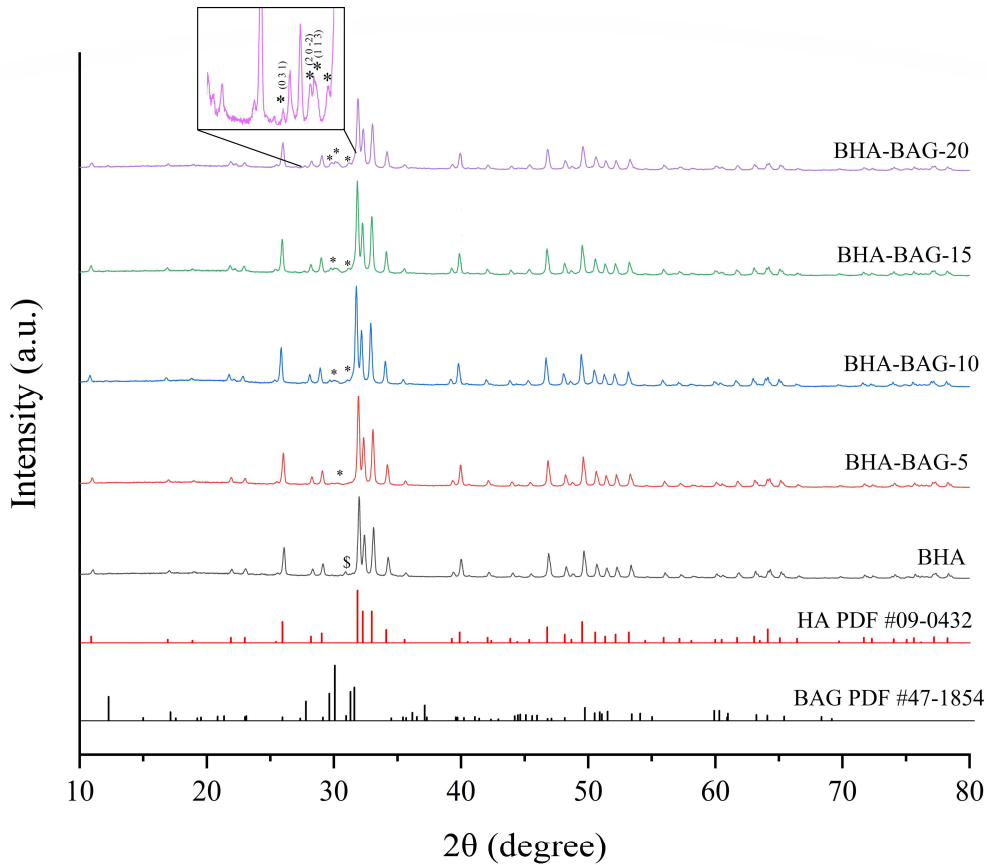


Figure 3.30. XRD pattern of BHA and composite BHA-BAG scaffolds after removing polymeric porogen agents. and The (*) indicates the presence of BAG phases in the XRD of samples.

Moreover, the relative intensities of XRD patterns decreased in composite scaffolds, which could be attributed to their lower crystallinity. The crystallinity degree (CD) of scaffolds (Table 3.6) confirms this observation, where the CD percentage of composites was less than the BHA sample. The lower crystallinity of composite scaffolds could be attributed to several reasons. For the most part, it is caused by the crystallinity of BHA as the major component. Trace ions' roles in the distribution of connection between calcium and phosphate units in the crystal structure of BHA

(Ding et al., 2014), as well as the combination of cations with the phosphate ions that reduces the effective supersaturation (Yang et al., 2011) are some of those reasons. The lower CD of the BAG component (87% due to our previous study), compared to 90 % of BHA, is another reason for observing lower CD in composite scaffolds, especially with higher BAG wt.%. Furthermore, the pressing of ceramics was also addressed as a subordinate reason that sometimes affects samples' crystallinity (Gorman et al., 2014; No et al., 2021).

Table 3.6 Crystallinity degree (CD) of scaffolds, as well as unit cell parameters and Phase percentage of scaffolds' constituent materials.

Sample	Phase wt. %		Unit cell parameters								CD %
			BHA				BAG				
	BHA	BAG	a (Å)	b (Å)	c (Å)	v (Å ³)	a (Å)	b (Å)	c (Å)	v (Å ³)	
BHA	99.9	0	9.426	9.426	6.885	529.83	--	--	--	--	90
BHA-BAG-5	98.6	1.4	9.423	9.423	6.886	529.53	7.36	10.18	10.45	782.72	87
BHA-BAG-10	93.5	6.5	9.417	9.417	6.883	528.65	7.27	10.19	10.46	774.94	87
BHA-BAG-15	91.3	8.7	9.420	9.420	6.884	528.98	7.28	10.17	10.44	773.58	83
BHA-BAG-20	88.5	11.5	9.423	9.423	6.886	529.51	7.28	10.18	10.46	775.47	82

FTIR spectra of the scaffolds are depicted in Figure 3.31, where all groups exhibited the characteristic bands of HA structure. In BHA scaffolds, symmetric $\nu_1(\text{PO}_4^{3-})$ and asymmetric $\nu_3(\text{PO}_4^{3-})$ stretch bands of phosphate were observed at 962 cm^{-1} and 1024 cm^{-1} , respectively. Asymmetric stretch $\nu_3(\text{PO}_4^{3-})$ of phosphate was slightly shifted to lower wavenumbers between $1025\text{-}1027 \text{ cm}^{-1}$ in BAG-containing scaffolds, while a shoulder at 1087 cm^{-1} didn't shift in those composites. However, symmetric stretching $\nu_1(\text{PO}_4^{3-})$ was observed at 962 cm^{-1} in composite groups similar to BHA.

The relatively weak symmetric bending mode of phosphate, $\nu_2(\text{PO}_4^{3-})$, appeared at 474 cm^{-1} in BHA; while this absorbance band had greater intensity in the BHA-BAG samples, and was seen with a slight shift at 473 cm^{-1} and 472 cm^{-1} .

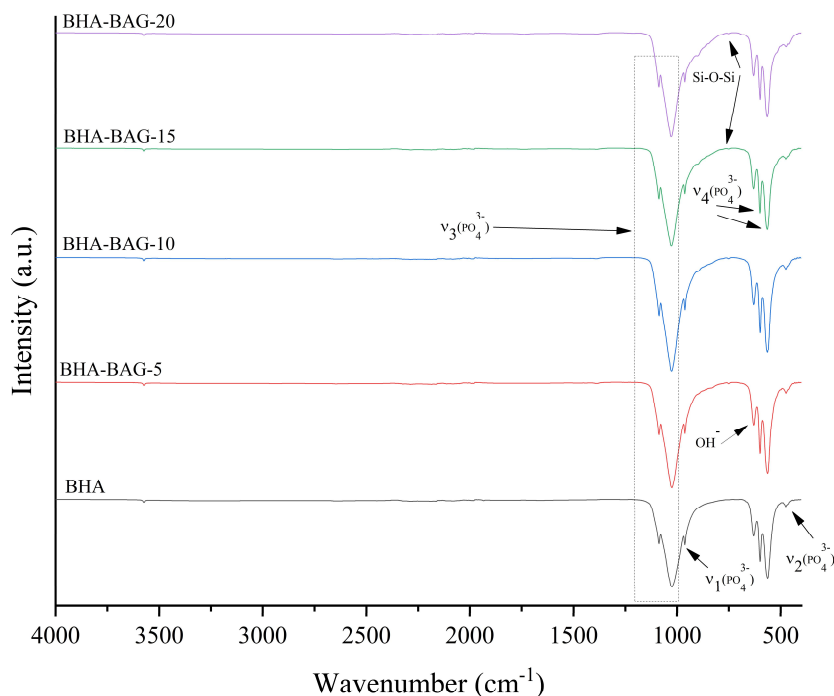


Figure 3.31. FTIR spectra of BHA and composite BHA-BAG scaffolds after removing polymeric porogen agents.

Similar to asymmetric stretching bands, The asymmetric bending of the phosphate group, $\nu_4(\text{PO}_4^{3-})$, was slightly shifted to a lower wavenumber by increasing the BAG amount in the composites, compared to their location at 552 cm^{-1} and 598 cm^{-1} in BHA. A common peak at 630 cm^{-1} was assigned to OH^- libration band. The intensity of this band at 630 cm^{-1} was lower in the spectra of the BHA-BAG composites, which indicates the decomposition of BHA as a result of increased BAG content, or the possibility of substitution of the OH^- with silicate in composite scaffolds (Khoshsima et al., 2016). Observing minute bands in BAG-containing scaffolds at about 750 cm^{-1}

¹ that belong to Si-O-Si vibration (Fu et al., 2014; Mehrafzoon et al., 2018) is a better indicator of the presence of silicate-containing BAG phase in the scaffolds. The very tiny band at 3573 cm⁻¹ was assigned to OH⁻ stretching vibration in the spectra of the composites.

The porosity, presented in Table 3.7, increased from 38% up to almost 45 % in BHA-BAG scaffolds, while there was no statistical difference between composite groups based on BAG component wt.%. The enhanced porosity of the composite scaffolds could be attributed to the improvement in the development of well-marked micropores (Sivashankari and Prabakaran, 2020). In some other studies, a decrease was reported in the porosity of BAG-incorporated scaffolds (Karimi et al., 2021; Khandan et al., 2015). However, we believe that this novel modified approach for synthesizing BAG nanoparticles as well as the method applied herein to prepare scaffolds are the predominant reasons that let us have well-defined micro/macropore and interconnected composite scaffolds with greater porosity.

The greater porosity resulted in the increase of micropore volume and SSA of composite scaffolds as seen in Table 3.7. A fraction of SSA increase has a root in the smaller micropore's size, where those sizes are smaller (~ 2-2.5 nm) in BHA-BAG composite scaffolds, compared to BHA (~ 3.5 nm). Greater porosity and resultant larger SSA contribute to better cell migration into, and interaction of cells with scaffolds (Turnbull et al., 2018). Furthermore, it ameliorates the nutrition and exchange of gases (Gao et al., 2014). My composite samples had a porosity greater than 40 % with macropores (in a range of 200-500 μm), and micropores which are appropriate for cell adhesion, migration, proliferation, differentiation, nutrient and oxygen supply, and even later in vivo vascularization and new bone formation (Jodati et al., 2020c).

Table 3.7 Porosity (n=3), specific surface area (SSA), micropore volume, and micropore sizes of scaffolds.

Sample	Porosity (%)	SSA (m ² /g)	Micropore volume (cc/g)	Micropore size (nm)
BHA	38.06±0.83	7.62	0.028	3.49
BHA-BAG-5	43.34±0.24	8.67	0.031	2.51
BHA-BAG-10	44.72±0.25	10.60	0.033	2.00
BHA-BAG-15	44.16±0.76	11.74	0.037	1.99
BHA-BAG-20	44.48±0.59	16.73	0.031	2.24

3.3.2 Mechanical properties of scaffolds

Figure 3.32 includes compressive strength (C), diametral tensile strength (S), and Vicker's microhardness (HV) values of ceramic-based scaffolds. The results demonstrated that involving BAG as a minor phase in the structure of BHA-BAG composite scaffolds caused decreases in the mechanical properties, compared to BHA. The significant differences have been indicated with an Asterisk (*) mark. The BAG content's wt.% did not affect the tensile strength of composite scaffolds; however, specimens with higher BAG wt.% possessed weaker compressive strength and even microhardness characteristics than the groups with lower BAG. The compressive strength of BHA-BAG scaffolds were matching the mechanical strength of cancellous bones (Sadeghzade et al., 2017); and despite the mentioned reduction, as far as we know, their strength was higher than nearly all produced BAG-containing scaffolds available in the literature (Jodati et al., 2020b), except for studies by Schumacher et al. (Schumacher et al., 2014) and No et al. (No et al., 2021), where their samples were denser and sintered at higher temperatures.

The adverse relation between porosity and stiffness is the leading reason for the reduction of compressive and tensile strengths as well as the hardness of BHA-BAG scaffolds (Kariem et al., 2015). Herein, the composite scaffolds with higher porosity percentages (~ 43-45 %) had weaker mechanical properties (Table 3.7) than denser BHA samples with a porosity of about 38%. A similar trend was also observed in Khandan et al. (Khandan et al., 2015), where the increase of porosity from 49% to 65% led to a decrease in compressive strength from 2.8 MPa to 1.6 MPa. In addition, the 0.59 MPa of the strength of 70% porous composite scaffolds versus 0.18 MPa of compressive strength of 83% porous ones is another example (Arefpour et al., 2019b). Schumacher et al. (Schumacher et al., 2015) stated that not observing the remarkable difference in porosity and grain size was the reason for almost no change in the mechanical characteristic of their samples; Meanwhile, the reduced porosity introduced by Abbasian et al. (Abbasian et al., 2020) as the main cause of higher compressive strength in their composite scaffolds.

Furthermore, the accumulation of the second phase in grain boundaries of composites was declared as a minor reason for weakened mechanical features in composite scaffolds (Sadeghzade et al., 2019). Likewise, Samani et al. (Samani et al., 2019) mentioned that the recorded decline in the mechanical strength by adding more BAG content (over 3 wt.%) was due to the agglomeration of nanoparticles and heterogeneity of their composite scaffolds' structure. Additionally, crystallinity and grain size are also influential factors that play role in the mechanical properties of scaffolds (Khoshshima et al., 2018). Thus, the non-uniform distribution of BAG particles in the BHA matrix and the interface interaction between them were minor reasons for the lower mechanical properties of BHA-BAG scaffolds (Abbasian et al., 2020). The lower crystallinity of BHA-BAG samples with greater BAG wt.% (Table 3.6) caused more amorphous phases and consequent smaller hardness values (Albayrak, 2016; Jodati et al., 2022a).

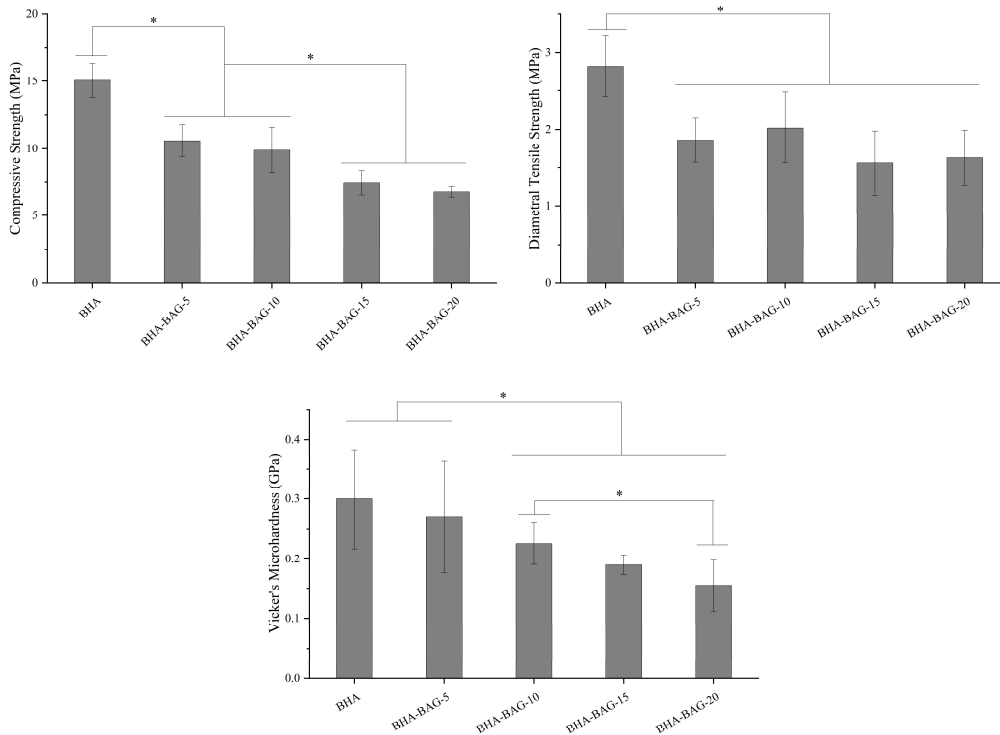


Figure 3.32. The mean and standard deviation values of compressive strength (n=5), diametral tensile strength (n=5), and microhardness (n=30) of scaffolds. (*) indicates a significant difference between that groups ($p \leq 0.05$).

3.3.3 *In vitro* bioactivity and biodegradability of scaffolds

The apatite formation on surfaces of scaffolds is illustrated in Figure 3.33, and it is defined as bioactivity that contributes to the bonding of scaffolds with surrounding tissues during further *in vivo* and even clinical trials. The SEM images revealed apatite formation on the surface of submerged BHA-BAG-5, BHA-BAG-10, BHA-BAG-15, and BHA-BAG-20 composite scaffolds in SBF 1 day after incubation at 37 °C; however, no hint of apatite formation was observed on the BHA sample during

the first 24 h period. Apatite depositions were observed on all scaffolds after 7 days, where the mass of formed layers increased gradually throughout time until day 14. The presence of tightly packed flake-shape apatites that formed agglomerated granules throughout the surface of BHA-BAG-10, BHA-BAG-15, and BHA-BAG-20 scaffolds was obviously visible in Figure 3.33. Both the quantity and rate of apatite deposition of these groups were higher than BHA, and even BHA-BAG-5 samples. The presence of Ca, P, C, and O elements, detected by the EDX analysis as major available components, confirmed the CaP nature of formed apatites. However, minor amounts of Si, Zr, and Cl were also detected in the BHA-BAG groups.

The Ca^{2+} diffusion of BHA-BAG-10, BHA-BAG-15, and BHA-BAG-20, especially the latter two groups with higher BAG amounts, was remarkably higher than the Ca^{2+} release of BHA and BHA-BAG-5 samples (Figure 3.34). Thus, positively charged Ca^{2+} ions in those groups immediately reacted with PO_4^{3-} negative ions of SBF and formed amorphous calcium phosphates during the first day of immersion (Liu et al., 2002). These CaP apatites were more like carbonated HA, rather than stoichiometric ones (Lepry et al., 2017). Concerning B ion, its diffusion from submerged scaffolds to SBF solution was remarkably smaller in composite groups than in BHA. This reduction could be explained by the lesser amount of BHA and therefore B in their structure. However, the accumulation of negatively charged borate increased in scaffolds after the first day helped to change the charge of calcium-poor amorphous apatite again and started interacting with Ca^{2+} , especially in the BHA group (Jodati et al., 2022a; Pazarçeviren et al., 2021).

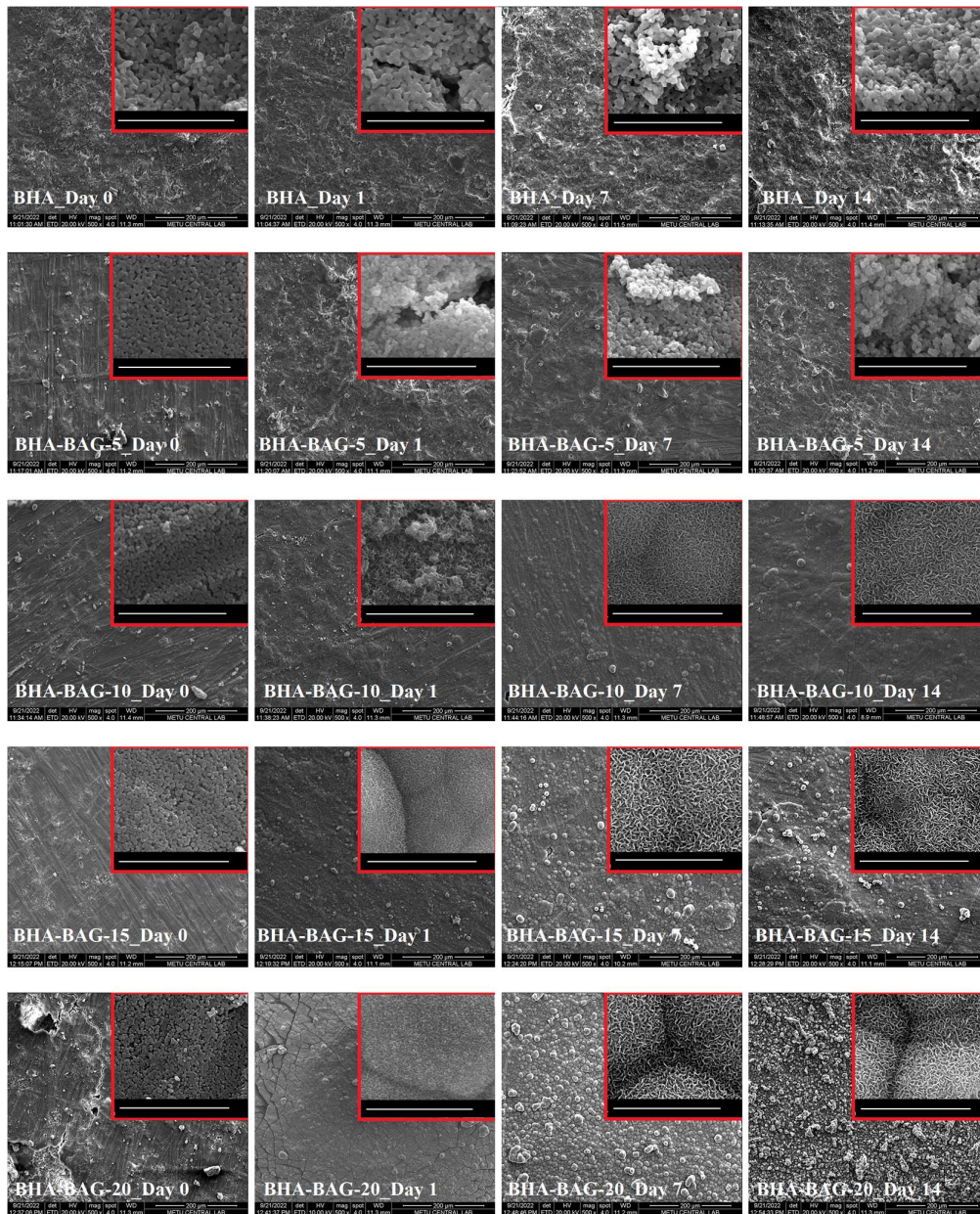


Figure 3.33. Apatite formation on scaffolds after specified immersion time inside SBF, as well as SEM micrographs of scaffolds' surface before immersion (Day 0). The scale bar of magnified images in red windows is 5 μm , while the scale bar length on main images is 200 μm .

Meanwhile, in BAG-containing groups, Si ions released from BAG (Figure 3.34) made Si-OH groups on the surface of the sample, changed the surface's charge to negative, and caused faster deposition of Ca ions on the surface of composite scaffolds (Sadeghzade et al., 2017). The apatite formation continued until day 14, where amorphous apatites eventually were converted to more stable crystalline apatites and the balance between precipitated and diffused ions among the scaffold's surface and SBF solution was sustained. Moreover, according to Wang et al. (Wang et al., 2017), higher SSA and microporosity (Table 3.7) are other reasons for faster apatite formation on composite scaffolds.

Different apatite morphologies were observed in SEM images of BHA-BAG composite scaffolds, compared to BHA one. The morphology of formed apatites depends on various factors, such as the composition of precipitates (e.g. Ca/P ratio), pH of the solution, and ion concentrations in the solution (Lu et al., 2019). Similar morphology has been observed for BHA in our previous study (Jodati et al., 2022a) as well as in others (Atila et al., 2019). The observed flake-like shape of apatites in BHA-BAG scaffolds was also reported in studies in the presence of Si and/or B (Gerhardt and Boccaccini, 2010; Lu et al., 2016). Thus, the higher Ca/P ratio of the three groups of BHA-BAG composites (1.75-1.83), compared to BHA (1.57) and even BHA-BAG-5 (1.6), higher pH (Figure 3.34), and the presence of minor ions such as Cl (Kirste et al., 2017), Si, and even Zr had an influential effect on the chemical composition and consequent morphology of composite samples.

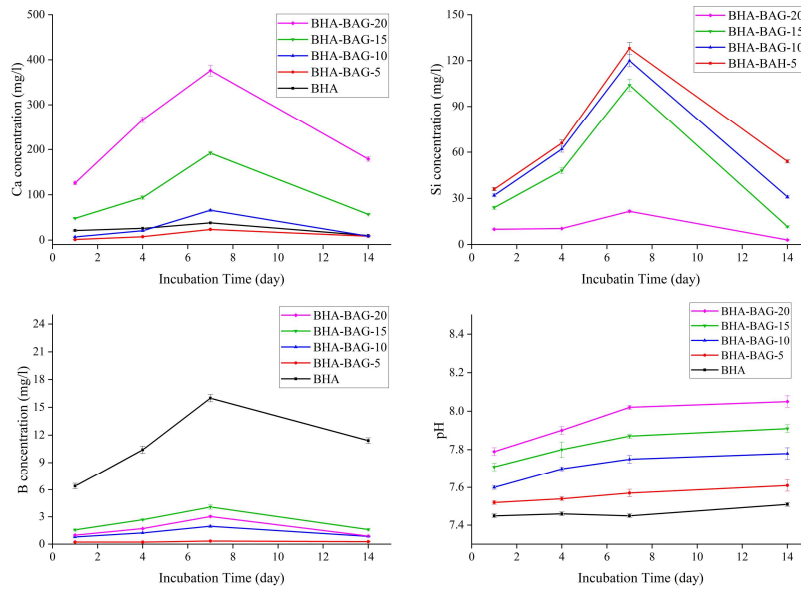


Figure 3.34. Ion release profiles of Ca, Si, and B; pH of SBF filtrate during bioactivity test.

The biodegradability was measured by the weight loss percentage of scaffolds (Figure 3.35) incubated in acetic acid and sodium acetate buffer solution (AcOH-AcONa, pH=5.5), which resembles the pH of the defected area and osteoclastic resorption of bone (Arnett, 2008; Ito et al., 2006). My results show that the degradation increased at each time point in all groups throughout the test period. However, the degradation percentage of BHA-BAG composite scaffolds was higher than BHA samples, and a faster rate of weight loss was observed after the first week of incubation, especially in BHA-BAG groups.

Almost throughout all those weeks, there were significant differences between scaffolds with BAG and those without BAG, and the differences increased as a function of BAG content in composite samples (Figure 3.35). My findings conformed to previous studies, which also reported higher degradability in the company of BAG (Abbasian et al., 2020). The biodegradation rate of my BHA-BAG samples after 28 days was somewhere about 20 %, which was higher than the 10 % of the study by Roohani et al. (Roohani-Esfahani et al., 2012) and less than 51 % of Sadeghzadeh et al. (Sadeghzade et al., 2019).

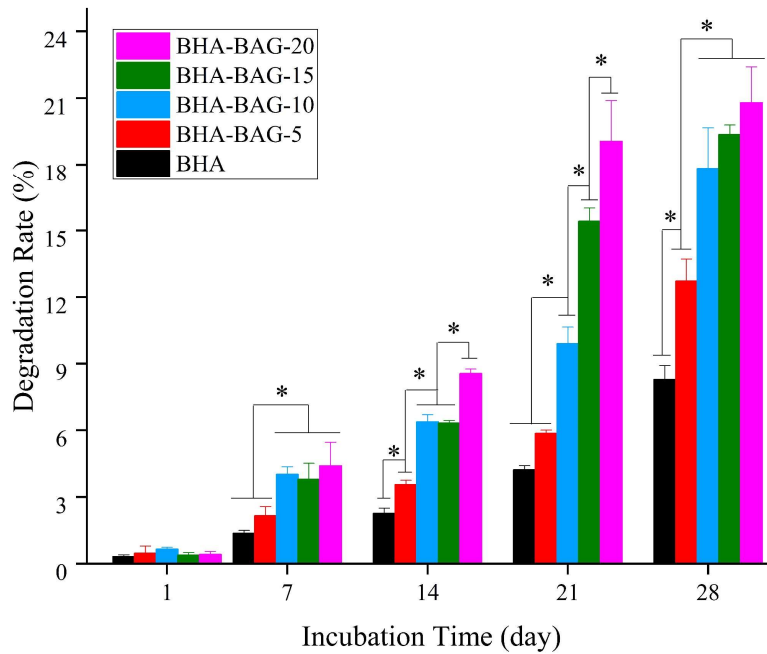


Figure 3.35. Biodegradation rate (n=3) of scaffolds throughout 4 weeks of incubation. The asterisk mark indicates a significant difference between groups.

A low degradation rate has been introduced as one of the major disadvantages of HA-based scaffolds, but the higher dissolution rate of CaSi-based ceramics like BAG contributed to improving this feature in composite BHA-BAG scaffolds. Furthermore, the more porous structure of composite samples could also be named as a structural factor that caused higher solubility in those samples. Herein, BHA-BAG composites underwent nearly 20 wt.% biodegradation during 28 days, where the rate of weight loss was in the perfect range in terms of timing between degradation rate and strengthening of newly formed bones (Chandra and Pandey, 2020), which plays a pivotal role in transferring loads from the implanted scaffold to newly formed bone tissues to inhibit failure of implants during in vivo and clinical applications (Jodati et al., 2020b). Moreover, higher degradations of BHA-BAG composites led to having sufficient influential ions (e.g. Ca^{2+} and SiO_4^{4-}) and therefore higher bioactivity (Najafinezhad et al., 2017).

3.3.4 Cell culture studies of scaffolds

The viability of hFOB cells that were cultured on BHA and BHA-BAG scaffolds was evaluated with AlamarBlue assay at each time point of incubation (Rampersad, 2012). Based on the knowledge that BHA is biocompatible with no negative cytotoxic effect on cells (Atila et al., 2019; Ciftci et al., 2015; Pazarçeviren et al., 2021; Tunçay et al., 2017), especially our previous study (Jodati et al., 2022a), cell viability on BHA scaffolds was considered as 100 % at each time point, where it was used as a reference point to monitor the BAG effects on composite scaffolds.

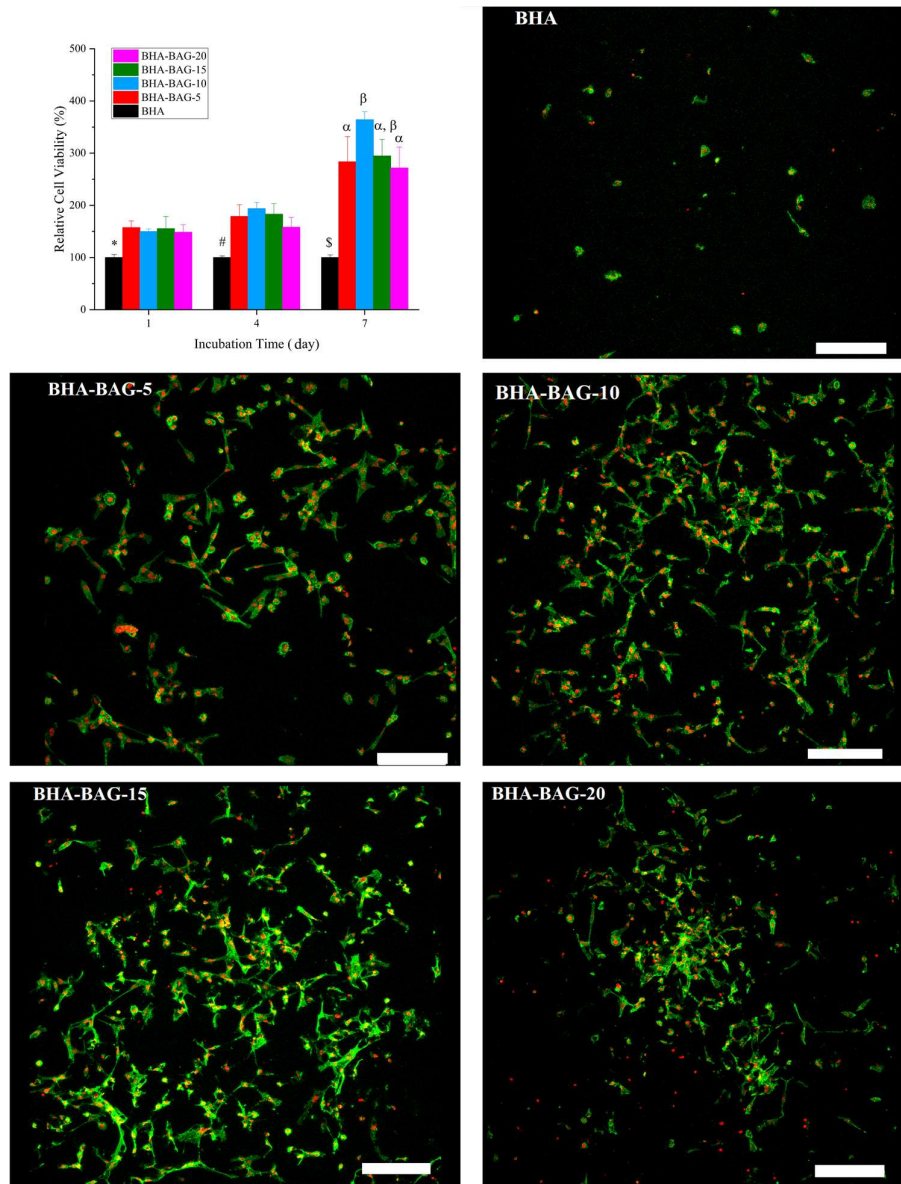


Figure 3.36. Relative cell viability histogram of composite BHA-BAG scaffolds with respect to BHA (100%) at each time point of incubation (n=4), and laser scanning confocal microscopy analysis of hFOB cells on scaffolds after 7 days of incubation. The (*), (#), (\$), (α), and (β) marks on bar histograms indicate significant differences ($p \leq 0.05$) between groups. The groups with the same marks are not different statistically. Green and red colors on the confocal images are representing F-actin filaments and nuclei of cells, respectively; and the scale bars are 400 μm .

The results in Figure 3.36 demonstrated a remarkable enhancement in the viability and proliferation of cells seeded on BHA-BAG scaffolds in comparison to BHA, especially after 7 days. Confocal imaging observations were in excellent agreement with cell viability results. The confocal microscopy images visualized the configuration of hFOB cells on scaffolds on day 7, where the higher cell density with an interacted network of cells was observed in BHA-BAG scaffolds. The larger number of cells, which were highly extended on surfaces and interacted with neighbor cells to a great degree, approves biocompatibility of BHA-BAG composite scaffolds, and their superior proliferation potential over BHA scaffolds with a lesser number of cells that were not well interacted with each other.

The reasons for different cell proliferation results have roots in either structural or chemical features of scaffolds. concerning the physical structures of BHA-BAG samples, they had higher porosity with larger surface area and micropore volumes than BHA samples (Table 3.7), which facilitates cell accommodation, attachment, and migration (Jodati et al., 2020c). Furthermore, higher protein adsorptions were reported in samples with higher SSA and micropores as another influential factor in cell proliferation and differentiation (Zhu et al., 2009). Improved spreading of hFOB cells on the surface of BHA-BAG scaffolds, especially BHA-BAG-5, BHA-BAG-10, and BHA-BAG-15 was detected in SEM images (Figure 3.37).

It is obvious that hFOB cells attached and spread during 7 days of incubation and they had both flattened and even elongated morphologies with characteristic filopodia-like processes to migrate and interact with other cells in composite scaffolds (Pham et al., 2019). hFOB cells failed to spread and form a highly organized cytoskeleton with stress fibers, which is a requirement for cell adhesion, on the weaker adhesive surface of BHA, compared to BHA-BAG scaffolds (Badley et al., 1980; Ramaswamy et al., 2008). Cell attachment and spreading were introduced as effective items in the elevated proliferation of cells, reported in other studies as results of BAG incorporation (Abbasian et al., 2020; Arefpour et al., 2019b; Bakhsheshi-Rad et al., 2017; Samani et al., 2019).

Observation of more particles with Ca/P apatite nature in BHA-BAG composite scaffolds surface (Figure 3.37) implies that higher apatite deposition on BHA-BAG scaffolds is another physicochemical reason for enhanced adhesion and proliferation of cells on BHA-BAG scaffolds (Morejón-Alonso et al., 2012). Moreover, as I discussed in BHA samples, the smaller grain size of the BAG component increases cell proliferation in composite scaffolds. In fact, smaller grain sizes lead to higher surface area and therefore higher surface energy. Surfaces with higher energies contribute to higher adsorption of cell adhesive proteins and better cell-surface interaction. This better interaction shows its effect in promoting cell proliferation and faster osteogenic differentiation (Dasgupta et al., 2013).

Regarding chemical aspects, similar to its effect on skeletal development (Soundrapandian et al., 2010), Si ion (silicate) release was playing a key role in the higher proliferation rate of BHA-BAG composites, especially in BHA-BAG-5, BHA-BAG-10, and BHA-BAG-15 groups with higher release values (Figure 3.34). Formation of the negatively charged Si-OH group (silanol) caused to the better spreading of hFOB cells on composite scaffolds by obtaining active binding sites for proteins to attach and resultant enhanced proliferation (Sadeghzade et al., 2020).

Furthermore, presence of Zr might be influential in the proliferation of BAG-containing scaffolds (Roohani-Esfahani et al., 2012). Herein, the Zr was not detected in the ion release test due to a lower concentration than 3 $\mu\text{g/l}$ and the sensitivity of our device, but it existed on the surface of composite scaffolds due to ICP-MS (Table 3.5) and EDX tests. Similarly, despite detecting no Zr element in culture media of ceramics, Ramaswamy et. al (Ramaswamy et al., 2008) documented higher cell proliferation in $\text{Ca}_3\text{ZrSi}_2\text{O}_9$ (BAG) than CaSiO_3 , which had all essential elements like Ca and Si, but Zr. The role of Zr could be explained through its effect on surface roughness or the chemical stability of BAG, which leads to adjusting other ions' release rate (e.g. Si), available in BAG composition (X. Zhang et al., 2014).

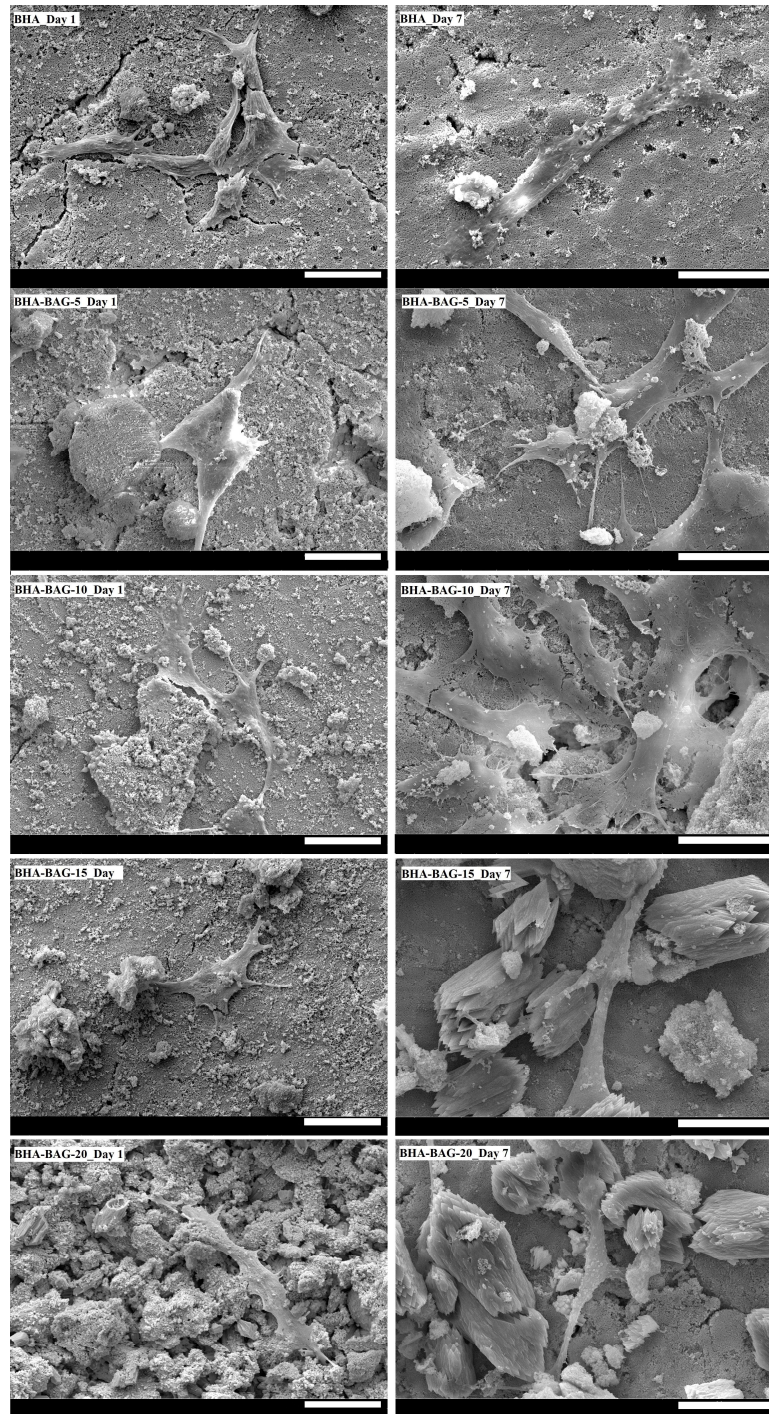


Figure 3.37. SEM images of the morphology of hFOB cells on scaffolds after 1 and 7 days of incubation at 37 °C. The scale bar is 20 μm length.

The osteogenic effect of the composite scaffolds on the differentiation of hFOB cells was measured with ALP activity and intracellular Ca^{2+} deposition amount, as depicted in Figure 3.38. There was no significant difference between groups in terms of osteogenic differentiation after 1 week of incubation. Regarding intracellular Ca^{2+} , a statistical difference was not also observed between samples in spite of apparent greater calcium deposition amounts in composite groups. However, similar to a study by Karimi et al. (Karimi et al., 2019), ALP activity levels elevated during the second week of incubation, where higher levels of osteogenic differentiation were observed in BHA-BAG-15 and BHA-BAG-20 composite groups than others (Figure 3.38). The intracellular calcium deposition as a late marker of osteogenic differentiation increased with the same trend as ALP.

My findings are in good agreement with previous studies that addressed the release of Ca and Si ions as a reason for the enhanced osteoinductive effect of BAG-containing scaffolds (Arefpour et al., 2019a; Farnoosh Pahlevanzadeh et al., 2018; X. Zhang et al., 2014). Herein, Ca release from BHA-BAG-15 and BHA-BAG-20 groups was higher than other groups (Figure 3.34), which influenced ALP activity, and mineralization of the extracellular matrix (ECM) of cells on these scaffolds. Even the BHA-BAG-20 groups with the greatest Ca ion release amount demonstrated the highest levels of ALP and calcium deposition (Figure 3.38). On the other hand, the lower levels of Si ion releases in BHA-BAG-15 and BHA-BAG-20 groups simulated osteogenic differentiation of cells, which is in good agreement with Ramaswamy et al. (Ramaswamy et al., 2008) that stated ion releases must also be in an appropriate range.

The presence of Zr in the structure of composite scaffolds could influence their roughness (X. Zhang et al., 2014), which is also an effective feature in the cellular response (Anselme et al., 2000). Thus, enhanced proliferation and osteogenic differentiations of hFOB on BHA-BAG-15 and BHA-BAG-20 scaffolds could also be attributed to their rougher surface compared to other groups (Figure 3.37).

My previous study (Jodati et al., 2022a), as well as a study by Gizer (Gizer et al., 2020), demonstrated that the B ion behavior is dose-dependent and higher rates decrease the osteogenic activity of cells. Based on them, I believe that the higher B ion dissolution rate in BHA inhibited its osteoinductive aspect. However, making composite scaffolds restricted B ion release to beneficial ranges in BHA-BAG-15 and BHA-BAG 20 scaffolds. Eventually, it can be summarized that BAG presence and consequent changes in scaffolds and their microenvironment induced RUNX2 gene expressions, which translated as bone morphologic proteins (BMPs) that resulted in enhanced osteogenic differentiation of hFOB cells (Karimi et al., 2019; Lu et al., 2014).

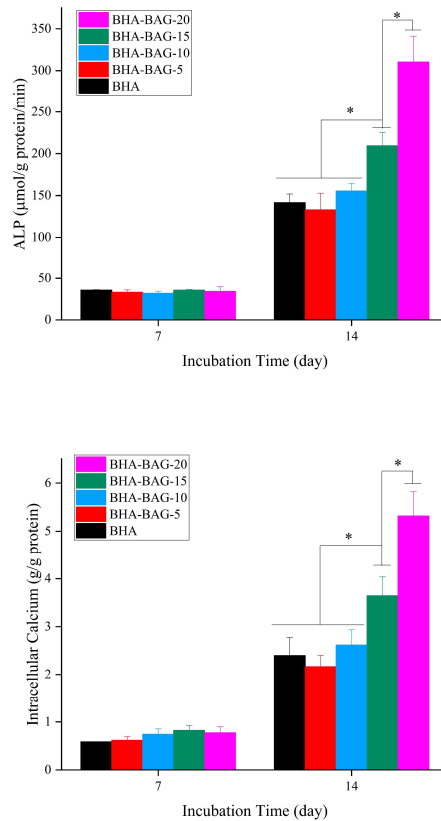


Figure 3.38. ALP activity and intracellular Ca²⁺ deposition of hFOB cells seeded on scaffolds after 7 and 14 days of incubation at 37 °C. The Asterisk mark indicates significant differences between groups.

CHAPTER 4

CONCLUSION

In this thesis, boron-doped hydroxyapatite and baghdadite bioceramic composite (BHA-BAG) was introduced as novel chemical composition to fabricate 3D porous scaffolds for the first time. Aim of this thesis was to improve scaffold properties and performance in terms of bone tissue engineering applications, which was accomplished in the steps as follows.

First, the BHA powders with four different molar ratios of dopant B were synthesized, characterized, and compared with HA. After evaluation of the B dosage effect on various properties of HA, the group with the lowest amount of B (referred to as 0.05BHA) was selected as the optimum group because of higher bioactivity and promoted cell proliferation, as well as no adverse effect on osteogenic activity and mechanical properties of HA. Moreover, this was the first time in literature that the effects of concentration of doping B on various properties of HA have been evaluated comprehensively concerning its applications in bone defect treatment.

Second, BAG bioceramic was synthesized and optimized through a modified sol-gel method, proposed for the first time in the literature, where the problem with premature gelation of sol before the complete dissolution of precursor salts was solved, and BAG nanoparticles with very slight impurities were synthesized. The following characterizations of BAG demonstrated that it possesses no cytotoxic effect on cells and has osteoinductive features as well as admissible mechanical and biological properties, such as bioactivity and biodegradability for being used in BTE.

Third, BHA and BAG powders were used to produce novel 3D porous composite scaffolds to benefit from the advantages of both components. The results of physicochemical investigations show that the porosity, specific surface area, and micropore volumes of composite scaffolds increased, compared to BHA ones.

Besides higher bioactivity, the incorporation of BAG with BHA contributed to having a higher degradation rate, which not only solves the low biodegradability of BHA but also I hope it prevents implant failure during further in vivo or clinical uses because of matched degradation rate with the rate of new bone formation. Moreover, the cultured cells demonstrated higher proliferation and osteogenic differentiation in composite scaffolds, compared to BHA. Although mechanical properties decreased slightly in composite scaffolds, BHA served as the base for BAG to possess mechanical strength in the range of spongy bone. Moreover, these BHA-BAG scaffolds were stronger in terms of compressive strength than all composite scaffolds made by incorporation of BAG except in two studies. In conclusion, fabricated BHA-BAG composite scaffolds, especially the one with 15 wt.% of BAG, brought the benefits of both components together and could be considered in BTE applications as a novel composition with promoted properties.

REFERENCES

- Abbasian, V., Emadi, R., Kharaziha, M., 2020. Biomimetic nylon 6-baghdadite nanocomposite scaffold for bone tissue engineering. *Mater. Sci. Eng. C* 109, 110549. <https://doi.org/10.1016/j.msec.2019.110549>
- Abdelnour, S.A., Abd El-Hack, M.E., Swelum, A.A., Perillo, A., Losacco, C., 2018. The vital roles of boron in animal health and production: A comprehensive review. *J. Trace Elem. Med. Biol.* 50, 296–304. <https://doi.org/10.1016/j.jtemb.2018.07.018>
- Aguirre, T.G., Cramer, C.L., Torres, V.P., Hammann, T.J., Holland, T.B., Ma, K., 2019. Effects of the addition of boron nitride nanoplate on the fracture toughness, flexural strength, and Weibull distribution of hydroxyapatite composites prepared by spark plasma sintering. *J. Mech. Behav. Biomed. Mater.* 93, 105–117. <https://doi.org/10.1016/J.JMBBM.2019.01.021>
- Ahmad, M.K., Rusop, M., 2009. Influence of glacial acetic acid and nitric acid as a chelating agent in sol-gel process to the nanostructured titanium dioxide thin films. *AIP Conf. Proc.* 1136, 339. <https://doi.org/10.1063/1.3160160>
- Al-Hermezi, H.M., McKie, D., Hall, A.J., 1986. Baghdadite, a new calcium zirconium silicate mineral from Iraq. *Mineral. Mag.* 50, 119–123. <https://doi.org/10.1180/minmag.1986.050.355.15>
- Albayrak, O., 2016. Structural and mechanical characterization of boron doped biphasic calcium phosphate produced by wet chemical method and subsequent thermal treatment. *Mater. Charact.* 113, 82–89. <https://doi.org/10.1016/J.MATCHAR.2016.01.006>
- Albrektsson, T., Johansson, C., 2001. Osteoinduction, osteoconduction and osseointegration. *J. Eur. Spine* 10, 96–101. <https://doi.org/DOI 10.1007/s005860100282>

- Aldaadaa, A., Al Qaysi, M., Georgiou, G., MA Leeson, R., Knowles, J.C., 2018. Physical properties and biocompatibility effects of doping SiO₂ and TiO₂ into phosphate-based glass for bone tissue engineering. *J. Biomater. Appl.* 33, 271–280. <https://doi.org/10.1177/0885328218788832>
- Alhilou, A., Do, T., Mizban, L., Clarkson, B.H., Wood, D.J., Katsikogianni, M.G., 2016. Physicochemical and antibacterial characterization of a novel fluorapatite coating. *ACS Omega* 1, 264–276. https://doi.org/10.1021/ACSOMEGA.6B00080/SUPPL_FILE/AO6B00080_SI_001.PDF
- Ali, M.S., Mohamed Ariff, A.H., Jaafar, C.N.A., Tahir, S.M., Mazlan, N., Maori, K.A., Naser, H., 2017. Factors affecting the porosity and mechanical properties of porous ceramic composite materials. *Ref. Modul. Mater. Sci. Mater. Eng.* 1–54. <https://doi.org/10.1016/B978-0-12-803581-8.10131-6>
- Alshemary, A.Z., Akram, M., Goh, Y.-F., Tariq, U., Butt, F.K., Abdolahi, A., Hussain, R., 2015. Synthesis, characterization, in vitro bioactivity and antimicrobial activity of magnesium and nickel doped silicate hydroxyapatite. *Ceram. Int.* 41, 11886–11898. <https://doi.org/10.1016/J.CERAMINT.2015.06.003>
- Alshemary, A.Z., Goh, Y.-F., Akram, M., Razali, I.R., Abdul Kadir, M.R., Hussain, R., 2013. Microwave assisted synthesis of nano sized sulphate doped hydroxyapatite. *Mater. Res. Bull.* 48, 2106–2110. <https://doi.org/10.1016/J.MATERRESBULL.2013.02.015>
- Alshemary, A.Z., Pazarçeviren, A.E., Keskin, D., Tezcaner, A., Hussain, R., Evis, Z., 2019a. Porous clinoptilolite-nano biphasic calcium phosphate scaffolds loaded with human dental pulp stem cells for load bearing orthopedic applications. *Biomed. Mater.* 14, 055010. <https://doi.org/10.1088/1748-605X/AB3714>
- Alshemary, A.Z., Pazarceviren, A.E., Tezcaner, A., Evis, Z., 2018. Fe³⁺/SeO₄²⁻

- dual doped nano hydroxyapatite: A novel material for biomedical applications. *J. Biomed. Mater. Res. - Part B Appl. Biomater.* 106, 340–352. <https://doi.org/10.1002/jbm.b.33838>
- Alshemary, A.Z., Pazarceviren, A.E., Tezcaner, A., Evis, Z., 2016. Mesoporous strontium doped nano sized sulphate hydroxyapatite as a novel biomaterial for bone tissue applications. *RSC Adv.* 6, 68058–68071. <https://doi.org/10.1039/c6ra16809d>
- Alshemary, A.Z., Pazarçeviren, E.A., Dalgic, A.D., Tezcaner, A., Keskin, D., Evis, Z., 2019b. Nanocrystalline Zn²⁺ and SO₄²⁻ binary doped fluorohydroxyapatite: A novel biomaterial with enhanced osteoconductive and osteoinconductive properties. *Mater. Sci. Eng. C* 104, 109884. <https://doi.org/10.1016/j.msec.2019.109884>
- Alvarez-Urena, P., Kim, J., Bhattacharyya, S., Ducheyne, P., 2017. Bioactive ceramics and bioactive ceramic composite based scaffolds, *Comprehensive Biomaterials II*. Elsevier Ltd. <https://doi.org/10.1016/b978-0-12-803581-8.10136-5>
- Alzahrani, J.S., Midala, I.H., Kamari, H.M., Al-Hada, N.M., Tim, C.K., Nidzam, N.N.S., Alrowaili, Z.A., Al-Buriahi, M.S., 2022. Effect of calcination temperature on the structural and optical properties of (ZnO)_{0.8} (ZrO₂)_{0.2} nanoparticles. *J. Inorg. Organomet. Polym. Mater.* 32, 1755–1765. <https://doi.org/10.1007/S10904-022-02238-8/FIGURES/9>
- Amini, A.R., Laurencin, C.T., Nukavarapu, S.P., 2012. Bone tissue engineering: recent advances and challenges. *Crit. Rev. Biomed. Eng.* 40, 363–408. <https://doi.org/10.1615/critrevbiomedeng.v40.i5.10>
- Aminian, A., Solati-Hashjin, M., Samadikuchaksaraei, A., Bakhshi, F., Gorjipour, F., Farzadi, A., Moztarzadeh, F., Schmücker, M., 2011. Synthesis of silicon-substituted hydroxyapatite by a hydrothermal method with two different phosphorous sources. *Ceram. Int.* 37, 1219–1229.

<https://doi.org/10.1016/j.ceramint.2010.11.044>

- Anselme, K., Linez, P., Bigerelle, M., Le Maguer, D., Le Maguer, A., Hardouin, P., Hildebrand, H.F., Iost, A., Leroy, J.M., 2000. The relative influence of the topography and chemistry of TiAl6V4 surfaces on osteoblastic cell behaviour. *Biomaterials* 21, 1567–1577. [https://doi.org/10.1016/S0142-9612\(00\)00042-9](https://doi.org/10.1016/S0142-9612(00)00042-9)
- Arefpour, A., Kasiri-Asgarani, M., Monshi, A., Doostmohammadi, A., Karbasi, S., 2019a. Fabrication, characterization and examination of in vitro of baghdadite nanoparticles for biomedical applications. *Mater. Res. Express* 6, 1–13. <https://doi.org/10.1088/2053-1591/ab318c>
- Arefpour, A., Kasiri-Asgarani, M., Monshi, A., Karbasi, S., Doostmohammadi, A., 2019b. Baghdadite/Polycaprolactone nanocomposite scaffolds: preparation, characterisation, and in vitro biological responses of human osteoblast-like cells (Saos-2 cell line). *Mater. Technol.* 35, 411–432. <https://doi.org/10.1080/10667857.2019.1692161>
- Arnett, T.R., 2008. Extracellular pH regulates bone cell function. *J. Nutr.* 138, 415–418. <https://doi.org/10.1093/jn/138.2.415s>
- Arslan, A., Çakmak, S., Gümüşderelioğlu, M., 2018. Enhanced osteogenic activity with boron-doped nanohydroxyapatite-loaded poly(butylene adipate-co-terephthalate) fibrous 3D matrix. *Artif. Cells, Nanomedicine Biotechnol.* 46, 790–799. <https://doi.org/10.1080/21691401.2018.1470522>
- Arya, S., Mahajan, P., Mahajan, S., Khosla, A., Datt, R., Gupta, V., Young, S.-J., Oruganti, S.K., 2021. Review—Influence of processing parameters to control morphology and optical properties of sol-gel synthesized ZnO nanoparticles. *ECS J. Solid State Sci. Technol.* 10, 023002. <https://doi.org/10.1149/2162-8777/ABE095>
- ASTM International, 2017. E384 -17 Standard Test Method for Microindentation Hardness of Materials 1–40. <https://doi.org/10.1520/E0384-17>

- Atila, D., Karataş, A., Evcin, A., Keskin, D., Tezcaner, A., 2019. Bacterial cellulose-reinforced boron-doped hydroxyapatite/gelatin scaffolds for bone tissue engineering. *Cellulose* 26, 9765–9785. <https://doi.org/10.1007/s10570-019-02741-1>
- Averardi, A., Cola, C., Zeltmann, S.E., Gupta, N., 2020. Effect of particle size distribution on the packing of powder beds: A critical discussion relevant to additive manufacturing. *Mater. Today Commun.* 24, 100964. <https://doi.org/10.1016/J.MTCOMM.2020.100964>
- Badley, R.A., Woods, A., Carruthers, L., Rees, D.A., 1980. Cytoskeleton changes in fibroblast adhesion and detachment. *J. Cell Sci.* 43, 379–390. <https://doi.org/10.1242/JCS.43.1.379>
- Baino, F., Novajra, G., Vitale-Brovarone, C., 2015. Bioceramics and scaffolds: A winning combination for tissue engineering. *Front. Bioeng. Biotechnol.* 3, 1–17. <https://doi.org/10.3389/fbioe.2015.00202>
- Bakhsheshi-Rad, H.R., Hamzah, E., Ismail, A.F., Aziz, M., Hadisi, Z., Kashefian, M., Najafinezhad, A., 2017. Novel nanostructured baghdadite-vancomycin scaffolds: In-vitro drug release, antibacterial activity and biocompatibility. *Mater. Lett.* 209, 369–372. <https://doi.org/10.1016/J.MATLET.2017.08.027>
- Balasubramanian, P., Büttner, T., Miguez Pacheco, V., Boccaccini, A.R., 2018. Boron-containing bioactive glasses in bone and soft tissue engineering. *J. Eur. Ceram. Soc.* 38, 855–869. <https://doi.org/10.1016/j.jeurceramsoc.2017.11.001>
- Balasubramanian, P., Grünewald, A., Detsch, R., Hupa, L., Jokic, B., Tallia, F., Solanki, A.K., Jones, J.R., Boccaccini, A.R., 2016. Ion release, hydroxyapatite conversion, and cytotoxicity of boron-containing bioactive glass scaffolds. *Int. J. Appl. Glas. Sci.* 7, 206–215. <https://doi.org/10.1111/ijag.12206>
- Barheine, S., Hayakawa, S., Jäger, C., Shirotsaki, Y., Osaka, A., 2011. Effect of disordered structure of boron-containing calcium phosphates on their in vitro biodegradability. *J. Am. Ceram. Soc.* 94, 2656–2662.

<https://doi.org/10.1111/j.1551-2916.2011.04400.x>

- Barheine, S., Hayakawa, S., Osaka, A., Jaeger, C., 2009. Surface, interface, and bulk structure of borate containing apatitic biomaterials. *Chem. Mater.* 21, 3102–3109. <https://doi.org/10.1021/cm900204q>
- Barradas, A.M.C., Yuan, H., Van Blitterswijk, C.A., Habibovic, P., 2011. Osteoinductive biomaterials: current knowledge of properties, experimental models and biological mechanisms. *Eur. Cells Mater.* 21, 407–429. <https://doi.org/10.22203/ecm.v021a31>
- Basar, B., Tezcaner, A., Keskin, D., Evis, Z., 2010. Improvements in microstructural, mechanical, and biocompatibility properties of nano-sized hydroxyapatites doped with yttrium and fluoride. *Ceram. Int.* 36, 1633–1643. <https://doi.org/10.1016/J.CERAMINT.2010.02.033>
- Basu, D., Banerjee, A.N., 1994. Dynamic mechanical thermal analysis - crystallinity and tensile-strength of PBT/ABS blends: their interdependency and variations with ABS content. *Indian J. Chem. Technol.* 1, 31–34.
- Baumhauer, J., Pinzur, M.S., Donahue, R., Beasley, W., DiGiovanni, C., 2014. Site selection and pain outcome after autologous bone graft harvest. *Foot Ankle Int.* 35, 104–107. <https://doi.org/10.1177/1071100713511434>
- Berthiaume, F., Maguire, T.J., Yarmush, M.L., 2011. Tissue engineering and regenerative medicine: History, progress, and challenges. *Annu. Rev. Chem. Biomol. Eng.* 2, 403–430. <https://doi.org/10.1146/annurev-chembioeng-061010-114257>
- Bhattacharjee, P., Kundu, B., Naskar, D., Kim, H.-W., Maiti, T.K., Bhattacharya, D., Kundu, S.C., 2017. Silk scaffolds in bone tissue engineering: An overview. *Acta Biomater.* 63, 1–17. <https://doi.org/10.1016/J.ACTBIO.2017.09.027>
- Biagioni, C., Bonaccorsi, E., Perchiazzi, N., Merlino, S., 2010. Single crystal refinement of the structure of baghdadite from Fuka (Okayama Prefecture,

- Japan). *Period. di Mineral.* 79, 1–9. <https://doi.org/10.2451/2010PM0013>
- Blair, H.C., Sun, L., Kohanski, R.A., 2007. Balanced regulation of proliferation, growth, differentiation, and degradation in Skeletal Cells. *Ann. N. Y. Acad. Sci.* 1116, 165–173. <https://doi.org/10.1196/annals.1402.029>
- Blokhuis, T.J., 2013. Autograft versus BMPs for the treatment of non-unions: What is the evidence? *Injury* 44, S40–S42. [https://doi.org/10.1016/S0020-1383\(13\)70009-3](https://doi.org/10.1016/S0020-1383(13)70009-3)
- Bohner, M., Galea, L., Doebelin, N., 2012. Calcium phosphate bone graft substitutes: Failures and hopes. *J. Eur. Ceram. Soc.* 32, 2663–2671. <https://doi.org/10.1016/j.jeurceramsoc.2012.02.028>
- Bohner, M., Santoni, B.L.G., Döbelin, N., 2020. β -tricalcium phosphate for bone substitution: Synthesis and properties. *Acta Biomater.* 113, 23–41. <https://doi.org/10.1016/J.ACTBIO.2020.06.022>
- Boivin, G., Bala, Y., Doublier, A., Farlay, D., Ste-Marie, L.G., Meunier, P.J., Delmas, P.D., 2008. The role of mineralization and organic matrix in the microhardness of bone tissue from controls and osteoporotic patients. *Bone* 43, 532–538. <https://doi.org/10.1016/j.bone.2008.05.024>
- Bonfield, W., 2006. Designing porous scaffolds for tissue engineering. *Philos. Trans. R. Soc. A Math. Phys. Eng. Sci.* 364, 227–232. <https://doi.org/10.1098/rsta.2005.1692>
- Bonfield, W., Gibson, I.R., 2002. Novel synthesis and characterization of an AB-type carbonate-substituted hydroxyapatite. *J. Biomed. Mater. Res.* 59, 697–708. <https://doi.org/10.1002/jbm.10044>
- Bose, S., Ke, D., Sahasrabudhe, H., Bandyopadhyay, A., 2018. Additive manufacturing of biomaterials. *Prog. Mater. Sci.* 93, 45–111. <https://doi.org/10.1016/j.pmatsci.2017.08.003>
- Bouet, G., Marchat, D., Cruel, M., Malaval, L., Vico, L., 2015. In vitro three-

dimensional bone tissue models: from cells to controlled and dynamic environment. *Tissue Eng. Part B. Rev.* 21, 133–56. <https://doi.org/10.1089/ten.TEB.2013.0682>

Bretcanu, O., Baino, F., Verné, E., Vitale-Brovarone, C., 2014. Novel resorbable glass-ceramic scaffolds for hard tissue engineering: From the parent phosphate glass to its bone-like macroporous derivatives. *J. Biomater. Appl.* 28, 1287–1303. <https://doi.org/10.1177/0885328213506759>

Brown, X.Q., Ookawa, K., Wong, J.Y., 2005. Evaluation of polydimethylsiloxane scaffolds with physiologically-relevant elastic moduli: interplay of substrate mechanics and surface chemistry effects on vascular smooth muscle cell response. *Biomaterials* 26, 3123–3129. <https://doi.org/10.1016/J.BIOMATERIALS.2004.08.009>

Campana, V., Milano, G., Pagano, E., Barba, M., Cicione, C., Salonna, G., Lattanzi, W., Logroscino, G., 2014. Bone substitutes in orthopaedic surgery: from basic science to clinical practice. *J. Mater. Sci. Mater. Med.* 25, 2445–2461. <https://doi.org/10.1007/s10856-014-5240-2>

Capati, M.L.F., Nakazono, A., Igawa, K., Ookubo, K., Yamamoto, Y., Yanagiguchi, K., Kubo, S., Yamada, S., Hayashi, Y., 2016. Boron accelerates cultured osteoblastic cell activity through calcium flux. *Biol. Trace Elem. Res.* 174, 300–308. <https://doi.org/10.1007/s12011-016-0719-y>

Casillas, R., Nagy, G., Demény, A., Ahijado, A., Fernández, C., 2008. Cuspidine-niocalite-baghdadite solid solutions in the metacarbonatites of the basal complex of fuerteventura (Canary Islands). *Lithos* 105, 25–41. <https://doi.org/10.1016/j.lithos.2008.02.003>

Chandra, G., Pandey, A., 2020. Biodegradable bone implants in orthopedic applications: a review. *Biocybern. Biomed. Eng.* 40, 596–610. <https://doi.org/10.1016/j.bbe.2020.02.003>

Chen, P.-Y., Lin, A.Y.M., Lin, Y.-S., Seki, Y., Stokes, A.G., Peyras, J., Olevsky,

- E.A., Meyers, M.A., McKittrick, J., 2008. Structure and mechanical properties of selected biological materials. *J. Mech. Behav. Biomed. Mater.* 1, 208–226. <https://doi.org/10.1016/J.JMBBM.2008.02.003>
- Chen, Q., Miyaji, F., Kokubo, T., Nakamura, T., 1999. Apatite formation on PDMS-modified CaO-SiO₂-TiO₂ hybrids prepared by sol-gel process. *Biomaterials* 20, 1127–1132. [https://doi.org/10.1016/S0142-9612\(99\)00015-0](https://doi.org/10.1016/S0142-9612(99)00015-0)
- Chen, X., Yu, J., Guo, S., Lu, S., Luo, Z., He, M., 2009. Surface modification of magnesium hydroxide and its application in flame retardant polypropylene composites. *J. Mater. Sci.* 44, 1324–1332. <https://doi.org/10.1007/S10853-009-3273-6/FIGURES/11>
- Chen, Y., Frith, J.E., Dehghan-Manshadi, A., Attar, H., Kent, D., Soro, N.D.M., Bermingham, M.J., Dargusch, M.S., 2017. Mechanical properties and biocompatibility of porous titanium scaffolds for bone tissue engineering. *J. Mech. Behav. Biomed. Mater.* 75, 169–174. <https://doi.org/10.1016/J.JMBBM.2017.07.015>
- Chen, Z., Liu, Y., Mao, L., Gong, L., Sun, W., Feng, L., 2018. Effect of cation doping on the structure of hydroxyapatite and the mechanism of defluoridation. *Ceram. Int.* 44, 6002–6009. <https://doi.org/10.1016/J.CERAMINT.2017.12.191>
- Ciftci, E., Köse, S., Korkusuz, P., Timuçin, M., Korkusuz, F., 2015. Boron containing nano hydroxyapatites (B-n-HAp) stimulate mesenchymal stem cell adhesion, proliferation and differentiation. *Key Eng. Mater.* 631, 373–378. <https://doi.org/10.4028/WWW.SCIENTIFIC.NET/KEM.631.373>
- Coldrey, J.M., Purton, M.J., 2007. Application of thermal analysis in investigations on calcium silicate bricks. *J. Appl. Chem.* 18, 353–360. <https://doi.org/10.1002/jctb.5010181203>
- Cooper, D.M.L., Kawalilak, C.E., Harrison, K., Johnston, B.D., Johnston, J.D., 2016. Cortical bone porosity: What is it, why is it important, and how can we detect it? *Curr. Osteoporos. Rep.* 14, 187–198. <https://doi.org/10.1007/s11914-016->

0319-y

- Cooper, D.M.L., Matyas, J.R., Katzenberg, M.A., Hallgrimsson, B., 2004. Comparison of microcomputed tomographic and microradiographic measurements of cortical bone porosity. *Calcif. Tissue Int.* 74, 437–447. <https://doi.org/10.1007/s00223-003-0071-z>
- Corcione, C.E., Gervaso, F., Scalera, F., Montagna, F., Maiullaro, T., Sannino, A., Maffezzoli, A., 2017. 3D printing of hydroxyapatite polymer-based composites for bone tissue engineering. *J. Polym. Eng.* 37, 741–746. <https://doi.org/10.1515/polyeng-2016-0194>
- Crouzier, T., Sailhan, F., Becquart, P., Guillot, R., Logeart-Avramoglou, D., Picart, C., 2011. The performance of BMP-2 loaded TCP/HAP porous ceramics with a polyelectrolyte multilayer film coating. *Biomaterials* 32, 7543–7554. <https://doi.org/10.1016/J.BIOMATERIALS.2011.06.062>
- Darus, F., Isa, R.M., Mamat, N., Jaafar, M., 2018. Techniques for fabrication and construction of three-dimensional bioceramic scaffolds: Effect on pores Size, porosity and compressive Strength. *Ceram. Int.* 44, 18400–18407. <https://doi.org/10.1016/j.ceramint.2018.07.056>
- Dasgupta, S., Tarafder, S., Bandyopadhyay, A., Bose, S., 2013. Effect of grain size on mechanical, surface and biological properties of microwave sintered hydroxyapatite. *Mater. Sci. Eng. C* 33, 2846–2854. <https://doi.org/10.1016/J.MSEC.2013.03.004>
- De Aza, P.N., Fernández-Pradas, J.M., Serra, P., 2004. In vitro bioactivity of laser ablation pseudowollastonite coating. *Biomaterials* 25, 1983–1990. <https://doi.org/10.1016/j.biomaterials.2003.08.036>
- Deb, P., Deoghare, A.B., Borah, A., Barua, E., Lala, S. Das, 2018. Scaffold development using biomaterials: A review. *Mater. Today Proc.* 5, 12909–12919. <https://doi.org/10.1016/j.matpr.2018.02.276>

- Delloye, C., Cornu, O., Druetz, V., Barbier, O., 2007. Bone allografts. *J. Bone Joint Surg. Br.* 89-B, 574–580. <https://doi.org/10.1302/0301-620X.89B5.19039>
- Demirtaş, T.T., Kaynak, G., Gümüşderelioğlu, M., 2015. Bone-like hydroxyapatite precipitated from 10×SBF-like solution by microwave irradiation. *Mater. Sci. Eng. C* 49, 713–719. <https://doi.org/10.1016/j.msec.2015.01.057>
- Devirian, T.A., Volpe, S.L., 2003. The physiological effects of dietary boron. *Crit. Rev. Food Sci. Nutr.* 43, 219–231. <https://doi.org/10.1080/10408690390826491>
- Dewi, A.H., Ana, I.D., 2018. The use of hydroxyapatite bone substitute grafting for alveolar ridge preservation, sinus augmentation, and periodontal bone defect: A systematic review. *Heliyon* 4, e00884. <https://doi.org/10.1016/J.HELIYON.2018.E00884>
- Diba, M., Kharaziha, M., Fathi, M.H., Gholipourmalekabadi, M., Samadikuchaksaraei, A., 2012. Preparation and characterization of polycaprolactone/forsterite nanocomposite porous scaffolds designed for bone tissue regeneration. *Compos. Sci. Technol.* 72, 716–723. <https://doi.org/10.1016/J.COMPSCITECH.2012.01.023>
- Ding, H., Pan, H., Xu, X., Tang, R., 2014. Toward a detailed understanding of magnesium ions on hydroxyapatite crystallization inhibition. *Cryst. Growth Des.* 14, 763–769. https://doi.org/10.1021/CG401619S/SUPPL_FILE/CG401619S_SI_001.PDF
- Ding, S.J., Shie, M.Y., Wang, C.Y., 2009. Novel fast-setting calcium silicate bone cements with high bioactivity and enhanced osteogenesis in vitro. *J. Mater. Chem.* 19, 1183–1190. <https://doi.org/10.1039/B819033J>
- Doostmohammadi, A., Karimzadeh Esfahani, Z., Ardeshiryajimi, A., Rahmati Dehkordi, Z., 2019. Zirconium modified calcium-silicate-based nanoceramics: An in vivo evaluation in a rabbit tibial defect model. *Int. J. Appl. Ceram. Technol.* 16, 431–437. <https://doi.org/10.1111/ijac.13076>

- Dorozhkin, S. V., 2018. Calcium orthophosphate (CaPO₄) scaffolds for bone tissue engineering applications. *J. Biotechnol. Biomed. Sci.* 1, 25–93. <https://doi.org/10.14302/issn.2576-6694.jbbs-18-2143>
- Du, M., Chen, J., Liu, K., Xing, H., Song, C., 2021. Recent advances in biomedical engineering of nano-hydroxyapatite including dentistry, cancer treatment and bone repair. *Compos. Part B Eng.* 215, 108790. <https://doi.org/10.1016/J.COMPOSITESB.2021.108790>
- Eliaz, N., Metoki, N., 2017. Calcium phosphate bioceramics: A review of their history, structure, properties, coating technologies and biomedical applications. *Mater.* 10, 1–104. <https://doi.org/10.3390/ma10040334>
- Evis, Z., 2007. Reactions in hydroxylapatite–zirconia composites. *Ceram. Int.* 33, 987–991. <https://doi.org/10.1016/J.CERAMINT.2006.02.012>
- Evis, Z., Webster, T.J., 2013. Nanosize hydroxyapatite: doping with various ions. *Adv. Appl. Ceram.* 110, 311–320. <https://doi.org/10.1179/1743676110Y.0000000005>
- Evis, Z., Yilmaz, B., Usta, M., Levent Aktug, S., 2013. X-ray investigation of sintered cadmium doped hydroxyapatites. *Ceram. Int.* 39, 2359–2363. <https://doi.org/10.1016/J.CERAMINT.2012.08.087>
- Faour, O., Dimitriou, R., Cousins, C.A., Giannoudis, P. V., 2011. The use of bone graft substitutes in large cancellous voids: Any specific needs? *Injury* 42, S87–S90. <https://doi.org/10.1016/J.INJURY.2011.06.020>
- Farokhi, M., Mottaghitalab, F., Samani, S., Shokrgozar, M.A., Kundu, S.C., Reis, R.L., Fatahi, Y., Kaplan, D.L., 2018. Silk fibroin/hydroxyapatite composites for bone tissue engineering. *Biotechnol. Adv.* 36, 68–91. <https://doi.org/10.1016/J.BIOTECHADV.2017.10.001>
- Feng, P., Wei, P., Li, P., Gao, C., Shuai, C., Peng, S., 2014. Calcium silicate ceramic scaffolds toughened with hydroxyapatite whiskers for bone tissue engineering.

- Mater. Charact. 97, 47–56. <https://doi.org/10.1016/J.MATCHAR.2014.08.017>
- Feng, X., 2009. Chemical and biochemical basis of cell-bone matrix interaction in health and disease. *Curr. Chem. Biol.* 3, 189–196. <https://doi.org/10.2174/187231309788166398>
- Fernandez de Grado, G., Keller, L., Idoux-Gillet, Y., Wagner, Q., Musset, A.M., Benkirane-Jessel, N., Bornert, F., Offner, D., 2018. Bone substitutes: a review of their characteristics, clinical use, and perspectives for large bone defects management. *J. Tissue Eng.* 9, 1–18. <https://doi.org/10.1177/2041731418776819>
- Florencio-Silva, R., Sasso, G.R. da S., Sasso-Cerri, E., Simões, M.J., Cerri, P.S., 2015. Biology of bone tissue: structure, function, and factors that influence bone cells. *Biomed Res. Int.* 2015, 1–17. <https://doi.org/10.1155/2015/421746>
- Follet, H., Boivin, G., Rumelhart, C., Meunier, P., 2004. The degree of mineralization is a determinant of bone strength: a study on human calcanei. *Bone* 34, 783–789. <https://doi.org/10.1016/j.bone.2003.12.012>
- Fu, C.J., Zhan, Z.W., Yu, M., Li, S.M., Liu, J.H., Dong, L., 2014. Influence of Zr/Si molar ratio on structure, morphology and corrosion resistance of organosilane coatings doped with zirconium(IV) n-propoxide. *Int. J. Electrochem. Sci.* 9, 2603–2619.
- Fu, H., Fu, Q., Zhou, N., Huang, W., Rahaman, M.N., Wang, D., Liu, X., 2009. In vitro evaluation of borate-based bioactive glass scaffolds prepared by a polymer foam replication method. *Mater. Sci. Eng. C* 29, 2275–2281. <https://doi.org/10.1016/j.msec.2009.05.013>
- Fu, Q., 2019. Bioactive glass scaffolds for bone tissue engineering, in: *Biomedical, Therapeutic and Clinical Applications of Bioactive Glasses*. Woodhead Publishing, pp. 417–442. <https://doi.org/10.1016/B978-0-08-102196-5.00015-X>

- Fu, Q., Rahaman, M.N., Bal, B.S., Brown, R.F., 2009. In vitro cellular response to hydroxyapatite scaffolds with oriented pore architectures. *Mater. Sci. Eng. C* 29, 2147–2153. <https://doi.org/10.1016/J.MSEC.2009.04.016>
- Fu, Y.P., Su, Y.H., Lin, C.H., 2004. Comparison of microwave-induced combustion and solid-state reaction for synthesis of $\text{LiMn}_{2-x}\text{Cr}_x\text{O}_4$ powders and their electrochemical properties. *Solid State Ionics* 166, 137–146. <https://doi.org/10.1016/J.SSI.2003.09.018>
- Gaffney-Stomberg, E., 2019. The impact of trace minerals on bone metabolism. *Biol. Trace Elem. Res.* 188, 26–34. <https://doi.org/10.1007/s12011-018-1583-8>
- Gao, C., Deng, Y., Feng, P., Mao, Z., Li, P., Yang, B., Deng, J., Cao, Y., Shuai, C., Peng, S., 2014. Current progress in bioactive ceramic scaffolds for bone repair and regeneration. *Int. J. Mol. Sci.* 15, 4714–4732. <https://doi.org/10.3390/ijms15034714>
- García-Gareta, E., Coathup, M.J., Blunn, G.W., 2015. Osteoinduction of bone grafting materials for bone repair and regeneration. *Bone* 81, 112–121. <https://doi.org/10.1016/j.bone.2015.07.007>
- Gariboldi, M.I., Best, S.M., 2015. Effect of ceramic scaffold architectural parameters on biological response. *Front. Bioeng. Biotechnol.* 3, 1–11. <https://doi.org/10.3389/fbioe.2015.00151>
- Gauvin, R., Chen, Y.-C., Lee, J.W., Soman, P., Zorlutuna, P., Nichol, J.W., Bae, H., Chen, S., Khademhosseini, A., 2012. Microfabrication of complex porous tissue engineering scaffolds using 3D projection stereolithography. *Biomaterials* 33, 3824–3834. <https://doi.org/10.1016/J.BIOMATERIALS.2012.01.048>
- Gerhardt, L.C., Boccaccini, A.R., 2010. Bioactive glass and glass-ceramic scaffolds for bone tissue engineering. *Materials (Basel)*. 3, 3867–3910. <https://doi.org/10.3390/ma3073867>

- Ghanizadeh, G., Babaei, M., Naghii, M.R., Mofid, M., Torkaman, G., Hedayati, M., 2014. The effect of supplementation of calcium, vitamin D, boron, and increased fluoride intake on bone mechanical properties and metabolic hormones in rat. *Toxicol. Ind. Health* 30, 211–217. <https://doi.org/10.1177/0748233712452775>
- Ginebra, M.-P., Espanol, M., Maazouz, Y., Bergez, V., Pastorino, D., 2018. Bioceramics and bone healing. *EFORT open Rev.* 3, 173–183. <https://doi.org/10.1302/2058-5241.3.170056>
- Gizer, M., Köse, S., Karaosmanoglu, B., Taskiran, E.Z., Berkkan, A., Timuçin, M., Korkusuz, F., Korkusuz, P., 2020. The effect of boron-containing nano-hydroxyapatite on bone cells. *Biol. Trace Elem. Res.* 193, 364–376. <https://doi.org/10.1007/s12011-019-01710-w>
- Gorman, C.M., Horgan, K., Dollard, R.P., Stanton, K.T., 2014. Effects of repeated processing on the strength and microstructure of a heat-pressed dental ceramic. *J. Prosthet. Dent.* 112, 1370–1376. <https://doi.org/10.1016/J.PROSDENT.2014.06.015>
- Gritsch, L., Perrin, E., Chenal, J.M., Fredholm, Y., Maçon, A.L., Chevalier, J., Boccaccini, A.R., 2021. Combining bioresorbable polyesters and bioactive glasses: Orthopedic applications of composite implants and bone tissue engineering scaffolds. *Appl. Mater. Today* 22, 100923. <https://doi.org/10.1016/J.APMT.2020.100923>
- Guerreiro-Tanomaru, J.M., Trindade-Junior, A., Cesar Costa, B., Da Silva, G.F., Drullis Cifali, L., Basso Bernardi, M.I., Tanomaru-Filho, M., 2014. Effect of zirconium oxide and zinc oxide nanoparticles on physicochemical properties and antibiofilm activity of a calcium silicate-based material. *Sci. World J.* 2014, 1–6. <https://doi.org/10.1155/2014/975213>
- Güler, H., Gündoğmaz, G., Kurtuluş, F., Çelik, G., Gacanoğlu, Ş.S., 2011. Solid state synthesis of calcium borohydroxyapatite. *Solid State Sci.* 13, 1916–1920.

<https://doi.org/10.1016/J.SOLIDSTATESCIENCES.2011.08.016>

Gümüşderelioglu, M., Tunçay, E.Ö., Kaynak, G., Demirtaş, T.T., Aydın, S.T., Hakkı, S.S., 2015. Encapsulated boron as an osteoinductive agent for bone scaffolds. *J. Trace Elem. Med. Biol.* 31, 120–128. <https://doi.org/10.1016/J.JTEMB.2015.03.008>

Guo, Y.-P., Lü, J., Ke, Q.-F., 2019. Mesoporous bioactive glasses: Fabrication, structure, drug delivery property, and therapeutic potential, in: *Biomedical, Therapeutic and Clinical Applications of Bioactive Glasses*. Woodhead Publishing, pp. 127–151. <https://doi.org/10.1016/B978-0-08-102196-5.00004-5>

Habraken, W., Habibovic, P., Epple, M., Bohner, M., 2016. Calcium phosphates in biomedical applications: materials for the future? *Mater. Today* 19, 69–87. <https://doi.org/10.1016/J.MATTOD.2015.10.008>

Hakki, S.S., Bozkurt, B.S., Hakki, E.E., 2010. Boron regulates mineralized tissue-associated proteins in osteoblasts (MC3T3-E1). *J. Trace Elem. Med. Biol.* 24, 243–250. <https://doi.org/10.1016/J.JTEMB.2010.03.003>

Hanh, L., Van Hai, L., The Hoang, N., Thi Hong Hanh, D., Minh Hai, L., Viet Nam, N., 2021. In vitro biodegradation behavior of biodegradable hydroxyapatite coated AZ31 alloy treated at various pH values. *J. Appl. Biomater. Funct. Mater.* 19, 228080002110100. <https://doi.org/10.1177/22808000211010037>

Hannink, G., Arts, J.J.C., 2011. Bioresorbability, porosity and mechanical strength of bone substitutes: What is optimal for bone regeneration? *Injury* 42, S22–S25. <https://doi.org/10.1016/J.INJURY.2011.06.008>

Haro Durand, L.A., Góngora, A., Porto López, J.M., Boccaccini, A.R., Zago, M.P., Baldi, A., Gorustovich, A., 2014. In vitro endothelial cell response to ionic dissolution products from boron-doped bioactive glass in the SiO₂-CaO-P₂O₅-Na₂O system. *J. Mater. Chem. B* 2, 7620–7630. <https://doi.org/10.1039/c4tb01043d>

- Haugen, H.J., Lyngstadaas, S.P., Rossi, F., Perale, G., 2019. Bone grafts: which is the ideal biomaterial? *J. Clin. Periodontol.* 46, 92–102. <https://doi.org/10.1111/jcpe.13058>
- Hayakawa, S., 2015. In vitro degradation behavior of hydroxyapatite. *Hydroxyapatite Biomed. Appl.* 85–105. <https://doi.org/10.1016/B978-1-78242-033-0.00004-3>
- Hayakawa, S., Kanaya, T., Tsuru, K., Shirotsaki, Y., Osaka, A., Fujii, E., Kawabata, K., Gasqueres, G., Bonhomme, C., Babonneau, F., Jäger, C., Kleebe, H.J., 2013. Heterogeneous structure and in vitro degradation behavior of wet-chemically derived nanocrystalline silicon-containing hydroxyapatite particles. *Acta Biomater.* 9, 4856–4867. <https://doi.org/10.1016/j.actbio.2012.08.024>
- Hayakawa, S., Sakai, A., Tsuru, K., Osaka, A., Fujii, E., Kawabata, K., Jaeger, C., 2008. Preparation and characterization of boron-containing hydroxyapatite. *Key Eng. Mater.* 361–363, 191–194. <https://doi.org/10.4028/www.scientific.net/KEM.361-363.191>
- He, Z., Jiao, C., Zhang, H., Xie, D., Ge, M., Yang, Y., Wu, G., Liang, H., Shen, L., Wang, C., 2022. Fabrication of a zirconia/calcium silicate composite scaffold based on digital light processing. *Ceram. Int.* 48, 25923–25932. <https://doi.org/10.1016/J.CERAMINT.2022.05.269>
- Hench, L.L., 2015. The future of bioactive ceramics. *J. Mater. Sci. Mater. Med.* 26, 86–90. <https://doi.org/10.1007/s10856-015-5425-3>
- Hench, L.L., Splinter, R.J., Allen, W.C., Greenlee, T.K., 1971. Bonding mechanisms at the interface of ceramic prosthetic materials. *J. Biomed. Mater. Res.* 5, 117–141. <https://doi.org/10.1002/jbm.820050611>
- Hendi, A.A., 2017. Hydroxyapatite based nanocomposite ceramics. *J. Alloys Compd.* 712, 147–151. <https://doi.org/10.1016/J.JALLCOM.2017.04.021>
- Henkel, J., Woodruff, M.A., Epari, D.R., Steck, R., Glatt, V., Dickinson, I.C.,

- Choong, P.F.M., Schuetz, M.A., Hutmacher, D.W., 2013. Bone regeneration based on tissue engineering conceptions — A 21st century perspective. *Bone Res.* 1, 216–248. <https://doi.org/10.4248/BR201303002>
- Hing, K.A., Best, S.M., Tanner, K.E., Bonfield, W., Revell, P.A., 2004. Mediation of bone ingrowth in porous hydroxyapatite bone graft substitutes. *J. Biomed. Mater. Res.* 68A, 187–200. <https://doi.org/10.1002/jbm.a.10050>
- Hollister, S.J., Maddox, R.D., Taboas, J.M., 2002. Optimal design and fabrication of scaffolds to mimic tissue properties and satisfy biological constraints. *Biomaterials* 23, 4095–4103. [https://doi.org/10.1016/S0142-9612\(02\)00148-5](https://doi.org/10.1016/S0142-9612(02)00148-5)
- Howard, D., Buttery, L.D., Shakesheff, K.M., Roberts, S.J., 2008. Tissue engineering: strategies, stem cells and scaffolds. *J. Anat.* 213, 66. <https://doi.org/10.1111/J.1469-7580.2008.00878.X>
- Hu, M.L., Fang, M.H., Tang, C., Yang, T., Huang, Z.H., Liu, Y.G., Wu, X.W., Min, X., 2015. Erratum to: The effects of atmosphere and calcined temperature on photocatalytic activity of TiO₂ nanofibers prepared by electrospinning. *Nanoscale Res. Lett.* 10, 1. <https://doi.org/10.1186/s11671-015-0840-4>
- Hu, X., Shen, H., Shuai, K., Zhang, E., Bai, Y., Cheng, Y., Xiong, X., Wang, S., Fang, J., Wei, S., 2011. Surface bioactivity modification of titanium by CO₂ plasma treatment and induction of hydroxyapatite: In vitro and in vivo studies. *Appl. Surf. Sci.* 257, 1813–1823. <https://doi.org/10.1016/j.apsusc.2010.08.082>
- Hu, Y., Chen, J., Fan, T., Zhang, Y., Zhao, Y., Shi, X., Zhang, Q., 2017. Biomimetic mineralized hierarchical hybrid scaffolds based on in situ synthesis of nano-hydroxyapatite/chitosan/chondroitin sulfate/hyaluronic acid for bone tissue engineering. *Colloids Surfaces B Biointerfaces* 157, 93–100. <https://doi.org/10.1016/j.colsurfb.2017.05.059>
- Hunt, C.D., 2012. Dietary boron: Progress in establishing essential roles in human physiology. *J. Trace Elem. Med. Biol.* 26, 157–160. <https://doi.org/10.1016/j.jtemb.2012.03.014>

- Inzana, J.A., Olvera, D., Fuller, S.M., Kelly, J.P., Graeve, O.A., Schwarz, E.M., Kates, S.L., Awad, H.A., 2014. 3D printing of composite calcium phosphate and collagen scaffolds for bone regeneration. *Biomaterials* 35, 4026–4034. <https://doi.org/10.1016/j.biomaterials.2014.01.064>
- Ito, A., Senda, K., Sogo, Y., Oyane, A., Yamazaki, A., LeGeros, R.Z., 2006. Dissolution rate of zinc-containing β -tricalcium phosphate ceramics. *Biomed. Mater.* 1, 134–139. <https://doi.org/10.1088/1748-6041/1/3/007>
- Jodati, H., Güner, B., Evis, Z., Keskin, D., Tezcaner, A., 2020a. Synthesis and characterization of magnesium-lanthanum dual doped bioactive glasses. *Ceram. Int.* 46, 10503–10511. <https://doi.org/10.1016/j.ceramint.2020.01.050>
- Jodati, H., Tezcaner, A., Alshemary, A.Z., Şahin, V., Evis, Z., 2022a. Effects of the doping concentration of boron on physicochemical, mechanical, and biological properties of hydroxyapatite. *Ceram. Int.* 48, 22743–22758. <https://doi.org/10.1016/J.CERAMINT.2022.04.058>
- Jodati, H., Tezcaner, A., Evis, Z., Alshemary, A.Z., Çelik, E., 2022b. Synthesis of baghdadite using modified sol–gel route and investigation of its properties for bone treatment applications. *J. Korean Ceram. Soc.* 2022 1–18. <https://doi.org/10.1007/S43207-022-00275-0>
- Jodati, H., Yilmaz, B., Evis, Z., 2020b. Calcium zirconium silicate (baghdadite) ceramic as a biomaterial. *Ceram. Int.* 46, 21902–21909. <https://doi.org/10.1016/j.ceramint.2020.06.105>
- Jodati, H., Yilmaz, B., Evis, Z., 2020c. A review of bioceramic porous scaffolds for hard tissue applications: Effects of structural features. *Ceram. Int.* 46, 15725–15739. <https://doi.org/10.1016/j.ceramint.2020.03.192>
- Jones, J.R., 2015. Review of bioactive glass: From Hench to hybrids. *Acta Biomater.* 23, 4457–4486. <https://doi.org/10.1016/j.actbio.2015.07.019>
- Kahaie Khosrowshahi, A., Khoshfetrat, A.B., Khosrowshahi, Y.B., Maleki-Ghaleh,

- H., 2021. Cobalt content modulates characteristics and osteogenic properties of cobalt-containing hydroxyapatite in in-vitro milieu. *Mater. Today Commun.* 27, 102392. <https://doi.org/10.1016/J.MTCOMM.2021.102392>
- Karageorgiou, V., Kaplan, D., 2005. Porosity of 3D biomaterial scaffolds and osteogenesis. *Biomaterials* 26, 5474–5491. <https://doi.org/10.1016/j.biomaterials.2005.02.002>
- Karamian, E., Nasehi, A., Saber-samandari, S., Khandan, A., 2017. Fabrication of hydroxyapatite-baghdadite nanocomposite scaffolds coated by PCL / Bioglass with polyurethane polymeric sponge technique. *Nanomed. J.* 4, 177–183. <https://doi.org/10.22038/nmj.2017.8959>
- Kariem, H., Pastrama, M.-I., Roohani-Esfahani, S.I., Pivonka, P., Zreiqat, H., Hellmich, C., 2015. Micro-poro-elasticity of baghdadite-based bone tissue engineering scaffolds: A unifying approach based on ultrasonics, nanoindentation, and homogenization theory. *Mater. Sci. Eng. C* 46, 553–564. <https://doi.org/10.1016/J.MSEC.2014.10.072>
- Karimi, M., Asefnejad, A., Aflaki, D., Surendar, A., Baharifar, H., Saber-Samandari, S., Khandan, A., Khan, A., Toghraie, D., 2021. Fabrication of shapeless scaffolds reinforced with baghdadite-magnetite nanoparticles using a 3D printer and freeze-drying technique. *J. Mater. Res. Technol.* 14, 3070–3079. <https://doi.org/10.1016/J.JMRT.2021.08.084>
- Karimi, Z., Seyedjafari, E., Mahdavi, F.S., Hashemi, S.M., Khojasteh, A., Kazemi, B., Mohammadi-Yeganeh, S., 2019. Baghdadite nanoparticle-coated poly l-lactic acid (PLLA) ceramics scaffold improved osteogenic differentiation of adipose tissue-derived mesenchymal stem cells. *J. Biomed. Mater. Res. - Part A* 107, 1284–1293. <https://doi.org/10.1002/jbm.a.36638>
- Kaya, Y., Jodati, H., Evis, Z., 2021. Effects of biomimetic synthesis route and sintering temperature on physicochemical, microstructural, and mechanical properties of hydroxyapatite. *J. Aust. Ceram. Soc.* 57, 1117–1129.

<https://doi.org/10.1007/s41779-021-00609-x>

- Keaveny, T.M., Morgan, E.F., Niebur, G.L., Yeh, O.C., 2001. Biomechanics of trabecular bone. *Annu. Rev. Biomed. Eng.* 3, 307–333. <https://doi.org/10.1146/annurev.bioeng.3.1.307>
- Keikhosravani, P., Maleki-Ghaleh, H., Khosrowshahi, A.K., Bodaghi, M., Dargahi, Z., Kavanlouei, M., Khademi-Azandehi, P., Fallah, A., Beygi-Khosrowshahi, Y., Siadati, M.H., 2021. Bioactivity and antibacterial behaviors of nanostructured lithium-doped hydroxyapatite for bone scaffold application. *Int. J. Mol. Sci.* 22, 1–17. <https://doi.org/10.3390/IJMS22179214>
- Keller, T.S., Liebschner, M.A.K., 2000. Tensile and compression testing of bone, in: An, Y.H., Draughn, R.A. (Eds.), *Mechanical Testing of Bone and the Bone–Implant Interface*. CRC Press, Boca Raton, pp. 175–206.
- Khandan, A., Karamian, E., Mehdikhani-Nahrkhalaji, M., Mirmohammadi, H., Farzadi, A., Ozada, N., Heidarshenas, B., Zamani, K., 2015. Influence of spark plasma sintering and baghdadite powder on mechanical properties of hydroxyapatite. *Procedia Mater. Sci.* 11, 183–189. <https://doi.org/10.1016/J.MSPRO.2015.11.087>
- Khoshshima, S., Alshemary, A.Z., Tezcaner, A., Surdem, S., Evis, Z., 2018. Impact of B₂O₃ and La₂O₃ addition on structural, mechanical and biological properties of hydroxyapatite. *Process. Appl. Ceram.* 12, 143–152. <https://doi.org/10.1007/s10832-013-9852-6>
- Khoshshima, S., Yilmaz, B., Tezcaner, A., Evis, Z., 2016. Structural, mechanical and biological properties of hydroxyapatite-zirconia-lanthanum oxide composites. *Ceram. Int.* 42, 15773–15779. <https://doi.org/10.1016/J.CERAMINT.2016.07.041>
- Kim, D.-H., Kim, K.-L., Chun, H.-H., Kim, T.-W., Park, H.-C., Yoon, S.-Y., 2014. In vitro biodegradable and mechanical performance of biphasic calcium phosphate porous scaffolds with unidirectional macro-pore structure. *Ceram.*

Int. 40, 8293–8300. <https://doi.org/10.1016/J.CERAMINT.2014.01.031>

Kirste, G., Brandt-Slowik, J., Bocker, C., Steinert, M., Geiss, R., Brauer, D.S., 2017. Effect of chloride ions in Tris buffer solution on bioactive glass apatite mineralization. *Int. J. Appl. Glas. Sci.* 8, 438–449. <https://doi.org/10.1111/IJAG.12288>

Kitamura, E., Stegaroiu, R., Nomura, S., Miyakawa, O., 2004. Biomechanical aspects of marginal bone resorption around osseointegrated implants: considerations based on a three-dimensional finite element analysis. *Clin. Oral Implants Res.* 15, 401–412. <https://doi.org/10.1111/j.1600-0501.2004.01022.x>

Knudsen, F.P., 1959. Dependence of mechanical strength of Brittle polycrystalline specimens on porosity and grain size. *J. Am. Ceram. Soc.* 42, 376–387. <https://doi.org/10.1111/J.1151-2916.1959.TB13596.X>

Kobayashi, Y., Uehara, S., Udagawa, N., Takahashi, N., 2016. Regulation of bone metabolism by Wnt signals. *J. Biochem.* 159, 387–392. <https://doi.org/10.1093/jb/mvv124>

Kohli, N., Ho, S., Brown, S.J., Sawadkar, P., Sharma, V., Snow, M., García-Gareta, E., 2018. Bone remodelling in vitro: Where are we headed?: -A review on the current understanding of physiological bone remodelling and inflammation and the strategies for testing biomaterials in vitro. *Bone* 110, 38–46. <https://doi.org/10.1016/J.BONE.2018.01.015>

Kokubo, T., Takadama, H., 2008. Simulated body fluid (SBF) as a standard tool to test the bioactivity of implants. *Handb. Biominer. Biol. Asp. Struct. Form.* 3, 97–109. <https://doi.org/10.1002/9783527619443.ch51>

Kokubo, T., Takadama, H., 2006. How useful is SBF in predicting in vivo bone bioactivity? *Biomaterials* 27, 2907–2915. <https://doi.org/10.1016/j.biomaterials.2006.01.017>

Kolmas, J., Velard, F., Jaguszewska, A., Lemaire, F., Kerdjoudj, H., Gangloff, S.C.,

- Kaflak, A., 2017. Substitution of strontium and boron into hydroxyapatite crystals: Effect on physicochemical properties and biocompatibility with human Wharton-Jelly stem cells. *Mater. Sci. Eng. C* 79, 638–646. <https://doi.org/10.1016/J.MSEC.2017.05.066>
- Kosmač, T., Kocjan, A., 2012. Ageing of dental zirconia ceramics. *J. Eur. Ceram. Soc.* 32, 2613–2622. <https://doi.org/10.1016/j.jeurceramsoc.2012.02.024>
- Kucko, N.W., Herber, R.-P., Leeuwenburgh, S.C.G., Jansen, J.A., 2018. Calcium phosphate bioceramics and cements, in: *Principles of Regenerative Medicine*. pp. 591–611. <https://doi.org/10.1016/b978-0-12-809880-6.00034-5>
- Kunjalukkal Padmanabhan, S., Gervaso, F., Carrozzo, M., Scalera, F., Sannino, A., Licciulli, A., 2013. Wollastonite/hydroxyapatite scaffolds with improved mechanical, bioactive and biodegradable properties for bone tissue engineering. *Ceram. Int.* 39, 619–627. <https://doi.org/10.1016/j.ceramint.2012.06.073>
- Lafon, J.P., Champion, E., Bernache-Assollant, D., 2008. Processing of AB-type carbonated hydroxyapatite $\text{Ca}_{10-x}(\text{PO}_4)_6-x(\text{CO}_3)_x(\text{OH})_{2-x-2y}(\text{CO}_3)_y$ ceramics with controlled composition. *J. Eur. Ceram. Soc.* 28, 139–147. <https://doi.org/10.1016/j.jeurceramsoc.2007.06.009>
- Lakshmi, R., Velmurugan, V., Sasikumar, S., 2013. Preparation and phase evolution of Wollastonite by sol-gel combustion method using Sucrose as the fuel. *Combust. Sci. Technol.* 185, 1777–1785. <https://doi.org/10.1080/00102202.2013.835308>
- Langencach, F., Handschel, J., 2013. Effects of dexamethasone, ascorbic acid and β -glycerophosphate on the osteogenic differentiation of stem cells in vitro. *Stem cell Res. Ther.* 4, 117–123. <https://doi.org/10.1089/ten.teb.2011.0199>
- Lawson-wood, K., Robertson, I., 2016. Study of the decomposition of calcium oxalate monohydrate using a hyphenated thermogravimetric analyser - FT-IR System (TG-IR). PerkinElmer 1–3.

- Lee, J.W., Ahn, G., Kim, J.Y., Cho, D.-W., 2010. Evaluating cell proliferation based on internal pore size and 3D scaffold architecture fabricated using solid freeform fabrication technology. *J. Mater. Sci. Mater. Med.* 21, 3195–3205. <https://doi.org/10.1007/s10856-010-4173-7>
- Lee, Y.L., Wang, W.H., Lin, F.H., Lin, C.P., 2017. Hydration behaviors of calcium silicate-based biomaterials. *J. Formos. Med. Assoc.* 116, 424–431. <https://doi.org/10.1016/J.JFMA.2016.07.009>
- Lepry, W.C., Naseri, S., Nazhat, S.N., 2017. Effect of processing parameters on textural and bioactive properties of sol–gel-derived borate glasses. *J. Mater. Sci.* 52, 8973–8985. <https://doi.org/10.1007/s10853-017-0968-y>
- Li, B., Liao, X., Zheng, L., He, H., Wang, H., Fan, H., Zhang, X., 2012. Preparation and cellular response of porous A-type carbonated hydroxyapatite nanoceramics. *Mater. Sci. Eng. C* 32, 929–936. <https://doi.org/10.1016/j.msec.2012.02.014>
- Li, J.J., Akey, A., Dunstan, C.R., Vielreicher, M., Friedrich, O., Bell, D.C., Zreiqat, H., 2018. Effects of material–tissue interactions on bone regeneration outcomes using baghdadite implants in a large animal model. *Adv. Healthc. Mater.* 7, 1–9. <https://doi.org/10.1002/adhm.201800218>
- Li, J.J., Roohani-Esfahani, S.I., Dunstan, C.R., Quach, T., Steck, R., Saifzadeh, S., Pivonka, P., Zreiqat, H., 2016. Efficacy of novel synthetic bone substitutes in the reconstruction of large segmental bone defects in sheep tibiae. *Biomed. Mater.* 11, 1–12. <https://doi.org/10.1088/1748-6041/11/1/015016>
- Li, M., Xiong, P., Yan, F., Li, S., Ren, C., Yin, Z., Li, A., Li, H., Ji, X., Zheng, Y., Cheng, Y., 2018. An overview of graphene-based hydroxyapatite composites for orthopedic applications. *Bioact. Mater.* 3, 1–18. <https://doi.org/10.1016/j.bioactmat.2018.01.001>
- Li, X., Wang, X., Jiang, X., Yamaguchi, M., Ito, A., Bando, Y., Golberg, D., 2016. Boron nitride nanotube-enhanced osteogenic differentiation of mesenchymal

- stem cells. *J. Biomed. Mater. Res. - Part B Appl. Biomater.* 104, 323–329.
<https://doi.org/10.1002/jbm.b.33391>
- Liang, Y., Xie, Y., Ji, H., Huang, L., Zheng, X., 2010. Excellent stability of plasma-sprayed bioactive Ca₃ZrSi₂O₉ ceramic coating on Ti–6Al–4V. *Appl. Surf. Sci.* 256, 4677–4681. <https://doi.org/10.1016/J.APSUSC.2010.02.071>
- Lin, K., Liu, P., Wei, L., Zou, Z., Zhang, W., Qian, Y., Shen, Y., Chang, J., 2013. Strontium substituted hydroxyapatite porous microspheres: Surfactant-free hydrothermal synthesis, enhanced biological response and sustained drug release. *Chem. Eng. J.* 222, 49–59. <https://doi.org/10.1016/J.CEJ.2013.02.037>
- Liu, X., Ding, C., 2002. Morphology of apatite formed on surface of wollastonite coating soaked in simulate body fluid. *Mater. Lett.* 57, 652–655.
[https://doi.org/10.1016/S0167-577X\(02\)00848-0](https://doi.org/10.1016/S0167-577X(02)00848-0)
- Liu, X., Tao, S., Ding, C., 2002. Bioactivity of plasma sprayed dicalcium silicate coatings. *Biomaterials* 23, 963–968. [https://doi.org/10.1016/S0142-9612\(01\)00210-1](https://doi.org/10.1016/S0142-9612(01)00210-1)
- Liu, Y., Zheng, Y., Hayes, B., 2017. Degradable, absorbable or resorbable—what is the best grammatical modifier for an implant that is eventually absorbed by the body? *Sci. China Mater.* 2017 605 60, 377–391.
<https://doi.org/10.1007/S40843-017-9023-9>
- Loh, Q.L., Choong, C., 2013. Three-dimensional scaffolds for tissue engineering applications: Role of porosity and pore size. *Tissue Eng. Part B Rev.* 19, 485–502. <https://doi.org/10.1089/ten.teb.2012.0437>
- Lou, W., Dong, Y., Zhang, H., Jin, Y., Hu, X., Ma, J., Liu, J., Wu, G., 2015. Preparation and characterization of lanthanum-incorporated hydroxyapatite coatings on titanium substrates. *Int. J. Mol. Sci* 16, 21070–21086.
<https://doi.org/10.3390/ijms160921070>
- Lu, J., Descamps, M., Dejou, J., Koubi, G., Hardouin, P., Lemaitre, J., Proust, J.-P.,

2002. The biodegradation mechanism of calcium phosphate biomaterials in bone. *J. Biomed. Mater. Res.* 63, 408–412. <https://doi.org/10.1002/jbm.10259>
- Lu, X., Kolzow, J., Chen, R.R., Du, J., 2019. Effect of solution condition on hydroxyapatite formation in evaluating bioactivity of B₂O₃ containing 45S5 bioactive glasses. *Bioact. Mater.* 4, 207–214. <https://doi.org/10.1016/j.bioactmat.2019.05.002>
- Lu, X., Li, K., Xie, Y., Huang, L., Zheng, X., 2016. Chemical stability and osteogenic activity of plasma-sprayed boron-modified calcium silicate-based coatings. *J. Mater. Sci. Mater. Med.* 27, 166. <https://doi.org/10.1007/s10856-016-5781-7>
- Lu, Z., Wang, G., Roohani-esfahani, I., 2014. Baghdadite ceramics modulate the cross talk between human adipose stem cells and osteoblasts. *Tissue Eng. Part A* 20, 992–1003. <https://doi.org/10.1089/ten.tea.2013.0470>
- Luo, T., Wu, C., Zhang, Y., 2012. The in vivo osteogenesis of Mg or Zr-modified silicate-based bioceramic spheres. *J. Biomed. Mater. Res. Part A* 100, 2269–2277. <https://doi.org/10.1002/jbm.a.34161>
- Ma, H., Feng, C., Chang, J., Wu, C., 2018. 3D-printed bioceramic scaffolds: From bone tissue engineering to tumor therapy. *Acta Biomater.* 79, 37–59. <https://doi.org/10.1016/j.actbio.2018.08.026>
- Ma, S., Tang, Q., Feng, Q., Song, J., Han, X., Guo, F., 2019. Mechanical behaviours and mass transport properties of bone-mimicking scaffolds consisted of gyroid structures manufactured using selective laser melting. *J. Mech. Behav. Biomed. Mater.* 93, 158–169. <https://doi.org/10.1016/J.JMBBM.2019.01.023>
- Maleki-Ghaleh, H., Hossein Siadati, M., Fallah, A., Zarrabi, A., Afghah, F., Koc, B., Dalir Abdolahinia, E., Omidi, Y., Barar, J., Akbari-Fakhrabadi, A., Beygi-Khosrowshahi, Y., Adibkia, K., 2021. Effect of zinc-doped hydroxyapatite/graphene nanocomposite on the physicochemical properties and osteogenesis differentiation of 3D-printed polycaprolactone scaffolds for bone

- tissue engineering. *Chem. Eng. J.* 426, 131321.
<https://doi.org/10.1016/J.CEJ.2021.131321>
- Marie, P.J., 2010. The calcium-sensing receptor in bone cells: A potential therapeutic target in osteoporosis. *Bone* 46, 571–576.
<https://doi.org/10.1016/j.bone.2009.07.082>
- Marks, S.C., Odgren, P.R., 2002. Structure and Development of the Skeleton, in: Bilezikian, J.P., Raisz, L.G., Rodan, G.A. (Eds.), *Principles of Bone Biology*. Academic Press, pp. 3–15. <https://doi.org/10.1016/B978-012098652-1.50103-7>
- Martín-Garrido, M., Teresa Molina-Delgado, M., Martínez-Ramírez, S., 2020. A comparison between experimental and theoretical Ca/Si ratios in C–S–H and C–S(A)–H gels. *J. Sol-Gel Sci. Technol.* 94, 11–21.
<https://doi.org/10.1007/S10971-019-05097-X/FIGURES/5>
- Mawuntu, V.J., Yusuf, Y., 2019. Porous structure engineering of bioceramic hydroxyapatite-based scaffolds using PVA, PVP, and PEO as polymeric porogens. *J. Asian Ceram. Soc.* 7, 161–169.
<https://doi.org/10.1080/21870764.2019.1595927>
- Meacham, S., Karakas, S., Wallace, A., Altun, F., 2010. Boron in human health: Evidence for dietary recommendations and public policies. *Open Miner. Process. J.* 3, 36–53. <https://doi.org/10.2174/1874841401003010036>
- MediPoint: Bone Grafts and Substitutes - Global Analysis and Market Forecasts 2017. GlobalData. URL <https://www.globaldata.com/store/report/medipoint-bone-grafts-substitutes-global-analysis-and-market-forecasts/> (accessed 7.19.19).
- Mehrafzoon, S., Hassanzadeh-Tabrizi, S.A., Bigham, A., 2018. Synthesis of nanoporous Baghdadite by a modified sol-gel method and its structural and controlled release properties. *Ceram. Int.* 44, 13951–13958.
<https://doi.org/10.1016/J.CERAMINT.2018.04.244>

- Melchels, F.P.W., Barradas, A.M.C., van Blitterswijk, C.A., de Boer, J., Feijen, J., Grijpma, D.W., 2010. Effects of the architecture of tissue engineering scaffolds on cell seeding and culturing. *Acta Biomater.* 6, 4208–4217. <https://doi.org/10.1016/J.ACTBIO.2010.06.012>
- Method, S.T., 2008. ASTM Standard - D3967-08: Standard test method for splitting tensile strength of intact rock core specimens. *Test* 8–11. <https://doi.org/10.1520/D3967-16>.
- Mohammadi, H., Hafezi, M., Nezafati, N., Heasarki, S., Nadernezhad, A., Ghazanfari, S.M.H., Sepantafar, M., 2014. Bioinorganics in bioactive calcium silicate ceramics for bone tissue repair: Bioactivity and biological properties. *J. Ceram. Sci. Technol.* 5, 1–12. <https://doi.org/10.4416/JCST2013-00027>
- Mohammadi Zerankeshi, M., Mofakhami, S., Salahinejad, E., 2022. 3D porous HA/TCP composite scaffolds for bone tissue engineering. *Ceram. Int.* 48, 22647–22663. <https://doi.org/10.1016/J.CERAMINT.2022.05.103>
- Mondal, S., Hoang, G., Manivasagan, P., Moorthy, M.S., Kim, H.H., Vy Phan, T.T., Oh, J., 2019. Comparative characterization of biogenic and chemical synthesized hydroxyapatite biomaterials for potential biomedical application. *Mater. Chem. Phys.* 228, 344–356. <https://doi.org/10.1016/J.MATCHEMPHYS.2019.02.021>
- Monshi, A., Foroughi, M.R., Monshi, M.R., 2012. Modified Scherrer equation to estimate more accurately nano-crystallite size using XRD. *World J. Nano Sci. Eng.* 02, 154–160. <https://doi.org/10.4236/wjnse.2012.23020>
- Moonesi Rad, R., Atila, D., Akgün, E.E., Evis, Z., Keskin, D., Tezcaner, A., 2019. Evaluation of human dental pulp stem cells behavior on a novel nanobiocomposite scaffold prepared for regenerative endodontics. *Mater. Sci. Eng. C* 100, 928–948. <https://doi.org/10.1016/J.MSEC.2019.03.022>
- Moore, W.R., Graves, S.E., Bain, G.I., 2001. Synthetic bone graft substitutes. *ANZ J. Surg.* 71, 354–361. <https://doi.org/10.1046/j.1440-1622.2001.02128.x>

- Morejón-Alonso, L., Ferreira, O.J.B., Carrodeguas, R.G., Dos Santos, L.A., 2012. Bioactive composite bone cement based on α -tricalcium phosphate/tricalcium silicate. *J. Biomed. Mater. Res. Part B Appl. Biomater.* 100B, 94–102. <https://doi.org/10.1002/JBM.B.31926>
- Motamedian, S.R., Hosseinpour, S., Ahsaie, M.G., Khojasteh, A., 2015. Smart scaffolds in bone tissue engineering: A systematic review of literature. *World J. Stem Cells* 7, 657–68. <https://doi.org/10.4252/wjsc.v7.i3.657>
- Mountziaris, P.M., Mikos, A.G., 2008. Modulation of the inflammatory response for enhanced bone tissue regeneration. *Tissue Eng. Part B Rev.* 14, 179–186. <https://doi.org/10.1089/ten.teb.2008.0038>
- Movahedi Najafabadi, B.-A.-H., Abnosi, M.H., 2016. Boron induces early matrix mineralization via calcium deposition and elevation of alkaline phosphatase activity in differentiated rat bone marrow mesenchymal stem cells. *Cell J.* 18, 62–73. <https://doi.org/10.22074/cellj.2016.3988>
- Murphy, C.M., Haugh, M.G., O'Brien, F.J., 2010. The effect of mean pore size on cell attachment, proliferation and migration in collagen-glycosaminoglycan scaffolds for bone tissue engineering. *Biomaterials* 31, 461–466. <https://doi.org/10.1016/j.biomaterials.2009.09.063>
- Murray, E., Provvedini, D., Curran, D., Catherwood, B., Sussman, H., Manolagas, S., 1987. Characterization of a human osteoblastic osteosarcoma cell line (SAOS-2) with high bone alkaline phosphatase activity. *J. Bone Miner. Res.* 2, 231–238. <https://doi.org/10.1002/jbmr.5650020310>
- Murugan, R., Ramakrishna, S., 2006. Production of ultra-fine bioresorbable carbonated hydroxyapatite. *Acta Biomater.* 2, 201–206. <https://doi.org/10.1016/j.actbio.2005.09.005>
- Naghizadeh, M., Mirzadeh, H., 2019. Effects of grain size on mechanical properties and work-hardening behavior of AISI 304 austenitic stainless steel. *Steel Res. Int.* 90, 1–9. <https://doi.org/10.1002/srin.201900153>

- Najafinezhad, A., Abdellahi, M., Ghayour, H., Soheily, A., Chami, A., Khandan, A., 2017. A comparative study on the synthesis mechanism, bioactivity and mechanical properties of three silicate bioceramics. *Mater. Sci. Eng. C* 72, 259–267. <https://doi.org/10.1016/J.MSEC.2016.11.084>
- Nakamura, M., Zhuang, Z., Aizawa, M., 2012. Fabrications of boron-containing apatite ceramics via ultrasonic spray-pyrolysis route and their surface properties. *Key Eng. Mater.* 529–530, 109–113. <https://doi.org/10.4028/www.scientific.net/KEM.529-530.109>
- Ni, S., Chang, J., Chou, L., Zhai, W., 2007. Comparison of osteoblast-like cell responses to calcium silicate and tricalcium phosphate ceramics *in vitro*. *J. Biomed. Mater. Res. Part B Appl. Biomater.* 80B, 174–183. <https://doi.org/10.1002/jbm.b.30582>
- No, Y.J., Holzmeister, I., Lu, Z., Prajapati, S., Shi, J., Gbureck, U., Zreiqat, H., 2019. Effect of baghdadite substitution on the physicochemical properties of brushite cements. *Materials (Basel)*. 12, 1–15. <https://doi.org/10.3390/MA12101719>
- No, Y.J., Nguyen, T., Lu, Z., Mirkhalaf, M., Fei, F., Foley, M., Zreiqat, H., 2021. Development of a bioactive and radiopaque bismuth doped baghdadite ceramic for bone tissue engineering. *Bone* 153, 116147. <https://doi.org/10.1016/J.BONE.2021.116147>
- O'Brien, F.J., 2011. Biomaterials & scaffolds for tissue engineering. *Mater. Today* 14, 88–95. [https://doi.org/10.1016/S1369-7021\(11\)70058-X](https://doi.org/10.1016/S1369-7021(11)70058-X)
- O'Keefe, R.J., Mao, J., 2011. Bone tissue engineering and regeneration: From discovery to the clinic—An overview. *Tissue Eng. Part B Rev.* 17, 389–392. <https://doi.org/10.1089/ten.teb.2011.0475>
- Obada, D.O., Dauda, E.T., Abifarin, J.K., Dodoo-Arhin, D., Bansod, N.D., 2020. Mechanical properties of natural hydroxyapatite using low cold compaction pressure: Effect of sintering temperature. *Mater. Chem. Phys.* 239, 122099. <https://doi.org/10.1016/j.matchemphys.2019.122099>

- Okamoto, H., 2008. B-Ca (Boron-calcium). *J. Phase Equilibria Diffus.* 29, 379–379.
<https://doi.org/10.1007/s11669-008-9301-4>
- Padmanabhan, S.K., Ul Haq, E., Licciulli, A., 2014. Rapid synthesis and characterization of silicon substituted nano hydroxyapatite using microwave irradiation. *Curr. Appl. Phys.* 14, 87–92.
<https://doi.org/10.1016/J.CAP.2013.08.022>
- Pahlevanzadeh, F., Bakhsheshi-Rad, H.R., Hamzah, E., 2018. In-vitro biocompatibility, bioactivity, and mechanical strength of PMMA-PCL polymer containing fluorapatite and graphene oxide bone cements. *J. Mech. Behav. Biomed. Mater.* 82, 257–267. <https://doi.org/10.1016/j.jmbbm.2018.03.016>
- Pahlevanzadeh, Farnoosh, Bakhsheshi-Rad, H.R., Ismail, A.F., Aziz, M., 2018. Apatite-forming ability cytocompatibility and mechanical properties enhancement of poly methyl methacrylate-based bone cements by incorporating of baghdadite nanoparticles. *Int. J. Appl. Ceram. Technol.* 16, 2006–2019.
- Panda, S., Biswas, C.K., Paul, S., 2021. A comprehensive review on the preparation and application of calcium hydroxyapatite: A special focus on atomic doping methods for bone tissue engineering. *Ceram. Int.* 47, 28122–28144.
<https://doi.org/10.1016/J.CERAMINT.2021.07.100>
- Park, M., Li, Q., Shcheynikov, N., Zeng, W., Muallem, S., 2004. NaBC1 is a ubiquitous electrogenic Na⁺-coupled borate transporter essential for cellular boron homeostasis and cell growth and proliferation. *Mol. Cell* 16, 331–341.
<https://doi.org/10.1016/j.molcel.2004.09.030>
- Pazarçeviren, A.E., Evis, Z., Keskin, D., Tezcaner, A., 2019. Resorbable PCEC/gelatin-bismuth doped bioglass-graphene oxide bilayer membranes for guided bone regeneration. *Biomed. Mater.* 14, 035018.
<https://doi.org/10.1088/1748-605X/AB007B>
- Pazarçeviren, A.E., Tahmasebifar, A., Tezcaner, A., Keskin, D., Evis, Z., 2018.

- Investigation of bismuth doped bioglass/graphene oxide nanocomposites for bone tissue engineering. *Ceram. Int.* 44, 3791–3799. <https://doi.org/10.1016/j.ceramint.2017.11.164>
- Pazarçeviren, A.E., Tezcaner, A., Keskin, D., Kolukisa, S.T., Sürdem, S., Evis, Z., 2021. Boron-doped biphasic hydroxyapatite/ β -tricalcium phosphate for bone tissue engineering. *Biol. Trace Elem. Res.* 199, 968–980. <https://doi.org/10.1007/s12011-020-02230-8>
- Perez, R.A., Mestres, G., 2016. Role of pore size and morphology in musculo-skeletal tissue regeneration. *Mater. Sci. Eng. C* 61, 922–939. <https://doi.org/10.1016/j.msec.2015.12.087>
- Pérez, R.A., Won, J.-E., Knowles, J.C., Kim, H.-W., 2013. Naturally and synthetic smart composite biomaterials for tissue regeneration. *Adv. Drug Deliv. Rev.* 65, 471–496. <https://doi.org/10.1016/J.ADDR.2012.03.009>
- Pham, D.Q., Berndt, C.C., Gbureck, U., Zreiqat, H., Truong, V.K., Ang, A.S.M., 2019. Mechanical and chemical properties of Baghdadite coatings manufactured by atmospheric plasma spraying. *Surf. Coatings Technol.* 378, 124945. <https://doi.org/10.1016/j.surfcoat.2019.124945>
- Pickup, D.M., Mountjoy, G., Wallidge, G.W., Newport, R.J., Smith, M.E., 1999. Structure of $(\text{ZrO}_2)_x(\text{SiO}_2)_{(1-x)}$ xerogels ($x = 0.1, 0.2, 0.3$ and 0.4) from FTIR, ^{29}Si and ^{17}O MAS NMR and EXAFS. *Phys. Chem. Chem. Phys.* 1, 2527–2533. <https://doi.org/10.1039/a901401b>
- Piconi, C., Maccauro, G., 1999. Zirconia as a ceramic biomaterial. *Biomaterials* 20, 1–25. [https://doi.org/10.1016/S0142-9612\(98\)00010-6](https://doi.org/10.1016/S0142-9612(98)00010-6)
- Plaister, J.R., Jansen, J., De Graaff, R.A.G., Ijdo, D.J.W., 1995. Structure determination of $\text{Ca}_3\text{HfSi}_2\text{O}_9$ and $\text{Ca}_3\text{ZrSi}_2\text{O}_9$ from powder diffraction. *J. Solid State Chem.* 115, 464–468. <https://doi.org/10.1006/jssc.1995.1160>
- Punj, S., Singh, J., Singh, K., 2021. Ceramic biomaterials: Properties, state of the art

- and future perspectives. *Ceram. Int.* 47, 28059–28074.
<https://doi.org/10.1016/J.CERAMINT.2021.06.238>
- Quiroga, L.C.R., Balestieri, J.A.P., Ávila, I., 2017. Thermal behavior and kinetics assessment of ethanol/gasoline blends during combustion by thermogravimetric analysis. *Appl. Therm. Eng.* 115, 99–110.
<https://doi.org/10.1016/j.applthermaleng.2016.12.051>
- Rajesh, R., Hariharasubramanian, A., Ravichandran, Y.D., 2012. Chicken bone as a bioresource for the bioceramic (hydroxyapatite). *Phosphorus, Sulfur Silicon Relat. Elem.* 187, 914–925. <https://doi.org/10.1080/10426507.2011.650806>
- Ramaswamy, Y., Wu, C., Van Hummel, A., Combes, V., Grau, G., Zreiqat, H., 2008. The responses of osteoblasts, osteoclasts and endothelial cells to zirconium modified calcium-silicate-based ceramic. *Biomaterials* 29, 4392–4402.
<https://doi.org/10.1016/J.BIOMATERIALS.2008.08.006>
- Rampersad, S.N., 2012. Multiple applications of alamar Blue as an indicator of metabolic function and cellular health in cell viability bioassays. *Sensors* 2012, Vol. 12, Pages 12347-12360 12, 12347–12360.
<https://doi.org/10.3390/S120912347>
- Ranjakesh, B., Isidor, F., Dalstra, M., Løvschall, H., 2016. Diametral tensile strength of novel fast-setting calcium silicate cement. *Dent. Mater. J.* 35, 559–563.
<https://doi.org/10.4012/DMJ.2015-390>
- Rao, S.H., Harini, B., Shadamarshan, R.P.K., Balagangadharan, K., Selvamurugan, N., 2018. Natural and synthetic polymers/bioceramics/bioactive compounds-mediated cell signalling in bone tissue engineering. *Int. J. Biol. Macromol.*
<https://doi.org/10.1016/j.ijbiomac.2017.09.029>
- Ren, F., Leng, Y., 2012. Carbonated apatite, Type-A or Type-B?, in: *Key Engineering Materials*. Trans Tech Publications Ltd, pp. 293–297.
<https://doi.org/10.4028/www.scientific.net/KEM.493-494.293>

- Ren, X., Chen, X., Geng, Z., Su, J., 2022. Bone-targeted biomaterials: Strategies and applications. *Chem. Eng. J.* 446, 137133. <https://doi.org/10.1016/J.CEJ.2022.137133>
- Rho, J.-Y., Kuhn-Spearing, L., Zioupos, P., 1998. Mechanical properties and the hierarchical structure of bone. *Med. Eng. Phys.* 20, 92–102. [https://doi.org/10.1016/S1350-4533\(98\)00007-1](https://doi.org/10.1016/S1350-4533(98)00007-1)
- Rondanelli, M., Faliva, M.A., Peroni, G., Infantino, V., Gasparri, C., Iannello, G., Perna, S., Riva, A., Petrangolini, G., Tartara, A., 2020. Pivotal role of boron supplementation on bone health: A narrative review. *J. Trace Elem. Med. Biol.* <https://doi.org/10.1016/j.jtemb.2020.126577>
- Roohani-Esfahani, S.I., Dunstan, C.R., Davies, B., Pearce, S., Williams, R., Zreiqat, H., 2012. Repairing a critical-sized bone defect with highly porous modified and unmodified baghdadite scaffolds. *Acta Biomater.* 8, 4162–4172. <https://doi.org/10.1016/J.ACTBIO.2012.07.036>
- Roseti, L., Parisi, V., Petretta, M., Cavallo, C., Desando, G., Bartolotti, I., Grigolo, B., 2017. Scaffolds for bone tissue engineering: State of the art and new perspectives. *Mater. Sci. Eng. C* 78, 1246–1262. <https://doi.org/10.1016/j.msec.2017.05.017>
- Rouahi, M., Gallet, O., Champion, E., Dentzer, J., Hardouin, P., Anselme, K., 2006. Influence of hydroxyapatite microstructure on human bone cell response. *J. Biomed. Mater. Res. Part A* 78A, 222–235. <https://doi.org/10.1002/jbm.a.30682>
- Sadat-Shojai, M., Khorasani, M.T., Dinpanah-Khoshdargi, E., Jamshidi, A., 2013. Synthesis methods for nanosized hydroxyapatite with diverse structures. *Acta Biomater.* 9, 7591–7621. <https://doi.org/10.1016/j.actbio.2013.04.012>
- Sadeghpour, S., Amirjani, A., Hafezi, M., Zamanian, A., 2014. Fabrication of a novel nanostructured calcium zirconium silicate scaffolds prepared by a freeze-casting method for bone tissue engineering. *Ceram. Int.* 40, 16107–16114.

<https://doi.org/10.1016/J.CERAMINT.2014.07.039>

- Sadeghzade, S., Emadi, R., Ahmadi, T., Tavangarian, F., 2019. Synthesis, characterization and strengthening mechanism of modified and unmodified porous diopside/baghdadite scaffolds. *Mater. Chem. Phys.* 228, 89–97. <https://doi.org/10.1016/j.matchemphys.2019.02.041>
- Sadeghzade, S., Emadi, R., Labbaf, S., 2016. Formation mechanism of nano-hardystonite powder prepared by mechanochemical synthesis. *Adv. Powder Technol.* 27, 2238–2244. <https://doi.org/10.1016/j.appt.2016.08.010>
- Sadeghzade, S., Emadi, R., Tavangarian, F., Doostmohammadi, A., 2020. In vitro evaluation of diopside/baghdadite bioceramic scaffolds modified by polycaprolactone fumarate polymer coating. *Mater. Sci. Eng. C* 106, 110176. <https://doi.org/10.1016/j.msec.2019.110176>
- Sadeghzade, S., Shamoradi, F., Emadi, R., Tavangarian, F., 2017. Fabrication and characterization of baghdadite nanostructured scaffolds by space holder method. *J. Mech. Behav. Biomed. Mater.* 68, 1–7. <https://doi.org/10.1016/J.JMBBM.2017.01.034>
- Sadetskaya, A. V., Bobrysheva, N.P., Osmolowsky, M.G., Osmolovskaya, O.M., Voznesenskiy, M.A., 2021. Correlative experimental and theoretical characterization of transition metal doped hydroxyapatite nanoparticles fabricated by hydrothermal method. *Mater. Charact.* 173, 110911. <https://doi.org/10.1016/J.MATCHAR.2021.110911>
- Safarzadeh, M., Ramesh, S., Tan, C.Y., Chandran, H., Noor, A.F.M., Krishnasamy, S., Alengaram, U.J., 2019. Effect of multi-ions doping on the properties of carbonated hydroxyapatite bioceramic. *Ceram. Int.* 45, 3473–3477. <https://doi.org/10.1016/j.ceramint.2018.11.003>
- Samani, D.A., Doostmohammadi, A., Nilforoushan, M.R., Nazari, H., 2019. Electrospun polycaprolactone/graphene/baghdadite composite nanofibres with improved mechanical and biological properties. *Fibers Polym.* 20, 982–990.

<https://doi.org/10.1007/s12221-019-1161-5>

- Sasaki, K., Toshiyuki, K., Guo, B., Ideta, K., Hayashi, Y., Hirajima, T., Miyawaki, J., 2018. Calcination effect of borate-bearing hydroxyapatite on the mobility of borate. *J. Hazard. Mater.* 344, 90–97. <https://doi.org/10.1016/j.jhazmat.2017.10.003>
- Sathiyavimal, S., Vasantharaj, S., LewisOscar, F., Selvaraj, R., Brindhadevi, K., Pugazhendhi, A., 2020. Natural organic and inorganic–hydroxyapatite biopolymer composite for biomedical applications. *Prog. Org. Coatings* 147, 105858. <https://doi.org/10.1016/j.porgcoat.2020.105858>
- Schumacher, T.C., Aminian, A., Volkmann, E., Lührs, H., Zimnik, D., Pede, D., Wosniok, W., Treccani, L., Rezwan, K., 2015. Synthesis and mechanical evaluation of Sr-doped calcium-zirconium-silicate (baghdadite) and its impact on osteoblast cell proliferation and ALP activity. *Biomed. Mater.* 10, 1–16. <https://doi.org/10.1088/1748-6041/10/5/055013>
- Schumacher, T.C., Volkmann, E., Yilmaz, R., Wolf, A., Treccani, L., Rezwan, K., 2014. Mechanical evaluation of calcium-zirconium-silicate (baghdadite) obtained by a direct solid-state synthesis route. *J. Mech. Behav. Biomed. Mater.* 34, 294–301. <https://doi.org/10.1016/j.jmbbm.2014.02.021>
- Seeman, E., 2009. Bone modeling and remodeling. *Crit. Rev. Eukaryot. Gene Expr.* 19, 219–233.
- Sehgal, R.R., Roohani-Esfahani, S.I., Zreiqat, H., Banerjee, R., 2017. Nanostructured gellan and xanthan hydrogel depot integrated within a baghdadite scaffold augments bone regeneration. *J. Tissue Eng. Regen. Med.* 11, 1195–1211. <https://doi.org/10.1002/term.2023>
- Seyed Shirazi, S.F., Gharekhani, S., Cornelis Metselaar, H.S., Nasiri-Tabrizi, B., Yarmand, H., Ahmadi, M., Abu Osman, N.A., 2015. Ion size, loading, and charge determine the mechanical properties, surface apatite, and cell growth of silver and tantalum doped calcium silicate. *RSC Adv.* 6, 190–200.

<https://doi.org/10.1039/c5ra17326d>

- Shiraga, K., Kusachi, I., Kobayashi, S., 2001. Baghdadite from Fuka, Okayama prefecture, Japan. *J. Mineral. Petrol. Sci.* 96, 43–47.
- Shuai, C., Yu, L., Feng, P., Gao, C., Peng, S., 2020. Interfacial reinforcement in bioceramic/biopolymer composite bone scaffold: The role of coupling agent. *Colloids Surfaces B Biointerfaces* 193, 111083. <https://doi.org/10.1016/J.COLSURFB.2020.111083>
- Singh, P., Yu, X., Kumar, A., Dubey, A.K., 2022. Recent advances in silicate-based crystalline bioceramics for orthopedic applications: a review. *J. Mater. Sci.* 2022 5728 57, 13109–13151. <https://doi.org/10.1007/S10853-022-07444-W>
- Siriphannon, P., Kameshima, Y., Yasumori, A., Okada, K., Hayashi, S., 2002. Formation of hydroxyapatite on CaSiO₃ powders in simulated body fluid. *J. Eur. Ceram. Soc.* 22, 511–520. [https://doi.org/10.1016/S0955-2219\(01\)00301-6](https://doi.org/10.1016/S0955-2219(01)00301-6)
- Sivashankari, P.R., Prabakaran, M., 2020. Three-dimensional porous scaffolds based on agarose/chitosan/graphene oxide composite for tissue engineering. *Int. J. Biol. Macromol.* 146, 222–231. <https://doi.org/10.1016/j.ijbiomac.2019.12.219>
- Soni, R., Kumar, N.V., Chameettachal, S., Pati, F., Narayan Rath, S., 2019. Synthesis and optimization of PCL-bioactive glass composite scaffold for bone tissue engineering. *Mater. Today Proc.* 15, 294–299. <https://doi.org/10.1016/J.MATPR.2019.05.008>
- Soundrapandian, C., Datta, S., Kundu, B., Basu, D., Sa, B., 2010. Porous bioactive glass scaffolds for local drug delivery in osteomyelitis: Development and in vitro characterization. *AAPS PharmSciTech* 11, 1675–1683. <https://doi.org/10.1208/s12249-010-9550-5>
- Spahiu, E., 2015. ATR-FTIR evaluation of structural and functional changes on murine macrophage cells upon activation and suppression by immuno-

therapeutic oligodeoxynucleotides. M.Sc. Thesis. Middle East Technical University.

Sri Devi, P., Vijayalakshmi, K.A., 2020. Analysis of antibacterial activity and cytotoxicity of silver oxide doped hydroxyapatite exposed to DC glow discharge plasma. *Mater. Today Proc.* 26, 3604–3608. <https://doi.org/10.1016/J.MATPR.2019.09.204>

Stratton, S., Shelke, N.B., Hoshino, K., Rudraiah, S., Kumbar, S.G., 2016. Bioactive polymeric scaffolds for tissue engineering. *Bioact. Mater.* 1, 93–108. <https://doi.org/10.1016/J.BIOACTMAT.2016.11.001>

Suchanek, W., Yashima, M., Kakihana, M., Yoshimura, M., 1997. Hydroxyapatite ceramics with selected sintering additives. *Biomaterials* 18, 923–933. [https://doi.org/10.1016/S0142-9612\(97\)00019-7](https://doi.org/10.1016/S0142-9612(97)00019-7)

Sun, J.-Y., Yang, T.-S., Zhong, J., Greenspan, D.C., 2007. The effect of the ionic products of Bioglass® dissolution on human osteoblasts growth cycle in vitro. *J. Tissue Eng. Regen. Med.* 1, 281–286. <https://doi.org/10.1002/term>

Syed-Picard, F.N., Jayaraman, T., Lam, R.S.K., Beniash, E., Sfeir, C., 2013. Osteoinductivity of calcium phosphate mediated by connexin 43. *Biomaterials* 34, 3763–3774. <https://doi.org/10.1016/J.BIOMATERIALS.2013.01.095>

Tahmasebifar, A., Evis, Z., 2013. Structural and mechanical characteristics of hydroxyapatite and tri-calcium phosphates doped with Al³⁺ and F-ions. *J. Ceram. Process. Res.* 14, 549–556.

Takemoto, S., Kusudo, Y., Tsuru, K., Hayakawa, S., Osaka, A., Takashima, S., 2004. Selective protein adsorption and blood compatibility of hydroxy-carbonate apatites. *J. Biomed. Mater. Res.* 69A, 544–551. <https://doi.org/10.1002/jbm.a.30039>

Tampieri, A., D'Alessandro, T., Sandri, M., Sprio, S., Landi, E., Bertinetti, L., Panseri, S., Pepponi, G., Goettlicher, J., Bañobre-López, M., Rivas, J., 2012.

- Intrinsic magnetism and hyperthermia in bioactive Fe-doped hydroxyapatite. *Acta Biomater.* 8, 843–851. <https://doi.org/10.1016/j.actbio.2011.09.032>
- Taylor, D., Lee, T.C., 2003. Microdamage and mechanical behaviour: predicting failure and remodelling in compact bone. *J. Anat.* 203, 203–211. <https://doi.org/10.1046/J.1469-7580.2003.00194.X>
- Ternane, R., Cohen-Adad, M.T., Panczer, G., Goutaudier, C., Kbir-Arighuib, N., Trabelsi-Ayedi, M., Florian, P., Massiot, D., 2002. Introduction of boron in hydroxyapatite: synthesis and structural characterization. *J. Alloys Compd.* 333, 62–71. [https://doi.org/10.1016/S0925-8388\(01\)01558-4](https://doi.org/10.1016/S0925-8388(01)01558-4)
- Thangavel, K., Balamurugan, A., Venkatachalam, T., Ranjith Kumar, E., 2016. Structural, morphological and optical properties of ZnO nano-fibers. *Superlattices Microstruct.* 90, 45–52. <https://doi.org/10.1016/J.SPML.2015.12.004>
- Thian, E.S., Huang, J., Best, S.M., Barber, Z.H., Bonfield, W., 2006. Novel silicon-doped hydroxyapatite (Si-HA) for biomedical coatings: An in vitro study using acellular simulated body fluid. *J. Biomed. Mater. Res. Part B Appl. Biomater.* 76B, 326–333. <https://doi.org/10.1002/JBM.B.30368>
- Tozar, A., Karahan, İ.H., 2018. A comprehensive study on electrophoretic deposition of a novel type of collagen and hexagonal boron nitride reinforced hydroxyapatite/chitosan biocomposite coating. *Appl. Surf. Sci.* 452, 322–336. <https://doi.org/10.1016/J.APSUSC.2018.04.241>
- Tsigkou, O., Jones, J.R., Polak, J.M., Stevens, M.M., 2009. Differentiation of fetal osteoblasts and formation of mineralized bone nodules by 45S5 Bioglass® conditioned medium in the absence of osteogenic supplements. *Biomaterials* 30, 3542–3550. <https://doi.org/10.1016/j.biomaterials.2009.03.019>
- Tsui, Y.C., Doyle, C., Clyne, T.W., 1998. Plasma sprayed hydroxyapatite coatings on titanium substrates. Part 2: Optimisation of coating properties. *Biomaterials* 19, 2031–2043. [https://doi.org/10.1016/S0142-9612\(98\)00104-5](https://doi.org/10.1016/S0142-9612(98)00104-5)

- Tunçay, E.Ö., Demirtaş, T.T., Gümüşderelioğlu, M., 2017. Microwave-induced production of boron-doped HAp (B-HAp) and B-HAp coated composite scaffolds. *J. Trace Elem. Med. Biol.* 40, 72–81. <https://doi.org/10.1016/J.JTEMB.2016.12.005>
- Turnbull, G., Clarke, J., Picard, F., Riches, P., Jia, L., Han, F., Li, B., Shu, W., 2018. 3D bioactive composite scaffolds for bone tissue engineering. *Bioact. Mater.* 3, 278–314. <https://doi.org/10.1016/j.bioactmat.2017.10.001>
- Uskoković, V., 2020. Ion-doped hydroxyapatite: An impasse or the road to follow? *Ceram. Int.* 46, 11443–11465 <https://doi.org/10.1016/j.ceramint.2020.02.001>
- Uysal, İ., Yılmaz, B., Evis, Z., 2020. Boron doped hydroxyapatites in biomedical applications. *J. Boron* 5, 192–201. <https://doi.org/10.30728/boron.734804>
- Uysal, T., Ustdal, A., Sonmez, M.F., Ozturk, F., 2009. Stimulation of bone formation by dietary boron in an orthopedically expanded suture in rabbits. *Angle Orthod.* 79, 984–990. <https://doi.org/10.2319/112708-604.1>
- Vacanti, J.P., Langer, R., 1999. Tissue engineering: The design and fabrication of living replacement devices for surgical reconstruction and transplantation. *Lancet* 354, 32–34. [https://doi.org/10.1016/s0140-6736\(99\)90247-7](https://doi.org/10.1016/s0140-6736(99)90247-7)
- Veljović, D., Čolić, M., Kojić, V., Bogdanović, G., Kojić, Z., Banjac, A., Palcevskis, E., Petrović, R., Janačković, D., 2012. The effect of grain size on the biocompatibility, cell–materials interface, and mechanical properties of microwave-sintered bioceramics. *J. Biomed. Mater. Res. Part A* 100A, 3059–3070. <https://doi.org/10.1002/JBM.A.34225>
- Von Euw, S., Wang, Y., Laurent, G., Drouet, C., Babonneau, F., Nassif, N., Azaïs, T., 2019. Bone mineral: new insights into its chemical composition. *Sci. Rep.* 9, 1–11. <https://doi.org/10.1038/s41598-019-44620-6>
- Wagoner Johnson, A.J., Herschler, B.A., 2011. A review of the mechanical behavior of CaP and CaP/polymer composites for applications in bone replacement and

- repair. *Acta Biomater.* 7, 16–30.
<https://doi.org/10.1016/J.ACTBIO.2010.07.012>
- Walthers, C.M., Nazemi, A.K., Patel, S.L., Wu, B.M., Dunn, J.C.Y., 2014. The effect of scaffold macroporosity on angiogenesis and cell survival in tissue-engineered smooth muscle. *Biomaterials* 35, 5129–5137.
<https://doi.org/10.1016/J.BIOMATERIALS.2014.03.025>
- Wang, G., Qian, G., Zan, J., Qi, F., Zhao, Z., Yang, W., Peng, S., Shuai, C., 2021. A co-dispersion nanosystem of graphene oxide @silicon-doped hydroxyapatite to improve scaffold properties. *Mater. Des.* 199, 109399.
<https://doi.org/10.1016/J.MATDES.2020.109399>
- Wang, J., Wang, L., Zhou, Z., Lai, H., Xu, P., Liao, L., Wei, J., Wang, Jiaolong, Wang, L., Zhou, Z., Lai, H., Xu, P., Liao, L., Wei, J., 2016. Biodegradable polymer membranes applied in guided Bone/tissue regeneration: A review. *Polymers (Basel)*. 8, 115. <https://doi.org/10.3390/polym8040115>
- Wang, L., Wang, C., Wu, S., Fan, Y., Li, X., 2020. Influence of the mechanical properties of biomaterials on degradability, cell behaviors and signaling pathways: Current progress and challenges. *Biomater. Sci.* 8, 2714–2733.
<https://doi.org/10.1039/d0bm00269k>
- Wang, S., Liu, L., Li, K., Zhu, L., Chen, J., Hao, Y., 2019. Pore functionally graded Ti6Al4V scaffolds for bone tissue engineering application. *Mater. Des.* 168, 107643. <https://doi.org/10.1016/J.MATDES.2019.107643>
- Wang, W., Yeung, K.W.K., 2017. Bone grafts and biomaterials substitutes for bone defect repair: A review. *Bioact. Mater.* 2, 224–247.
<https://doi.org/10.1016/J.BIOACTMAT.2017.05.007>
- Wang, X., Ao, Q., Tian, X., Fan, J., Wei, Y., Hou, W., Tong, H., Bai, S., 2016. 3D bioprinting technologies for hard tissue and organ engineering. *Mater. (Basel, Switzerland)* 9, 802. <https://doi.org/10.3390/ma9100802>

- Wang, X., Xu, S., Zhou, S., Xu, W., Leary, M., Choong, P., Qian, M., Brandt, M., Xie, Y.M., 2016. Topological design and additive manufacturing of porous metals for bone scaffolds and orthopaedic implants: A review. *Biomaterials* 83, 127–141. <https://doi.org/10.1016/J.BIOMATERIALS.2016.01.012>
- Wang, X., Zhang, Y., Lin, C., Zhong, W., 2017. Sol-gel derived terbium-containing mesoporous bioactive glasses nanospheres: In vitro hydroxyapatite formation and drug delivery. *Colloids Surfaces B Biointerfaces* 160, 406–415. <https://doi.org/10.1016/J.COLSURFB.2017.09.051>
- Webber, M.J., Khan, O.F., Sydlik, S.A., Tang, B.C., Langer, R., 2015. A perspective on the clinical translation of scaffolds for tissue engineering. *Ann. Biomed. Eng.* 43, 641–656. <https://doi.org/10.1007/s10439-014-1104-7>
- Woo, K.M., Chen, V.J., Ma, P.X., 2003. Nano-fibrous scaffolding architecture selectively enhances protein adsorption contributing to cell attachment. *J. Biomed. Mater. Res.* 67A, 531–537. <https://doi.org/10.1002/jbm.a.10098>
- Wu, C., Chang, J., 2013. A review of bioactive silicate ceramics. *Biomed. Mater.* 8, 1–12. <https://doi.org/10.1088/1748-6041/8/3/032001>
- Wu, C., Ramaswamy, Y., Chang, J., Woods, J., Chen, Y., Zreiqat, H., 2008a. The effect of Zn contents on phase composition, chemical stability and cellular bioactivity in Zn-Ca-Si system ceramics. *J. Biomed. Mater. Res. - Part B Appl. Biomater.* 87, 346–353. <https://doi.org/10.1002/jbm.b.31109>
- Wu, C., Ramaswamy, Y., Soeparto, A., Zreiqat, H., 2008b. Incorporation of titanium into calcium silicate improved their chemical stability and biological properties. *J. Biomed. Mater. Res. - Part A* 86, 402–410. <https://doi.org/10.1002/jbm.a.31623>
- Wu, S.-C., Hsu, H.-C., Hsiao, S.-H., Ho, W.-F., 2009. Preparation of porous 45S5 Bioglass®-derived glass–ceramic scaffolds by using rice husk as a porogen additive. *J. Mater. Sci. Mater. Med.* 20, 1229–1236. <https://doi.org/10.1007/s10856-009-3690-8>

- Wu, S.-C., Hsu, H.-C., Hsu, S.-K., Wang, W.-H., Ho, W.-F., 2011. Preparation and characterization of four different compositions of calcium phosphate scaffolds for bone tissue engineering. *Mater. Charact.* 62, 526–534. <https://doi.org/10.1016/J.MATCHAR.2011.03.014>
- Xiang, G., Zhang, J., Hao, Z., Zhang, X., Pan, G.H., Luo, Y., Zhao, H., 2015. Decrease in particle size and enhancement of upconversion emission through Y³⁺ ions doping in hexagonal NaLuF₄:Yb³⁺/Er³⁺ nanocrystals. *CrystEngComm* 17, 3103–3109. <https://doi.org/10.1039/c5ce00294j>
- Xue, W., Liu, X., Zheng, X. Bin, Ding, C., 2005. In vivo evaluation of plasma-sprayed wollastonite coating. *Biomaterials* 26, 3455–3460. <https://doi.org/10.1016/j.biomaterials.2004.09.027>
- Yang, X., Li, Y., He, W., Huang, Q., Zhang, R., Feng, Q., 2018. Hydroxyapatite/collagen coating on PLGA electrospun fibers for osteogenic differentiation of bone marrow mesenchymal stem cells. *J. Biomed. Mater. Res. - Part A* 106, 2863–2870. <https://doi.org/10.1002/jbm.a.36475>
- Yang, X., Xie, B., Wang, L., Qin, Y., Henneman, Z.J., Nancollas, G.H., 2011. Influence of magnesium ions and amino acids on the nucleation and growth of hydroxyapatite. *CrystEngComm* 13, 1153–1158. <https://doi.org/10.1039/C0CE00470G>
- Yazdanpanah, A., Kamalian, R., Moztafzadeh, F., Mozafari, M., Ravarian, R., Tayebi, L., 2012. Enhancement of fracture toughness in bioactive glass-based nanocomposites with nanocrystalline forsterite as advanced biomaterials for bone tissue engineering applications. *Ceram. Int.* 38, 5007–5014. <https://doi.org/10.1016/J.CERAMINT.2012.02.097>
- Ye, H., Liu, X.Y., Hong, H., 2009. Characterization of sintered titanium/hydroxyapatite biocomposite using FTIR spectroscopy. *J. Mater. Sci. Mater. Med.* 20, 843–850. <https://doi.org/10.1007/s10856-008-3647-3>
- Yedekçi, B., Tezcaner, A., Alshemary, A.Z., Yılmaz, B., Demir, T., Evis, Z., 2021.

- Synthesis and sintering of B, Sr, Mg multi-doped hydroxyapatites: Structural, mechanical and biological characterization. *J. Mech. Behav. Biomed. Mater.* 115, 104230. <https://doi.org/10.1016/j.jmbbm.2020.104230>
- Yilmaz, B., Alshemary, A.Z., Evis, Z., 2019. Co-doped hydroxyapatites as potential materials for biomedical applications. *Microchem. J.* 144, 443–453. <https://doi.org/10.1016/J.MICROC.2018.10.007>
- Yilmaz, B., Evis, Z., 2016. Boron-substituted bioceramics: A review. *J. Boron* 1, 6–14.
- Yilmaz, B., Pazarcevirin, A.E., Tezcaner, A., Evis, Z., 2020. Historical development of simulated body fluids used in biomedical applications: A review. *Microchem. J.* 155, 104713. <https://doi.org/10.1016/j.microc.2020.104713>
- Ying, X., Cheng, S., Wang, W., Lin, Z., Chen, Q., Zhang, W., Kou, D., Shen, Y., Cheng, X., Rompis, F.A., Peng, L., Zhu Lu, C., 2011. Effect of boron on osteogenic differentiation of human bone marrow stromal cells. *Biol. Trace Elem. Res.* 144, 306–315. <https://doi.org/10.1007/s12011-011-9094-x>
- Yurddaskal, M., Celik, E., 2018. Effect of halogen-free nanoparticles on the mechanical, structural, thermal and flame retardant properties of polymer matrix composite. *Compos. Struct.* 183, 381–388. <https://doi.org/10.1016/J.COMPSTRUCT.2017.03.093>
- Zadorozhnaya, O.Y., Khabas, T.A., Tiunova, O. V., Malykhin, S.E., 2019. Effect of grain size and amount of zirconia on the physical and mechanical properties and the wear resistance of zirconia-toughened alumina. *Ceram. Int.* 46, 9263–9270. <https://doi.org/10.1016/j.ceramint.2019.12.180>
- Zhang, B., Pei, X., Zhou, C., Fan, Y., Jiang, Q., Ronca, A., D'Amora, U., Chen, Y., Li, H., Sun, Y., Zhang, X., 2018. The biomimetic design and 3D printing of customized mechanical properties porous Ti6Al4V scaffold for load-bearing bone reconstruction. *Mater. Des.* 152, 30–39. <https://doi.org/10.1016/J.MATDES.2018.04.065>

- Zhang, H., Li, X., Wen, J., Zhao, C., 2017. Preparation and characterisation of HA/TCP biphasic porous ceramic scaffolds with pore-oriented structure. *Ceram. Int.* 43, 11780–11785. <https://doi.org/10.1016/J.CERAMINT.2017.06.014>
- Zhang, J., Liu, W., Schnitzler, V., Tancrét, F., Bouler, J.-M., 2014. Calcium phosphate cements for bone substitution: Chemistry, handling and mechanical properties. *Acta Biomater.* 10, 1035–1049. <https://doi.org/10.1016/J.ACTBIO.2013.11.001>
- Zhang, W., Zhu, Y., Li, J., Guo, Q., Peng, J., Liu, S., Yang, J., Wang, Y., 2016. Cell-derived extracellular matrix: Basic characteristics and current Applications in orthopedic tissue engineering. *Tissue Eng. Part B. Rev.* 22, 193–207. <https://doi.org/10.1089/ten.TEB.2015.0290>
- Zhang, X., Han, P., Jaiprakash, A., Wu, C., Xiao, Y., 2014. A stimulatory effect of Ca₃ZrSi₂O₉ bioceramics on cementogenic/osteogenic differentiation of periodontal ligament cells. *J. Mater. Chem. B* 2, 1415–1423. <https://doi.org/10.1039/c3tb21663b>
- Zhao, A., Xiong, B., Han, Y., Tong, H., 2022. Thermal decomposition paths of calcium nitrate tetrahydrate and calcium nitrite. *Thermochim. Acta* 714, 179264. <https://doi.org/10.1016/J.TCA.2022.179264>
- Zhao, C., Liu, W., Zhu, M., Wu, C., Zhu, Y., 2022. Bioceramic-based scaffolds with antibacterial function for bone tissue engineering: A review. *Bioact. Mater.* 18, 383–398. <https://doi.org/10.1016/J.BIOACTMAT.2022.02.010>
- Zhao, G., Huang, C., Liu, H., Zou, B., Zhu, H., Wang, J., 2013. Preparation of in-situ growth TaC whiskers toughening Al₂O₃ ceramic matrix composite. *Int. J. Refract. Met. Hard Mater.* 36, 122–125. <https://doi.org/10.1016/J.IJRMHM.2012.08.003>
- Zhou, H., Lee, J., 2011. Nanoscale hydroxyapatite particles for bone tissue engineering. *Acta Biomater.* 7, 2769–2781.

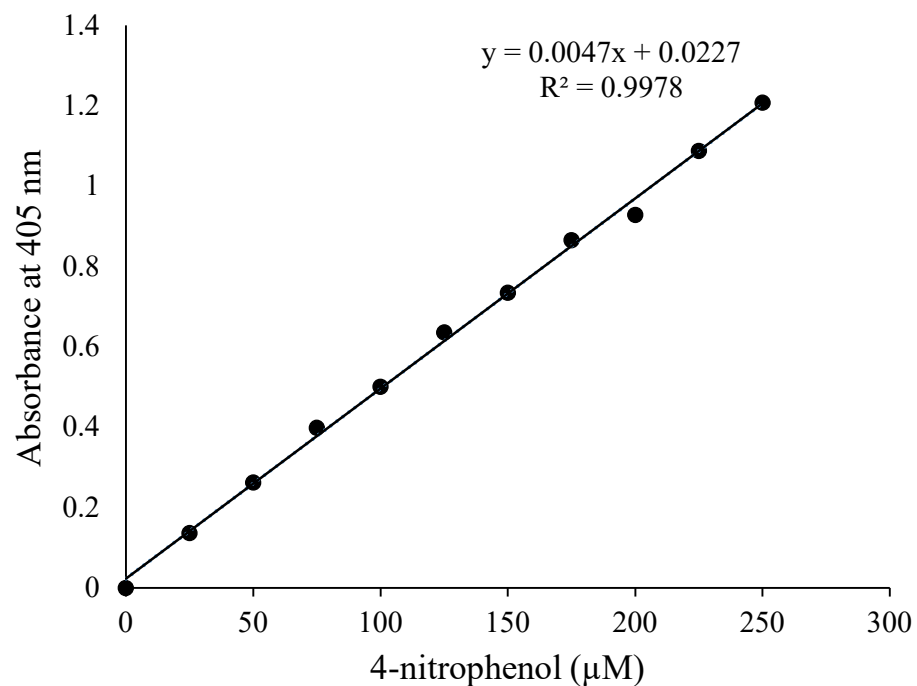
<https://doi.org/10.1016/j.actbio.2011.03.019>

Zhu, X.D., Fan, H.S., Xiao, Y.M., Li, D.X., Zhang, H.J., Luxbacher, T., Zhang, X.D., 2009. Effect of surface structure on protein adsorption to biphasic calcium-phosphate ceramics in vitro and in vivo. *Acta Biomater.* 5, 1311–1318. <https://doi.org/10.1016/J.ACTBIO.2008.11.024>

Zysset, P.K., Edward Guo, X., Edward Hoffler, C., Moore, K.E., Goldstein, S.A., 1999. Elastic modulus and hardness of cortical and trabecular bone lamellae measured by nanoindentation in the human femur. *J. Biomech.* 32, 1005–1012. [https://doi.org/10.1016/S0021-9290\(99\)00111-6](https://doi.org/10.1016/S0021-9290(99)00111-6)

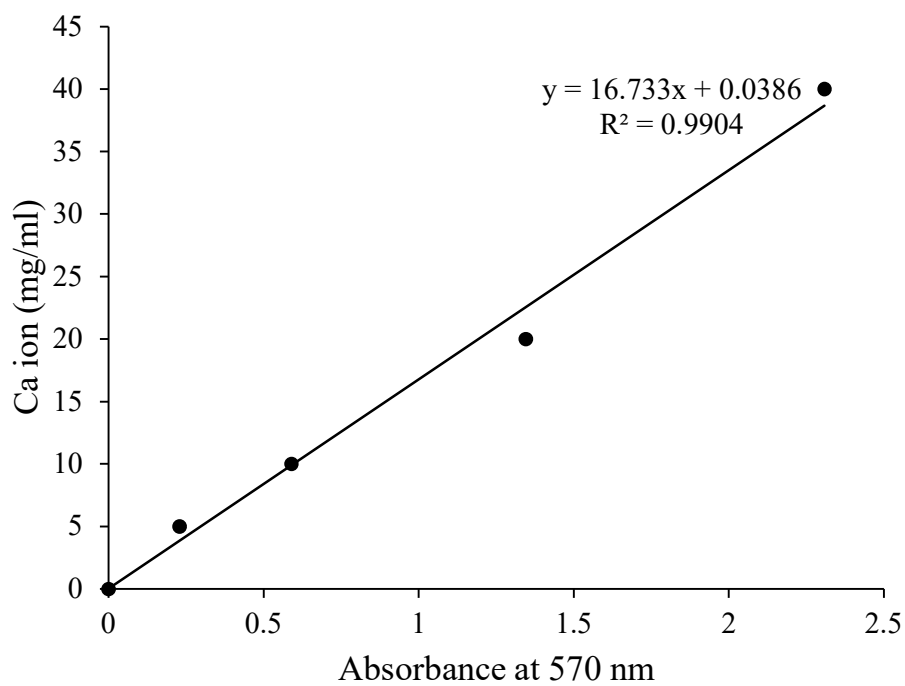
APPENDICES

A. Calibration Curve used to calculate ALP Activity



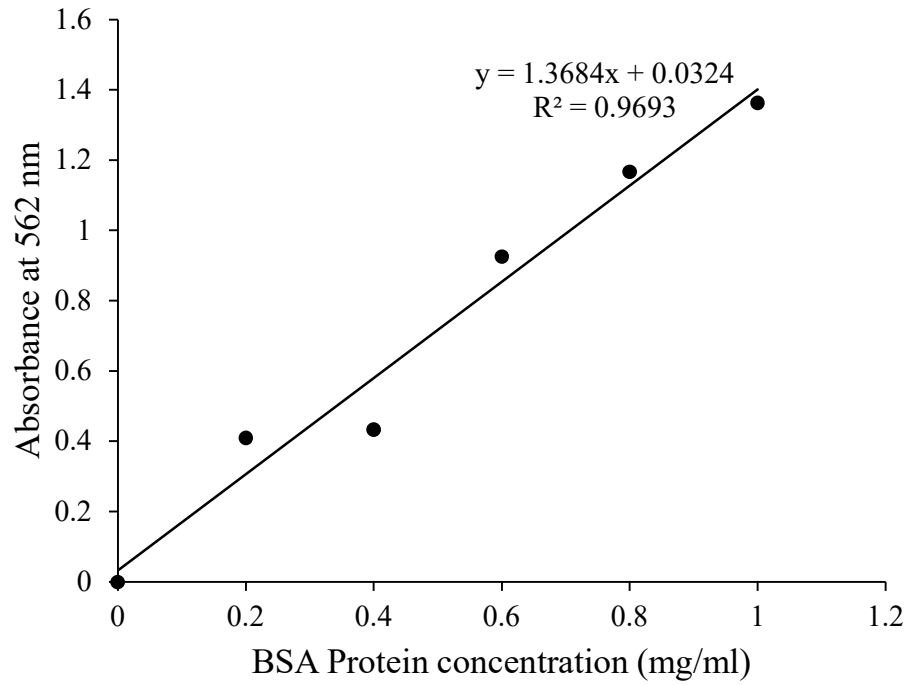
Appendix A1. Calibration curve determined by change in absorbance of different concentrations (0-250 μM) of 4-nitrophenol at 405 nm (n=3).

B. Calibration Curve Used to Calculate Intracellular Calcium



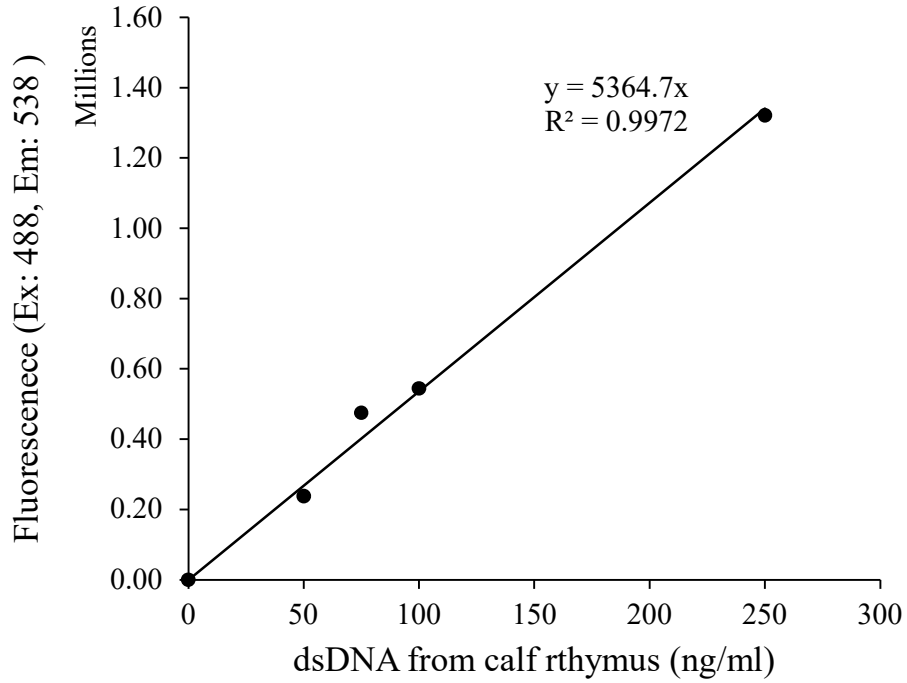
Appendix B1. Calibration curve determined by change in absorbance of different concentrations (0-40 mg/ml) of CaCl_2 at 570 nm (n=3).

C. Calibration Curve Used in BCA assay



Appendix C1. Calibration curve determined by change in absorbance of different concentrations (0-1.2 mg/ml) of BSA at 562 nm (n=3).

D. Calibration Curve Used to Calculate DNA Using Pricogreen Dye



Appendix D1. Calibration curve determined by changes in fluorescence intensity of different concentrations (0-250 ng/mL) of dsDNA from calf thymus (n=3).

CURRICULUM VITAE

PERSONAL INFORMATION

Surname, Name: Jodati, Hossein
Nationality: Iranian (I.R.I)
Date and Place of Birth: 7 September 1983, Tabriz
Marital Status: Married
Phone: +90 538 731 8356
email: hossein.jodati@metu.edu.tr

EDUCATION

Degree	Institution	Year of Graduation
MS	METU Biomedical Engineering	2015
BS	Uni. of Tabriz Mechanical Engineering	2007
High School	Alborz High School, Tehran, Iran	2001

FOREIGN LANGUAGES

Advanced English, Fluent Turkish, Native Farsi, Native Azari

PUBLICATIONS

1. Jodati H., Tezcaner A., Evis Z., Alshemary A.Z., Çelik E., 2022. Synthesis of baghdadite using modified sol-gel route and investigation of its properties for bone treatment applications. *J Korean Ceram Soc.*,1-18. <https://doi.org/10.1007/S43207-022-00275-0>
2. Lakrat M., Jodati H., Mejdoubi E.M., Evis Z., 2022. Synthesis and characterization of pure and Mg, Cu, Ag, and Sr doped calcium-deficient hydroxyapatite from brushite as precursor using the dissolution-precipitation method. *Powder Technol.* 413, 118026. <https://doi.org/10.1016/J.POWTEC.2022.118026>

3. Jodati H., Tezcaner A., Alshemary A.Z., Şahin V., Evis Z., Effects of the doping concentration of boron on physicochemical, mechanical, and biological properties of hydroxyapatite. *Ceram Int.* 48 (16), 22743–22758. <https://doi.org/10.1016/J.CERAMINT.2022.04.058>
4. Jodati H., Yilmaz B., Evis Z., 2021. In vitro and in vivo properties of graphene-incorporated scaffolds for bone defect repair. *Ceram Int.* 47(21), 29535–29549. <https://doi.org/10.1016/J.CERAMINT.2021.07.136>
5. Kaya Y., Jodati H., Evis Z., 2021. Effects of biomimetic synthesis route and sintering temperature on physicochemical, microstructural, and mechanical properties of hydroxyapatite. *J Aust Ceram Soc.* 57(4), 1117–1129. <https://doi.org/10.1007/s41779-021-00609-x>
6. Jodati H., Yilmaz B., Evis Z., 2020. A review of bioceramic porous scaffolds for hard tissue applications: Effects of structural features. *Ceram Int.* 46(10),15725–15739. <https://doi.org/10.1016/j.ceramint.2020.03.192>
7. Jodati H., Yilmaz B., Evis Z., 2020. Calcium zirconium silicate (baghdadite) ceramic as a biomaterial. *Ceram Int.* 46(14), 21902–21909. <https://doi.org/10.1016/j.ceramint.2020.06.105>
8. Jodati H., Güner B., Evis Z., Keskin D., Tezcaner A., 2020. Synthesis and characterization of magnesium-lanthanum dual doped bioactive glasses. *Ceram Int.* 46, 10503-10511. <https://doi.org/10.1016/j.ceramint.2020.01.050>
9. Jodati H., Erdekli Y.K., Tokdemir O.B., Evis Z., 2020. Global Scientific Research Trend on Hydroxyapatite and Scaffold During the Period of 1991-2019: A Bibliometric Analysis. *Ceram Mod Technol.* 2(1), 38–49. <https://doi.org/10.29272/CMT.2019.0014>
10. Sahin V., Jodati H., Evis Z., 2019. Effect of storage time on mechanical properties of extended-pour irreversible hydrocolloid impression materials. *J. Prosthet Dent.* 124(1), 69–74. <https://doi.org/10.1016/j.prosdent.2019.09.001>
11. Şahin V., Jodati H., Evis Z., 2018. Effect of storage time on tear strength of extended-pour irreversible hydrocolloid impression materials. *Süleyman Demirel Üniversitesi Sağlık Bilim Derg.* 9(3), 26–30. <https://doi.org/10.22312/SDUSBED.326886>